

JYU DISSERTATIONS 852

---

Jussi Louko

# Probing Neutron Deficient Trans-Lead Nuclei with $\gamma$ -Ray Spectroscopy Using In-Flight Separator and Recoil-Decay Tagging Method

---



UNIVERSITY OF JYVÄSKYLÄ  
FACULTY OF MATHEMATICS  
AND SCIENCE

JYU DISSERTATIONS 852

---

Jussi Louko

# Probing Neutron Deficient Trans-Lead Nuclei with $\gamma$ -Ray Spectroscopy Using In-Flight Separator and Recoil-Decay Tagging Method

Esitetään Jyväskylän yliopiston matemaattis-luonnontieteellisen tiedekunnan suostumuksella  
julkisesti tarkastettavaksi Ylistönrinteen auditoriossa FYS1  
joulukuun 13. päivänä 2024 kello 12.

Academic dissertation to be publicly discussed, by permission of  
the Faculty of Mathematics and Science of the University of Jyväskylä,  
in Ylistönrinne, auditorium FYS1, on December 13, 2024, at 12 o'clock noon.



JYVÄSKYLÄN YLIOPISTO  
UNIVERSITY OF JYVÄSKYLÄ

JYVÄSKYLÄ 2024



Editors

Ilari Maasilta

Department of Physics, University of Jyväskylä

Timo Hautala

Open Science Centre, University of Jyväskylä

Copyright © 2024, by the author and University of Jyväskylä

ISBN 978-952-86-0403-7 (PDF)

URN:ISBN:978-952-86-0403-7

ISSN 2489-9003

Permanent link to this publication: <http://urn.fi/URN:ISBN:978-952-86-0403-7>

## ABSTRACT

Louko, Jussi

Probing neutron deficient trans-lead nuclei with  $\gamma$ -ray spectroscopy using in-flight separator and recoil-decay tagging method

This thesis describes the experimental setup, techniques, and analysis methods employed in the experiment probing neutron-deficient trans-lead nuclei  $^{213}\text{Ac}$ ,  $^{211}\text{Ac}$ , and  $^{211}\text{Ra}$ . Particular attention is given to certain aspects of the used correlation techniques. The nuclei were produced using  $^{180}\text{Hf}(^{37}\text{Cl}, 4n)^{213}\text{Ac}$ ,  $^{175}\text{Lu}(^{40}\text{Ar}, 4n)^{211}\text{Ac}$ , and  $^{175}\text{Lu}(^{40}\text{Ar}, 1p3n)^{211}\text{Ra}$  fusion-evaporation reactions. The reaction products were separated using in-flight separator MARA and identified at its focal plane using the recoil-decay-tagging method. Extended level schemes were established for these nuclei. Level-energies of the low-lying yrast states in the  $^{213}\text{Ac}$  and  $^{211}\text{Ac}$  follow the analogue states in  $^{212}\text{Ra}$  and  $^{210}\text{Ra}$ , respectively.

This thesis also discusses the differences and advantages between the MARA and RITU separators, especially from the perspective of the heavy element studies. Upgrades to the RITU's focal plane setup are also presented. The thesis also introduces the newly developed and built automatic liquid nitrogen system made for cooling germanium detectors down to cryogenic temperatures.

Keywords: Nuclear physics, Spectroscopy, MARA, RITU, JUROGAM 3, Liquid nitrogen, Actinium, Radium,  $^{211}\text{Ac}$ ,  $^{212}\text{Ac}$ ,  $^{213}\text{Ac}$ ,  $^{211}\text{Ra}$

## TIIVISTELMÄ

Louko, Jussi

Raskaiden neutronivajaiden ytimien tutkimus gammaspektroskopiaa, rekyyli-separaattoria ja rekyyli-hajoamis-merkitsemistä hyödyntäen

Tämä väitöskirjatyö käsittelee koetta, jossa raskaita neutronivajaita ytimiä  $^{213}\text{Ac}$ ,  $^{211}\text{Ac}$  ja  $^{211}\text{Ra}$  tutkittiin  $\gamma$ -spektroskopian avulla. Ytimet tuotettiin käyttäen  $^{180}\text{Hf}(^{37}\text{Cl}, 4n)^{213}\text{Ac}$ ,  $^{175}\text{Lu}(^{40}\text{Ar}, 4n)^{211}\text{Ac}$  ja  $^{175}\text{Lu}(^{40}\text{Ar}, 1p3n)^{211}\text{Ra}$  fuusiohöyrystys reaktioita. Syntyneet energeettiset rekyylit ohjattiin MARA separaattorin läpi fokustasolle, jossa ne tunnistettiin ja merkittiin  $\alpha$ -hajoamisten avulla. Havaittujen  $\gamma$ -siirtymien avulla näille ytimille pystyttiin laatimaan tasokaaviot ja vertaamalla niitä  $^{212}\text{Ra}$  ja  $^{210}\text{Ra}$  ytimiin, havaittiin tiettyjen tilojen välillä selvä korrelaatio.

Tässä väitöstyössä käydään läpi kokeeseen käytetty koelaitteisto ja analyysimenetelmät, sekä keskustellaan tietyistä vaaranpaikoista korrelaatiotekniikoissa. Työssä vertaillaan myös MARA ja RITU separaattoreiden eroja ja etuja erityisesti liittyen raskaiden ytimien tutkimukseen. Myös päivitykset RITU:n fokusteroon käydään läpi. Lisäksi esitellään uusi automaattinen nestetyypijäähdytysjärjestelmä, joka on tarkoitettu germaniumilmaisimien jäähdyttämiseen kryogeenisiin lämpötiloihin.

Avainsanat: Ydinfysiikka, Spektroskopia, MARA, RITU, JUROGAM 3, Nestetyppi, Aktinium, Radium,  $^{211}\text{Ac}$ ,  $^{212}\text{Ac}$ ,  $^{213}\text{Ac}$ ,  $^{211}\text{Ra}$

<b>Author</b>	MSc Jussi Louko Department of Physics University of Jyväskylä Finland
<b>Supervisors</b>	Dr Juha Uusitalo Department of Physics University of Jyväskylä Finland  Dr Kalle Auranen Department of Physics University of Jyväskylä Finland
<b>Reviewers</b>	Dr Karl Hauschild IJCLab, IN2P3-CNRS Université Paris-Saclay France  Dr Andrej Herzán Institute of Physics Slovak Academy of Sciences Slovak Republic
<b>Opponent</b>	Dr Kerttuli Helariutta Department of Physics University of Helsinki Finland



## PREFACE

The work presented in this thesis has been carried out at the Accelerator Laboratory of the University of Jyväskylä between 2019–2024.

First I want to thank my supervisors, Dr Juha Uusitalo and Dr Kalle Auranen, for their guidance during this thesis work and for proofreading the manuscripts. Thanks to Prof Rauno Julin for the excellent comments on the actinium manuscript. I would also like to express my gratitude towards the entire nuclear spectroscopy group, all the other colleagues, and my friends, and family. A big thanks to Anssi Ikonen and Dr Panu Rahkila for helping with  $\text{LN}_2$  shenanigans. Thanks to Kai Porras, Risto Kronholm, Marko Puskala, and Juha Tuunanen for dealing with my endless requests to order different things. Thanks to Einari Periainen for helping machining of urgent parts that “had to be ready yesterday”. Thanks to all the other technical personnel as well as to the department’s administrative staff. I also gratefully acknowledge the financial support from the Doctoral School of the University of Jyväskylä.


Keen-eyed readers might have already noticed that the nuclei studied in this work are rather heavy, but the experiment was still performed using MARA, which is not exactly designed for these kinds of experiments. This was due to the pandemic, which pushed the experiments that the author initially planned to do with international collaborators into the unforeseeable future. For the same reason, the experiment schedule was reorganised, as the groups could only perform experiments with the local personnel. It was then decided that an experiment aiming to study neutron-deficient actinium isotopes with RITU and the JUROGAM 3 setup, proposed by Dr K. Auranen, would be performed earlier than what was initially planned, and the author would get to have the data from that. However, the upgrade of RITU was not yet finished, and thus, it could not be used. The experiment was switched to MARA instead, which made these nuclei among the heaviest studied with it at the time. Even though the experiment should have been doable with MARA in principle, the success was still a little bit uncertain due to the expected lower transmission of MARA. However, after the initial test runs, it became clear that MARA was performing well even in this heavy mass region and in the end, the transmission ended up being comparable to what it would have been at RITU.

I would like to emphasize that any of this would not be possible without the cooperation between the different research groups, technical staff, and international collaborators, who come together even during the exceptional times. One should remember that most of the devices are being designed, built, and maintained by in-house personnel. Tedious work is always going on behind the curtains to keep the experiments running.

Jyväskylä, November 2024

Jussi Louko

## LIST OF INCLUDED ARTICLES

- [1] J. Louko  0000-0001-6645-9293, K. Auranen, J. Uusitalo, A. D. Briscoe, T. Grahn, P. T. Greenlees, A. Illana, H. Joukainen, R. Julin, H. Jutila, M. Leino, M. Luoma, J. Ojala, J. Pakarinen, A. Raggio, P. Rahkila, J. Romero, P. Ruotsalainen, M. Sandzelius, J. Sarén, A. Tolosa-Delgado and G. Zimba. *Phys. Rev. C* 110 (2024). DOI: [10.1103/PhysRevC.110.034311](https://doi.org/10.1103/PhysRevC.110.034311).

## AUTHOR'S CONTRIBUTION

During these doctoral studies, the author worked as a member of the Nuclear Spectroscopy Group (NSG) at the Accelerator Laboratory of the University of Jyväskylä (JYFL-ACCLAB). At this time, the author was involved in many projects. The upgrade of the RITU separator which included, for example, its integration into a new lab-wide Rockwell PLC-based control system and complete renewal of the focal plane setup. The author developed a new automatic liquid nitrogen filling system for the JUROGAM 3 germanium-detector array. The author also maintained the laboratory equipment and other infrastructure and wrote many scripts and programs for various purposes, ranging from system monitoring and integration to data analysis. The author participated in preparing and running experiments, public events, and laboratory assignments. In addition to coauthoring several peer-reviewed articles, published from the data collected in the experiments at JYFL-ACCLAB and GSI, the author analysed the data collected in the JR154 experiment, and published the results in the article, “*In-beam  $\gamma$ -ray spectroscopy of  $^{211,213}\text{Ac}$  and  $^{211}\text{Ra}$* ” [1], to which this work is based on.

# CONTENTS

ABSTRACT

TIIVISTELMÄ

PREFACE

LIST OF INCLUDED ARTICLES

AUTHOR'S CONTRIBUTION

CONTENTS

1	INTRODUCTION .....	11
1.1	Shell model.....	11
1.2	Beyond lead region.....	15
2	EXPERIMENTAL METHODS AND THE SETUP .....	18
2.1	Nuclear reactions and radioactive decays.....	19
2.1.1	Fusion-evaporation.....	21
2.1.2	Decays.....	23
2.2	Beam.....	25
2.3	Target.....	26
2.4	Detector types .....	26
2.5	Target position and the JUROGAM 3 spectrometer .....	29
2.5.1	Germanium detectors.....	29
2.5.2	Bismuth germanium oxide shields .....	31
2.6	In-flight recoil separators MARA and RITU .....	32
2.7	Focal plane .....	36
2.7.1	Double-sided silicon-strip detector .....	37
2.7.2	Multi-wire proportional counter .....	39
2.7.3	“Tunnel” detectors.....	40
2.7.4	“Punch-through” detectors.....	41
2.7.5	Focal plane germanium-detector array .....	41
3	NEW AUTOMATIC LIQUID NITROGEN FILLING SYSTEM.....	43
3.1	Problems with the old system .....	45
3.2	The new design .....	46
3.3	Performance.....	55
4	DATA ACQUISITION .....	57
4.1	Signal chain .....	57
4.2	Digitisers, merger, and filewriter .....	59
4.3	Data format.....	62
5	ANALYSIS.....	64
5.1	Parsing the data .....	65
5.2	Building logical events.....	66
5.3	Identifying, tagging, and correlating .....	69



5.4	Energy calibration .....	75
5.5	Relative detection efficiency and angular distributions.....	77
5.6	Statistical methods, uncertainty analysis, and background .....	80
5.7	Setup limitations and things to watch out for .....	84
5.7.1	Nanosecond scale isomeric states .....	84
5.7.2	Contaminants and other reaction channels.....	86
5.7.3	Sorting biases .....	86
6	JR154: PROMPT AND DELAYED $\gamma$ -RAY SPECTROSCOPY OF NEUTRON DEFICIENT TRANS-LEAD NUCLEI.....	93
6.1	Summary of $^{213}\text{Ac}$ , $^{211}\text{Ac}$ , and $^{211}\text{Ra}$ .....	93
6.2	Odd-odd isotope $^{212}\text{Ac}$ .....	95
6.3	Isomeric states in $^{177}\text{Ir}$ .....	96
6.4	Towards the drip line and remeasuring radium isotopes .....	98
7	SUMMARY .....	103
	REFERENCES.....	104
	INCLUDED ARTICLE .....	113

# 1 INTRODUCTION

The existence of the atomic nucleus results from the interplay between the fundamental forces. Peering deep down into this extremely dense state of matter can provide answers to many interesting questions about the nature of the universe. Atomic nucleus consist of protons and neutrons, both of which are fermions, and thus those obey the Pauli's exclusion principle. This means that nuclei are true quantum many-body objects. Many theories have been developed to model the structure and properties of nuclei, however, the nature of the nuclear force, that is the residual interaction between quarks, is complex and not well understood. As such, several open questions still remain. One of the reasons why experimental studies are needed is that they can provide inputs for these theoretical models and make sure that they accurately represent the reality. Measurements can also provide valuable clues for the theorists to which way to go to uncover the true nature of the nuclear matter and interactions that govern it. No new theoretical calculations were performed in this work, but as a context for some of the terminology and discussions used in the later chapters, and in the appended article, a brief overview of the relevant nuclear theory concepts as well as some further motivation for the work is given in this chapter.

## 1.1 Shell model

Since the quantum many-body problem is very hard to solve exactly from first principles, simple approximate models had to be developed to model nuclei. One of the earliest modern nuclear models was the liquid-drop model (Bethe-Weizsäcker formula) [1, 2]. It modelled the nucleus as an incompressible fluid and managed to reproduce some macroscopic properties, such as the nuclear binding energies, relatively well. However, it could not properly explain some other experimental observations, namely, the increased stability of nuclei with specific number of protons and/or neutrons i.e. the magic numbers (2, 8, 20, 28, 50, 82, 126). For this, a quantum approach was needed. The first theory to

explain the magic numbers was the spherical single-particle shell model [3–7]. These simple models also managed to predict several ground-state properties of nuclei decently. Those also work for some excited states close to shell closures, but begin to deviate when multiple particles start to contribute. The idea of the shell model was adapted from other many-fermion systems, such as the electron orbitals, that exhibit similar behaviour.

The single-particle shell model treats a nucleus as a collection of particles that move in a central potential created by all the other nucleons of the same nucleus. The exact shape of this potential depends on the model and on the nucleus. The potential and the order of the orbitals also slightly differs for the neutrons and protons due to the Coulomb force. Since no two identical fermions can occupy the same state, only a limited number of single-particle states can exist at lower energies. Above the potential, many states lie close in energy in a domain called the continuum. However, the stability of the nucleus also decreases dramatically above the barrier.

Simple spherically symmetric central potentials, such as the harmonic oscillator and Woods-Saxons potential, alone cannot correctly predict the shell structure of single-particle states. For this, an additional non-central term is needed. The spin-orbit interaction, also known as the spin-orbit coupling, was introduced to describe the part of the residual interactions that are not accounted for by the simple potentials [4, 5, 8, 9]. The origin of spin-orbit interaction is more complicated than the analog phenomena in electrons shells. According to the current models, the three most dominant components of the spin-orbit interaction are tensor force (configuration mixing) [10], two-body force (NN, LS, spin-orbit force), and three-body force (3N) [11]. However, the significance of higher-body interactions are not yet completely understood, but these probably are not negligible [12, 13]. Sometimes the spin-orbit interaction is used to reference only the LS dependent term. Regardless of the origin, the spin-orbit interaction effectively reduces or increases the energy of a state depending on whether the spin of a nucleon is parallel or antiparallel to the orbital angular momentum, which in turn causes specific orbitals to split.

The order of single-particle orbitals are not fixed. The importance of the different components of the spin-orbit interaction depend on the nuclei, and consecutively, the ordering evolves along the nuclear landscape [14]. In some nuclei, an intruder configuration can even become the ground state as the energy gained from the residual interactions, or shape, can flip the order the orbitals, predicted by some simpler models. Even the magic numbers can change far from the stability [15].

In the context of the single-particle shell models states are indicated using the modified spectroscopic notation:  $nl_j$ , where  $n$  is the principal quantum number (sometimes counted from 0, sometimes from 1),  $l$  is the orbital angular momentum quantum number, and  $j$  indicates the (individual) total angular momentum. A state in this scheme can fit  $2j + 1$  nucleons due to the degeneracy in the magnetic quantum number  $m_j$ . For historical reasons, the orbital angular momentum is denoted with letters:  $0 = s$ ,  $1 = p$ ,  $2 = d$ ,  $3 = f$ ,  $4 = g$ ,  $5 = h$ ,  $6 = i$ ,  $7 = j$ ,

and so on. The principal quantum number is sometimes omitted in the notation, since it depends on the potential, and it is not very important for practical purposes. For example, the  $h_{9/2}$  proton orbital, which is of particular importance for the single-particle states of the actinium isotopes studied in this work, actually refers to the  $1h_{9/2}$  orbital within a shell model calculation that includes a spin-orbit interaction. The  $1h_{9/2}$  orbital can hold a maximum of 10 nucleons, of which 7 are occupied in the ground state of actinium. As mentioned, the ordering of the orbitals depends on the model, but other relevant nearby orbitals for this work include  $2f_{7/2}$  and  $1i_{13/2}$  proton orbitals and  $3p_{1/2}$ ,  $2f_{5/2}$ , and  $3p_{3/2}$  neutron orbitals.

The total angular momentum, the nuclear spin, of a state is the vector sum of the angular momentum of the individual nucleons including the orbital and intrinsic spin angular momentum. The nuclear spin is denoted with  $J$  (or  $I$ ). Another intrinsic property of a nuclear state is the parity. Parity indicates how the nucleus (wave function) would behave if the spatial positions of the nucleons are mirrored. The parity can be either even (symmetric), if the mirrored nucleus is identical or odd (antisymmetric) if not. In the level schemes of nuclei the total nuclear spin and parity of a state is denoted  $J^\pi$ , where  $\pi$  is the parity, and it is indicated by symbols  $+$  or  $-$ , for even and odd, respectively.

Predicting the nuclear spin of a heavy nucleus would be very difficult, however, nucleons have a strong tendency to pair up to cancel their spins (pairing correlations), as indicated by the fact that the ground states of all even-even nuclei have spin and parity of  $0^+$ . The ground states of the odd-even and even-odd nuclei, on the other hand, all have a half-integer spin, i.e. the spin of the unpaired particle. Due to the pairing, it is sometimes advantageous to think of certain states in terms of quasi-particles rather than particles. Such "hole states" arise from the unfilled positions of the orbitals instead of filled [16]. However, the problem becomes much more challenging for multiparticle states as a very accurate understanding of the strength of the residual interaction is required. The seniority scheme is a more general case of the pairing and it can, in some cases, help to predict state configurations and spins [16].

In addition to the single-particle states and the quantum properties, nuclei can also exhibit collective phenomena where several nucleons, or even the whole nucleus, act as one entity. One such property, that is relevant for this work, is the shape of the nucleus. Simple single-particle shell models cannot account for these collective effects due to the spherical potential and many-particle involvement. More sophisticated shell models introduced deformations to address this problem. For example, the Nilsson model (deformed shell model) [17] uses a deformation dependent potential to catch some collective and single-particle effects. One of the simplest deformations is the quadrupole deformation that effectively elongates or squashes a sphere along its symmetry axes. The resulting nuclei are called prolate, oblate or triaxially deformed depending on the magnitude and direction of the axis on which the deformation acts. Prolate- and oblate-deformed nuclei are not fundamentally more special or rare, in fact, those can be found throughout the entire nuclear landscape. However, nuclei at and close to the

shell closures tend to have more spherical ground states and deformation develops when nucleons are removed from these orbitals. These shell effects appear very distinctively in the theoretical ground-state deformation calculations by Hilaire and Girod [18], shown in the top plot in Figure 1.

Whilst the modern extensions of the single-particle shell model can describe both, the macroscopic, and the microscopic properties of nuclei relatively well, those are still just approximations of the underlying many-body problem. The currently available computational power is nowhere near enough to solve the Schrödinger equation for massive nuclei, such as the ones studied in this experiment. For example, the exact solution for the actinium nucleus would involve

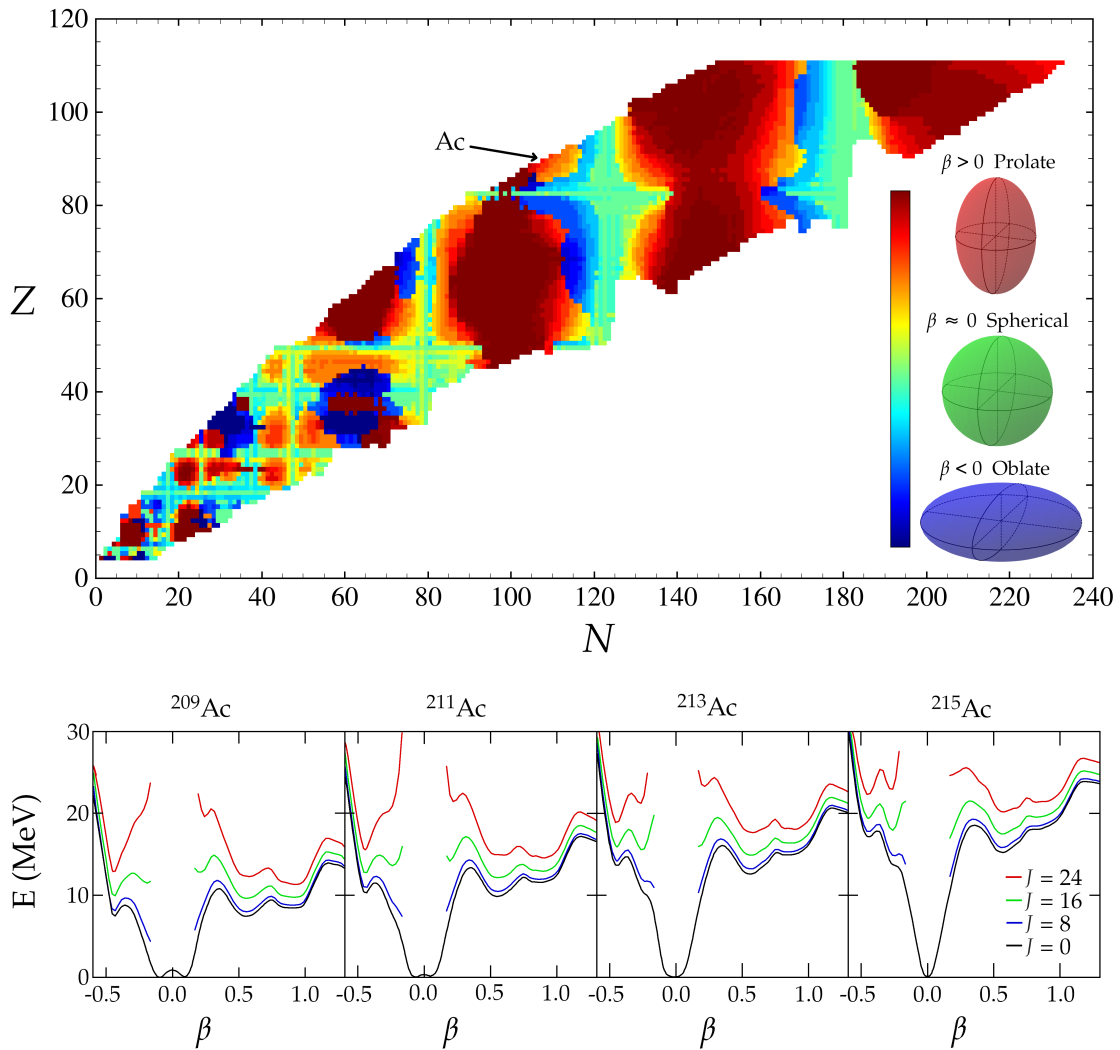


FIGURE 1 Top: ground-state deformation,  $\beta$ , is plotted across the nuclear landscape as predicted by the mean-field calculations by Hilaire and Girod [18]. The ground-state shape of the actinium nucleus is predicted to change from spherical to oblate and then to prolate when moving towards the proton drip line. Calculated angular momentum projected potential energy surfaces for selected actinium isotopes are shown in the bottom graphs. Data are also from References [18, 19]. Local minima predicted on higher energies and angular momenta can give rise to metastable isomeric states.

solving the Schrödinger equation with a matrix that would have more than  $10^{50}$  elements. However, some approximations can be made to reduce the complexity of these “ab initio” calculations. In the context of the shell models, one such simplification is the truncation method, in which some orbitals and nucleons are assumed to be inert and only a few nucleons and orbitals are active in the excitations. The model space is then restricted and effectively divided into three subspaces, the inert core, the valence space, and the inactive external space. The model space has to be selected so that it includes the most dominant components to keep predictions accurate. This is essentially the same idea as with the electron shells, where the valence electrons dominate the chemical properties of the atoms. Even though there are many codes (ANTOINE, NATHAN, OXBASH, MSHELL, NUSHELL, NUSHELLX,...) freely available to do these calculations, they become quite involved as they need the empirical two-body and three-body interaction strengths as an input. If no experimental data is available, some form of theoretical calculations are needed to approximate them. In the end, their accuracy rapidly diverge outside the fitting points and the results may not be good enough to be used to interpret the experimental results of heavier and exotic nuclei.

One complementary approach to these configuration-interaction shell models [20] are self-consistent mean-field methods [21]. In these methods the more complex effective single-particle potential is directly obtained using energy density functionals. Several methods exist to find these functionals and the approximate solutions to the Schrödinger equation [21, 22]. These mean-field methods are especially suited for macroscopic properties, which is why they were used for the aforementioned deformation calculations by Hilaire and Girod. Attempts have been also made to combine these two methods [23]. Beyond mean-field methods also incorporate the non-central interactions on to the mean-field.

## 1.2 Beyond lead region

Nuclei in the trans-lead,  $N < 126$  region, highlighted in Figure 2, have been studied at the Accelerator Laboratory of the University of Jyväskylä (JYFL-ACCLAB) for half a century [24–26]. These nuclei reside in the region where interesting collective phenomena of massive nuclei, shape changes, shape co-existence, and shape isomerism manifest. By studying the onset of the deformation and other shell effects when moving away from the near spherical nuclei in the vicinity of the  $Z = 82$  and  $N = 126$  magic numbers provides an excellent ground for testing and developing nuclear structure theories.

The past studies investigating odd-even astatine and francium nuclei in this region have shown that the level-energy systematics of the low-lying yrast states of these nuclei closely follow their respective even-even core analogue states [28–31]. However, due to the low production cross sections, no in-beam  $\gamma$ -ray spectroscopy studies have been performed in the actinium isotopes in this region. The models predict that the deformation should develop earlier in nuclei with

more protons when moving towards the proton drip line [18, 32]. Investigating whether the neutron-deficient actinium isotopes,  $^{213}\text{Ac}$  and  $^{211}\text{Ac}$ , already exhibit any of these interesting collective effects was one of the motivations of this work. Additionally, the actinium nuclei also mark a point in which the  $h_{9/2}$  proton orbital becomes more than half full, and it was not known what effect this has and if the inert-core and the “spectator” nucleon interpretation is still valid for the actinium nuclei.

In addition to more directly measurable indications of the deformation, such as the electric quadrupole moment, the deformation also leaves an identifiable fingerprint in the energy levels of the nuclei. The collective states of the spherical nuclei are formed from vibrations (phonons) whereas in the deformed nuclei the origins of the collective states are typically rotational [33, 34]. Vibrations and rotations can also exist simultaneously, and these can be also built on top of the single-particle states and vice versa.  $\gamma$ -ray spectroscopy provides a method to probe the development of the deformation in the higher energy and angular momentum states, before a change is observed for the ground state, by observing  $\gamma$ -rays from the characteristic de-excitation bands from collective states. Another indication of the shape change and the deformation is the appearance of longer-living isomeric states due to shallow local minima in the nuclear potential. Examples of the predicted development of the nuclear potential for selected actinium isotopes are shown in the bottom graphs in Figure 1

As said, no theoretical calculations were done in this work, as such, the interpretation of the observed states are purely based on the systematics of the nearby even-even nuclei. Namely,  $^{212}\text{Ra}$  and  $^{210}\text{Ra}$ , that were taken as the cores

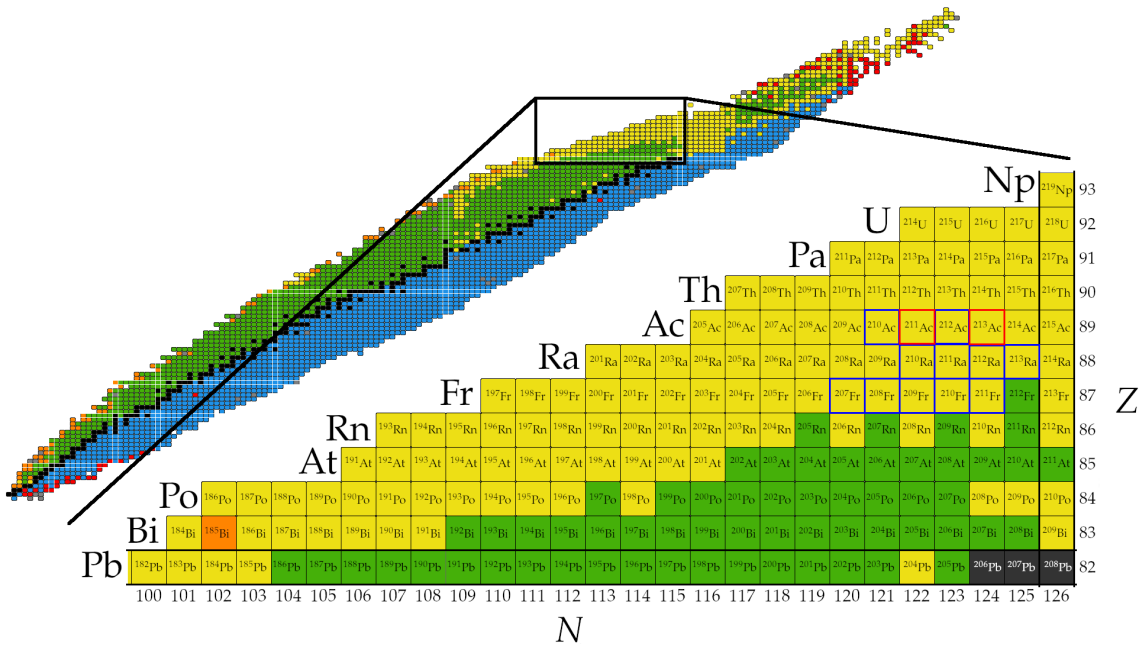


FIGURE 2 The nuclear region under investigation. Nuclei populated directly in this work are circled in red and blue.  $^{211,213}\text{Ac}$  were the primary nuclei of interest, but new information about  $^{211}\text{Ra}$  and some other nuclei were also obtained. Figure adapted from [27]



of the actinium isotopes. The nucleon configurations of the single-particle states in the radium cores have been proposed in the past works based on the semiempirical shell-model calculations [35]. As the present experimental observations show, the structure of the nuclei in question closely resemble their nearest even-even nuclei. Most states in the actinium nuclei are proposed to arise from the loose coupling of the odd nucleon to the core state.  $^{211}\text{Ra}$  states, on the other hand, are interpreted as a hole states coupled to  $^{212}\text{Ra}$  core states.

To avoid excessively repeating what has already been written in past works, this thesis attempts to approach the subject from a slightly more technical perspective and show how the instrumentation needs to be considered during the analysis. The thesis is divided into seven chapters, the first one being this introduction. In the second chapter, “[Experimental Methods and the Setup](#)”, the experimental setup, the detectors, and their operation principles are discussed. The third chapter, “[New automatic liquid nitrogen filling system](#)”, describes the design of the newly built  $\text{LN}_2$  filling system. This chapter also serves as a short technical documentation for the system. The fourth chapter, “[Data acquisition system](#)”, briefly introduces the data acquisition system. The fifth chapter, “[Analysis](#)”, discusses the code written to analyse this data, the associated techniques, and rarely mentioned intricacies. The sixth chapter “[JR154: Prompt and delayed  \$\gamma\$ -ray spectroscopy of neutron deficient trans-lead nuclei](#)” is about the obtained and published physics results from the present work. The last chapter, “[Summary](#)”, sums up this work. More details about the experiment and further discussion can be found in the included article I.



## 2 EXPERIMENTAL METHODS AND THE SETUP

The properties of nuclear matter and its interactions can be studied by observing energetic photons emitted when nuclei in excited states relax. Nuclei can end up in these excited states, for example, when they are formed in nuclear reactions, such as fusion. The fusion reaction can be experimentally induced by an energetic particle beam from an accelerator that is collided with stationary target nuclei. The energetic photons,  $\gamma$  rays, from these nuclei can then be observed and studied with a detector system around the target. This method is known as in-beam  $\gamma$ -ray spectroscopy.

For more than twenty years, the main in-beam experimental apparatus for the nuclear spectroscopy group at the JYFL-ACCLAB has been the JUROGAM germanium-detector array coupled with either the RITU gas-filled separator [25, 36], or more recently, the MARA vacuum-mode separator [37, 38] and their respective focal planes. Figure 3 depicts the MARA and RITU setups with the JUROGAM 3-array [39] and the focal planes from above. The target resides in the centre of the JUROGAM 3-array, after which MARA or RITU is used to separate the reaction products from the primary beam. Identification and selection of the nuclei of interest is done at the focal plane.

If the nucleus of interest is not the primary product in a reaction, distinguishing the  $\gamma$  rays belonging to it can be difficult as they are drowned in the vast background. In some cases, alternative reactions are not feasible, so instead, the peak-to-background ratio (P/B) has to be increased by some other means. The advantage of combining an in-flight separator with an in-beam  $\gamma$ -ray array is to leverage the power of sophisticated tagging techniques that would not work unless the high-intensity primary beam is first separated from the reaction products. One of these techniques is the so-called Recoil-Decay-Tagging (RDT) method [40]. In this type of experiment, a recoiling reaction product, a recoil, is implanted into a detector at the focal plane. If it undergoes a radioactive decay, it can be identified based on its characteristic decay properties. The RDT method provides a high selectivity and can be used to significantly enhance the P/B at the target position through correlations, which is why it was used in the present work to tag the  $^{211}\text{Ac}$ ,  $^{213}\text{Ac}$ , and  $^{211}\text{Ra}$  nuclei via their  $\alpha$ -decay properties.

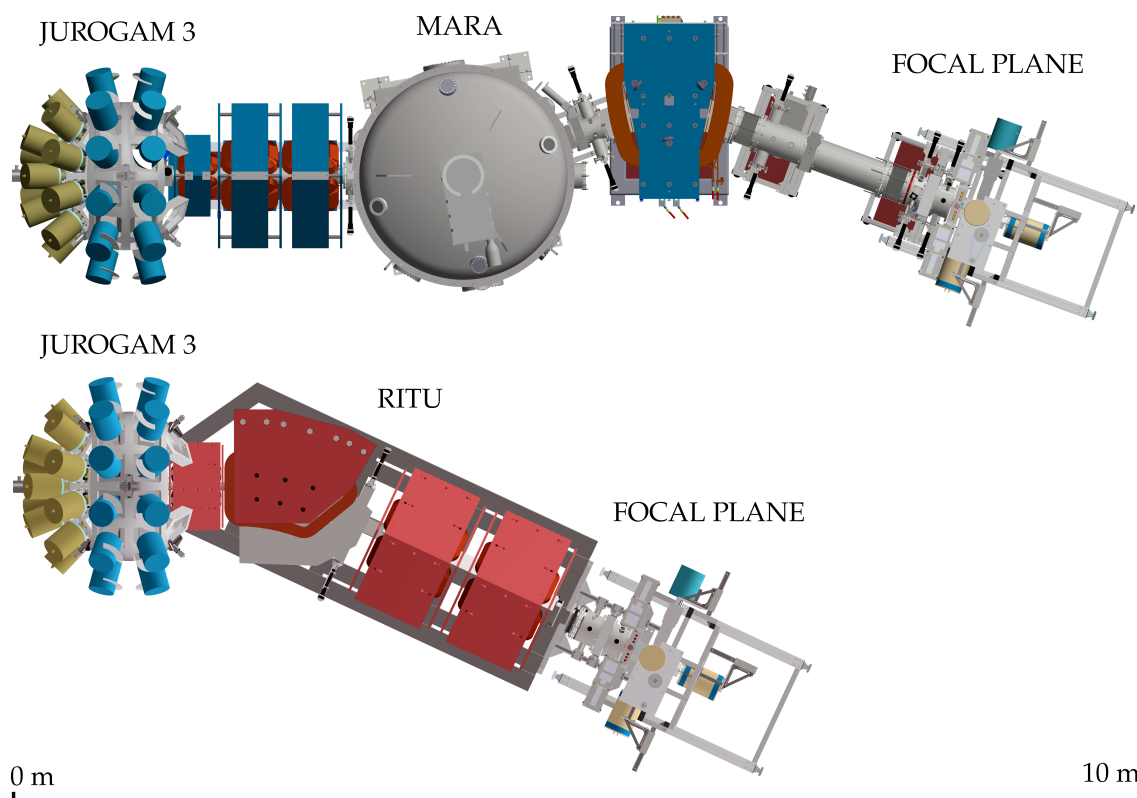


FIGURE 3 Top view of the MARA and RITU separators combined with the JUROGAM 3 and the focal plane setups. The JUROGAM 3 and the focal plane Ge-detector arrays are shared and can be easily swapped between the setups.

## 2.1 Nuclear reactions and radioactive decays

Exotic and excited nuclei can be produced in nuclear reactions. This work mainly discusses topics within the context of the accelerator-based physics. In this context, interacting particles are often preferred as a beam particle or a projectile and a target particle. Many nuclear reactions exist, such as fusion, fission, fragmentation, transfer, elastic, inelastic, and knockout reactions. Some reactions are direct, while others proceed via compound stages [41, 42].

In this work, the main focus will be on the fusion-evaporation reactions. However, it should be kept in mind that many reaction modes are always present in experiments. The likelihood of a particular reaction to take place greatly depends on the local microscopic conditions, namely the properties of the reacting nuclei, available energy, and the impact parameter (distance between the “centres” of the participant nuclei). While the beam energy might be optimised for a specific reaction channel, the beam particles or, subsequently, the reaction products sometimes hit unintended targets like surrounding materials. A completely different reaction mode can dominate in those conditions. An overview of the domains of some reaction modes as a function of the incident energy and impact parameter is shown in Figure 4. The experimental reaction rate correlates with the beam flux and the target number density, which, through dimensional analysis, has units of area, hence, the reaction probability is called a “cross section” [43].

Another relevant feature related to nuclear reactions is kinematics, i.e. the velocity distribution of the particles after the collision. When a projectile is lighter than the target particle, the reaction is said to be in normal kinematics. Inverse kinematics is the opposite. The reaction is called symmetric when a projectile and a target particle have similar masses. Kinematics does not play a role in the nuclear reaction per se, but the slowing down of the beam through the target volume can have the following effects. The energy loss of the beam within the target can change the average excitation energy at which the nuclei are produced and, thus to cross sections of different reaction channels. The energy loss also affects the average depth at which the reaction occurs, affecting the velocity distribution of the products after the target. Kinematics also directly affects the velocity distribution due to the conservation of energy and momentum. Optimal reaction kinematics depend on the experimental setup and the available beam and target materials. In principle, every setup has its own set of variables and weights to optimise to achieve the best result. With the setup used in this work, it is advantageous to have the heavy evaporation residues fly into as small a forward angle as possible with a narrow velocity distribution, whilst simultaneously trying to minimise all other reaction products from going through the separator.

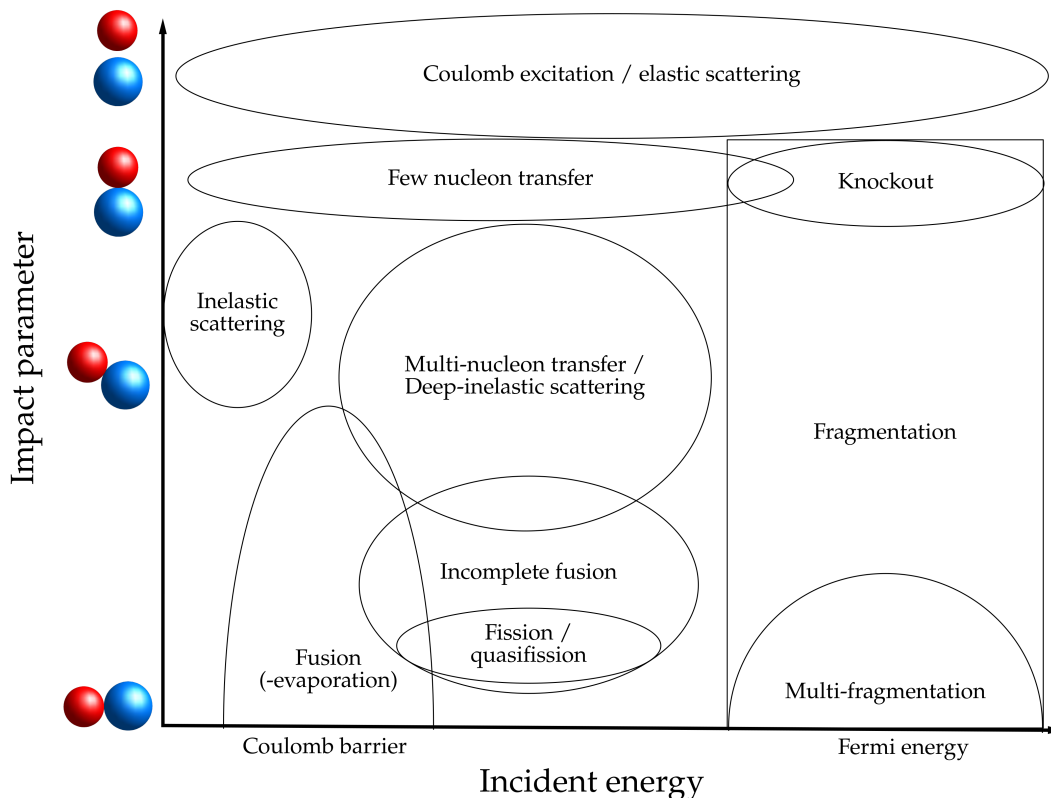


FIGURE 4 Some nuclear reaction types as a function of incident energy and impact parameter. During an experiment, the incident energy can be controlled, but not the impact parameter, which means that reactions within a vertical slice are present. Fusion-evaporation reactions are typically performed in the vicinity of the Coulomb barrier energy.

### 2.1.1 Fusion-evaporation

The fusion-evaporation reaction is the most regularly exploited reaction type in MARA and RITU experiments. In these reactions a beam and target particle undergoes a complete fusion. The compound nucleus then evaporates some number of neutrons, protons, or even smaller clusters, like  $\alpha$  particles to get rid of most of its excess excitation energy and angular momentum and reach a stage called evaporation residue. The minimum energy required for a fusion-evaporation reaction is generally taken as the Coulomb barrier energy, although slightly sub-barrier fusion is also possible through quantum mechanical tunnelling. The optimal beam energy needs to be adjusted for each evaporation channel. Instead of particle evaporation, the compound nucleus can also undergo fission. As a matter of fact, in the present work the fission branch was around 99.4%, according to the PACE4 [44, 45] calculations, which is typical for these heavy compound nuclei. Consequently, selecting the best beam-target combination and beam energy is a decent multivariate optimisation problem.

After ejecting some nucleons, the residues still have excess energy and angular momentum. One way the nuclei can get rid of the rest is by emitting  $\gamma$  rays, or electrons, if an internal conversion takes a place. The relaxation usually happens in femto to nanosecond scales. These quickly emitted  $\gamma$  rays are called prompt  $\gamma$  rays. The evaporation residues are also briefly aligned relative to the beam axis, which allows for measuring the angular distributions of the prompt  $\gamma$ -ray transitions. The angular distribution correlates with the properties of the transition. In some cases, the nuclei can end up in metastable states with lifetimes of several orders of magnitude longer than typical. The  $\gamma$  rays emitted after such states relax are called delayed  $\gamma$  rays. In general, the smaller the energy difference and/or larger the angular momentum difference between the initial and final states, the longer the initial state's lifetime is. A state can also have a longer lifetime for other reasons, such as when the final state has significantly different nucleon configuration. Electric transitions are generally faster than the equivalent magnetic ones [46]. Additionally, almost the only way the  $0^+ \rightarrow 0^+$  transitions can proceed is via an internal conversion, since no angular momentum is available for a photon to form [47].

Different nuclear reactions populate nuclei in certain regions of the nuclear chart more strongly than others, and the reaction products have distinct excitation energy and angular momentum distributions. Fusion-evaporation reactions tend to populate relatively high excitation energy and angular momentum states, which makes them suitable for studying a wide range of nuclear phenomena. The exact distribution depends on the number of evaporated particles, as illustrated in Figure 5. From the initial evaporation entry region, relaxation of the residues first progresses down in the excitation energy, until they reach the yrast line, below which no states are available at the same angular momentum. The relaxation then progresses along the yrast line via so-called yrast-cascades. The relative intensities of the observed transitions and their coincidences can be used to deduce the level structure of the nuclei albeit sometimes it can be somewhat challenging.

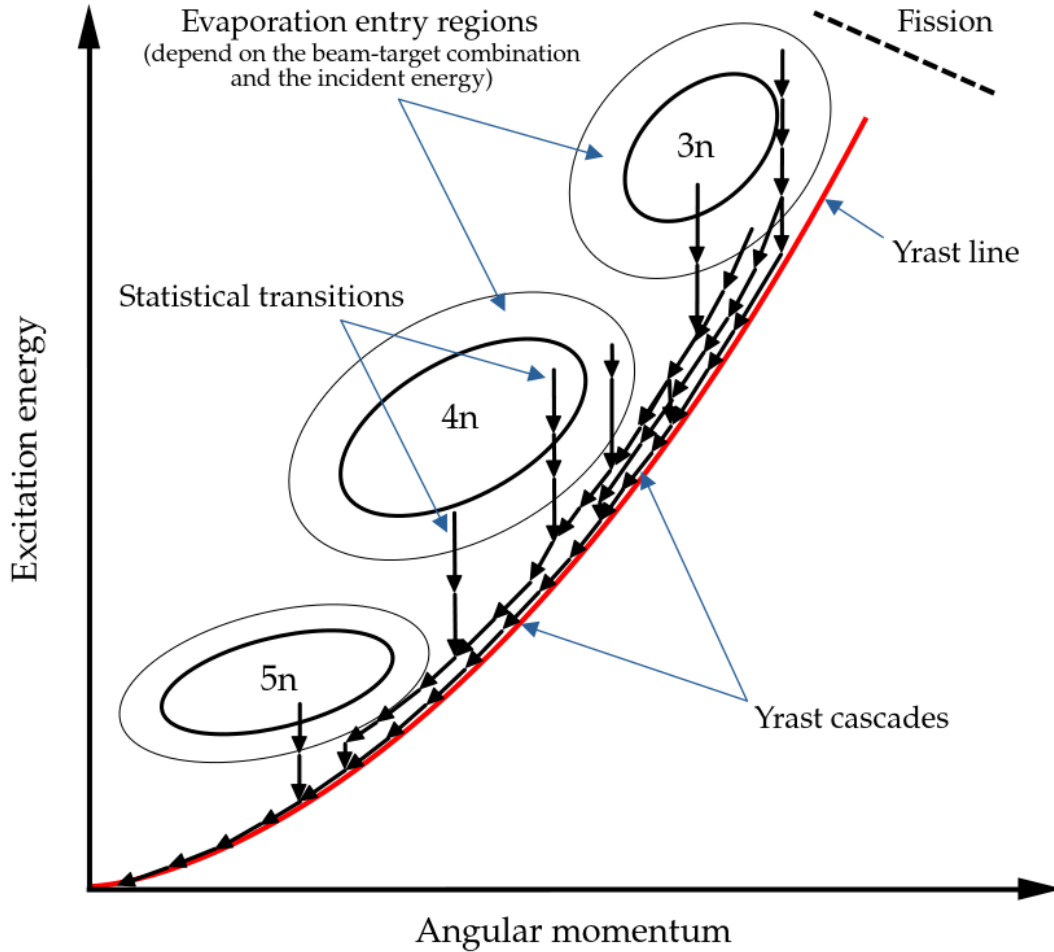


FIGURE 5 Evaporation residues have specific excitation energy and angular momentum distributions depending on how many particles have evaporated. The more particles were evaporated given the same incident beam energy, the less excitation energy and angular momentum the residues have. Residues first de-excite down through the energy via statistical transitions in the continuum region until they get close to the yrast line, below which no states are available, from which they then continue towards the ground-state close or at the yrast line via so-called yrast cascades. Fission starts to dominate at a high energy and angular momentum region.

Due to the nature of the fusion-evaporation process, it can only populate nuclei with fewer protons and neutrons than in the compound nucleus. It is also difficult to produce super-heavy elements with these reactions as the fission eats up the yield in the compound stage. There are also difficulties associated with beam and target materials. Optimal fusion-evaporation reactions would require the use of unstable beams and/or targets. As such, alternative reactions have been sought. In recent years, Multi-Nucleon-Transfer (MNT) and Quasi-Fission (QF) reactions used in combination with the in-flight separator setups and RDT method have gained a lot of attention. It is speculated that these reactions could be used to produce neutron-rich nuclei with a higher yield and perhaps, therefore, reach the predicted “island of stability” around  $Z = 114$  and  $N = 184$  more easily [48]. Domains of different nuclear reactions are illustrated in Figure 6.

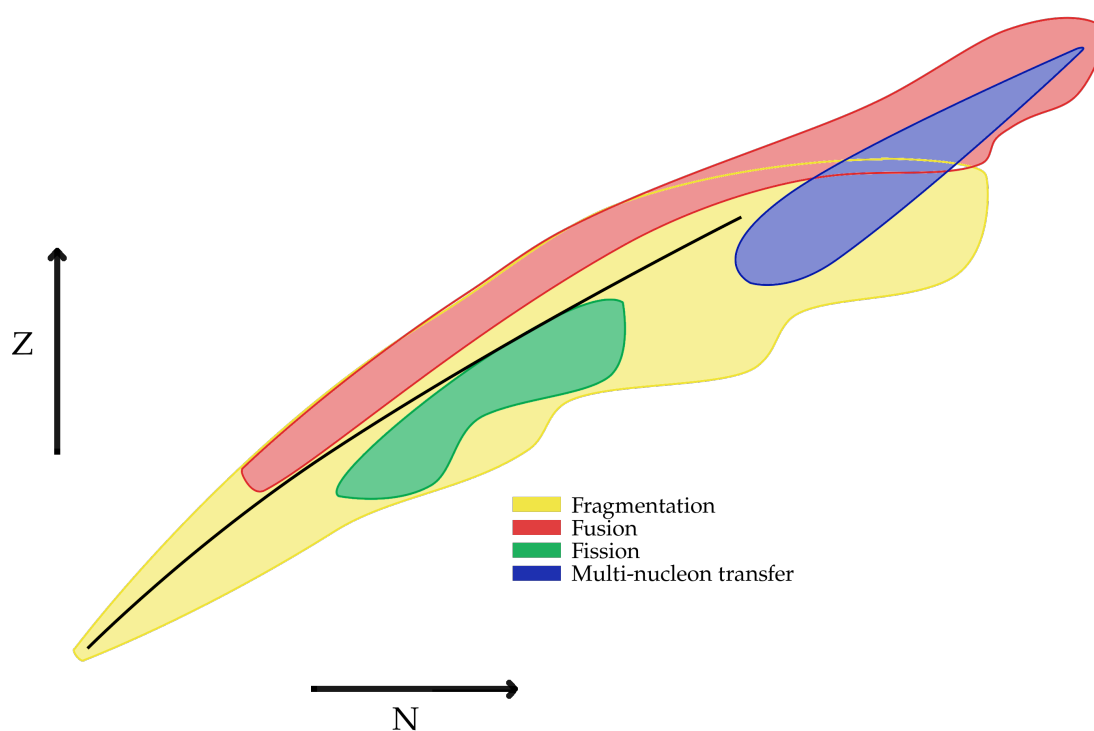


FIGURE 6 Some nuclear reactions populate different regions of the nuclear chart more strongly than others. Illustrative figure showing which reaction types have been commonly used to populate nuclei in the past studies and where they can roughly reach. Recently, multi-nucleon transfer reactions have gained attention as a method to study heavy neutron-rich regions. Of course, multi-nucleon reactions come with the light partner as well. The light partner can be also interesting, or it can be used to gain access to the complete reaction kinematics when both are observed simultaneously.

### 2.1.2 Decays

Nuclei can also remove excess energy and reach more stable states by undergoing radioactive decay.  $\alpha$ ,  $\beta^+$  and  $\beta^-$  decays, electron capture, and spontaneous fission are perhaps the most recognised ones, but many other decay modes exist, such as double- $\beta$  decay, neutron, cluster, proton, and  $\beta$ -delayed proton emissions. As a matter of fact,  $\gamma$ -ray emission, particle evaporation, and other nuclear processes discussed earlier have very similar origins to radioactive decay, the nucleus is trying to reach a more stable and less energetic state. Internal transitions are just typically several orders of magnitude faster than radioactive decay. Therefore, radioactive decay usually has time to take place only after the nucleus has reached its ground state. However, sometimes the lifetime of an excited state is sufficiently long that radioactive decay can compete, and proceed directly from that state instead. Much like the nuclear reactions, different decays are also driven by different fundamental forces and several decay modes are competing at the same time. Different decay paths of the same nucleus are called decay branches.



The most suitable decays to be used for recoil-decay-tagging are the ones that have particularly narrow and distinct decay energy characteristics. Some decay modes that can be used for RDT are shown in Figure 7. Additionally, half-lives around a few microseconds to the second range are often advantageous for achieving a good balance between the background and the experimental yield. However, if a nucleus has a very short half-life, it can decay inside the separator or signals from the implantation and decay events may pile up.  $\alpha$  and proton decays are often good candidates. These decay modes are relatively easy to detect, have sharp energy peaks, and relatively high decay energies, so they can usually be selected more cleanly and can thus tolerate larger backgrounds. The  $\gamma$ -ray emission and the internal transition that were discussed earlier are somewhat intermediate processes as they do not transmute the nucleus and are not always classified as radioactive decay. Nevertheless, they serve similar physical purpose, and they too can be used as the “decay” tag in the so-called recoil-isomer-tagging [49, 50] variant of the RDT.

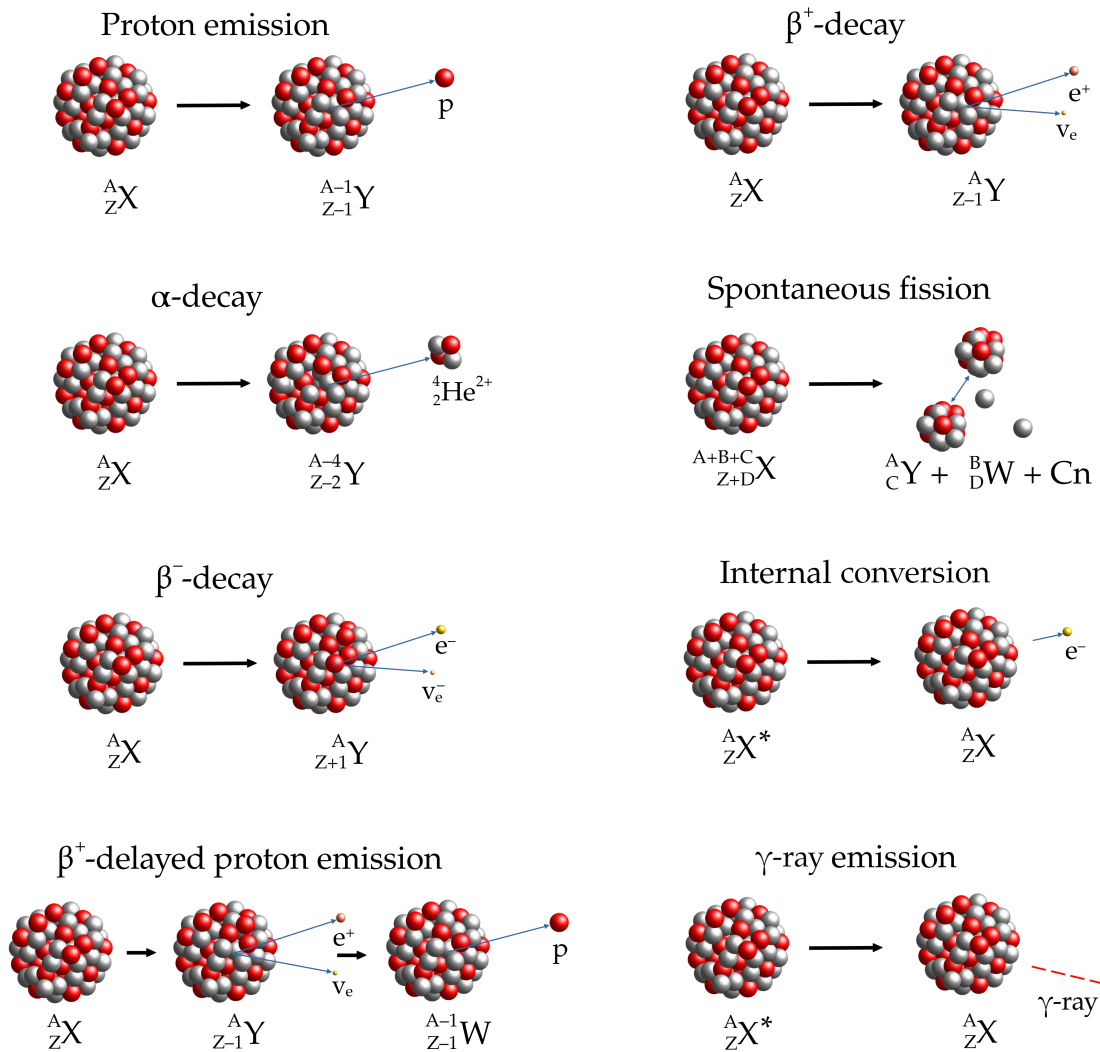


FIGURE 7 Radioactive decay modes that are the most relevant from the recoil-decay tagging point of view. The more distinct and unique trace the decay provides, the better.

## 2.2 Beam

JYFL-ACCLAB hosts four different particle accelerators, the beams for this work were provided by the main heavy-ion cyclotron K130 [51]. The K130 accompanied by its three Electron Cyclotron Resonance (ECR) ion sources (ECR1, ECR2, HIISI), and a multicusp light-ion source (LIISA) can provide a wide range of beam species that can be accelerated up to the energy of  $130 Q^2/A$  MeV. CAD renderings of the ECR2 and the K130 are shown in Figure 8. The energy spread of the cyclotron beam is typically less than 1% [52]. The variety of beam options accommodates studies of a broad range of phenomena, reaching all the way from cosmological events to radiation hardness testing, requiring beams from protons to heavy ions, such as gold. Multiple techniques can be used with the ECR sources to produce the desired beam composition. The beam material can be extracted from cylinders containing enriched gases [53], and different oven setups can be used to evaporate i.e. sputter solid materials. The MIVOC technique, on the other hand, can be used to directly extract the element of choice from a volatile compound [54].

It should be kept in mind that sometimes the beam might contain trace amounts of contaminants. These contaminants can originate from the actual beam material, but they can also be from the ion source buffer gas or from the residual air in the system. If the desired beam is similar to any of these contaminants, they can also pass through the accelerator stage and into the target. In this experiment, the 10–20 pA beams of  $^{40}\text{Ar}$  and  $^{37}\text{Cl}$  ( $E_{\text{lab}} = 182$  and  $170$  MeV) were relatively straightforward.  $^{40}\text{Ar}$ , 99.6% naturally abundance, was fed directly from a commercially available gas bottle and the chlorine was made from titanium tetrachloride ( $\text{TiCl}_4$ ) using the MIVOC technique. The only challenge was perhaps to keep the beam stable whilst not having too much free chlorine present at the ion source as it can start corroding metallic surfaces it gets in contact with.

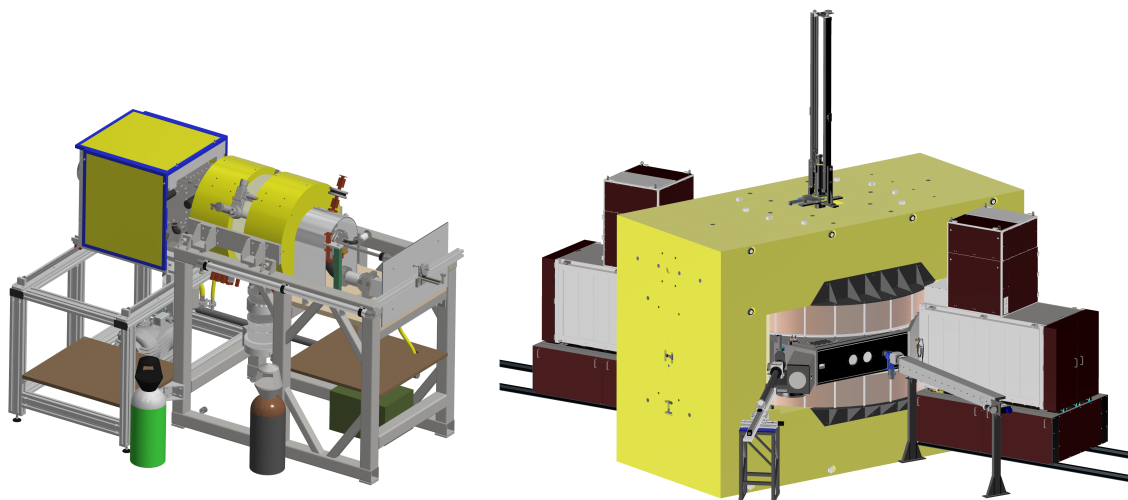


FIGURE 8 CAD renderings of the ECR2 ion source on the left and K130 cyclotron on the right (not to scale).



## 2.3 Target

Targets used in experiments vary in form, they can be thick, thin, chemically volatile, and some are even gaseous, liquid or radioactive. Typical targets used in RDT experiments are thin ( $\sim 1 \mu\text{m}$ ) self-supporting or backed foils. Similarly, as the materials used for the beam, targets can be made of a naturally occurring mixture of isotopes, or isotopically enriched materials. The purity of the beam and the target materials is of utmost importance, since the cross section for some other close-by isotopes and elements can be several orders of magnitude larger, which can cause problems during the experiment and the analysis.

Depending on the material, these foils can be prepared, for example, by rolling, sputtering or evaporation. Reactive materials can be rolled under an inert atmosphere to prevent oxidation since even the heat from the friction of the rollers or a static spark can burn a thin target. Some materials cannot be rolled, or they cannot support their weight due to their physical properties. Such target materials can be sputtered or evaporated on a thin backing material. Commonly used backing materials are, for example, carbon, gold, nickel, and aluminium. These are used for their properties, such as being light, strong, and having a high melting point. Targets can also need active cooling and can be rotated to distribute the heat load on a larger area.

Although the reaction rates are generally higher with thicker targets, the energy deposited in them is also larger, so they may melt more quickly. It might be tempting to use as thick a target as possible to maximise the yield, which might be the way to go, provided that the nucleus of interest is the most dominant reaction product. However, in RDT experiments, the yield for the product of interest is usually a small fraction of the total reaction cross section. One of the main reasons to use the RDT method is to be able to select these rare events from a strong background. If a too thick target is used all the particles are stopped inside, and RDT is not possible. A thicker target also causes larger velocity, energy, and angular distributions of the products due to scattering in the target material, which can lower the transmission and cause increases in the Doppler broadening of emitted  $\gamma$  rays. In addition, the energy loss inside the target means that the yield for the product of interest is not optimal throughout its whole thickness. On the other hand, when using a very thin target the yield is so low that multiple weeks may be needed for a measurement. For further beam and target details regarding this work, see article I.

## 2.4 Detector types

This work used ionisation, scintillation, and semiconductor-based detectors. These three technologies are common in the field of experimental nuclear physics. Not every detector type is the same, and it is important to know their

differences and what advantages they have to be able to plan experiments accordingly. Perhaps even more important is to know their limitations, not being able to observe something does not necessary mean that it does not have any effect on the measurements.

Ionisation-based detectors are one of the oldest types of radiation detectors. These measure small currents induced by particles passing through a detector medium and ionising it as they go. The medium usually has a low density, such as a gas, but it can also be a very thin foil. Particles can travel a long distance in the medium of a detector, which makes them ideal for tracking purposes. Since the particles can pass through the entire detector, they are often used for time-of-flight measurements and as dE-detectors in dE-E telescopes meant for particle identification. Those are also not very sensitive to electromagnetic radiation. The operation principle and construction of a generic multi-wire proportional counter is illustrated in Figure 9.

Scintillation detectors are devices that leverage a property of certain materials to emit photons, usually within wavelengths of visible light, when they are hit by ionising radiation. Scintillation detectors can be made of many base materials, and they can be doped differently depending on their desired properties, such as detection efficiency, output light wavelength, and signal characteristics. Scintillation detectors generally have good radiation hardness, fast response, and they do not need cooling (although it helps). They are also relatively cheap to build and the scintillator does not need external biasing. However, their energy resolution is not the best due to the non-proportionality of the light output. Plastic-based devices are commonly used for detecting heavier particles, such as  $\alpha$  and  $\beta$  particles while being relatively transparent to  $\gamma$  rays. Denser (higher proton and electron

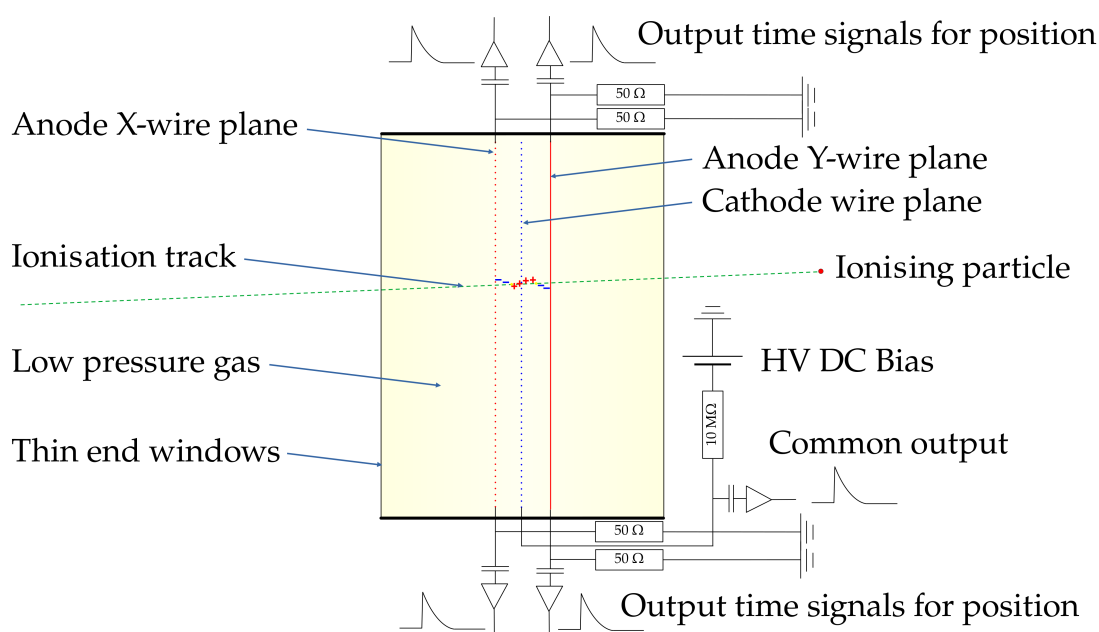


FIGURE 9 Illustration of a generic multi-wire proportional counter. Ionising particle enters the gas-filled volume and ionises some gas particles. Charges then propagate towards the electrodes which creates a measurable current signal.

density) materials are used for  $\gamma$ -ray detection. The photon interactions are electromagnetic in nature, so more charged particles translates to better attenuation and detection efficiency [55]. Some common materials used for  $\gamma$ -ray detection are Bismuth Germanium Oxide (BGO,  $\text{Bi}_4\text{Ge}_3\text{O}_{12}$ ), Thallium-doped sodium iodide ( $\text{NaI}(\text{Tl})$ ), and Cerium-doped Lanthanum Bromide ( $\text{LaBr}_3(\text{Ce})$ ). Even liquids can be used as the base material, which can be advantageous when building large or odd-shaped detectors. Light emitted by the dopants passes through the base material and is converted to an electrical signal, typically via analog PhotoMultiplier Tubes (PMT) or, nowadays, semiconductor-based Silicon Photo Multipliers (SiPM) are becoming more common because they are more compact and do not need high bias voltages. Figure 10 shows a generic construction and operation of a scintillation detector.

Semiconductor detectors measure small currents from electron-hole pairs induced in depleted P-I-N junctions (reverse biased diodes) by passing radiation. Commonly used semiconductors are silicon and germanium, but sometimes diamond or gallium compounds are used. Germanium-based devices are typically used to detect  $\gamma$  rays. It is preferred over silicon due to three main reasons. It has better attenuation for photons since it is about twice as dense as silicon. Germanium devices can be manufactured much thicker than silicon devices, which also increases the  $\gamma$ -ray detection efficiency. It has a lower band gap of around 0.7 eV compared to 1.1 eV of silicon, which is directly proportional to the intrinsic energy resolution of a detector. However, the gap is so low that the electrons can move into the conduction band even at room temperature, hence the detectors have to be cooled down. From the detection point of view, Compton scattering, photoelectric absorption, and pair production are the most relevant interaction processes [47]. Photoelectric and Compton effects involve the electrons of an atom while the pair production interacts with the protons in the core of the nucleus. These processes depend on the energy of the incident photon and determine the intrinsic detection efficiency of a detector, however, other effects, such as charge collection and recombination, usually dominate in the final detection efficiency. Compton scattering is also relevant due to the background it can cause. In the Compton process, photons interact electromagnetically with an electron

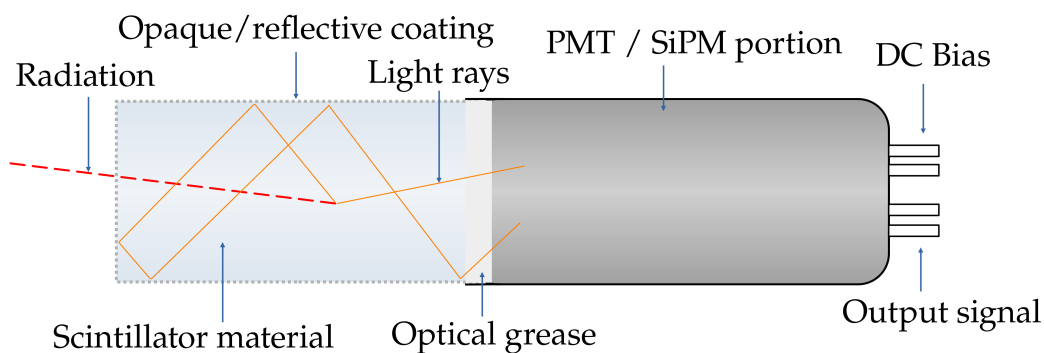


FIGURE 10 Illustration of a generic scintillation detector. Radiation penetrates the coating of the detector and interacts with the scintillator material, creating light. The photons are then converted into electrical signals with a PMT or SiPM.

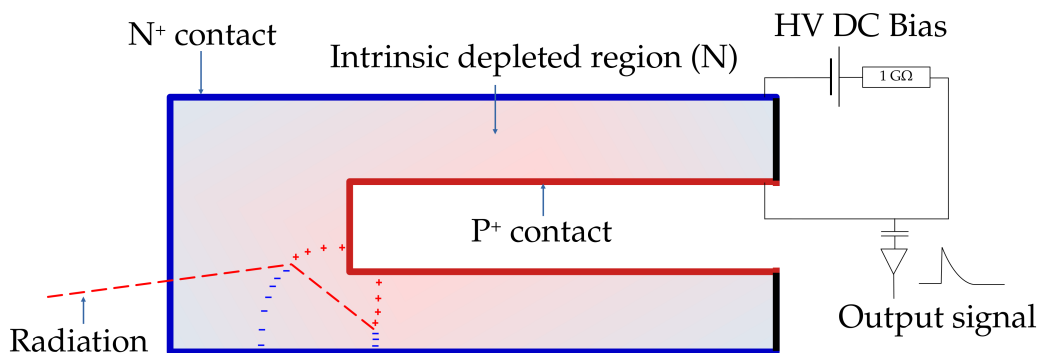


FIGURE 11 Illustration of a generic N-type coaxial germanium detector. Radiation interacts with the detector material and creates electron-hole pairs. These charges then drift towards the P<sup>+</sup> and N<sup>+</sup> contacts and an output current pulse is generated.

of an atom, lose some energy, and scatter off in a different direction, which can cause a continuous energy distribution below the photopeak in measured spectra. Germanium detectors are built with various crystal shapes and electrode configurations that try to optimise properties, such as energy range, resolution, efficiency, and radiation hardness. Figure 11 shows the operation and geometry of an N-type coaxial germanium detector.

## 2.5 Target position and the JUROGAM 3 spectrometer

Once a beam is extracted from the cyclotron, it is guided into the target area of the MARA or RITU setups. An overview of the target area and the JUROGAM 3 array is shown in Figure 12. The beam is focused on the target foil positioned at the centre of the detector array. The majority of the beam passes straight through the target, however, on rare occasions, the nucleus of a beam particle gets close enough to the target nucleus for a nuclear reaction to take place. The detectors of the JUROGAM 3 array and possible auxiliary detectors, such as charged particle evaporation detectors, are positioned around the target to observe the radiation emitted by the newly formed excited nuclei. It should also be mentioned that the JUROGAM 3 array cannot see the conversion electrons, so highly converted transitions and, of course,  $0^+ \rightarrow 0^+$  transitions can be missed. There are other ways to measure these transitions, such as in-beam electron spectroscopy, however, they are out of the scope of this work, but more details can be found in Reference [56].

### 2.5.1 Germanium detectors

The JUROGAM 3 array consists of 39 germanium detectors that are placed into four rings positioned around the target as seen in Figure 12. These detectors are intended for measuring prompt  $\gamma$  rays that excited nuclei emit in a span of  $\sim 10^{-15}$ – $10^{-9}$  s. The first ring has five detectors nominally at the angle of  $157.6^\circ$  with respect to the beam axis and the second one has ten detectors at  $133.6^\circ$ .

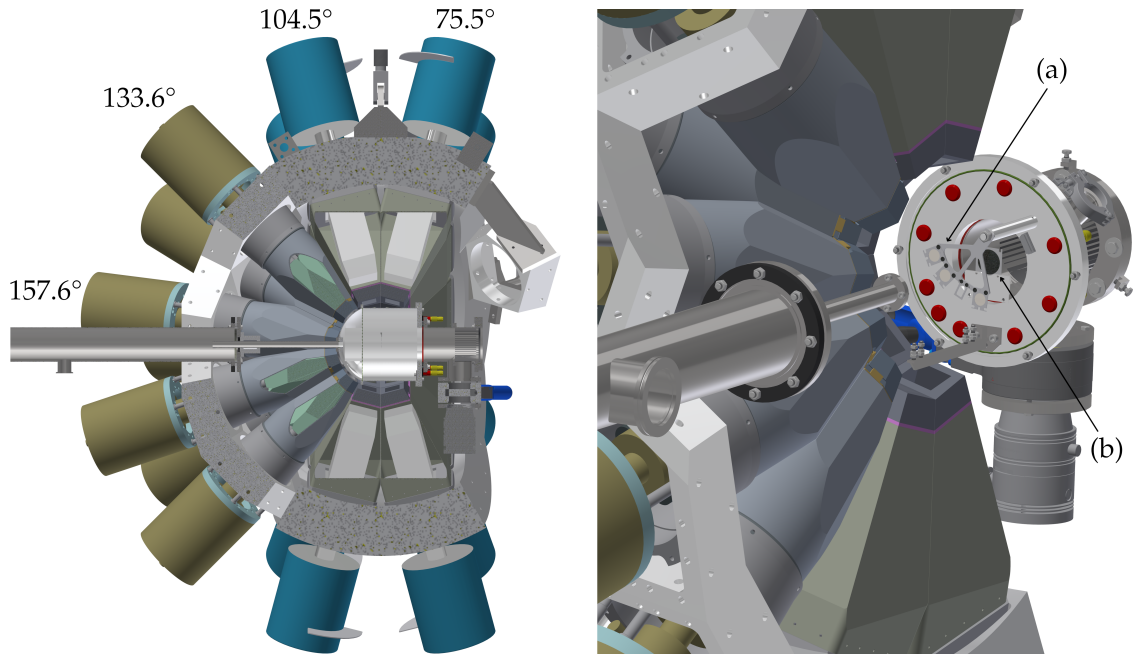


FIGURE 12 Cross-section view of the JUROGAM 3 array and the target position with (a) the target fan and target frames for four targets and (b) a charge reset carbon foil behind the target fan.

The remaining twenty-four detectors are divided between rings 3 and 4 at angles of  $104.5^\circ$  and  $75.5^\circ$ , respectively. The detectors in the first two rings have single N-type coaxial Ge-crystals. The detectors in rings 3 and 4 are Clover type detectors [57, 58] with four independent coaxial N-type Ge-crystals in the same housing. In the analysis, these two Clover-detector rings are sometimes further broken down into rings 3, 4, 5, and 6 nominally at the angles of  $110.5^\circ$ ,  $98.5^\circ$ ,  $81.5^\circ$ , and  $69.5^\circ$ , respectively. The coaxial crystal shape allows for a larger effective thickness whilst keeping the bias voltage reasonable. The typical bias voltage of these germanium detectors is around 4 kV.

There are many reasons for the spherical arrangement of the detectors in the JUROGAM 3 array and in any  $\gamma$ -ray spectrometer for that matter. The spherical symmetry allows for measuring the angular distributions (and correlations) of transitions, which is discussed in detail in section 5.5. The spherical packing also increases the geometric efficiency of the setup, whilst keeping the individual detector's solid angle coverage smaller which minimises the random pileup and coincidence summing events due to more than one  $\gamma$ -ray hitting the same detector during the signal's integration period. One of the main reasons why multi-detector setups are preferred over fewer but more closely positioned detectors is their ability to better resolve coincidences between the emitted  $\gamma$  rays. For example, suppose 100 keV, 200 keV, and 300 keV  $\gamma$  rays are associated with transitions in a nucleus and the 100 keV and 200 keV transitions are frequently observed in different detectors during a short ( $\sim 50$  ns) time window, whilst the 300 keV one does not appear simultaneously with the other two, it can be concluded that there are likely two parallel de-excitation paths, one via the 100-200 keV  $\gamma$ -ray cascade and one via the 300 keV transition.

## 2.5.2 Bismuth germanium oxide shields

As discussed in section 2.4, one of the interaction mechanisms of photons with matter is the Compton interaction, which causes the continuous energy tail below the photopeak as the scattered photons escape the active volume of a detector without depositing all of their energies. The compounding background from higher energy transitions can result in a large pedestal under the other peaks, overwhelm weaker transitions, and complicate the coincidence analysis.

One way to reduce the effect or veto these escaped photons is to use so-called Compton suppressors, also known as anti-Compton shields. The Germanium detectors of the JUROGAM 3 array are encapsulated by scintillation detectors made of Bismuth Germanium Oxide (BGO) crystals. A cross-section view of this arrangement is shown in Figure 13. The inorganic BGO crystals are relatively thick and dense and thus have an excellent  $\gamma$ -ray absorption and radiation hardness properties, which makes them particularly suitable for in-beam studies. If a photon Compton scatters out of the actual germanium detector, it will hit the scintillators, leaving a distinct signal that can be used to exclude these events in the analysis. A single BGO shield, surrounding a Ge detector of the JUROGAM 3 array, consists of 10 or 16 shield individual crystals with their PMTs and preamplifiers [59, 60]. The Ge detector resides relatively deep in the shield, which provides better collimation and increases the Compton back-scattering detection efficiency of the BGO shield. The tips of the shields are fitted with 35 mm-thick tungsten collimators to prevent possible false-veto signals from the  $\gamma$ -rays that would have only hit the BGO shields. Tin and copper absorbers can be placed on the tips of the collimators to prevent low-energy X-rays from reaching the Ge detectors.

While the BGO shields can be used to record the energy too, their energy resolution is not really adequate for add backing. A more expensive and complex method to get rid of these Compton tails, without sacrificing the efficiency, is to surround the target with a continuous volume of segmented germanium detectors, that can be used to track and add-back individual events. Examples of this approach are the next-generation tracking arrays AGATA [61] and GREINA [62].

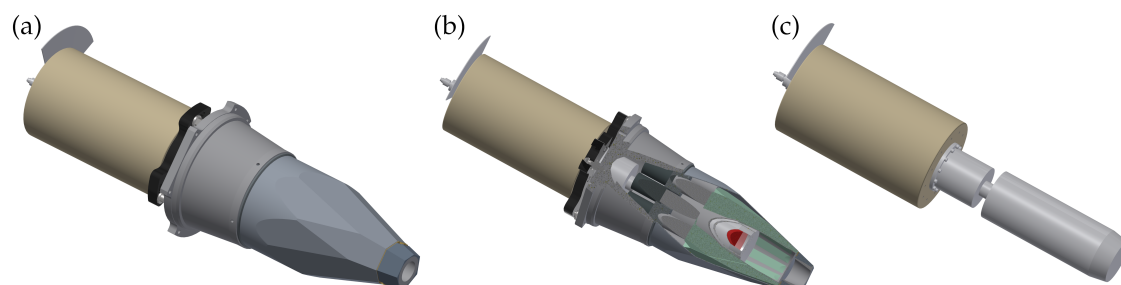


FIGURE 13 (a) Gasp-type Ge detector and a BGO shield surrounding it. (b) Cut-out exposing the arrangement of the individual crystals inside the detectors. (c) Gasp-type Ge detector without the BGO shield.



## 2.6 In-flight recoil separators MARA and RITU

MARA and RITU are the two electromagnetic in-flight recoil separators operated by the Nuclear Spectroscopy Group. As briefly mentioned before, an atom is a mostly empty space, so when a target is irradiated with a particle beam, most particles pass through it without any interaction. The purpose of MARA and RITU is to physically separate the unreacted primary beam from particles formed in the few collisions between the beam and the target, i.e. the recoils, and prevent it from reaching the focal plane.

The term in-flight refers to the operation principle in which the motion of (charged) particles (beam and recoils) is not completely stopped, but instead, their trajectories are altered by applying external magnetic and electric fields with ion optical elements. Moving charged particles in the presence of such fields experience the Lorentz force and are deflected accordingly. The cross-cut of the separators and illustrative paths of the primary beam and reaction products are shown in Figure 14.

The main element of the RITU separator is a large dipole magnet. This electromagnet creates a uniform and perpendicular magnetic field relative to the beam axis. The magnetic field causes passing charged particles to experience a Lorentz force, bending them into curved trajectories according to their magnetic rigidities (momentum per charge ratios). The primary beam gets bent onto a tighter gyroradius and hits the beam stopper, whilst the recoils continue to the focal plane.

The operation principle of the MARA separator is somewhat similar. However, MARA has a large electrostatic dipole deflector before the dipole magnet. The deflector is essentially two curved parallel titanium plates with a high electric potential difference across them. The trajectories of particles inside the deflector depend on their electric charges and velocities. Inside the magnetic dipole, the trajectories depend on the magnetic rigidities. The effective result is a separation of the primary beam and the recoils, similar to RITU, but also an additional physical separation (resolution) of the recoils based on their mass to charge ratios at the focal plane. The maximum magnetic field of RITU dipole is 1.25 T, and the electric field strength between the deflector plates of MARA can reach up to 3.5 MV/m.

A more technical difference between MARA and RITU is that their angular acceptances differ slightly. The conical acceptance distribution of RITU is asymmetric,  $\pm 25$  mrad in the horizontal direction and  $\pm 85$  mrad in the vertical direction, for a total acceptance of a solid angle of 8 msr [36]. For MARA, the acceptance is  $\pm 45$  mrad in the horizontal and  $\pm 55$  mrad in the vertical direction and thus a slightly larger, 10 msr, in total [37, 63]. With normal reaction kinematics, the angular cone of the fusion products is symmetric, for example,  $\pm 50$  mrad (FWHM). In such cases the transmission through RITU can be lower than through MARA.

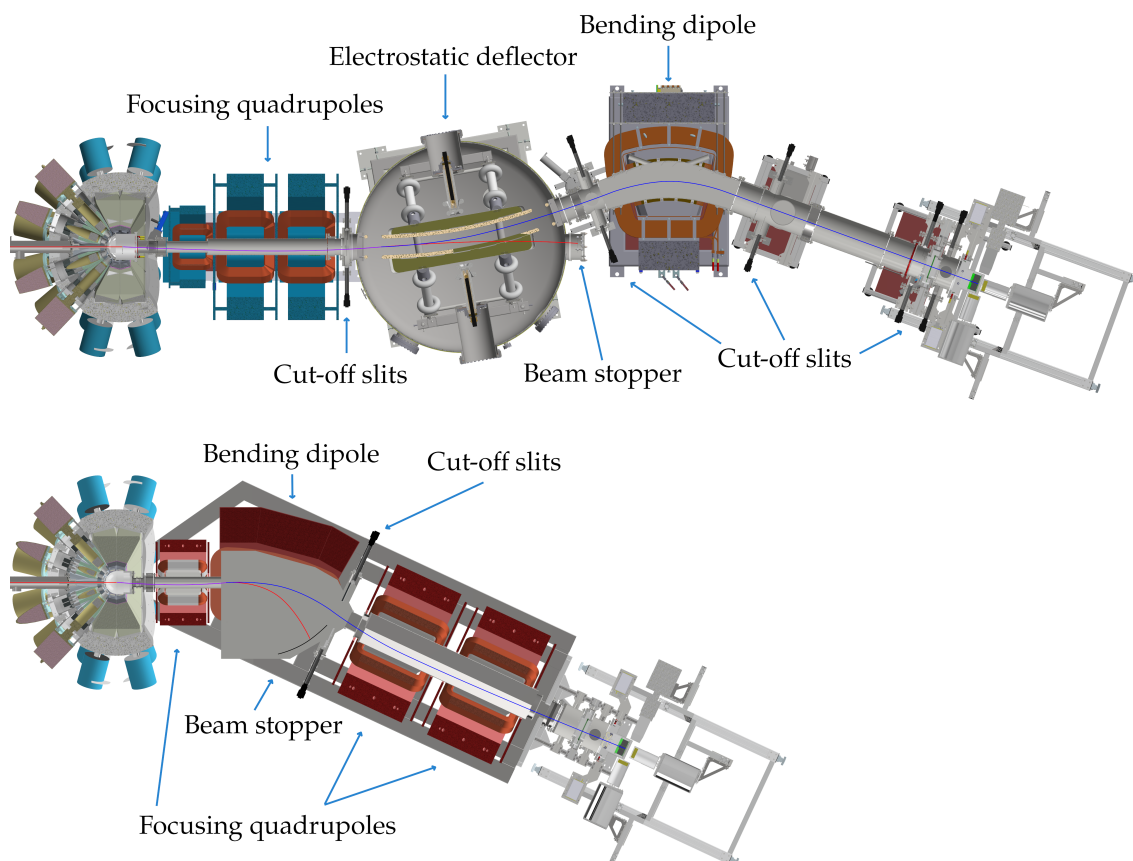


FIGURE 14 Cross-section along the horizontal plane of the MARA and RITU setups. The optical elements are labelled, and the illustrative trajectories of the primary beam and the recoils are shown.

Another difference between these two devices is that RITU can be operated in a gas-filled mode since it has no elements with high electric fields. Recoils have a multimodal Gaussian charge state distribution immediately after the target. Since the path an individual particle inside the separator depends on its charge state, the trajectories of particles with the charge state at the extremities of the distribution can bend too much and hit the walls of the separator or miss the active areas of the detector setup at the focal plane, leading to a loss of transmission efficiency. To alleviate this problem, RITU can be filled with low pressure ( $\sim 1$  mbar) helium gas that averages the charge states into singular, more narrow, average charge state distribution via charge exchange collisions with the helium atoms. The averaging can considerably increase the transmission of the setup, which is advantageous, particularly in the heavy and super-heavy element studies where the efficiency is favoured over the mass-resolving power due to very small production cross sections. RITU has this feature since it was originally designed for the decay studies of heavy elements, whereas the newer MARA separator was optimised especially for in-beam  $\gamma$ -ray spectroscopy studies of  $N \approx Z$  nuclei. Cross sections in the  $N \approx Z$  region are typically much higher, therefore, the beam intensity is limited by the count rates at the focal plane instead of the tar-



get. However, multiple elements with similar masses and electric properties are also produced in these reactions, hence the need for the mass per charge resolution at MARA. The helium gas also reduces the scattered beam and light particle components at the focal plane, and consecutively, RITU can have a lower background in the small cross section experiments when using asymmetric reactions in the heavy ( $Z > 82$ ) mass region. Figure 15 shows a comparison of the recoil distributions observed at the focal planes of MARA and RITU.

The electric charge of some particles might be too high or change after the target. Especially in the heavier mass region where low-energy transitions may be highly converted and/or slow enough that internal transitions occur after the target foil, where the recoils cannot exchange charges with the target atoms. Together with the conversion electrons, a cascade of Auger electrons may be emitted leading to an even further anomaly in the charge state distribution and a loss of transmission. To allow for more optimal charge state distributions, in MARA, 20–40  $\mu\text{g}/\text{cm}^2$ -thick charge reset carbon foil is usually mounted about 10 cm after the

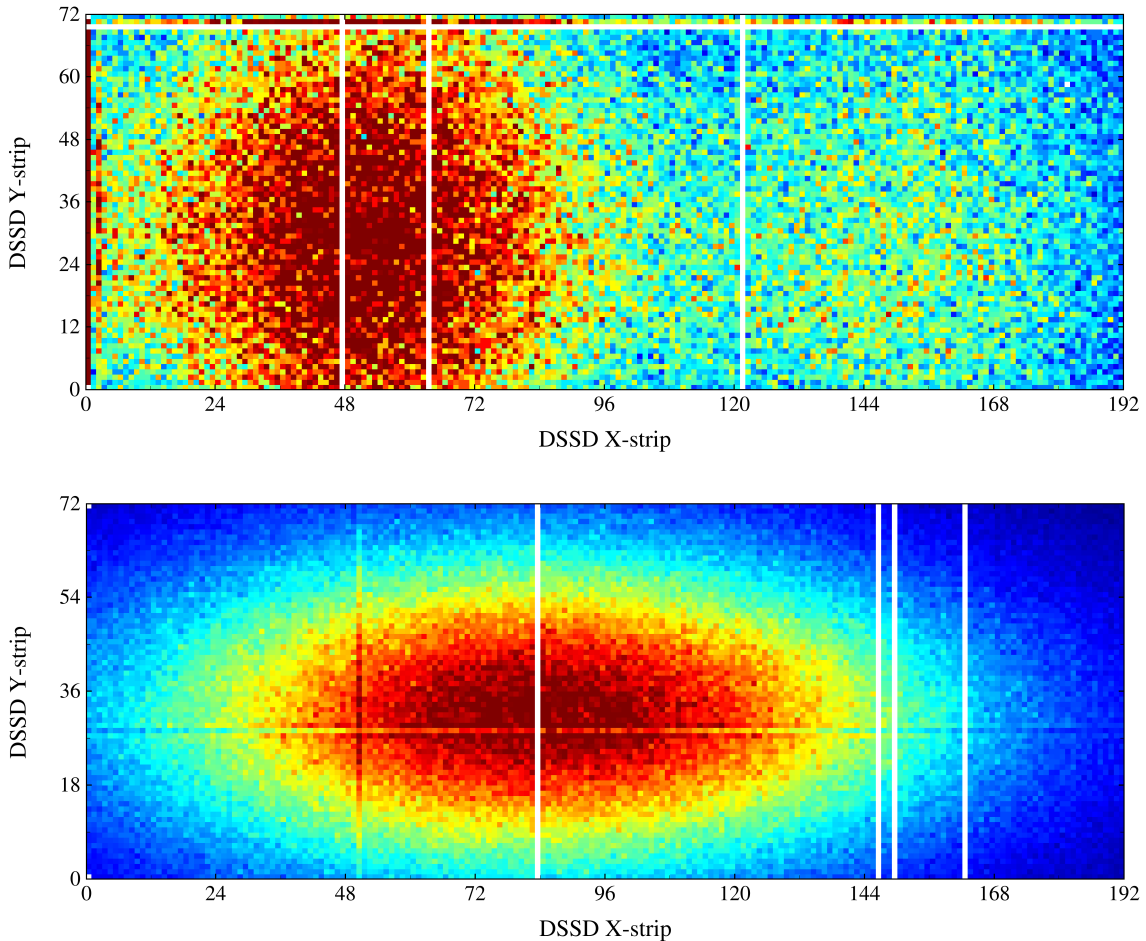


FIGURE 15 DSSD recoil event distribution from the reaction  $^{37}\text{Cl} + ^{180}\text{Hf}$  of this work at MARA (top) compared to a very similar reaction  $^{37}\text{Cl} + ^{175}\text{Lu}$  done using RITU (bottom). Two distinct charge state distributions are visible at MARA whereas the charge averaging effect of the helium gas inside RITU diffuses all the states into a single distribution.

target. Highly positively charged particles can recover some of the missing electrons from this foil. Even though the helium gas in RITU averages the charges, the optimal pressure for the fusion products is not the same for the primary beam entering the separator, so with RITU, the carbon foil is also advantageous for resetting the charge state distribution of the primary beam itself to lower its magnetic rigidity for easier bending. With RITU, the reset foil is also advantageous for preventing a stray beam component from reaching the focal plane. If there is a pinhole in the target, a beam ion may come through in its original charge state, causing it not to bend enough, and due to the geometry of RITU, it comes through the separator and hits the detectors at the focal plane.

This is still an extremely simplified description of MARA and RITU. In reality, their design includes many more components, such as multiple quadrupole magnets for focusing the particles before and after the dispersive elements to gather particles that are not flying along the optical axis, which increases the total transportation efficiency. In addition, multiple moveable slits are installed in different sections of the separators to physically cut out some of the unwanted parts of the beam and recoils. Tantalum collimators are also placed in the beam line before the separators to collimate the beam.

Once MARA and the JUROGAM 3 array setup came online and the first experimental campaign was started, a suitable time to upgrade RITU opened up. The upgrade was quite comprehensive. The separator section was completely refurbished, and the vacuum-pumps, valves, magnet power supplies, and other auxiliary equipment were integrated into the new Rockwell PLC-based lab-wide control and monitoring system. The target positions have also been designed to be dimensionally compatible, meaning that target chambers, targets, and auxiliary detectors therein can be swapped back and forth. The JUROGAM 3 array and its associated supporting devices hang from linear rails and the whole setup can be swiftly moved between the target positions. The germanium detectors can stay biased during the move, which is a significant advantage. Two sets of cabling has been prepared for quickly switching the setup to which the common data-acquisition system is connected. This interchangeability is part of a broader goal to unify the MARA and RITU setups, and it is not limited to just the target position. In addition to the work done at the separator end, the old GREAT focal plane system was also completely dismantled and replaced with an adaptation of the MARA's focal plane. Now, the only considerable mechanical difference between the MARA and RITU focal planes is that RITU has some additional modifications for a gas handling setup that injects the helium gas into the separator. It also lacks the physical cut-off slits, as they are not needed. As the focal planes are now practically identical, it is possible to use most devices interchangeably. The main advantage of this arrangement is to be able to run experimental campaigns back-to-back with both separators by making the switch as seamless as possible. Added benefits include lower running costs for not having to maintain two completely different technologies side-by-side, and being able to share parts that can be used in both the devices. It also helps to have backup options on hand should something fail. Doing general maintenance is also much more manageable now.

## 2.7 Focal plane

The primary function of a focal plane setup is to provide means to identify particles coming through the separator by measuring different properties they have, such as recoil time-of-flight, implantation energy, decay energy, and decay time. To achieve this, multiple detectors are employed at the focal planes of MARA and RITU. A cross-sectional view of the focal plane of MARA with some components and detectors labelled is shown in Figure 16.

Although the instrumentation at the focal planes can be configured quite freely depending on the experiment, a couple of bigger upgrades have been made for the standard setup during the past few years. Three Mirion Broad-Energy Germanium (BE $\text{Ge}^{\text{TM}}$ ) P-type detectors were acquired for the  $\gamma$ -ray array to replace the old Clover and Planar detectors. A novel position-sensitive scintillation detector, “Tuike” [64], was developed in-house. It is intended mainly for  $\beta$ -decay-tagging experiments. Several new gas counters built by the Slovak and Chinese collaborators were commissioned. Major upgrades were also made a bit earlier, during the development of the focal plane of MARA.

As mentioned, RITU’s new focal plane is now a copy of MARA’s. MARA’s focal plane, on the other hand, was designed to be the successor of the old GREAT spectrometer setup [65]. The biggest change between the MARA FP and the GREAT setup was the switch to a larger Double-sided Silicon-Strip Detector

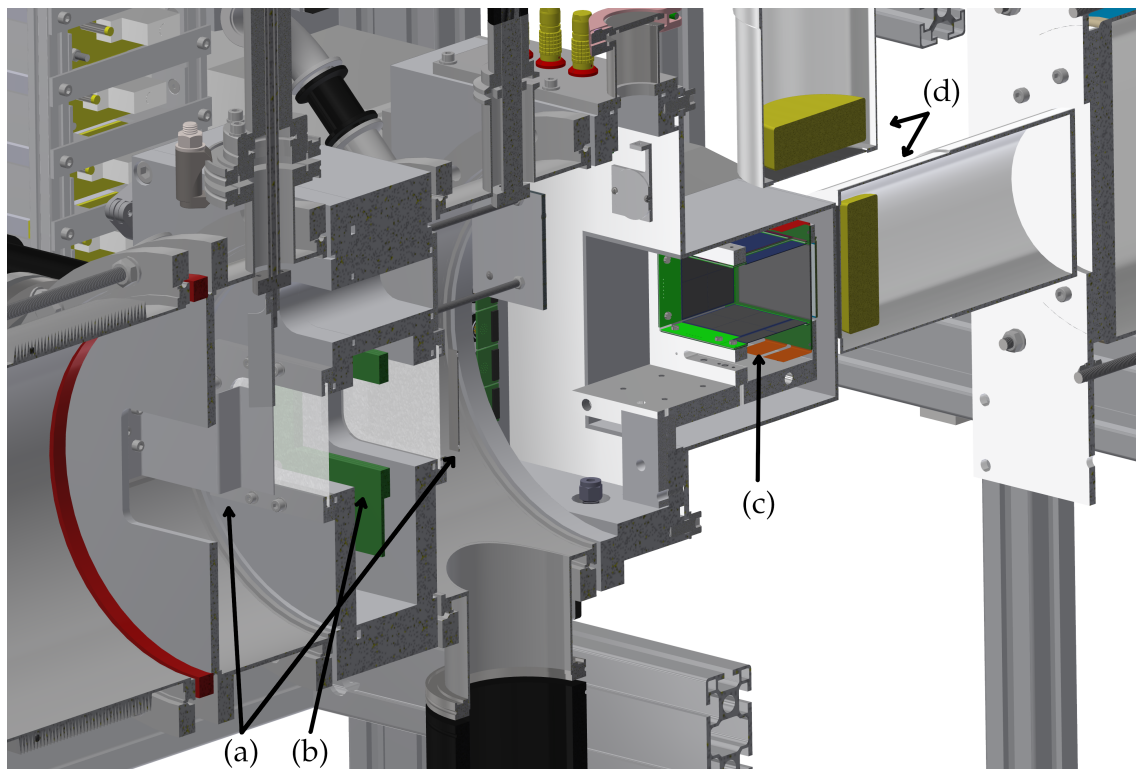


FIGURE 16 Cross-section of the focal plane of MARA. (a)  $5 \times$  cut-off slits. (b) MWPC and its chamber. (c) Tunnel, DSSD, and punch-through detectors. (d) Two of the total three BE $\text{Ge}^{\text{TM}}$ -detectors of the focal plane  $\gamma$ -ray array.

(DSSD) and moving its preamplifiers outside the vacuum-chamber, different MWPC design, more compact vacuum chamber design to increase the  $\gamma$ -ray detection efficiency, and the swap to an almost completely digital signal chain.

While the focus of this section will be more on the different detectors that were used in this particular work, the focal planes also house other dynamic components, such as the aforementioned moveable mass cut-off slits and energy degrader foils that are more important in other experiments.

### 2.7.1 Double-sided silicon-strip detector

A Double-sided Silicon-Strip Detector (DSSD) is probably the most often used detector at the focal planes of MARA and RITU. It is an integral part of the RDT experiments, where it is used for the recoil implantation and for measuring the energies of the subsequent radioactive decay. A DSSD is a semiconductor device with perpendicular (or at least not parallel) P and N strips, on the opposite surfaces of a bulk silicon substrate. When a particle hits the depleted region of this reverse biased detector, electron-hole pairs are created. Electrons and holes will propagate towards the strips on the opposite surfaces, due to the presence of a strong electric field, around 0.1–1 MV / m, depending on the distance to the strips. Current signals are then collected from the ends of each strip, and the channel information can be used to construct a quasi-pixel i.e. 2D spatial position of an event. However, the actual construction of a DSSD is quite a bit more complicated. The real device has, for example, drift-blocking strips, a guard ring, and many other structures near the edges for biasing and signal readout purposes.

The latest focal plane setup uses DSSD model BB20 [66], manufactured by Micron Semiconductor Ltd. BB20 was developed from an older BB17 model in collaboration with the JYFL-ACCLAB. BB20 has an active area of 128.61 mm by 48.21 mm (6200 mm<sup>2</sup>). The side facing the beam, “X-side”, has 192 vertical strips with 0.67 mm spacing. The backside, “Y-side”, has 72 horizontal strips, also spaced 0.67 mm apart. BB20 then has a total of 13824 quasi-pixels. The old GREAT spectrometer setup had two side-by-side 60 mm  $\times$  40 mm DSSDs (4800 mm<sup>2</sup> active area). These detectors had a 1 mm strip pitch, which translates to 4800 quasi-pixels in total. An even earlier setup had an 80 mm  $\times$  35 mm position-sensitive Passivated Implanted Planar Silicon (PIPS) detector with only 16 individual horizontal strips. Whilst more pixels equals greater spatial resolution and thus enables longer correlation times, the quasi-pixel size of BB20 (0.67 mm  $\times$  0.67 mm) is close to the practical limits in RDT experiments, since the range of  $\alpha$  and  $\beta$  particles would start to span multiple pixels and charges would drift to adjacent strips, which causes false correlations.

These types of devices are often manufactured with a metallic layer on the surfaces (metallisation) to help with the wire bonding and charge collection from the strips. However, the metallisation is not ideal if the device is used as an implantation detector due to the resulting dead layer. BB20s used in RDT studies are ordered with the metallisation layer only on the very edges of X-side of the detector, which is the side facing the beam. The Y-side has a uniform coverage.

However, the X-side still has an intrinsic dead layer of approximately  $0.3\ \mu\text{m}$ . The dead layer is problematic because it complicates the energy calibrations. It creates an offset between observed energies of events originating from inside the detectors versus those coming from outside the detector. As such, the dead layer must be considered when calibrating with external sources and measuring energies of internal decay events. Ideally, the calibrations would be done with a well-known implanted activity. However, this is not often feasible. Energy calibrations are discussed in detail in section 5.5.

Another important feature of a DSSD is its thickness. The BB20 detector is available, at least, in nominal thicknesses of 150, 300, and  $675\ \mu\text{m}$ . The dimensions are mostly dictated by the standard wafer sizes and manufacturing equipment used in the semiconductor industry. The thickness affects energy resolution through depletion voltage, capacitance, charge drift, and diffusion. Detector capacitance negatively affects the signal integrity and readout electronics. The charge drift and diffusion can cause a signal to spread across multiple strips, indirectly widening the measured energy distribution.

In our use case, the thickness also dictates whether a particle is completely stopped inside a detector, which can be an advantage or a disadvantage. With the typical masses and kinetic energies involved in these experiments, recoils can only penetrate around  $1\text{--}20\ \mu\text{m}$  deep into the silicon. The range of lighter decay particles is considerably longer. Thus, they can escape from the DSSD while only depositing a fraction of their energy, causing a continuous energy background. The radioactive decay distribution is generally isotropic, so about half of the decay particles i.e. those emitted back towards the separator, will escape. A diagram of a DSSD with different types of events encountered in RDT experiments is shown in Figure 17.  $\beta$  activity tends to build up inside a DSSD during exper-

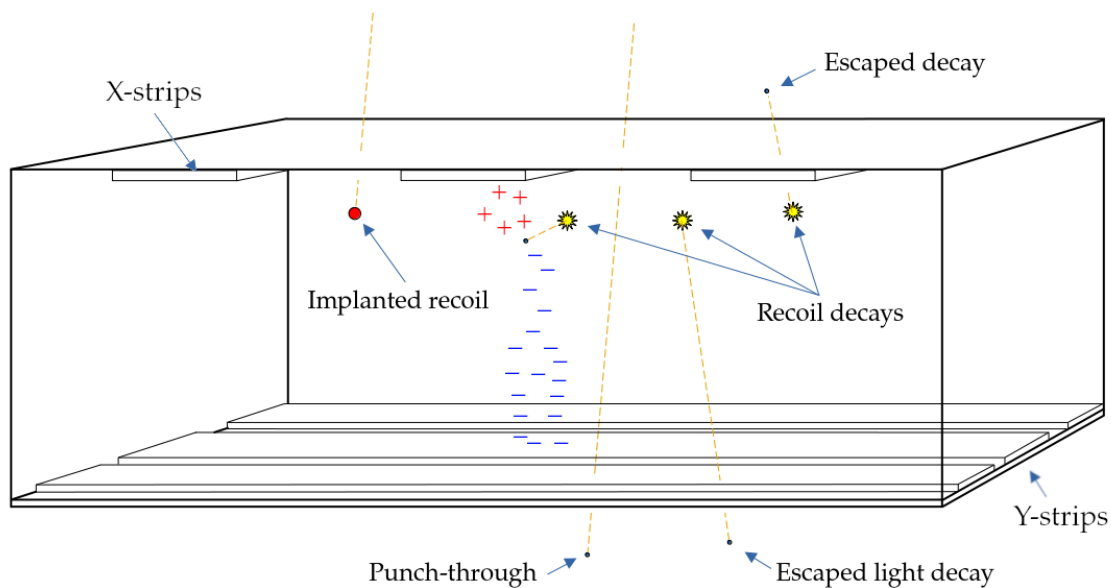


FIGURE 17 Simplified diagram of the structure of a DSSD and different event types. The recoil implantation depth is typically relatively shallow so that decay particles can escape upstream. The lightest particles can also escape downstream. Light beam particles can directly punch through the whole detector.

iments, since  $\beta$ -decaying isotopes are often produced abundantly and they can have long half-lives. Many  $\alpha$ -decay chains also end in  $\beta$  activity. Using a thinner DSSD can reduce the background and the count rate from the  $\beta$  particles. However, sometimes the  $\beta$  particles and internal conversion electrons are the events of interest. In these cases, using a thicker DSSD might be more beneficial. Implanted particles also cause defects in the device, increasing leakage current and noise. During experiments, the DSSD is cooled down to  $-20^\circ\text{C}$  to reduce the noise and afterwards it is heated up to  $35^\circ\text{C}$  to bake out the defects.

### 2.7.2 Multi-wire proportional counter

As discussed, the events seen in the DSSD can originate the outside or from the inside of the detector. Beam correlated events, such as recoils, beam-like particles, and target-like particles come through the beam line. In contrast, decay events from implanted activity happen inside the detector as illustrated in Figure 17. This difference is extremely advantageous, because it allows for the decay events to be easily separated from all the other events just by placing a “fly-through” detector directly in front of the DSSD. Some requirements are imposed for such a detector. Namely, it needs to be able to let through particles with a broad range of masses and energies while still producing a detectable signal. It also needs to be able to handle a relatively high event rate. Ionisation based detectors, more specifically, proportional counters, can fulfil these requirements. With MARA and RITU, a device known as a Multi-Wire Proportional Counter (MWPC) is used for internal or external event discrimination.

MWPC comprises several planes, each containing a parallel grid of thin wires. The wires in the separate planes are in different orientations allowing for a similar X–Y coordinate construction as with the DSSD. An illustration of a MWPC is shown in Figure 9. At the focal planes of MARA and RITU, a MWPC is mounted in front of the DSSD, but it is housed in a separate gas containment section to prevent straggling and allow for proper cooling of the DSSD. Openings on the opposite sides of the chamber are typically sealed with thin  $0.9\ \mu\text{m}$  Mylar® (Biaxially-oriented polyethylene terephthalate) film windows. While keeping a steady mass flow of gas, isobutane in this case, and a couple of millibars of pressure over the wire grids to reduce stagnation, the grids can be biased to several hundred volts. Passing particles cause an avalanche of secondary electrons (gas amplification) in the gas, and resulting current signals are collected from the ends of the wires. The spacing of the planes and the adjacent wires, the wire thickness and material, bias voltage, as well as the type of gas, its pressure, and flow rate all affect the characteristics and performance of a detector. The GREAT MWPC, used previously, had three planes, the middle cathode plane aluminized Mylar® middle plane, and the two anode wire planes were made of gold-plated  $50\text{-}\mu\text{m}$  thick tungsten wires with 1 mm spacings. Instead of the aluminized Mylar® middle plane, all three planes in the new gas counters are wire grid planes, which lets even lower energy recoils through. The wires are also slightly thinner at  $20\ \mu\text{m}$  and the X–Y spacings are 1 mm and 1.6 mm, respectively.



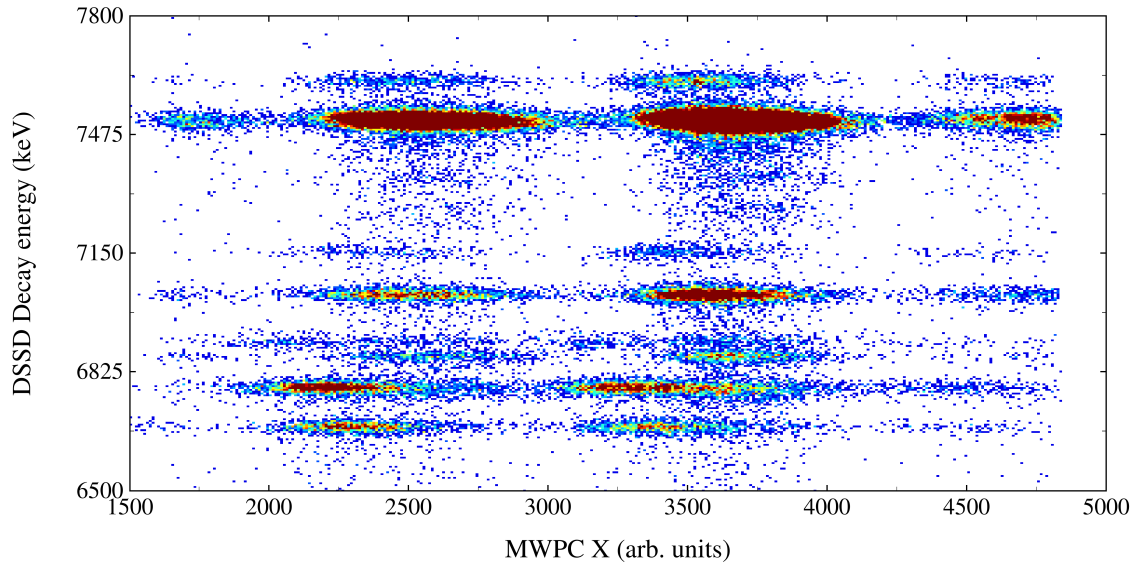


FIGURE 18 Decay energy in the DSSD versus the MWPC X position. The MWPC X position is proportional to the mass per charge ratio of the implantation event. Even with the relatively heavy nuclei of this work, MARA has some  $A/q$  resolution, as seen by the offset of the distributions on the X-axis. However, the  $A/q$  gating was unnecessary in this experiment due to the clear separation of the decay energies alone.

While just a simple logical signal is enough to differentiate decay events from beam-related events, evaporation residues are quite often just a small fraction of the implantation events. In these cases the signal from the MWPC also serves as a stop signal for a Time-of-Flight (ToF) measurement. Together, the energy and time-of-flight information can be used to classify the different beam-related events further. This is demonstrated in the [Analysis](#) chapter. Furthermore, the X–Y position information can be obtained by measuring signal arrival time differences from each end of a wire. The wires are separated by short delay lines to make the measurement more feasible. In MARA, the MWPC is positioned at the  $A/q$  focal plane and even better particle identification can be obtained with an additional gate on the MWPC X–Y event position (and decay energy in the DSSD), as seen in Figure 18. On the other hand, sometimes decay events occupy a completely different energy range as recoils, and hardly any other beam-related events are present. In such cases, MWPC is not strictly speaking needed, since only the energy of a particular event is enough to classify it.

### 2.7.3 “Tunnel” detectors

As discussed, light decay particles can escape the DSSD into the backward angles and only deposit part of their energy into the DSSD, which can be a problem if the full energy of the particle is needed for its clear identification or if the low-energy tail from these escaped events contaminate an energy range that contains other events of interest.

To increase the decay detection efficiency, additional segmented single-sided silicon pad detectors ( $6 \times$  Micron MSXP22 and  $2 \times$  MSXP21) can be arranged into a box/tunnel formation around the perimeter of the DSSD, as is shown in Figure 16(c). If a particle escapes the DSSD, and it is within a certain solid angle range, it will hit the tunnel detectors and most of its decay energy can be reconstructed by adding the two signals. However, the energy resolution will be degraded since the dead layer through which the particle travels depends on its escape angle and the initial position in the DSSD. In principle, this effect can be somewhat accounted for via internal calibrations.

Due to technical difficulties with the detector's cooling setup, the tunnel detectors were not used in this experiment. However, the escaped  $\alpha$  particles from the decays of the actinium and radium isotopes could still be reliably tagged as they occupied a decay energy-time domain, clean from most other events.

#### 2.7.4 "Punch-through" detectors

While the typical range of heavier particles in these experiments is only some tens of micrometers in the silicon, lighter and more energetic particles can pass straight through the whole thickness of the DSSD. These light particles are mostly electrons, protons, deuterium, and helium presumably coming from knockout reactions between the scattered primary beam and the walls of the separator and other beam line components. These events do not leave enough energy in the MWPC to trigger a veto signal. Partially deposited energy from these "punch through" events can result in a large background that can completely drown the actual decays of interest.

It is, therefore, useful to have auxiliary punch-through detectors directly behind the DSSD to filter out these problematic events. In the focal planes of MARA and RITU two thicker,  $500 \mu\text{m}$  or  $1000 \mu\text{m}$ , single-sided silicon detectors (Micron MSX35) are used.

In addition to the punch-through events, sometimes high energy decay particles, such as  $\beta$  particles and internal conversion electrons, can pass through the entire DSSD. These silicon detectors can also see some of those, but when performing recoil-beta tagging experiments, it is more beneficial to have additional dedicated tagging detectors behind the DSSD.

Other methods, such as beam pulsing may be applied to achieve similar beam-cleaning effects, but with a reduced effective beam time.

#### 2.7.5 Focal plane germanium-detector array

Usually the DSSD is also surrounded by an array of germanium detectors, which have a similar purpose to that of the JUROGAM 3. Sometimes nuclei can have metastable excited states with lifetimes long enough that these decay after reaching the focal plane. The existence of these states alone is already valuable information, but by measuring half-lives and determining the de-excitation paths of these so-called isomeric states, even more input can be provided for theoretical



models. These transitions can also be advantageous from an experimental point of view, as they can be used to identify and tag the nuclei similarly to the ground-state radioactive decays. Furthermore, the energy level structure can often be deduced more easily by tagging with these isomeric transitions and correlating back to the  $\gamma$  rays observed at the target position since they only bring up transitions residing above them in excitation energy. The focal plane germanium array can also be used for decay- $\gamma$  spectroscopy to probe whether the nuclei decay to excited states in the daughter nuclei that then emit  $\gamma$  rays when they relax.

In this experiment, three BEGe<sup>TM</sup>-type detectors (BE6530) by Mirion Technologies were placed behind, on top, and to one side of the DSSD. Two of these detectors are visible in Figure 16(d). The detectors are placed as close to the DSSD as possible to increase their geometrical coverage and detection efficiency. However, the large spatial coverage of a detector also increases the likelihood that more than one  $\gamma$ -ray hits it so close in time that their energies get summed together. Random summing is not really a problem due to the relatively low count rate at the focal plane. Still, some coincidence summing is usually observable when nuclei de-excite via a fast  $\gamma$ -ray cascade. The germanium crystals of the BEGe<sup>TM</sup> detectors are disk shaped ( $D = 91$  mm  $t = 30$  mm), and as the name suggest their optimal  $\gamma$ -ray energy resolution and detection efficiency range is rather broad, around 5–1500 keV. Nose caps of the detectors are fitted with thin carbon composite windows that let through low-energy photons. However, since the focal plane chamber is made of 3-mm thick aluminium it already limits the low-energy  $\gamma$ -ray detection efficiency much more than the entrance windows. The detectors have new intelligent preamplifiers (IPA<sup>TM</sup>) whose various parameters can be set in the software.

### 3 NEW AUTOMATIC LIQUID NITROGEN FILLING SYSTEM

As discussed earlier, germanium detectors must be cooled to low temperatures to reduce the electric noise induced by the thermal electrons and to lower the leakage current. For some types of detectors, the cooling also helps to preserve the lithium diffusion layer [67]. Common methods to achieve low temperatures are cryogenic liquids and electromechanical cooling devices, such as pulse-tube and Stirling coolers.

The germanium detectors of the JUROGAM3 and the focal plane arrays are cooled using Liquid Nitrogen (LN<sub>2</sub>). The detectors have multi-orientation cryostats that are thermally connected to the Ge-crystal via a cold finger, as illustrated in Figure 19. Liquid nitrogen is used, because of its low temperature of ~77 kelvin (−196 °C) at the normal atmospheric pressure. It is also chemically inert and relatively cheap. However, as with any cryogenic liquid, very real hazards are present, including asphyxiation, pressure explosions, and frost bites. A careful design and appropriate safety devices are needed to mitigate these risks. In fact, automatically cooling and monitoring the germanium detectors has been a long-standing technical challenge, not just at the JYFL-ACCLAB, but in the other laboratories operating similar equipment as well. Even at the JYFL-ACCLAB, many iterations of filling systems have been used over the years. Key operation requirements for such a filling system include:

1. Fill detectors on schedule, on demand and on temperature rise.
2. Monitor detector temperatures.
3. Alert personnel when necessary.

The operation principle of the existing setups have been much the same everywhere. Several, or all, the detector cryostats were filled simultaneously, either directly from a large cryogenic tank, usually situated a significant distance away and at a higher pressure or via an intermediate buffer dewar. A fill is started, either at a specific time of the day, or, in some designs, at a fixed period and/or also if a detector reaches a preset internal temperature. When a filling is initiated, a series of electronic or pneumatic valves are opened from the storage tank to

first cool down all associated lines and distribution manifolds. This is done to purge out the nitrogen gas that forms when LN<sub>2</sub> boils on contact with the warm pipes so that it does not unnecessarily warm up the Ge detectors. When the infrastructure is sufficiently cold, valves to the detectors are opened, and filling of the detector cryostats begins. The filling of a given cryostat is continued until, either the purge temperature sensor detects liquid nitrogen overflowing from the purge line or until a set filling time limit is reached. Warning and info messages regarding the status of the system and fillings, such as high temperature alerts, are sent out via a text message and/or by email to designated person(s).

Control electronics and programs of these systems were often developed in-house and in collaboration with other laboratories in a semi-prototype fashion. This made getting replacement parts and fixing program bugs difficult, especially after several years when people had moved on or retired. Even though different implementations of the design described above have been used successfully for a long time, they were not without their shortcomings. The most acute reason, however, as to why a new system was needed this time was because of the ageing electronics that were starting to fail frequently. Failing electronics caused a lot of high temperature alarms and unnecessary bias shutdowns, which translated to a lost beam time and statistics. Excess liquid nitrogen consumption, which followed, was not ideal either.

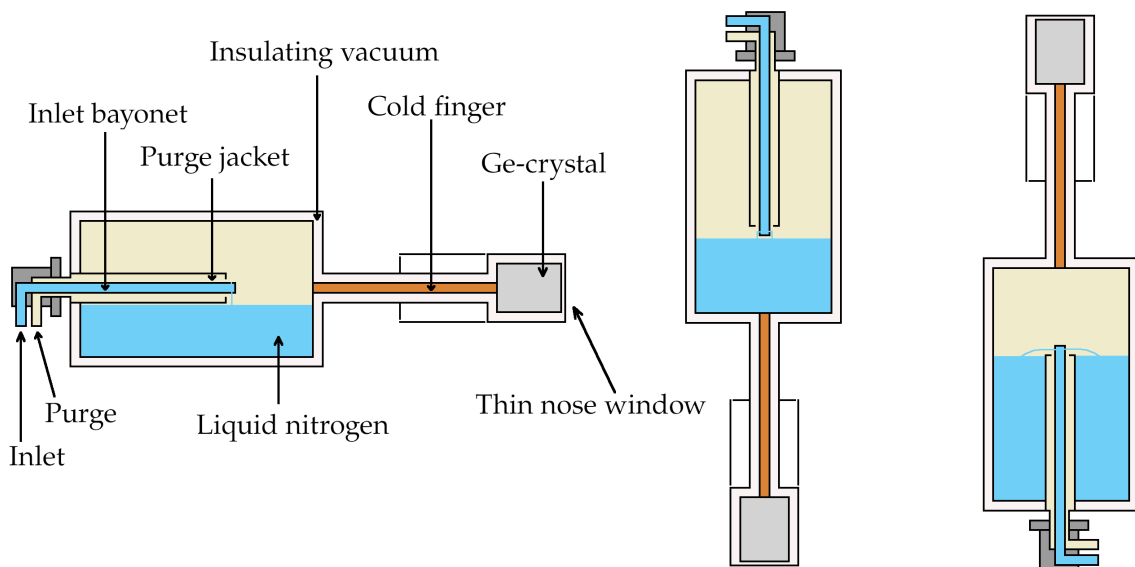


FIGURE 19 Cross-section diagram illustrating the inner workings of an “all-attitude” Ge-detector cryostat. This type of cryostat can be used in every orientation, but it can only hold LN<sub>2</sub> half of its total volume before it starts to overflow from the purge. In a nose-down position, when the liquid level reaches the end of the purge jacket, trapped gas pressurises, and pushes out the excess LN<sub>2</sub>. Slightly different Multi-Attitude Cryostats (MAC) can hold the full volume, but they can be only used horizontally or in nose up/down positions and their inlet and purge also switch places depending on the orientation. The whole assembly is vacuum insulated and the heat is removed from the Ge-crystal and the preamplifier front end via a copper cold finger.

### 3.1 Problems with the old system

Besides the aforementioned outdated hardware and software, which lacked modern connectivity and integration possibilities, some more fundamental problems were also present in the old design. The time it took to get LN<sub>2</sub> to a detector when a filling was requested was long for several reasons. The main 11000 litre storage tank is located outside the building, approximately 50 meters away, and a long vacuum-insulated pipe connected it directly to the old filling system. The whole pipe had to be cooled down before LN<sub>2</sub> could reach the detectors. Furthermore, after each filling, pressurised gas from boiling residual LN<sub>2</sub> left in the pipe quickly emptied and warmed it. The second reason was the coarse temperature resolution of the old readout device, which prolonged the time that the additional fillings could to be triggered in the first place. Filling the delicate detectors from a rather high pressure, 3.5 bar, of the storage tank was also not optimal. Furthermore, the pressure in the main storage tank does not stay very constant. For example, when it is being filled from the LN<sub>2</sub> delivery truck, the pressure in the tank rises to around 5 bar, where it stays for several hours. The boiling losses were also unnecessarily high due to the large pressure gradient between the storage tank and the detector cryostats.

Fillings were started on a schedule or if a set temperature threshold was exceeded (measured with Pt100 sensors coupled to the Ge-crystals). While every detector had minimum and maximum filling times, the primary shut-off happened based on a resistivity reading of a carbon resistor situated at the end of each detector purge hose. Scheduled filling started filling all the detectors simultaneously and then stopped them one by one based on purge resistor thresholds, which were tuned with 10-turn potentiometers located in the readout units.

The problem with the long waiting time before LN<sub>2</sub> reached the detectors was that they warmed excessively, sometimes leading to bias shutdowns. The bigger problem, however, was using the purge line resistors as the trigger for ending fillings. The assumption has been that there is a distinct resistance corresponding to the moment when the detector cryostat is full and starts to overflow from the purge. However, this is not true. Instead, the purge temperature reaches the minimum almost immediately, since the out-purging nitrogen gas is nearly as cold as the liquid phase. This led to constantly adjusting the potentiometers, which could only be done in situ. The carbon resistors were possibly also drifting a bit after each heat cycle. Another problem was triggering additional fillings based on a preset temperature threshold. The lowest temperature that a detector reaches after a filling is not always exactly the same, and if a detector was swapped, the new baseline had to be guessed, which often resulted in a need to make tedious adjustments in the software, which had poor remote operability. These, and some other problems combined, meant that the detectors could not really be cooled down from room temperature using the automatic system, but instead the first fillings were usually done by manually using Styrofoam boxes and funnels.

## 3.2 The new design

Learning from the past systems and doing extensive research and development with various test setups, a couple of design changes were conceived to address the problems discussed earlier. To fix the delay and pressure problem, an intermediate buffer dewar was introduced between the storage tank and the filling system. New electronics were designed based on a PLC platform, and an accompanying software was written in CODESYS 3.5. Some fundamental filling logic changes were also implemented. The prototype PLC setup and the first versions of the program were made by A. Ikonen. Later, the author continued the program development, and the final electronics design of the system was mainly done by Dr P. Rahkila. CAD rendering of the main mechanical components of the new setup is shown in Figure 20.

As mentioned earlier, intermediate buffer dewar setups are nothing new in these systems, in fact, even some of the past designs used them. However, these had suffered from some issues. Over time, the old buffer dewars started to consume a lot of LN<sub>2</sub>, since their vacuum insulation had not been maintained. Monitoring of the LN<sub>2</sub> level inside the buffer dewars, which was used for their automatic fillings, was done using capacitive sensors. However, those sensors were rather unreliable, especially during high flow conditions, which led to some problems with stopping the fillings. These issues, together with the problems with the filling logic, hid the benefits of the buffer dewars, which led to their removal in the past.

Another problem with the old buffer dewar setups has also been the lack of proper pressurisation. The nitrogen gas on top of the liquid phase in these dewars has to be pressurised to push out LN<sub>2</sub> when demanded. The previous buffer dewar setups relied only on a built-in auto-pressurisation circuit, in which an internal heat exchanger boils some LN<sub>2</sub> to generate the pressure. However, these could not match the demand needed for filling several detectors, so the pressure dropped and the LN<sub>2</sub> outflow halted. The lack of a high-capacity pressurisation circuit also meant that the buffer dewars could not deliver LN<sub>2</sub> during, and a few hours after, their own fillings from the big storage tank, as the pressurising gas was vented at that point. To fix this issue, the new buffer dewar setup uses pressurised nitrogen gas from the laboratory's main line. The gas is actually generated by boiling LN<sub>2</sub> from the same storage tank using a high-power heater element, however, it has more than enough capacity to support all the fillings. Additionally, the intermediate dewar is no longer vented during its filling, so it can supply LN<sub>2</sub> for the detectors at any time. To simplify the setup, the new system uses a single 400 L buffer dewar instead of the two 300 L dewar configuration used in the past. The buffer dewar can still accommodate fillings for 24 hours. Instead of the capacitive or differential pressure sensor, the LN<sub>2</sub> level in the buffer dewar is now monitored using an industrial weighing scale, on which the whole dewar setup is placed. This proved to be a very effective and robust solution. The scale also serves as a convenient platform to move the dewar with a pallet jack.

However, the problem of correctly determining when to stop a filling of a detector remained. Despite experimenting and testing with different ideas, a good shut-off trigger was not found. Coincidentally, the work done to the buffer dewar setup to fix the delivery and pressure problems also made the flow conditions so stable that it became evident that the detectors could be now simply filled based on time alone. Having said that, if all ~40 detectors were to be filled simultaneously, the LN<sub>2</sub> flow would have still been a little too erratic for the system to work reliably. Fortunately, the flow rate was now also so much higher

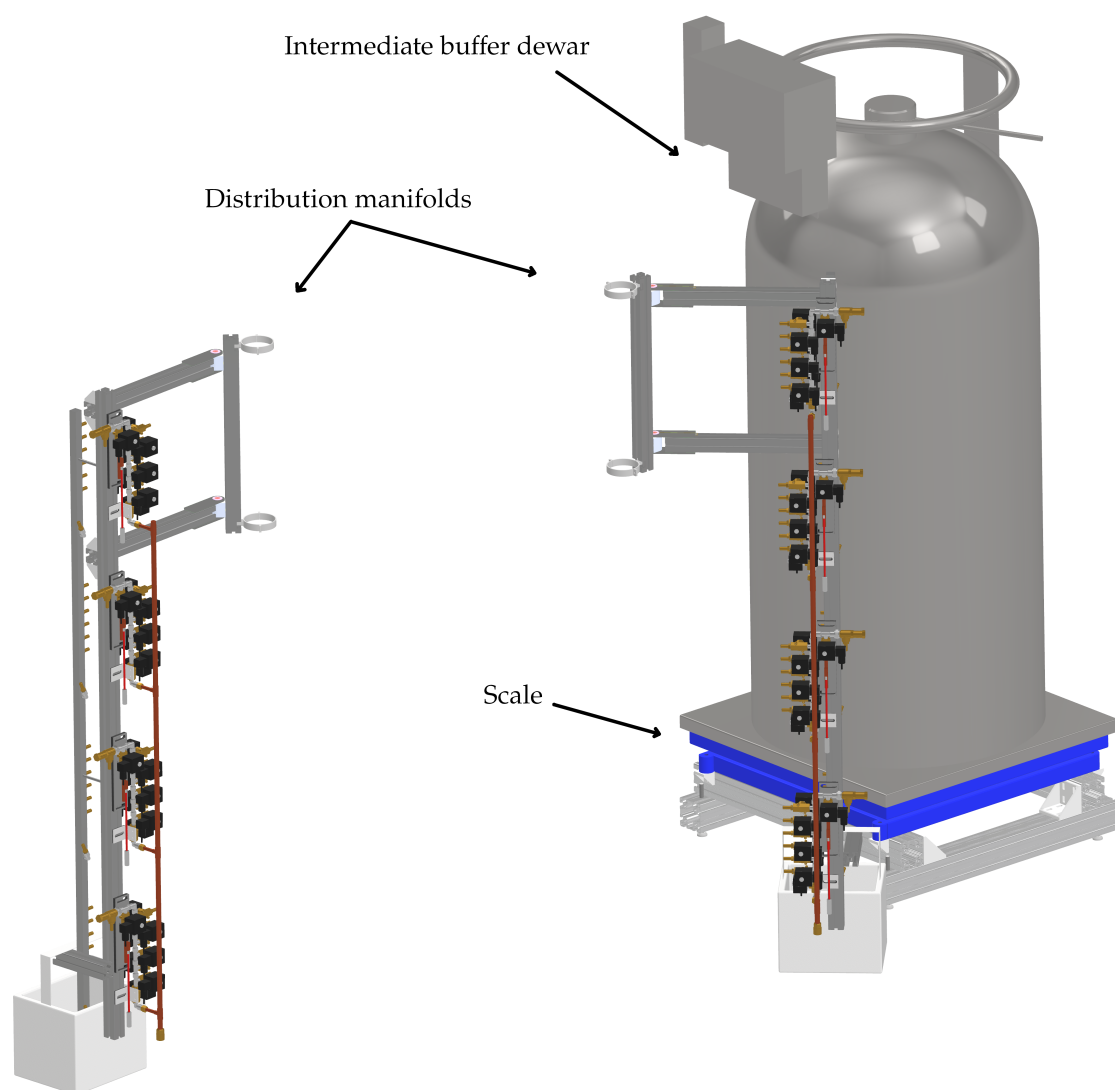


FIGURE 20 CAD rendering of the new filling setup. Distribution manifolds are attached to the support struts of the two JUROGAM 3 hemispheres and move independently with them. This arrangement minimises the length of the polyurethane hoses that go to the detectors, which puts less strain on them and makes the whole system more compact and efficient. The intermediate 400 L buffer dewar sits on an electronic weighing scale that indirectly measures the LN<sub>2</sub> level inside the tank.

that the detectors could be filled one by one in a cascade (three detectors simultaneously, one in each main branch) and the total filling time of the whole setup was still less than or equal to what it used to be when all the detectors were filled simultaneously. LN<sub>2</sub> enters the distribution manifolds from the lowest point and cascade fillings progress from the highest position down. This is done to cool down the whole setup properly at the beginning of each scheduled filling, which minimises unwanted boiling later and increases the efficiency of the system.

The detector purge lines were still fitted with temperature sensors (proper Pt1000 sensors) that are used to trigger various warnings. For example, an alarm SMS is sent if a sufficient purge temperature drop is not detected during a filling, indicating a mechanical failure, such as a kink in a hose or a failed solenoid, could be at fault. If filling the manifolds was solely based on a predetermined time, a lot of LN<sub>2</sub> could be wasted if a nearby manifold had been filled recently and the lines were already cold. Therefore, the only place where the purge sensors are still rather important is on these manifold purge lines, where they are used to roughly determine when LN<sub>2</sub> starts to come through.

The hassle associated with setting unique additional filling temperature triggers for every detector was fixed in the new software. The program compares the current detector temperature to its lowest temperature since the last filling and triggers an additional filling based on the value of this temperature difference. This way, the additional filling trigger corresponds to an actual warming of a detector, and the new system is therefore completely agnostic to a detector's unique characteristics like the baseline temperature. Since the filling temperature baseline is now updated dynamically, regardless of the absolute temperature of a detector, the new system can cool down a detector autonomously, all the way from the room temperature. Additional fillings were also made twice the length of a normal filling to account for warmer hoses and a completely empty detector cryostat. The measurement of a Pt100 sensor resistance in cryogenic temperatures is susceptible to electrical noise and moving of the cables. Even small changes in the measured resistance can trigger an additional filling unnecessarily. To minimise falsely triggered fillings, rapid sensor reading fluctuations that do not correspond to a real detector warming are flagged by a temperature gradient check in the program. The system can also operate without any sensor data by returning to a purely time-based protocol. A change of the operation mode happens automatically when a sensor fault is detected. A notification will also be sent out. For less critical sensors, like the purge sensors, the system will also automatically revert if the fault condition clears on its own. Most of the settings are accessible through the WebVisu interface. Figure 21 shows the main status page of the HMI and Figure 22 shows the parameter configuration page of a manifold. Any web client can reach the WebVisu control page, even with a smartphone, greatly reducing the urgency to go to the laboratory in person or even get up from bed should a minor problem occur at night.

LN<sub>2</sub> consumption of a detector and the required filling cycle is dictated by the size of its cryostat and the heat load it experiences. The heat load depends on the vacuum level of the cryostat, size of the Ge-crystal, the ambient





FIGURE 21 The new main page of the HMI provides a comprehensive overview of the system’s status. It shows, for example, the detector temperatures, voltages, and active channels.

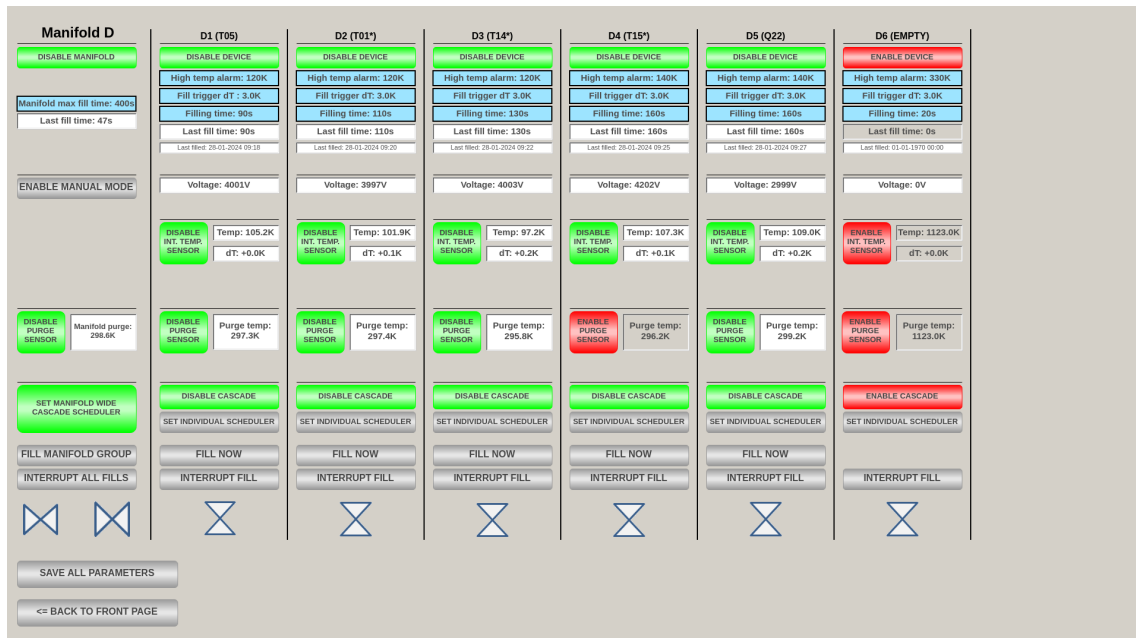


FIGURE 22 Configuration view of the new system. High temperature alarm level, warm-up trigger, filling time, active sensors, and scheduled fillings can be set up on detector by detector basis. When the manual mode is enabled, valves can be freely operated by hand.



temperature, and the heat generated by preamplifier and the BGO shields. From a cooling point of view, five different types of detectors are used in the standard setup. GASP-type detectors have the smallest Ge-crystals and the smallest cryostat capacity of ~2 L, EUROGAM Phase1 “tapered” detectors have slightly larger crystals and ~3 L cryostats, EUROGAM Phase2 Clover-type detectors have even larger 4-crystal configuration and ~3 L cryostats. At the focal plane, three BEGe™-type detectors have medium-size crystals and ~5 L multi-attitude cryostats. There are also a couple of newer Clover-type detectors that have a slightly larger cryostat. The holding time of the older GASP, Phase1, and Clover-type detectors is between 13–18 hours. The new Clover detectors can stay cold for about 24 hours and the BEGe™ detectors can go up to 4 days without needing to be filled.

One design consideration of the new electrical architecture was a modular construction to ease deployment and prevent extensive outages should any individual component fail. Another aspect was the use of standard off-the-shelf parts that are readily available from big suppliers for longevity and maintenance reasons. Following these principles, it was decided to use industry-standard programmable logic devices from WAGO Kontakttechnik GmbH & Co. KG. to implement all the logic and control components of the system. Low-power PLC modules and higher-power valve solenoid relays have separate power supplies. Modularity of the system is achieved with a common WAGO CPU module that controls the remote distributed I/O subunits that use WAGO MODBUS modules to extend the I/Os of the main PLC over the local area network. These submodules can be deployed anywhere with a connection to the network. They house all power supplies and the solid-state relays for controlling the LN<sub>2</sub> valves and ADC modules for reading the internal and purge temperature sensors.

Minimising the transmission of electrical noise from the outside environment into the internal Pt100 temperature readings and from the solenoids into the energy signals of the germanium detectors was a critical aspect of the electrical design. The old valve solenoids and the mechanical relays operated at 230 VAC, which was not optimal from the EMI or maintenance point of view. AC solenoids were used since they have more initial power to open the valves in case of elevated pressure, but now that the pressure was well-regulated and stable, it was possible to make a switch to 24 VDC solenoids. More modern opto-isolated solid-state relays also replaced the mechanical relays. In addition, now that the power supplies were separated, the more electrically noisy solenoid supplies could be plugged into the “dirty” electricity outlets. There are three electricity circuits in the laboratory: “dirty”, “clean”, and “UPS”. These come from different isolation transformers with separate grounds. Clean outlets power delicate low-noise devices, such as preamplifiers and Nuclear Instrument Modules (NIM). Dirty outlets are for all the noisy devices, such as motors, vacuum pumps, and inverter power supplies. UPS power is tied to the clean ground, and is also the battery back up in case of power outages. During the overhaul of the LN<sub>2</sub> system, the grounding was corrected, as it is very easy to have them mixed somewhere. An overview of the electronics layout is shown in a block diagram in Figure 23.

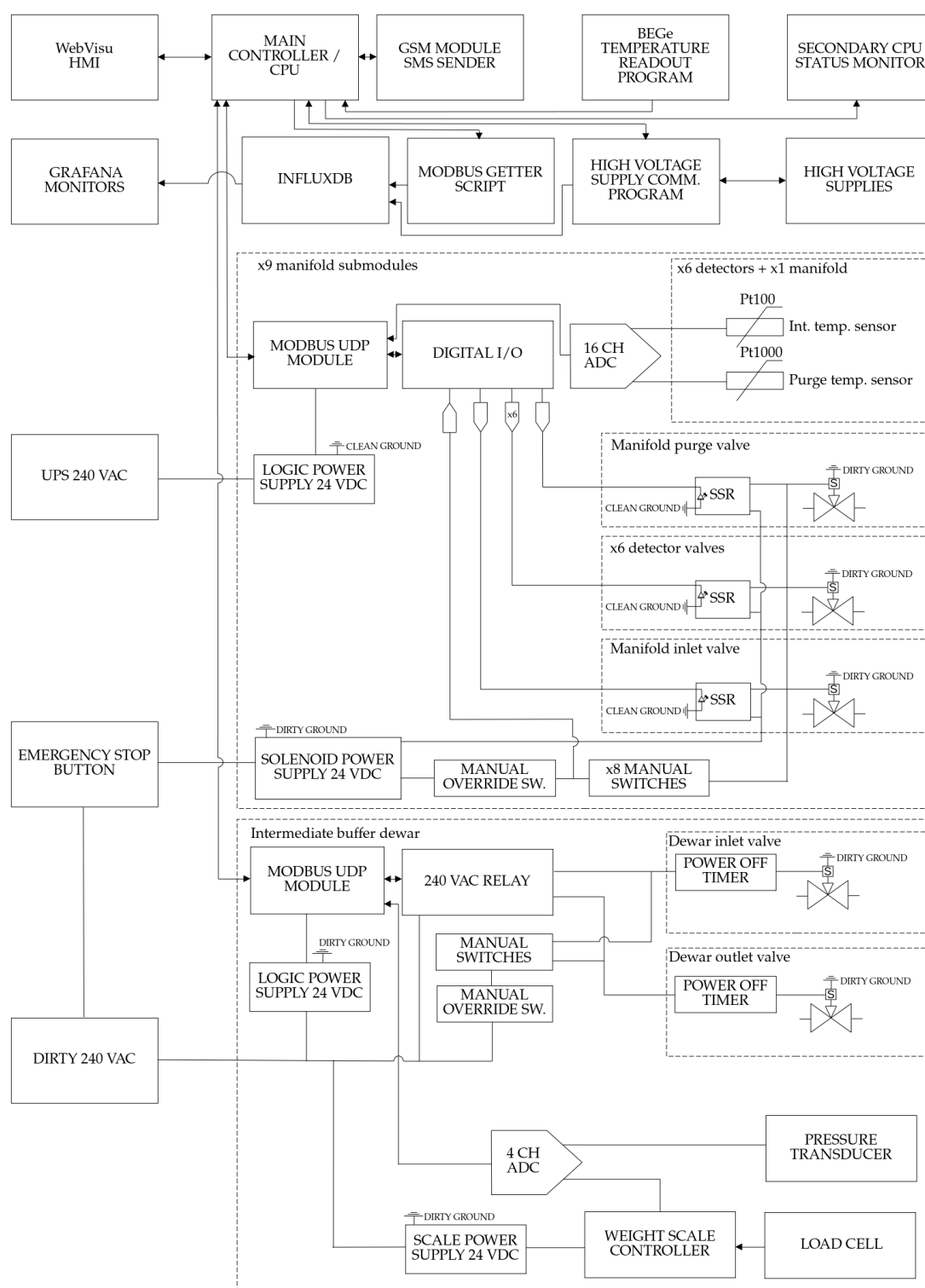


FIGURE 23 Block diagram of the electronic architecture of the new LN<sub>2</sub> filling system. Additional solenoid power off timers for the intermediate buffer dewar lines are yet to be put in place at the time of writing of this thesis. An integrated universal hardware bias shutdown module is also under development.

Regarding the mechanical design, reducing parasitic heat loads was an important consideration. The heat load has been minimised by making the new setup as compact as possible, reducing pipe and hose lengths, eliminating unnecessary bends and orifices in the manifolds, using low heat capacity materials, and having proper thermal insulation. Keeping the energy losses to a minimum reduces the LN<sub>2</sub> consumption, but even more importantly, it reduces the flow restrictions caused by gas bubbles from boiling LN<sub>2</sub> in the pipes and thus makes the fills a lot more reliable. Flow dynamics of cryogenic liquids are not very straightforward. It is like managing water in red-hot pipes, except that the viscosity of LN<sub>2</sub> is only 1/30 of that of water, so it really flows through the path of the least resistance, which is a big problem if multiple detectors are filled simultaneously.

The safety of the new system was also a high priority. There are mechanical safety devices, such as pressure relief valves and oxygen sensors, and then there are also safety features implemented in the software, such as filling thresholds and various sensor checks. In principle, the system always operates with pressures below 2 bar, but since cryogenic liquids are involved, every closed volume has the potential to reach pressures up to 700 bar. Therefore, every section of the system is protected by automatic pressure relief valves and rupture disks. These safety devices are situated so that any combination of opened or closed valves can not make a pressure to build up and bypassing them would require a considerable effort. Safety valves on the outlet side are set to 2 bar, whilst the intermediate buffer dewar is regulated at 1.5 bar. The inlet side is normally regulated at 3.5 bar by the regulator and safety devices at the storage tank end. However, an automatic 5.5 bar relief valve still protects the braided hose from the buffer dewar to the vacuum-insulated pipe if both hand valves are closed while still having some residual LN<sub>2</sub> inside. If the main pressure regulator valve of the buffer dewar gets stuck, the pressure starts to rise, and if the line to the storage tank is open, LN<sub>2</sub> will start to flow back into it, which is a desired outcome in this case. The buffer dewar is also fitted with a couple of 6-bar rupture discs should every other safety mechanism fail. All safety devices and valves are specifically designed to be used with cryogenic liquids. Standard ball valves for water can trap LN<sub>2</sub> inside the hollow ball and burst. The solenoid valves are of plunger type, so they let the pressure discharge in the opposite flow direction, but no part of the safety relies on this. Heat transfer must also be taken into account. All the parts must be able to endure extreme temperatures even if they are not in a direct contact with LN<sub>2</sub> they can still get very cold via conduction. The formation of ice due to the ambient moisture has to be considered, especially the relief valves, which must be positioned so that they cannot get blocked. Locations where LN<sub>2</sub> is used are fitted with oxygen sensors that will trigger a flashing red light and a loud sound signal if the oxygen level falls below 19%. Flashing blue lights are also installed next to the appropriate devices that activate when a filling occurs. Two additional power-off timers will soon be installed onto the solenoid power rails of the buffer dewar which should limit possible spilling of LN<sub>2</sub>, should all the other software features fail or if the physical bypass switch is left on. A schematic diagram of the system is shown in Figure 24.

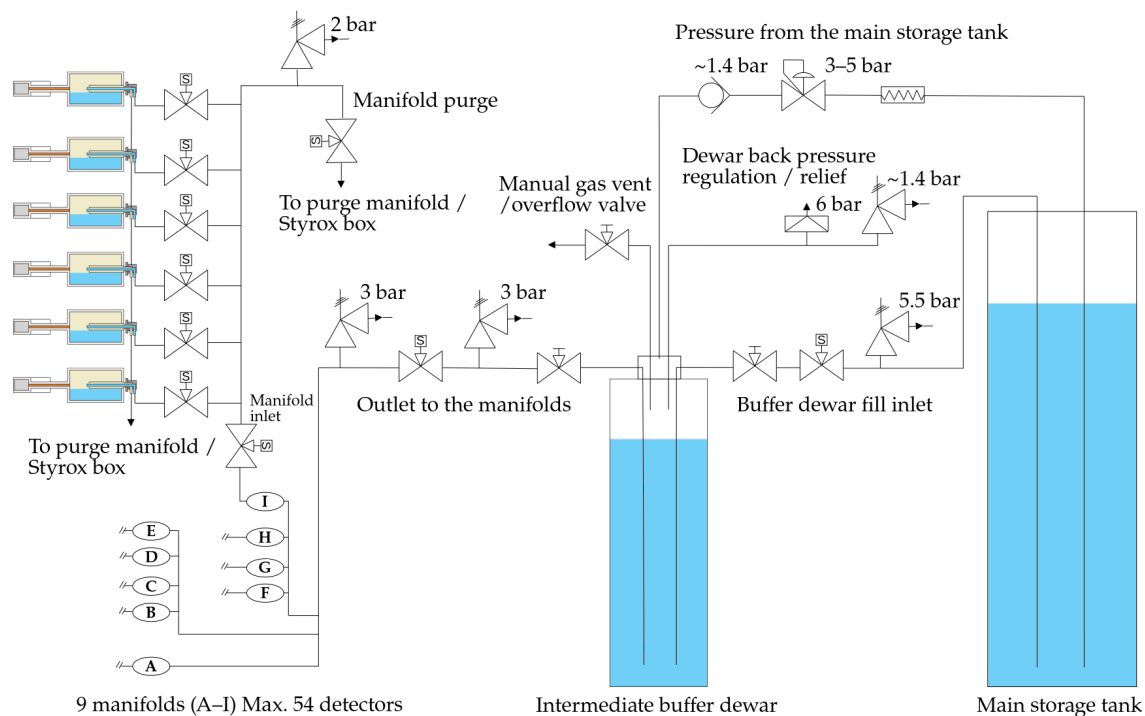


FIGURE 24 Schematic diagram of the cryogenic layout of the new system. A third backup pressure relief and electronic pressure transducer should be also added onto a separate branch of the intermediate buffer dewar in the future. The main storage tank is located outside the building.

Various safety functions and SMS alerts are implemented in software. Fillings have adjustable maximum times, and the submodules are configured to close all valves if the network connection to the main controller unit is lost. The LN<sub>2</sub> level in the intermediate buffer dewar is constantly monitored, and if a change in the weight of the dewar is detected, when the inlet or the outlet is not open, a text message is sent to the person on the LN<sub>2</sub> shift. The status of the main controller unit is also monitored by a completely independent script. This script monitors the temperature readings reported by the controller, and it can send out an SMS alarm via a USB GSM module if they stop changing. Detector bias voltages and additional status info from the CAEN high voltage supplies are piped directly to the main controller, and SMS alerts were implemented to monitor the status of the supplies indirectly. All the info is also forwarded into the Influx database and monitored from the Grafana panels displayed on the screens in the experiment control room. A separate program was also written to integrate the new digital IPA<sup>TM</sup> preamplifiers of the BEGe<sup>TM</sup>-detectors into the LN<sub>2</sub> system to read out their temperatures. The detector filling logic is summarised in a flowchart in Figure 25. As a side note, a new autofill system for the AGATA array has been under development over the past 15 years [68], and according to the technical report in Reference [69], they have recently made many similar design choices and conclusions as us. A scale to measure buffer dewar content is also used with the GEARS setup at NSL [70].

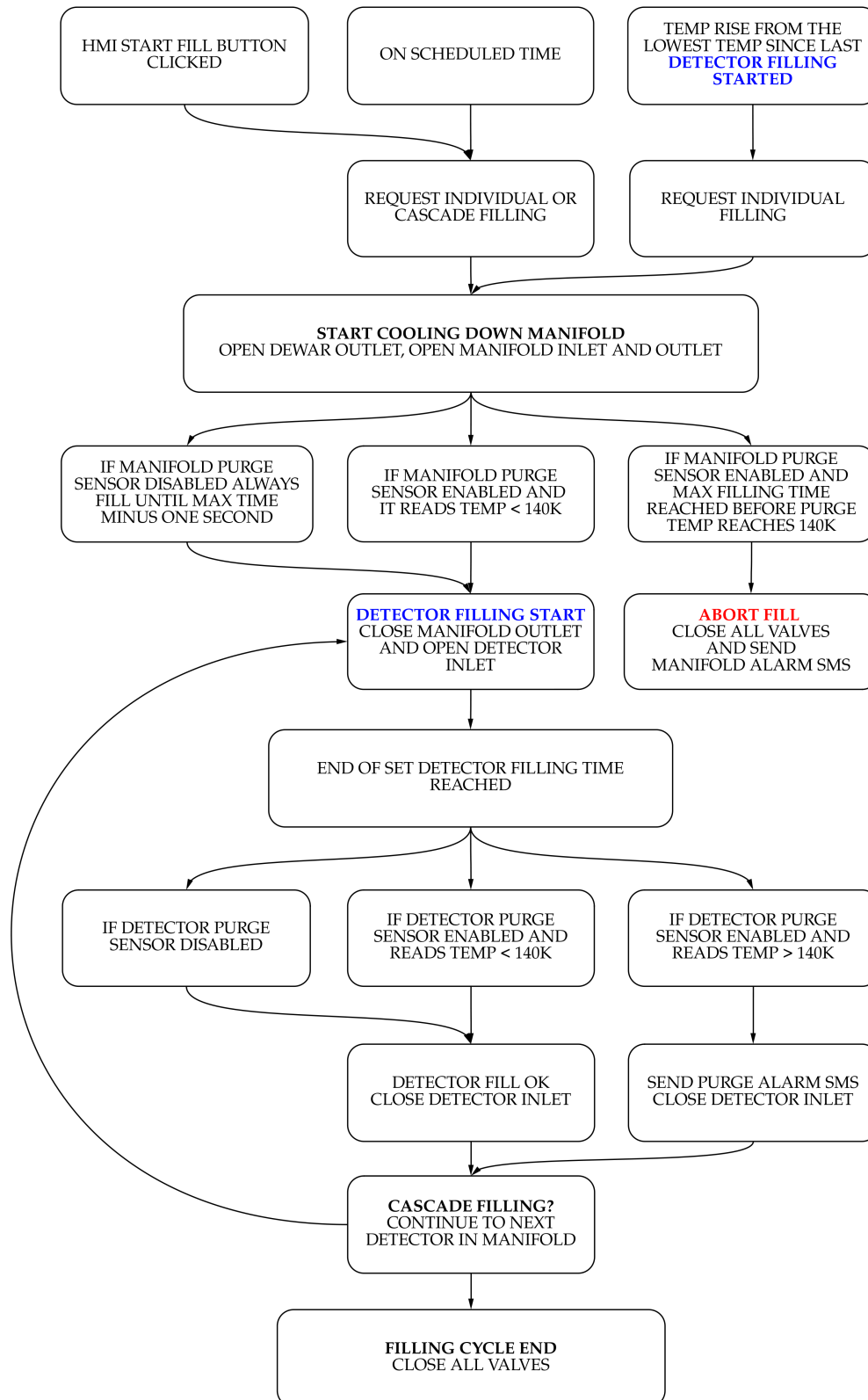


FIGURE 25 Logic flow when an automatic filling of a detector is requested. Automatic filling can be initiated in three ways: manually by pressing a button in the HMI, on a set schedule, or a temperature rise. Several checks are in place to validate the sensor data and connection integrity before allowing an automatic filling.

### 3.3 Performance

At the time of writing of this thesis, the new setup has been in use with a partial setup for around one year and about eleven months with a full standard setup consisting of 39 detectors in the JUROGAM 3 array and 3–4 detectors at the focal plane. Some performance data has been gathered during this time. The consumption of LN<sub>2</sub> has decreased to approximately 100000 litres per year compared to the previous 300000–500000 litres. Filling the full setup takes about 50 minutes, consuming ~140 litres of LN<sub>2</sub>. Larger detector cryostats typically require 120–180 s to fill. For small ones, 70–100 s is enough. Detectors are now filled only twice a day instead of three. Filling the buffer dewar is done once a day, and it takes about 2 hours. Currently, most of the LN<sub>2</sub> consumption is due the evaporation losses of the big storage tank, as its insulation is not in the best shape anymore. Relatively few detector bias shutdowns, warm-ups or even visits to the cave have occurred during the past year, and generally, only the daily status SMS is sent. This is a huge improvement to the previous record of dozens of text messages daily and regular laboratory visits to adjust the sensors by hand. Even the additional fillings are not that common any more, and they do not generally require any action from the person in a shift as a detector only warms a couple of degrees. As mentioned earlier, the array can now be cooled mostly autonomously starting from room temperature. The compact design and the common purge manifolds eliminated the tangling hoses, reduced kinking, and freed up space to work with the detectors. Since the LN<sub>2</sub> manifolds now move independently with the hemispheres of the array, opening, closing, and moving of the array has been made a lot more effortless. The temperature readout is now so stable and accurate that it allows for 0.1 K resolution. Consequently, a lot of insight has been gained regarding the temperature behaviour of the detectors, which can be used to predict problems or a need for maintenance. For example, if a detector starts to have regular additional fillings every couple of days, the set filling time is probably slightly too short. Whereas, a long-term upward temperature trend suggests a leak in a cryostat vacuum and high purge temperatures can reveal mechanical problems. Figure 26 shows the internal temperature trends of the detectors in manifold B. Noise induced into the detector energy signals during fillings has also significantly been reduced.

The commissioning of the new system went surprisingly well, especially considering that everything had to work on the first try after taking down the old system. Most of the software development was done on a small bench setup and, afterwards, on the real mission-critical system with no room to fail an update. Minor issues that have emerged have been mostly fixed, but as with any system of this scale and complexity, some improvement ideas become apparent with time. The three branches that feed the manifolds on both sides of the JUROGAM 3 and the focal plane share a common LN<sub>2</sub> outlet from the buffer dewar, which means that adding or removing in detectors or large filling time changes can throw off filling time parameters of other detectors. In hindsight, a little larger buffer dewar

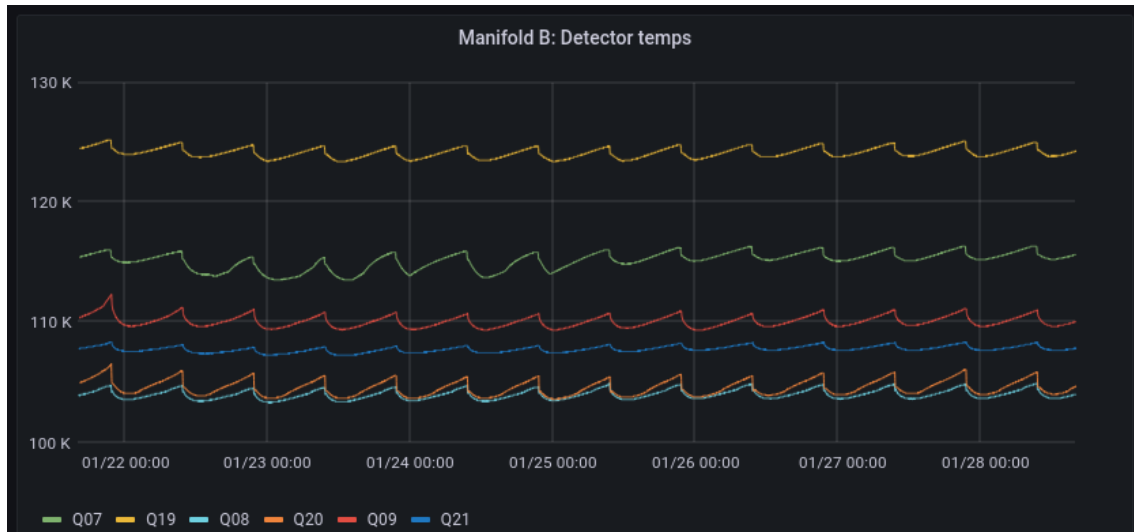


FIGURE 26 Internal temperature graphs of some detectors in the Grafana. Trends allow for assessing the condition of a detector and to monitor slowly developing faults. Detectors mounted in different orientations have different warm-up behaviour due to the varying contact patch of the LN<sub>2</sub> inside the cryostats.

with three independent outlets would have been better. A secondary automatic relief valve and pressure gauge should be added to the unused branch of the buffer dewar. At the moment, there is only one automatic 1.5 bar relief, and if it gets stuck, the rupture discs will trigger and have to be manually replaced before the system can be used again. Hose fittings in the detector filling bayonets should have barbs to prevent the fill hoses from slipping off. Stainless steel hoses that feed the manifolds on the different sides of the JUROGAM 3 are not the same length. When the array is moved between MARA and RITU, these hoses have to be switched, and all the filling times have to be interchanged also. Having symmetric hoses would be more convenient. Integration of a universal bias shutdown circuitry directly in the submodule assemblies is also planned. Currently, Ge detectors from different eras and manufacturers have a random assortment of bias shutdown signalling and unifying them would be good. Many features could be implemented on the program side, such as support for choosing the configuration file, remote logging, and some alarm indicators. The program could be imported to a different platform as the current controller is rather slow. The program could also be rewritten in a different language, making the long-term maintenance easier, since there are not many CODESYS programmers at the department. The data flow between devices and databases could be simplified and integrated into the controller itself. The current system also relies quite heavily on the GSM connection, so if the network goes down or the receiving phone does not have reception, it could take some time for somebody to notice a problem. Other single points of failure exist, such as the main CPU, so an adequate stock of replacement parts should be kept at hand.

To sum up, the idea that made this setup work so well is to make the LN<sub>2</sub> flow stable and predictable and then just fill a detector for a set time. This was done with a proper buffer dewar setup combined with cascade fillings.



## 4 DATA ACQUISITION

The Data Acquisition System (DAQ) of the MARA and RITU setups has been discussed thoroughly in the past works and the current setup is now at the end of its life cycle and will be replaced in the near future. However, a brief overview of the signal chain is still necessary as a background for the analysis chapter of this work.

### 4.1 Signal chain

As discussed in chapter 2, ionising radiation creates electron-hole pairs inside a semiconductor detector that induce electric currents as they move to the electrodes. However, the amplitude of these currents is very small, and the output signal shape depends on charge collection speed and physical location inside the detector where the interaction takes place. The raw signals are, therefore, not that easy to deal with, especially in terms of energy extraction. To make the signals more manageable, the first device in the signal chain is often a Charge-Sensitive Preamplifier (CSP). A CSP is essentially an operation amplifier with a feedback capacitor and a bleed resistor. The energy signal, i.e. the charge, is stored in the feedback capacitor, and as that charge then discharges through the bleed resistor, an amplified signal is generated at the output of the operation amplifier. The integrating property of the preamplifier also decouples the signal from the charge collection effects and averages noise peaks.

The output signal from CSP is still not optimal for all purposes as it has a long, exponentially decaying tail, which can start to pile up with the following events. Long signals generally need to be integrated longer, decreasing the maximum event rate the system can handle. Further signal processing is needed to reduce this issue. Traditionally this signal shaping has been done with analog devices, such as Timing Filter Amplifiers (TFA), but nowadays, with these relatively small bandwidth signals and count rates, fully digital setups have largely replaced them. Digital signal shaping is discussed more in the next section. How-



ever, one application in the current setup still uses some analog signal processing, and that is high-precision timing measurements. In this particular experiment, these are the time-of-flight measurements between the MWPC and the DSSD and the MWPC X–Y position readout.

Of these two, the ToF measurement between the MWPC and the DSSD is more relevant for the present work since the  $A/q$  resolution was unnecessary. With the time resolution of the main DAQ, 10 ns, it is difficult to achieve the required separation of flight times between recoils and other beam related products over the relatively short distance of 43 cm between the MWPC and the DSSD. The velocity difference between the different components can be less than 10%. For fast products, this means only a few nanosecond differences in the flight times, so a more accurate Time-to-Amplitude Converter (TAC) has to be used measure it. In practice, the ToF measurement can be started by a trigger signal from any of the 192 X-side strips of the DSSD. The twelve X-side Mesytec MPRT-16 preamplifiers of the DSSD have two built-in 8-channel Timing Filters (TF) that shape the signals from the CSPs to symmetric and more narrow Gaussian pulses from which Leading Edge Discriminators (LED), also built-in the preamplifiers, derive a common NIM-standard timing trigger output. The leading edge discriminators have a minimum voltage threshold that can be adjusted to an energy range where the recoils of interest reside, so low-energy noise and decays would not unnecessarily trigger the ToF measurement and create false correlations or saturate the TAC. These 24 timing pulses are then combined into a single signal via a standard Fan-In/Fan-Out (FIFO) module, which is the actual signal that is finally fed into the start input of the TAC. The stop input is derived from a common cathode signal of the MWPC. However, since the MWPC is situated before the DSSD at the focal plane, it sees the beam-related events first. Therefore, its signals must be delayed to make them reach the TAC only after the start signal from the DSSD has enabled it. The MWPC is not used to start the ToF measurement because it is physically larger than the DSSD and, therefore, also sees events that do not necessarily hit the DSSD at all. In these cases, the TAC would only reset after its time measuring range limit, usually set at 1  $\mu$ s, has been reached, increasing the ToF dead-time and random correlations. While the DSSD can see additional events, such as  $\alpha$ -decays and beam-related light particles, as demonstrated in Figure 36 later, in practice, the trigger rate of these events is almost always lower than the recoils and other beam-like events in the same energy range.

The output ToF signal from the TAC follows a similar path to every other single-ended signal in the setup. First, it is converted into a differential signal via a Single-ended to Differential (SoD) converter to minimise a common-mode noise pickup over the  $\sim$ 30 m cable to the DAQ cabinets. It is then converted back to single-ended via a Differential to Single-ended (DoS) converter before it enters a digitiser. The MPRT-16 preamplifiers for the DSSD have native differential outputs for the energy signals, but most other devices in the setup have single-ended outputs. The new digitisers will have differential inputs, eliminating the need for separate DoS cards in the future.

## 4.2 Digitisers, merger, and filewriter

Most of the signal shaping traditionally performed using analog devices, such as TFAs and Constant Fraction Discriminators (CFD) can be approximated with digital circuits. To achieve the speed necessary for real-time signal processing field-programmable-gate-arrays (FPGA) are used for synthesising these circuits. However, analog signals must be first digitised so that the FPGA logic can act on them.

The current DAQ is based on Lyrtech's (now Nutaq) VHS-ADC modules. Front-end of these modules is based on Analog Devices' AD6645 14-bit sigma-delta Analog-to-Digital Converters (ADC). The modules have Xilinx's (now AMD) Virtex-4 FPGAs that house the signal processing algorithms. One module has 16 single-ended analog inputs, and 7 of these modules fit into one CompactPCI (CPCI) crate, which also houses the required power supplies and a common backplane connecting all seven cards onto a CPU running the higher level code. The DAQ has 6 of these crates, for a total of 672 individual signal channels. A common 100 MHz clock signal is generated in an external metronome module, and it is distributed through Total Data Readout Interface (TDRI) modules to all the ADC cards to achieve a synchronisation lock and the 10 ns time resolution. The Adlink CPCI CPU modules in the crates handle the programming of the VHS-ADC cards and set-up of firmware parameters. They also send the data to the merge program via a GbE TCP/IP connection.

The merge program combines the data received from the six different crates into a chronological order based on their timestamps. In addition, slow control packets can be injected into the data stream at this stage with the new merge program. The merge program then forwards the time-ordered data stream to all connected clients. Usually, this means an online data-analysis program and a filewriter. The filewriter program manages writing the data to different outputs, such as the central Network Access Storage (NAS) of the University. If the amount of generated data is large, and not all the channels need to be recorded constantly, a software filter program can also be introduced between the merge and the filewriter programs. The filter can throw out packages from the channels based on specific criteria, greatly reducing the total amount of data written on the disk. One often used filter condition is that the data from high-counting devices at the target position, such as the JUROGAM 3 and JYTube, are only saved if any channel at the focal plane triggers shortly after. Extreme care is needed when implementing these filters not inadvertently bias the data.

As mentioned, the functionality of an arbitrary analog circuit can be synthesised using digital logic. Instead of the high level of abstraction and serial processing, typical to programs implemented for modern CPUs, the speed of an FPGA arises from the parallel operation and small overhead. The logic implemented in the FPGAs and their working, in general, more resembles that of the analog circuits. With every clock cycle, the state of a system advances one step. The signals can be, for example, duplicated, delayed, summed, and compared,

but more complex arithmetic operations and time referencing are not really feasible, at least not in real time. It is also crucial to take into account the propagation delay of different signal paths as the signals often need to be operated on with precise relative time offsets.

There are two firmware variants in use. One uses a gated integrator (GI), and the other uses a moving window deconvolution (MWD) algorithm to extract the “raw energies” from the signal traces. The output of these algorithms is referred to as a normal “ADC” value in the data stream, not to be confused with a raw ADC reading of a trace, as explained in the next section. Intricacies of these methods are out of the scope of this work. For more details see, for example, Reference [71]. However, a simplified idea of these algorithms follows to provide a quick background.

The gated integrator is a more universal algorithm. It triggers if a certain momentary signal amplitude level is exceeded. It then waits for a set delay period before integrating, or in this case, summing together a predetermined number of subsequent digitised signal readings. A signal baseline reading is also integrated before the trigger point, and it is subtracted from the aforementioned value to obtain the final energy output. The gated integrator algorithm, while rather basic, can still suppress random noise components effectively due to its averaging property. Gated integrators can sometimes be better suited for specific applications due to their simplicity and ability to deal with many different signal shapes. However, the gated integrator FPGA implementation does not always perform as well with long or piled-up exponential decaying signals. The GI firmware is often used for scintillation detectors that use SiPMs, since those have fast decaying and more Gaussian signals. They also do not typically experience that many pile-up events.

On the other hand, the moving window deconvolution algorithm is specially tailored for exponentially decaying signals with longer decay time constants. In this particular experiment, the MWD firmware was used for most channels, such as the DSSD and Ge detectors that use CSPs. The MWD firmware can resolve fast subsequent exponentially decaying signals better than the GI firmware. The MWD algorithm achieves this by effectively removing the signal tails. It does this by first deconvoluting the exponentially decaying signals into discrete step pulses, before differentiating them into square pulses. It then uses a moving window averaging algorithm to average out some noise. The averaging turns the square pulses into trapezoidal pulses from which the final amplitude, i.e. the energy, is extracted. Fast subsequent events are often present in the DSSD channels since, by definition, the decay of an implanted recoil happens in the same quasi-pixel.

Even more sophisticated signal processing, which is hard to implement in the FPGAs, or does not need to be in real-time can be done offline if raw signal traces are recorded, which the system can also do. However, collecting traces requires a lot of disk space and bandwidth and is therefore not always used if short-living states are not expected. The block diagram of the whole signal chain is shown in Figure 27.

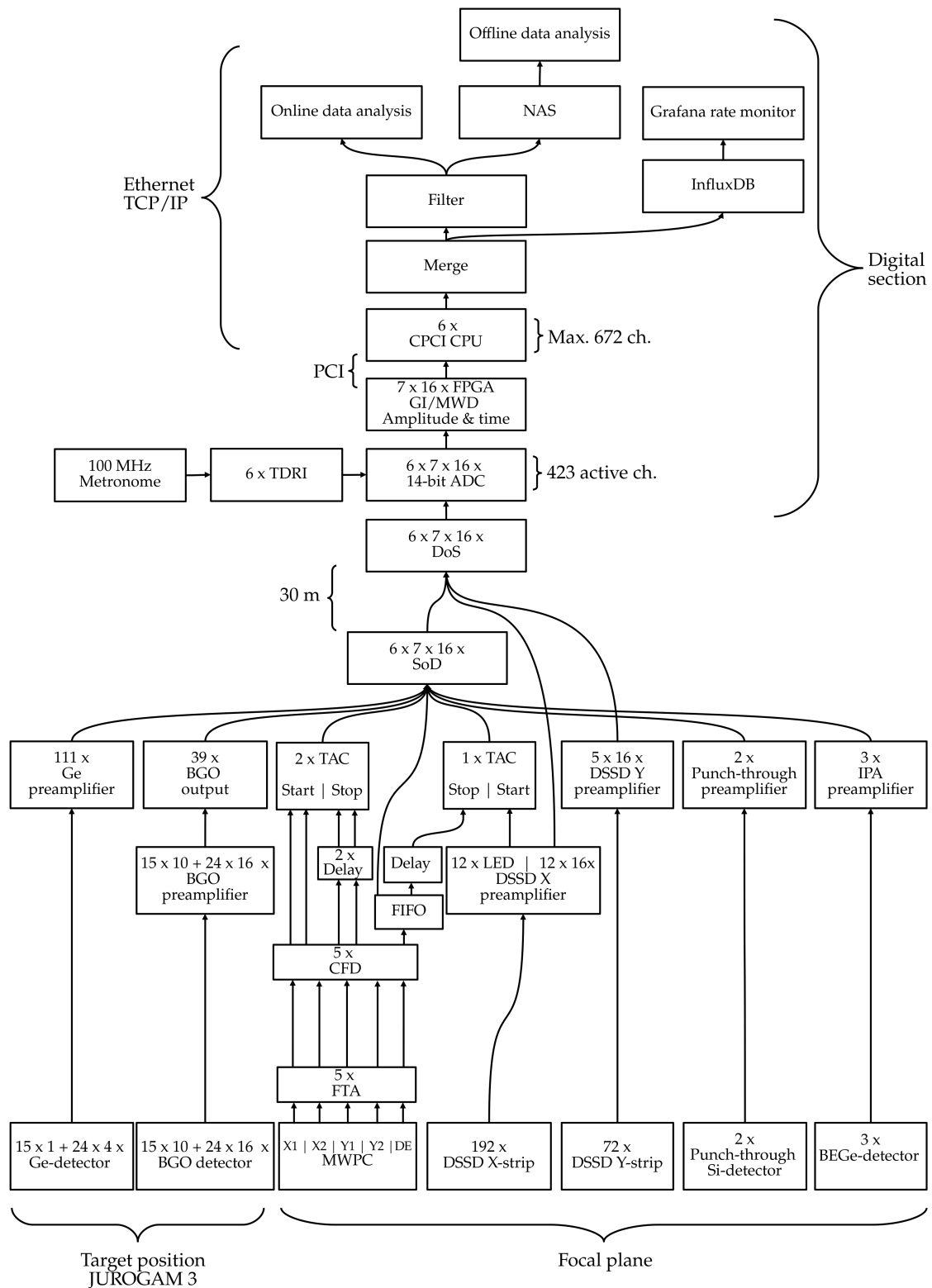


FIGURE 27 Block diagram of the signal chain of the present work. 16 BGO preamplifier outputs (one complete shield) are daisy-chained into a common output signal. The Ge-detector Compton veto-bit is derived from this signal in the FPGA firmware according to amplitude and time coincidence thresholds. The MWPC X–Y position was not needed to analyse this particular data.

### 4.3 Data format

The DAQ uses a data format called GREAT. The GREAT is comprised of 64-bit long packets in which values are encoded in a binary format. In the current DAQ implementation, due to technical reasons, packets are split and sent out as two 32-bit words in big-endian byte order for technical reasons.

There are four different types of these 64-bit packets, "INFO", "TRACE HEADER", "TRACE", and "ADC", identified by a 2-bit code. In INFO and ADC packets, the first (second in the data stream) 32 bits contain the associated payload and the second part (first in the stream) contains the lowest 28 bits of a 48-bit timestamp. In TRACE packets, both 32-bit words contain two raw ADC values, that is, 4 in total in one packet. The INFO packets can contain extra information about the last ADC packet, for example, pile-up, over-range, under-range, overflow, and underflow tags, or they can also encode some DAQ status flags. One of the most important INFO packets is a "SYNC100" data item that gets sent out periodically from every ADC card. It contains the top 19 bits of the timestamps, so, together with the lower 28 bits always contained in the other word, has the whole 48-bit timestamp. A full timestamp is sent every  $655\ \mu\text{s}$ , which means that at 100 MHz clock speed the lowest 28 bits of the timestamp correspond to about 2.7 s. It is then unlikely that a short timestamp in the other packets overflows before the next SYNC100 is received, and if that happens it can be often easily detected and corrected in offline code. The full 48-bit timestamp corresponds to  $\sim 33$  days, after which it rolls over. The first 32 bits of the ADC packets contain a 14-bit integer result from the MWD or GI algorithm. The ADC packet also includes the module number (5 bits) and the ADC channel number (4 bits). These two values combined equals the DAQ channel. The remaining bits indicate different things depending on the firmware version, such as veto and fail conditions.

The filewriter program writes the collected data on a file in 65536-byte (64 KiB) long blocks. The maximum file size is 2 GB for legacy reasons. A 64-KiB block starts with a 24-byte-long metadata header, which tells, for example, the number of valid 64-bit data packets following the header in the current block. The "Tape header" format dates back to when data was written on magnetic tapes, and there was a need for padding. There are no real technical reasons to write the data in this manner any more. It is only done to support legacy analysis codes. The GREAT format is also relatively old. It was originally developed for the now retired RITU focal plane spectrometer setup [65] with the same name in collaboration with the Daresbury laboratory in the UK. At that time link bandwidths and disk space were scarcer resources than they are today. A new data format will most likely be developed for the next generation DAQ. It may sacrifice some of the space efficiency in favour of versatility and simplicity to work smoother with modern hardware and higher-level programming languages. Full documentation of the GREAT and tape header formats are available on the Daresbury laboratory webpage [72], but most of their contents are summarised in Figures 28 and 29.

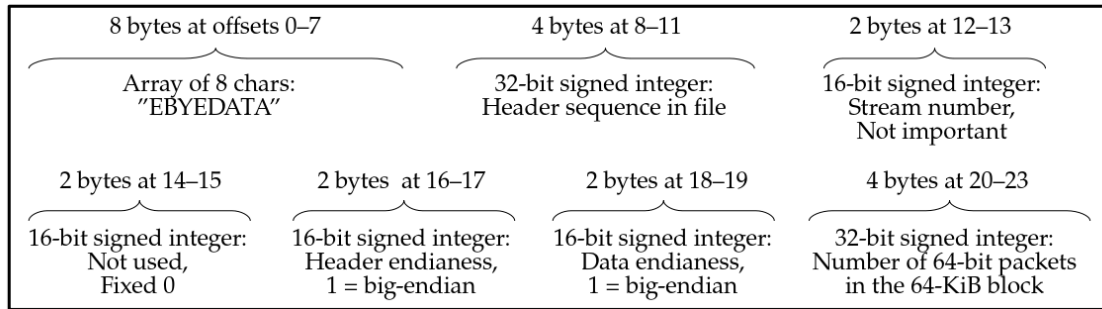


FIGURE 28 Format of the 24-byte-long header of the 64 kB tape data blocks.

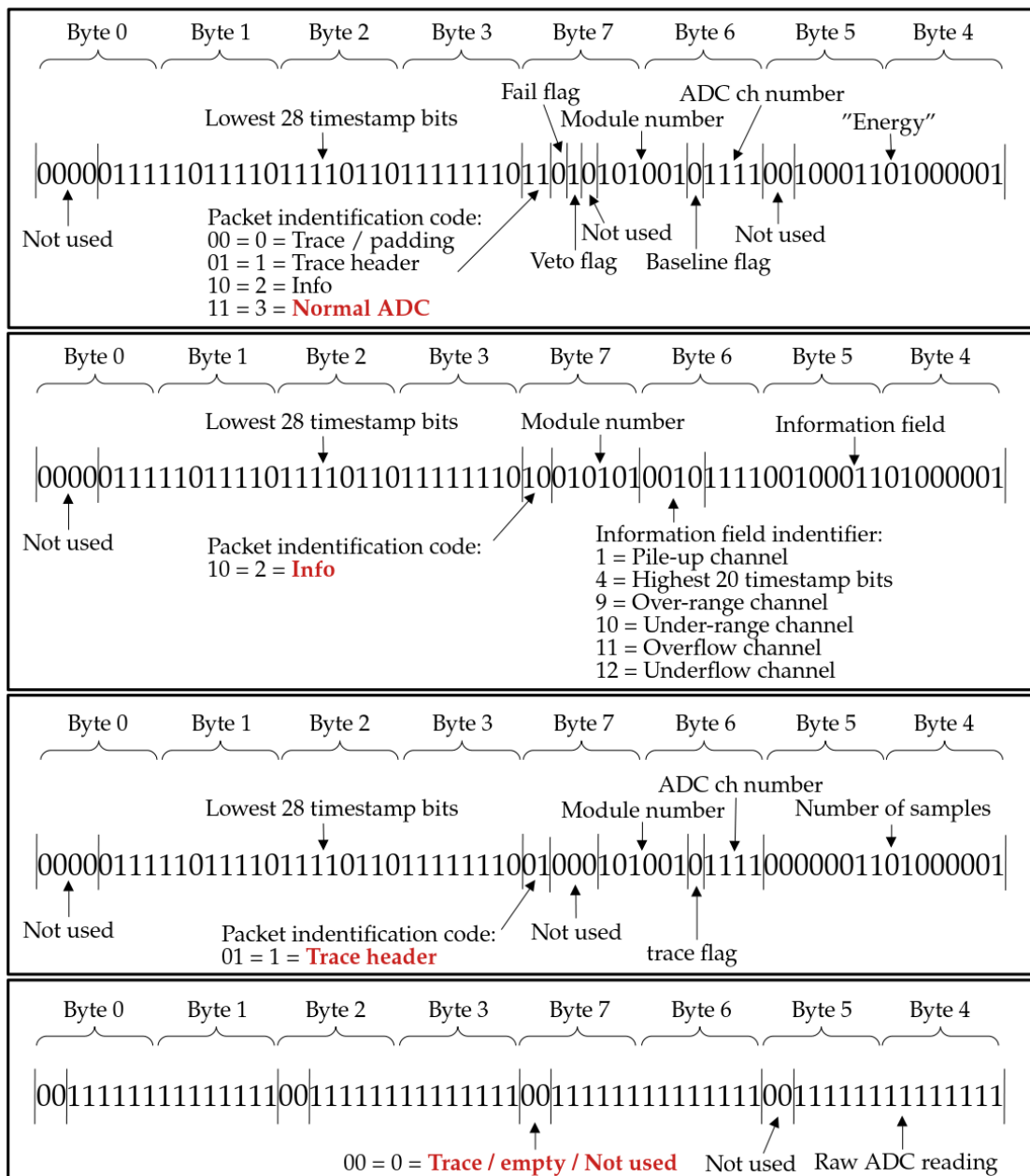


FIGURE 29 Structure of different data packets of the GREAT format. Values are encoded as binary unsigned integers. The number after the byte indicates the offset it appears in a big-endian ordered stream. Possible baseline, trace, or info packet associated with an ADC data packet should follow.

## 5 ANALYSIS

The data was analysed using a new program written by the author. The program handles everything from parsing of the raw data and event building to the correlation logic. Typically, the GRAIN software package [73] has been used to analyse data produced in MARA and RITU experiments. While the GRAIN would have been perfectly adequate to analyse the data from this work, the author wanted to perform some aspects of the analysis differently. Therefore, this project is mainly a personal venture to gain a deeper insight into the data analysis. This code may see little use outside this work since experimental setups are constantly evolving and experiments can have vastly different needs, so it is not feasible to deploy an analysis code and leave it without a maintainer. However, since JYFL-ACCLAB has recently adopted the open data policy, it is possible that the author can, in the future, download datasets and use this code to analyse them. Before continuing with the analysis, a summary of the experimental method is shown in Figure 30.

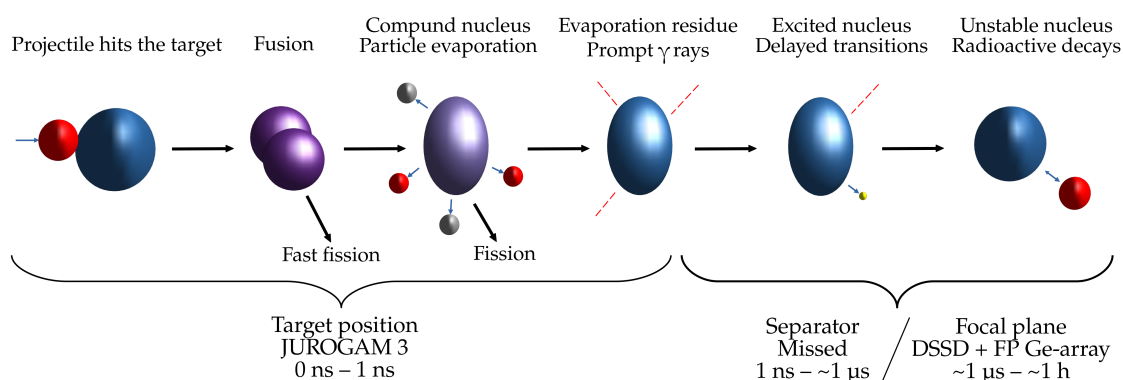


FIGURE 30 Summary of the general experimental method. A beam particle collides with a target nucleus and a fusion reaction occurs. A fused compound nucleus evaporates particles. Prompt  $\gamma$  rays are emitted from an evaporation residue and observed in the JUROGAM 3 array. Evaporation residue flies through the separator and gets implanted into a DSSD. Possible delayed  $\gamma$ -rays are detected in the FP Ge-array. Evaporation residue undergoes radioactive decay(s) and gets tagged.



## 5.1 Parsing the data

As discussed, data is saved in 2 GB files in the GREAT format. The naming scheme of these files is chronological and follows the format “Identifier\_RunNumber\_FileNumber”, for example, “JR154-RUN\_10\_36”. The numbers get incremented accordingly. When this experiment was performed, the old filewriter program was still in use. A slight oversight in the old filewriter was a lack of zero padding of the run and file numbers, which meant that the file explorers could not properly order them in the correct chronological order based on the file names. A workaround, if only a subset of a run had to be selected for analysis, was to organise the files based on the modification date. However, it did not work if the date changed. The new analysis program has a function to rename the files correctly, and the new filewriter natively has a proper padding.

The aforementioned padding issue was usually not really an issue, however, the new analysis program can modify the data files by discarding unnecessary packets, such as noise events or traces, if they are deemed unneeded. The DSSD thresholds were set very low in order to be sensitive to low-energy conversion electrons. However, this also meant that a lot of noisy data were saved on a disk. In total, the first part of the experiment accumulated ~3 TB of data, and after stripping out noisy DSSD packets (readings below the ADC channel 5), the data volume was reduced to ~1.3 TB. The analysis process itself is rather easy load for modern CPUs, so the analysis speed is mostly limited by the sequential reading speed of the storage media, and the reduced data volume is therefore advantageous. The new code is multithreaded and with a decent home PC, it is easy to achieve >2 GB / s throughput. Server machines can perform even better. Three example functions for parsing values from the GREAT-format data packets are shown in Listing 5.1.

```

1 //Extract ADC reading from the normal ADC packet
2 private int parseSignalAmplitude(byte b5, byte b4) {
3
4     return (b5 & 0x3F) << 8 | b4 & 0xFF;
5
6 }
7
8 //Extract channel number of the packet
9 private int parseDAQchannel(byte b7, byte b6) {
10
11     return (b7 & 0x07) << 7 | (b6 & 0xE0) >> 1 | (b6 & 0x0F);
12
13 }
14
15 //Combine complete 48-bit timestamp from the packet and the last SYNC100 packet
16 private long parseTimestamp(
17     byte hb6, byte hb5, byte hb4, byte b3, byte b2, byte b1, byte b0){
18
19     return
20     long)(hb6 & 0x0F) << 44 | (long)(hb5 & 0xFF) << 36 | (long)(hb4 & 0xFF) << 28 |
21     (b3 & 0x0F) << 24 | (b2 & 0xFF) << 16 | (b1 & 0xFF) << 8 | b0 & 0xFF;
22
23 }

```

LISTING 5.1 Three example functions for extracting some of the data fields from the GREAT-format packets that were described in the Figure 29.



Sometimes one of the ADC cards can lose the common clock and fall out of sync. After such an event, the timestamps are either resynchronised or zeroed. If a time discontinuity is detected in the data stream, the analysis software will correct for it based on the run and file numbers. This is necessary for achieving linear code flow and to make unlimited correlation and real-time gates work properly.

## 5.2 Building logical events

For many experiments, and especially for low cross-section RDT experiments, DSSD events are a good place to start the analysis logic. The DSSD can be described by how many pixels it has, however, this is not completely accurate. As discussed in section 2.7.1, the DSSD does not have any real independent pixels, but has horizontal and vertical strips on the opposite surfaces of the die. The strips are not completely decoupled and no pixel coordinate is available natively. Instead, the quasi-pixel has to be parsed in the analysis code from the individual strip signals. This parsing process is not entirely straightforward and different approaches can be taken. In addition to signals coming from real implantation or decay events, they can also be caused by electronic noise, cross-talk, and charge bleeding into neighbouring strips. In the ideal case, there would be just two events in a raw DSSD stream, one in X-strip and one in Y-strip, and their energies and timestamps would be almost identical. However, a significant fraction of the DSSD data streams looks something like what is shown in an example in Table 1. In the worst case, all 264 DSSD channels fire and the event length can be several microseconds long. Even though the DSSD has 13824 quasi-pixels, effective event parsing algorithms require that the whole DSSD has sufficiently long quiet periods when compared to the average event length. Generally, this condition is satisfied, but sometimes a long-lasting noise can push the event lengths so long that another event is appended into the same event stream. This is not too big of a problem unless the event rates are very high or there is a systematic noise present. For example, there is a systematic noise related to the timing signal in the DSSD preamplifiers, so some fast decay events can be missed. However, in such a case, a recovery can be attempted in the code. Of course, the intrinsic dead-time of an individual DSSD strip is the sum of the rise and flat-top times set in the MWD firmware, in this case  $\sim 5 \mu\text{s}$ . If the decay happens during this period, not much can be done without recording raw signal traces.

One way to parse the logical DSSD events is to use a fixed event length approach. With this method, the event building is started when a signal is seen in any DSSD strip, and then all subsequent DSSD signals are collected until a fixed maximum time is reached. This method is simple and usually works decently. However, sometimes it may parse a long event into several shorter ones or vice versa. For technical reasons, the minimum event length which was possible to use in the past was  $\sim 7 \mu\text{s}$  which means that the DSSD event-to-event dead-time was fixed, and it did not scale with the MWD integration time or noise.

TABLE 1 Example raw DSSD signal stream. The constructed logical DSSD event from this stream would have had an energy of 8755.66 keV, which is the sum of the highest Y-energy in strip 49 (blue) and adjacent Y-49 energy (green). The timestamp would have been taken from the Y-48 signal. The highest X-side event is in strip 69. Therefore, quasi-pixel assignment of this logical event would have been X,Y = (69,48). Notice how by filtering out (or by fixing the root cause which is probably related to some grounding/cross-talk issue), the noise counts below ~90 keV would have cut down the event length and thus the dead-time of the DSSD from 2  $\mu$ s to 20 ns, over hundredfold. It is also not 100 % guaranteed that the Y-coordinate assignment is correct as the energies measured in strips Y-49 and Y-48 are rather close.

DSSD channel	Energy (keV)	Time since previous reading (ns)	Event total length (ns)
Y-49	4035.16	54640	0
Y-48	4720.50	10	10
X-69	8722.17	10	20
X-147	1.58	910	930
X-99	1.44	70	1000
X-192	0.89	20	1020
X-81	79.66	550	1570
X-90	82.62	0	1570
X-87	73.71	20	1590
X-96	80.61	10	1600
X-93	78.73	10	1610
X-54	76.87	20	1630
X-51	88.84	10	1640
X-57	74.25	0	1640
X-75	73.95	10	1650
X-84	73.42	0	1650
X-60	71.73	0	1650
X-66	71.08	0	1650
X-63	83.46	20	1670
X-72	60.12	20	1690
X-78	64.91	70	1760
Y-25	5.73	110	1870
Y-29	3.84	90	1960
Y-35	4.45	10	1970
Y-65	14.55	40	2010
Y-32	6.72	50	2060
Y-28	6.44	0	2060
Y-26	1.32	0	2060
Y-31	0.99	0	2060

To get around these problems, the new code employs a dynamic event length parsing approach that adapts better to each individual event, however long or noisy. The dynamic algorithm starts similarly to the fixed one. When a signal is seen in some DSSD channel, the event building begins. The starting event and all consecutive DSSD signals are then collected into temporary buffer arrays. However, instead of the fixed time limit to stop the collecting, the dynamic algorithm monitors the time intervals between the DSSD signals. When the time difference between the subsequent data packets exceeds a set limit, indicating that the whole DSSD has fallen quiet and that all the signals related to the same event are stored in the buffers, the sort enters into a logical event-building branch. In this branch, the DSSD X and Y signal buffers are

looped over and the ones with the highest calibrated energies are selected to form the X–Y quasi-pixel. If some of the charge has partially escaped into the neighbouring DSSD strip(s), it can be added back to the corresponding X or Y side energy. Additional requirements can be imposed to control the add back, such as energy percentage and time difference thresholds. However, those should be used with care, as explained later. The final energy of the logical DSSD event can be determined based on the X and Y-strip energies, for example, it can be defined to be the higher one. Picking the higher value works well if the other strip has failed to collect the full charge, or if it was otherwise faulty. However, usually, the X-side has a slightly better energy resolution or the sides might have been set to different gains in an attempt to gain more dynamic range while preserving the energy resolution. In those cases a different approach can perform better. Usually there is not a huge time difference between the arrival times of the highest energy X-strip and Y-strip signals. Around  $\pm 30$  ns is typical. A couple of exceptions when the time difference can be more than  $\pm 1$   $\mu$ s, are when one of the strips is without bias or one of the signals has very low energy, for example, from  $\beta$ -decay. However, in all the cases, the most consistent time distribution appears to be obtained when the timestamp for the logical DSSD event is taken from whichever strip triggered the first.

The result of the parsing of the DSSD events done according to the previous description can be seen in Figure 31. In the top plot, readings from individual DSSD strips are plotted as they come in the data stream, without any parsing. The bottom plot shows the X and Y-strip energy readings of the parsed logical events. Y-strips are offset by 200 in the X-axis and their heights are also normalised to the X-strips for a better visualisation. In the top plot, strong electronic noise is present, in particular, the X-strips in the bottom left corner. However, since the random electronic noise is not correlated for both X and Y-strips simultaneously, it is very effectively removed during the parsing process, as seen when compared to the bottom plot. Another notable feature in the figure is the missing strips. A strip can be missing because it did not have a bias, in which case the whole electric field and charge collection in that region of the DSSD is disturbed. Sometimes, just the energy signal can be distorted or is completely lost in some step in the signal chain, for example, due to a faulty ADC or DoS channel. Picking the energy for the logical DSSD event from the higher reading strip instead of a fixed X or Y-side is especially helpful when dealing with these broken strips or the edge/inactive regions. If there are not too many broken strips in the DSSD, the correct quasi-pixel for a logical event that is affected can be recovered, since the charge is still partly collected by the adjacent strips, which leaves a distinct X–Y energy imbalance (see Figure 47 later). The counts seen at around 34 MeV are over-range events that do not correspond to the real energy of the event, since they have saturated the dynamic range of the preamplifier.

Data from the other detectors used in this experiment are not similarly coupled as the DSSD events and do not require parsing. While the signals from the DSSD strips are gathered and parsed, the data from the other channels is stored in temporary ring buffer arrays awaiting further use.

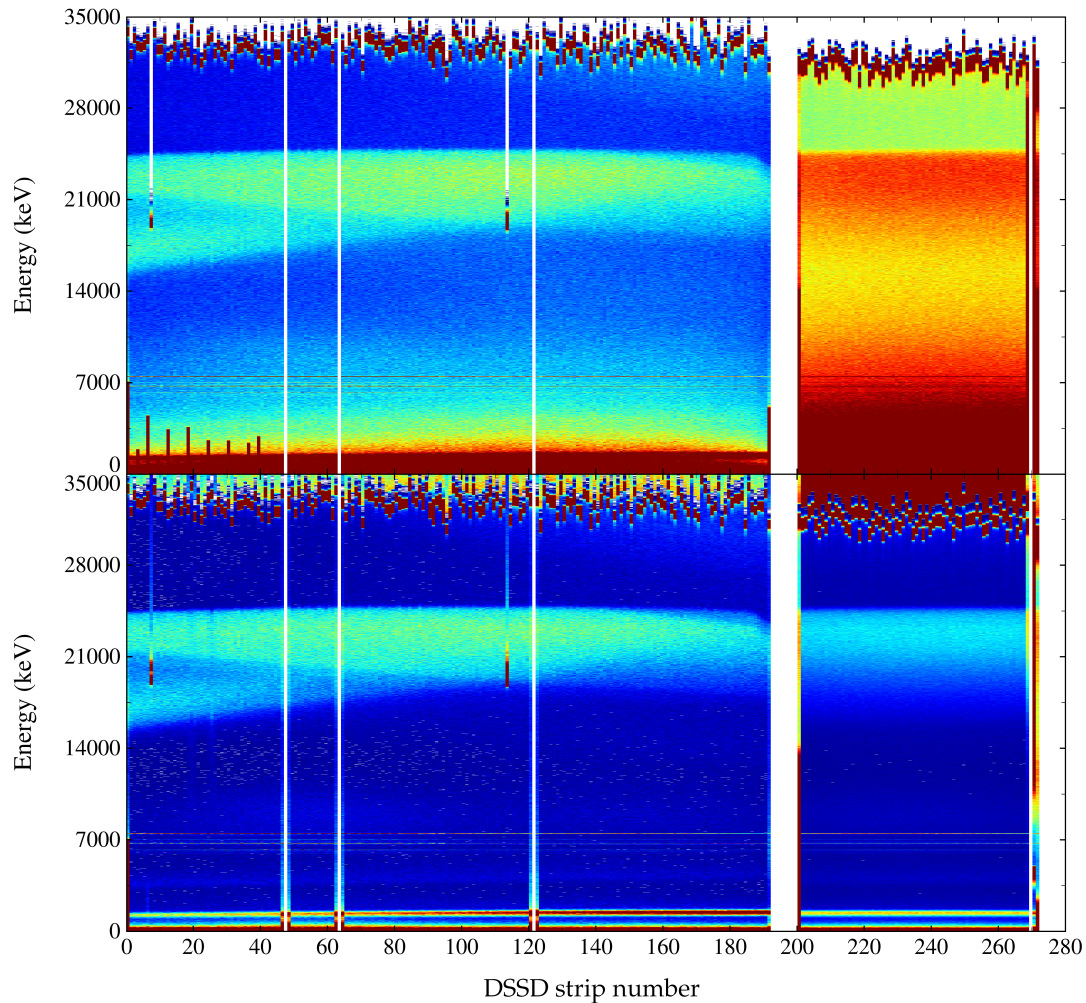


FIGURE 31 Raw DSSD readings by strips (top) compared to the parsed logical DSSD events (bottom). DSSD Y-strips have been offset by 200. Parsing is especially effective at removing uncorrelated noise. See the text for details.

### 5.3 Identifying, tagging, and correlating

Once a logical DSSD event has been successfully parsed i.e. it has been assigned with its X–Y quasi-pixel, energy, and timestamp, linking it with the information from the other detectors can begin. The information provided by the MWPC was particularly important in this experiment since the decay, punch-through, beam, and recoil events all overlap in the energy domain.

To separate the decay events from the beam-related events, it is checked whether a logical MWPC signal has been received within a certain time interval relative to the DSSD event. The time interval can also have an energy dependence. If the logical MWPC signal was not received within a set gate, event’s decay flag was set to true to indicate that it had not come through the separator, but instead, it was likely caused by some an internal event, such as radioactive

decay of an implanted recoil. An example DSSD event energy versus DSSD–MWPC time distribution plot and a selection gate is shown in Figure 32. As with any real system, the decay event separation is not 100 % efficient, not all beam-related light particles leave a signal in the MWPC, and if the count rates are high, some events can pass through during the dead time. Even if only a small fraction of the beam-related events get through unmarked, they might easily drown weak decay peaks.

Separating the actual recoil events from the other beam-related events is done with a two-dimensional constraint set on the DSSD event energy and its time-of-flight between the DSSD and MWPC, as shown in Figure 33. Since it cannot be exactly known which DSSD signal triggered the TAC and thus which ToF signal and logical DSSD event pair belong together, the DSSD event also has to satisfy a certain time interval criteria, see Figure 34. In the sorting code, the TAC reading can be added to the logical DSSD event attributes after it has already been parsed to enable event lengths shorter than the TAC delay. The resulting DSSD event distribution when gating on the recoil events was shown earlier in the section about the separators, in Figure 15(a).

Similarly, as with the MWPC and ToF signals, certain time differences and (2D) energy constraints could be set between the events observed in the punch-through detectors and the parsed DSSD events. When these conditions are satisfied the DSSD event gets flagged as a punch-through incident. The punch-through flagged DSSD events can be either all kept, thrown away, or partially

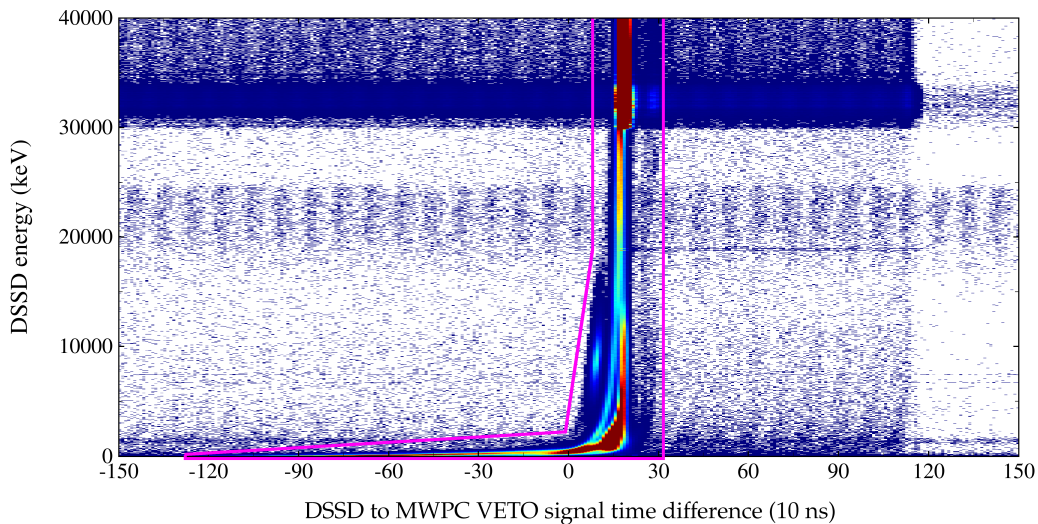


FIGURE 32 The logical MWPC signal usually arrives right after the DSSD signal. Events that fall inside the pink gate are flagged as “not decays”. The logical MWPC signal contains almost the same information as the ToF signal from the TAC, shown in Figure 33, but notably without any energy limits and not as much dead time. In this experiment, the recoils were sufficiently slow, that even with the global DAQ time resolution of 10 ns, they can be seen in a separate distribution at 10 MeV. The periodicity visible in the plot is caused by the pulsed structure of the beam, and it corresponds to the used cyclotron frequency, in this case around 10 Mhz (100 ns period).



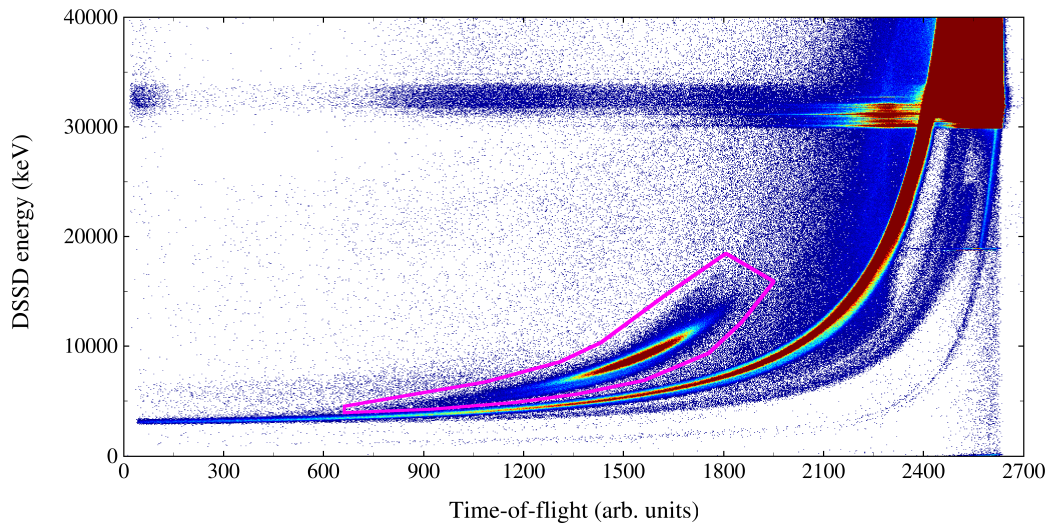


FIGURE 33 DSSD event energy versus TAC reading (DSSD–MWPC ToF). The recoil selection is indicated by the pink gate. Other events are mostly from the scattered beam. As can be seen, the energy threshold of the timing signal was set to around 3 MeV in the Mesytec preamplifiers. The response of the NIM time trigger of the preamplifiers is not very linear as a function of the energy, as it is just a simple leading-edge discriminator. Some of the events that have saturated the preamplifier protrude out as the timestamps slightly fails for overshoot signals. A value of 2600 on the X-axis corresponds to the fixed delay difference between TAC’s start–stop signals. Lower values are therefore less coincident i.e. slower flying particles.

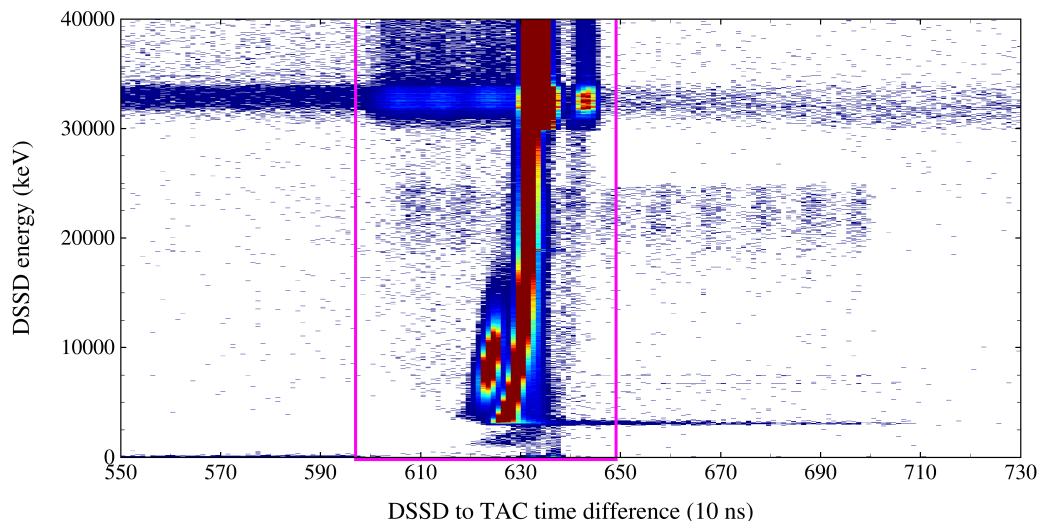


FIGURE 34 The ToF reading from the TAC arrives  $6.3\ \mu\text{s}$  after an event is observed in the DSSD due to processing delays in the signal chain components. DSSD–TAC event pairs inside the pink gate are correlated to each other.

accepted if they are actual light particles from real decay events.  $\beta$  particles, for example, can be easily distinguished from the beam-related events as is demonstrated in Figure 35(a). The punch-through decay energy can be added back to the logical DSSD event if so desired. Adding back the  $\beta$ -decay energies can be advantageous, since it lessens their low-energy tails and cleans up the proton decay and internal conversion electron region, or when doing  $\beta$ -tagging, targeting high endpoint energies. The small gap between the two separate punch-through Si-detectors can be seen at the centre of the DSSD, as shown in Figure 35(b). Interestingly, differences between the spatial distributions of the beam-related punch-through events of different species are also observed.

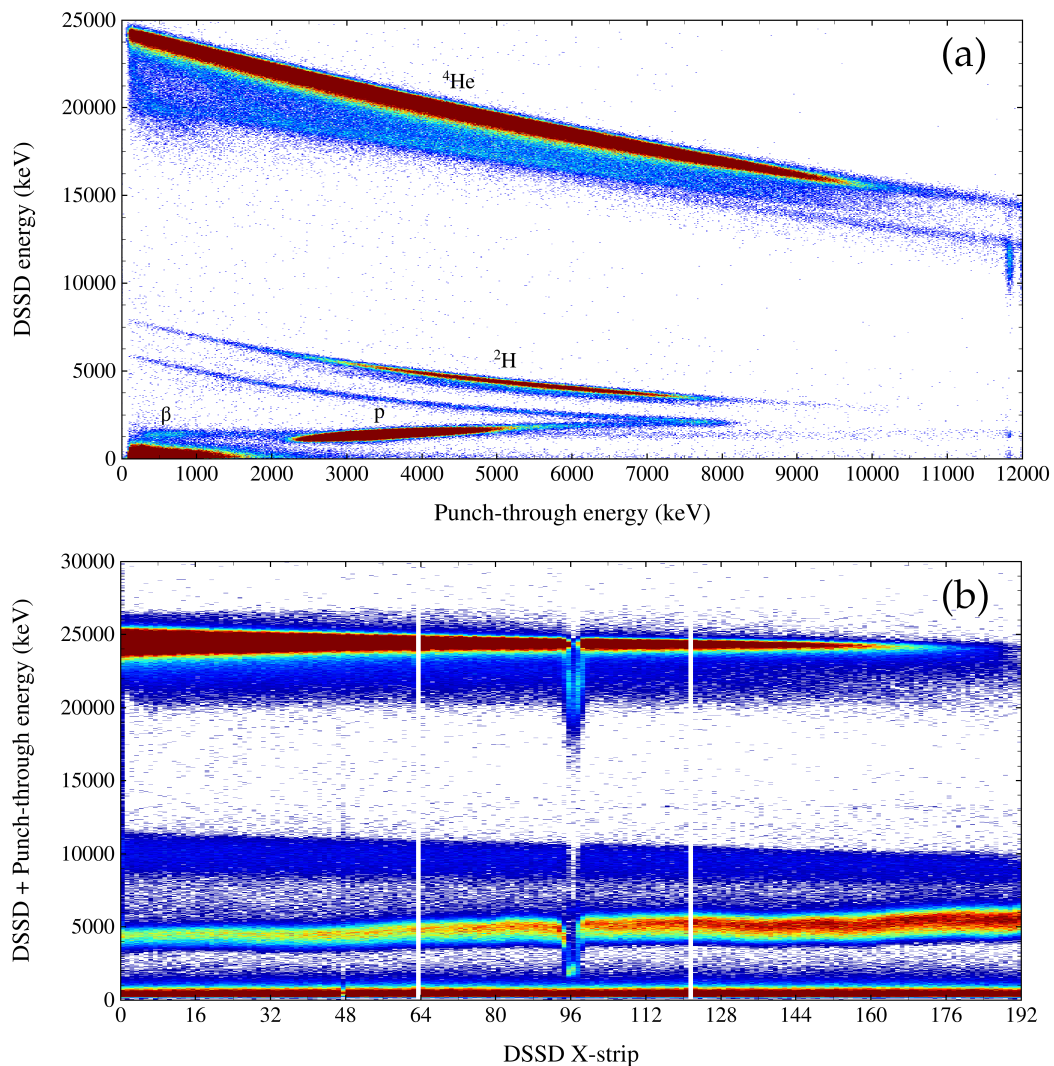


FIGURE 35 (a) Punch-through energy versus DSSD energy. Separate dE-E curves for  $\beta$ -decays (positrons/electrons), protons, deuterium, and helium are seen. (b) DSSD + punch-through energy versus DSSD X-strips. Again the different particles are separated, but now it can be seen that they have different distributions along the width of the DSSD. The ineffective veto area in the middle of the DSSD (X-95–99) due to the gap between the two individual punch-through detectors is also clearly visible.

The result of this classification process is shown in Figure 36, where the pink spectrum shows the decay events, the black spectrum the recoil events, the red spectrum the punch-through events, and the blue spectrum shows the beam and beam-like events.

When the DSSD event is deemed good, a decay or a recoil, for example, it is saved into a larger chronological data array. In this experiment, information from all the other channels, except the data from the germanium detectors, can be thought of as attributes of the DSSD event. Once a DSSD event is built, an adequate slice of the germanium detector data is saved in arrays for the final correlation at the end of the sorting routine.

After all the DSSD events have been parsed, classified, and placed into the time-ordered data arrays, recoil-decay correlation can begin. In general, events that are not in the recoil gate or classified as decays can be excluded from these correlations provided that no other short-living activities are present. When looping through the X–Y quasi-pixel event buffer, if an event is marked as a recoil and the subsequent event in the same pixel is marked as a decay, they are correlated to each other. In this particular code by adding the new attributes “decay energy” and “decay time” to the preceding logical recoil DSSD event. If a recoil-decay chain is still followed by another decay event, that event is also added to the recoil event attributes as “decay-decay energy” and “decay-decay time”. When encountering a decay-decay chain, due to the charge diffusion and light particle range in the DSSD, it is also justified to check for a recoil event in adjacent strips to increase the accuracy of the correlations. Decay events can also be indepen-

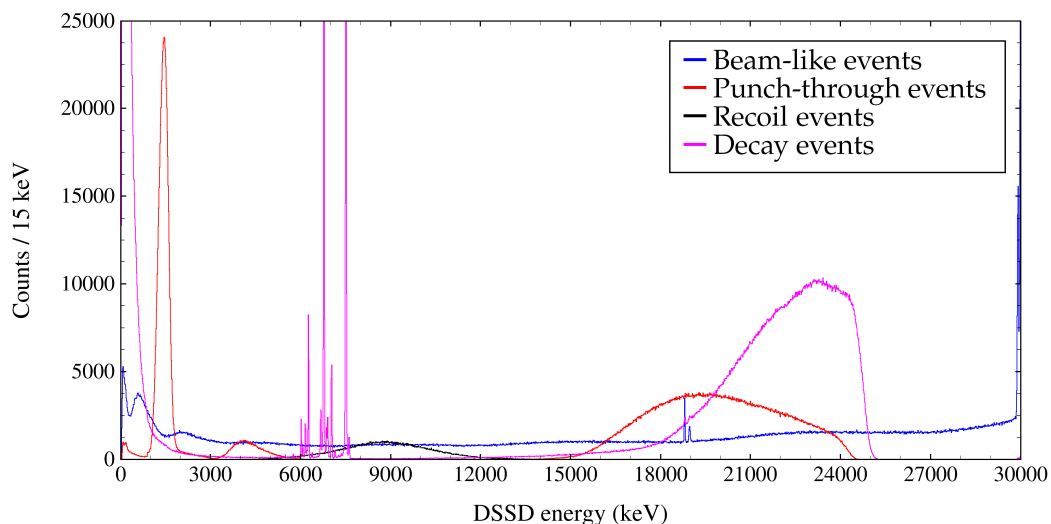


FIGURE 36 DSSD events are separated into different categories based on several tagging conditions. Beam-related light particle events that do not trigger the MWPC nor the punch-through detectors can contaminate the decay event region at energies  $>10$  MeV, as seen in the pink decay spectrum. The lower-energy decay region, proton decay, in particular, can be contaminated with noise, punch-through, beam, and  $\beta$ -decay events. Peaks at 19 MeV in the beam-like spectrum are artefacts from faulty ADC or DoS channels that do not have the full dynamic energy range.



dently correlated and added for a decay-spectroscopy analysis. The correlations are a statistical process, so it is not always guaranteed that a recoil event and the following decay event have a causal connection, but provided appropriate counting rates, it is the most likely case. Ultimately, the correlation time is limited by the recoil-recoil and decay-recoil rates. Recoils can be forced to correlate over the other recoils, but this quickly becomes computationally too expensive, and it is generally statistically more likely that the closest recoil in time is the parent of a subsequent decay event. All recoil and decay events can be included in the further analysis even if they cannot be correlated with any subsequent decay events, but in that case their identification can be difficult. Doing the event–event correlation according to this algorithm, identifiable recoil-decay distributions emerge in the decay energy versus decay time domain as shown in Figure 37. This is the core of the RDT method.

In  $\gamma$ -ray spectroscopy experiments, the next step is to correlate the DSSD events with the events observed in the Ge detectors at the target position and at the focal plane. The germanium buffers are looped through to connect them to the logical DSSD events based on temporal limits. The  $\gamma$ -ray events that have a significant statistical correlation with the DSSD events are usually easily identifiable from the background and a gate can be applied to select the interesting events, as shown in Figure 38.

Various static binned histograms and 2D heat maps are created at the sort time. However, since the conditions for filling these plots are decided beforehand, one has to have a good idea of what to look for and how. Modifying these histograms requires running the whole sort again, which can take a relatively long time. Instead of relying solely on static histograms, an n-tuple analysis is a more

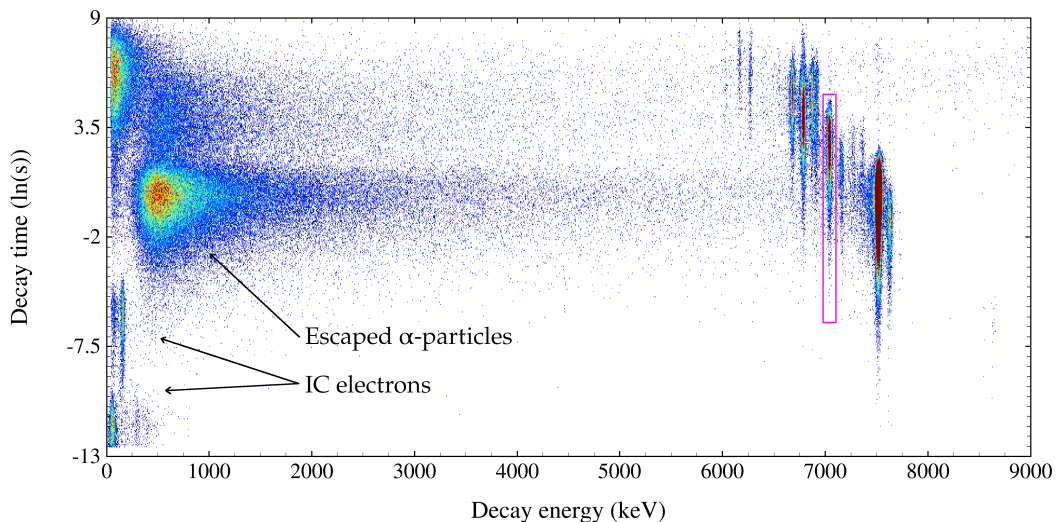


FIGURE 37 Decay energy ( $Q_\alpha$ ) versus the natural logarithm of the decay time. Plotting the data like this is useful when applying the RDT conditions. The example gate in pink shows conditions isolating  $^{212}\text{Ra}$  by its full energy  $\alpha$ -decay and decay time that were used to produce the prompt  $\gamma$ -ray energy spectrum in Figure 52(c). Conversion electrons from  $^{212}\text{Ra}$  and  $^{213}\text{Ra}$  are seen on the bottom left and escaped  $\alpha$ -decay events are seen slightly “northeast” of them.

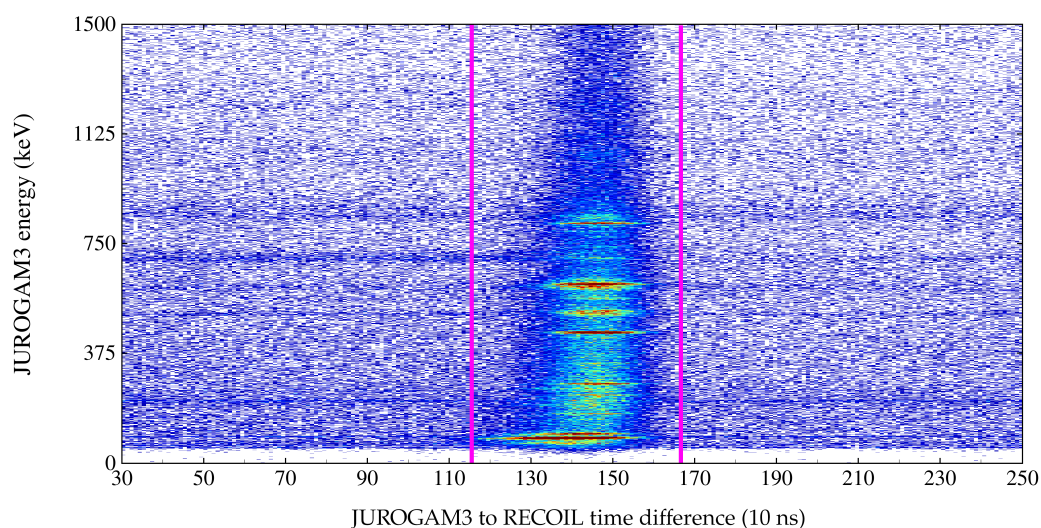


FIGURE 38 JUROGAM 3 ( $\gamma$ -ray) energy versus DSSD event to JUROGAM 3 event time difference (time-walk correction applied). A clearly distinguishable distribution of  $\gamma$ -ray events can be observed among the background at the time before the DSSD event that roughly corresponds to the time of flight through the separator. The pink lines indicate the time correlation window for a prompt  $\gamma$ -ray energy spectrum.

powerful tool. After the event parsing process and filtering out the unnecessary events, the data volume may have shrunk enough for it to be feasible to load in entirety to the RAM of an analysis machine as tuple objects. Tuples store multiple data fields linked to a single object. The best tuple layout depends on the experiment, in this case the  $\gamma$  rays were used as the basis, and they were given attributes like, channel, DSSD X-Y, decay energy, and ToF. The tuples can then be manipulated in arbitrary ways via a tuple analyser and dynamic histograms can show the result in real time. In this experiment, the main interest were the  $\gamma$  rays from  $^{213}\text{Ac}$  and  $^{211}\text{Ac}$  and the tuple analyser was used to apply different recoil-decay(-decay), X-Y, fold, and correlation time gates, adjust Doppler correction parameters, detector angles, calibrations, perform detection efficiency corrections, background subtractions, and to do the  $\gamma$ - $\gamma$  coincidence analysis.

## 5.4 Energy calibration

In most cases, an ADC channel reading needs to be calibrated to match some meaningful quantity to be more useful. For some devices, the output might correlate with time or position and indirectly to some other quantities. Sometimes, only boolean information is enough, and no real calibration is needed. However, one prominent quantity that needs thorough treatment is the energy. The energy signals from each detector have to be comparable with each other and with a convenient unit. In this work, the devices that strictly require energy calibrations are the DSSD and the germanium detectors.

Usually, the initial energy calibration of the DSSD is made using an external  $\alpha$ -particle source. The external calibration gets the gain-matching and energies of the strips close enough that an experiment can be started, and more general decisions can be made, such as if any changes should be made to the separator parameters or if the reaction is working as expected. However, calibration done with an external activity does not exactly match the implanted activity. The external  $\alpha$  particles are susceptible to the dead layer on the surface of the DSSD, to which some energy is deposited, but not collected. The dead layer thickness can vary slightly across the detector and the distance through which the particle has to travel depends on the incident angle. Another difference between the implanted and external activities is the presence of the relative massive parent nucleus. The parent nucleus is effectively a defect in the silicon lattice, which leads to increased electron-hole pair recombination in its immediate vicinity. Electron-hole pair recombination, loss of energy in the non-ionising events and in the dead layer vary depending on the mass, charge, and energy of a particle. Together these effects are called the Pulse Height Defect (PHD) [74]. The calibration source also has a thin window in which some energy is lost.

An internal calibration can be used to lessen the PHD offset. However, this requires that a well known activity is present in the data or in an additional calibration run, which has to match the experimental conditions and activity of the interest as closely as possible. For the implanted activity, the DSSD is also measuring, at least partly, the kinetic energy transferred to the parent nucleus, i.e. the Q-value of the decay. Also, it cannot be assumed that a calibration performed with  $\alpha$ -decays is accurate for beta and proton decays. The energies might be close, but there can still be systematic errors present. Even worse, the calibration energies themselves could be erroneous. For these reasons, the determination of decay energies can be very tedious and challenging.

Fortunately, in this experiment, an absolute energy calibration is only needed for the  $\gamma$  rays observed in the Ge detectors. For these, different complications exist, but these are perhaps a little bit more straightforward. The energy calibration for the Ge detectors at the focal plane can be done with many common  $\gamma$ -ray sources. For example, a  $^{152}\text{Eu} + ^{133}\text{Ba}$  mixed source can be used. The linearity and zero-offset of the modern devices (amplifiers, ADCs etc.) are so good that a simple factor coefficient might give the best result within the relatively small ranges usually involved. If, for some reason, the energy response is not linear, the situation is probably not any more salvageable by using a higher order polynomial corrections either. While the background caused by the partial  $\gamma$ -ray energy depositions due to the Compton scattering is not completely inconsequential for extracting the full peak energy, it is typically relatively small compared other uncertainties involved. A different challenge arises at the target position. Nuclei produced using thin targets emit  $\gamma$ -rays in-flight. The observed  $\gamma$ -ray energies are, therefore, shifted due to the Doppler effect, when detected at angles other than  $90^\circ$  relative to the velocity vector of a nucleus that emitted it. Since the germanium detectors of the JUROGAM 3 array are arranged in rings, at different angles, the measured in-beam  $\gamma$ -ray energies require a correction. The

unshifted energy  $E$  of the  $\gamma$ -ray follows the well known Doppler equation,

$$E = E_{\text{obs}} \frac{1 - \beta \cos \theta}{\sqrt{1 - \beta^2}} \quad (1)$$

where  $E_{\text{obs}}$  is the observed energy,  $\beta$  is the fraction of the speed of the light the emitting particle was travelling at, and  $\theta$  is the angle between the particle's velocity vector and the observer (detector), in this case, the JUROGAM 3 ring angles.

The detectors also have a finite size and the source has a certain position and velocity distributions. These variances cause additional smearing of the peaks called Doppler broadening [75]. The energy has other error sources, for example, the event rate also affects the readings. More discussion about the energy errors and errors in general in section 5.6.

## 5.5 Relative detection efficiency and angular distributions

As discussed in section 2.1.1, the relative intensities of the transitions can be used to deduce their ordering and are helpful when building the level scheme. To compare the relative  $\gamma$ -ray intensities, the relative detection efficiency of the detector setup has to be known. The relative detection efficiency is typically determined with a separate calibration measurement using a mixed  $^{152}\text{Eu}$  and  $^{133}\text{Ba}$  source. The calibration measurement should match the actual experiment as closely as possible, and therefore, the source is usually placed at the target holder, in the same position the actual target is placed during the in-beam experiment. A mixed  $^{152}\text{Eu}/^{133}\text{Ba}$  source is used, because it provides many  $\gamma$ -ray peaks that have very precisely known energies and intensities in the useful range of 50–1500 keV [76]. Of course, a source measurement cannot completely match the in-beam distribution and data rate conditions, but it is much more feasible to do than an in-beam calibration. Many efficiency functions have been devised for different energy ranges and different germanium and silicon detector types. In this study, an efficiency function (2) proposed by Hurtado et al. [77] was used. The function was developed for N-type Coaxial Ge detectors, and it applies to the  $\gamma$ -ray energy range 36–1500 keV. The energy relative  $\gamma$ -ray detection efficiency  $\varepsilon$  is

$$\varepsilon = A_1 (e^{-A_2 E^{A_3}} + e^{-A_4 E^{A_5}}) (1 - e^{A_6 E^{A_7}}) \quad (2)$$

where  $E$  is the  $\gamma$ -ray energy and  $A_{1,\dots,7}$  are the free parameters. The first part models the transmission of photons in the materials between the source and the detector, and the second part accounts for the absorption of the photons in the detector. The resulting fit using the function for the whole JUROGAM 3 array is shown in Figure 39. While the fit is for the whole array, the points have been taken from the intensities of the Gaussian curve fits of the individual detectors to increase the accuracy. The final uncertainty of the relative intensity of a peak comes from the errors of the Gaussian curve fit, the efficiency function errors, and the background under the peak.

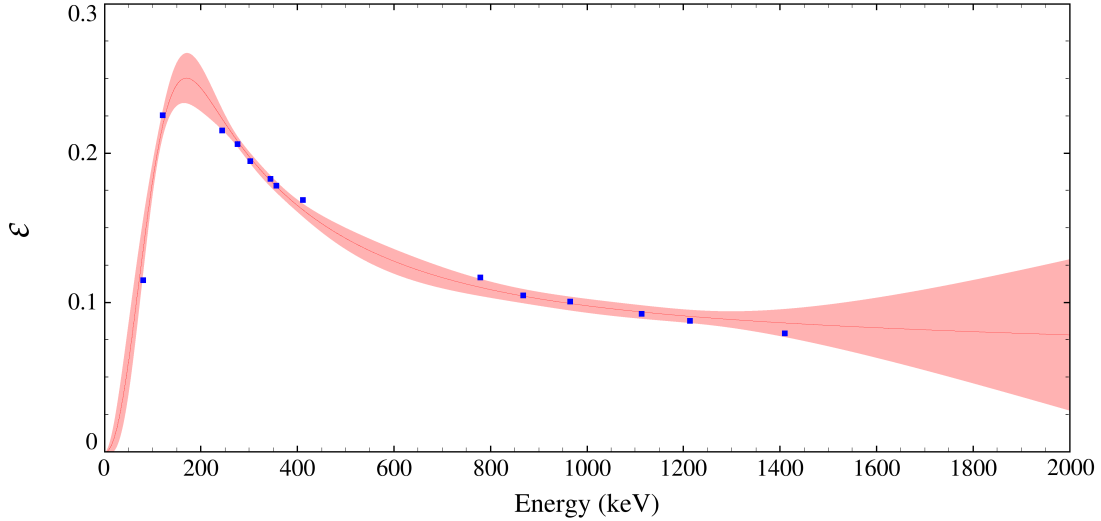


FIGURE 39 Relative  $\gamma$ -ray detection efficiency of the JUROGAM 3 array, determined using a mixed  $^{152}\text{Eu}$  and  $^{133}\text{Ba}$  calibration source. Below  $\sim 200$  keV, the efficiency changes rapidly, and the uncertainty increases. The red area indicates the 68% confidence interval of the fit.

Residues from fusion-evaporation reactions tend to be aligned relative to the beam axis [78], as such the relative intensity  $W$  as a function of the detection angle of a  $\gamma$ -ray (angular distribution) correlates with its  $\Delta J$  and multipolarity [79, 80]. This property can be helpful for deducing the spin and parity of a state if a transition can be connected to a known state. The angular distribution from a partially aligned state with the first two spherical terms is of form:

$$W = A_0(1 + A_2((1/2)(3x^2 - 1)) + A_4((1/8)(35x^4 - 30x^2 + 3))), \quad (3)$$

in which  $A_0$  is the normalisation parameter,  $A_2$  and  $A_4$  are the angular distribution parameters, and  $x$  is the cosine of the detection angle. Nominally for JUROGAM 3 rings,  $x$  is  $-0.9245$ ,  $-0.6896$ ,  $-0.2504$ , and  $0.2504$  for the rings 1, 2, 3, and 4, respectively. Or  $-0.9245$ ,  $-0.6896$ ,  $-0.3502$ ,  $-0.1478$ ,  $0.1478$ , and  $0.3502$ , if the Clover rings are to be divided into subrings 3, 4, 5, and 6. The collimation of the JUROGAM 3 detectors is around  $\pm 6^\circ$ . The angles and collimation only apply, if the source of the  $\gamma$  rays is at the focal point of the array, which might not be the case if longer-living isomeric states are present. The efficiencies of the JUROGAM 3 rings have to be normalised to each other, which can be done based on the efficiency calibration ( $^{152}\text{Eu}$  and  $^{133}\text{Ba}$ ) data, as shown in Figure 40. Relative efficiencies are not always very accurate in the low-energy region. Many authors use generic reference values for  $A_2$  and  $A_4$ , to assign the transition multipolarity [80]. Figure 41 shows the reference curves to which the fit can be compared. A certain degree of alignment is supposed for these reference values, and ideally, the data should contain a known transition from which the actual experiment and setup specific parameters are determined. The nuclei are aligned only a relatively short time after their formation, and if long-living isomers are present, the alignment can decrease [81]. Furthermore, since the angular resolution of the JUROGAM 3 is somewhat coarse, and the angular uncertainty can be relatively large, good statistics and low background are often necessary to obtain more accurate results.



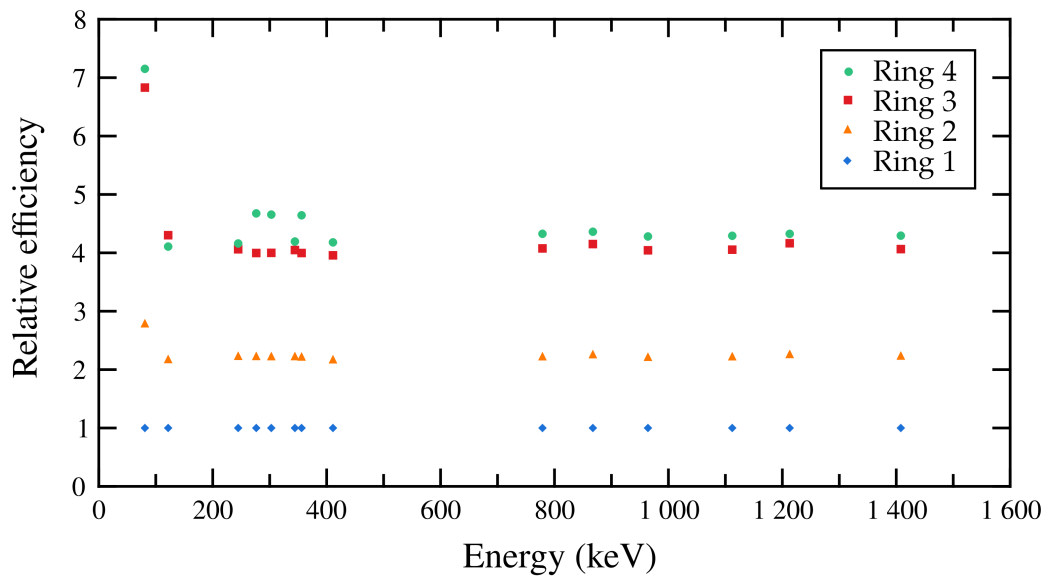


FIGURE 40 Relative efficiency of the JUROGAM 3, from the present experiment, when using the four-ring approach. Values are normalised to ring 1. The relative efficiencies appear to be roughly constant (1, 2.25, 4.1, 4.3) as a function of the  $\gamma$ -ray energy above 400 keV. However, below  $\sim 300$  keV some deviations start to develop.

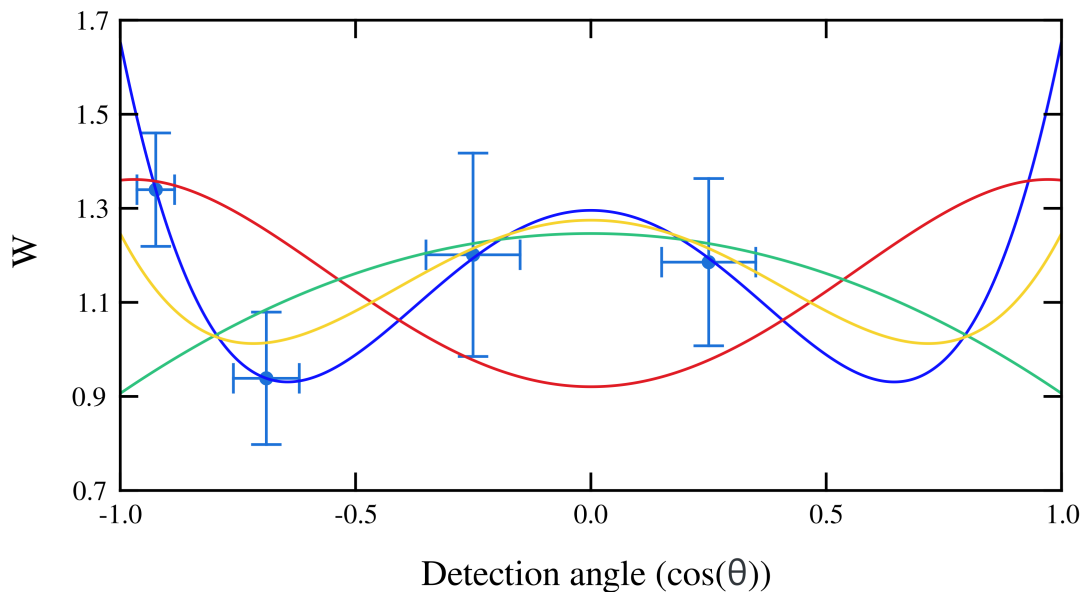


FIGURE 41 The angular distribution of  $\gamma$  rays emitted from an aligned nucleus is correlated to its multipolarity. Red, green, and yellow lines are the references for  $\Delta J = 2$  quadrupole ( $A_2 = 0.3$ ,  $A_4 = -0.1$ ),  $\Delta J = 1$  dipole ( $A_2 = -0.2$ ,  $A_4 = 0.0$ ), and  $\Delta J = 1$  quadrupole ( $A_2 = -0.1$ ,  $A_4 = 0.2$ ) transitions, respectively. For mixed D + Q,  $\Delta J = 1$  transitions the situation is more complicated and  $A_2$  and  $A_4$  can take values between  $-0.8$  to  $0.5$  and  $0.0$  to  $0.2$ , respectively. Blue line is the least-square fit to the 172 keV transition of  $^{212}\text{Ac}$ . The error in X represents the detector collimation width. Sometimes the intensity errors are large due to the background and multiple reference curves fit to the points.

State lifetimes, internal-conversion intensity ratios, and IC coefficients can also be used to narrow down the  $\Delta J$  and multipolarity possibilities. Transitions with certain multiplicities and energies would not be observed at the target position, since they would be too delayed. At the focal plane, the IC ratio can sometimes be directly obtained from the electron events in the DSSD, or the IC coefficient from the relative intensities of  $\gamma$ -ray cascades. Additionally, at the target position, the observed relative  $\gamma$ -ray intensity can be used to rule out certain types of transitions that would have very high conversion. When even higher  $\gamma$ - $\gamma$  statistics are available, angular correlations of successive  $\gamma$  rays [82] and linear polarisation [83] may also be used.

## 5.6 Statistical methods, uncertainty analysis, and background

The raw data is truncated in the FPGA firmware and is being sent as a 14-bit integer. The truncation destroys some information, so a (pseudo-)random floating point number between 0–1 has to be added to the raw ADC value in order to make it more continuous before applying the calibration function in the analysis software. The bin size of a histogram should be chosen so that the data does not get under or over-smoothed, but accurately represents the underlying distribution. The optimal bin width depends mainly on the sample size and number of counts per bin. Several methods exist to estimate the best bin width [84]. Technically, the bin width does not have to be fixed and sometimes combining bins with just a few counts might be justified, since a bin should have a certain amount of counts to be statistically significant enough to some methods to work properly. As the optimum bin size can be hard to choose, and it depends on the statistics, it can trick an eye, for example, over binning can create false peaks that do not exist. The tuple analyser in the new program includes a dynamic binning that can be adjusted on the fly.

Theoretically, the measured energy data should be normally distributed and when it is plotted on a binned histogram, a Gaussian curve least-square fitting can be used to extract centroid, area, and Full-Width at Half-Maximum (FWHM). For accurate fitting, the standard deviation of bin heights needs to be known. Since that is not usually the case, the first approximation is the square root of the bin height (Poisson distribution). This estimation can be further improved upon by iterating the fitting process and obtaining new error estimates by comparing the distance of the previously fitted curve to the data. The uncertainties of the Gaussian fit parameters follow from the covariance matrix of the fitting. Scaling the errors by the number of Degrees-of-Freedom (DoF) might yield more realistic estimations. Even still, the obtained uncertainties do not necessarily accurately reflect the true errors, since some general assumptions are made about the data that might not exactly hold. The first assumption is that the data is ideally Gaussian distributed, however, this is not always true. Often the data from many individual channels are summed together, as done with the DSSD and Ge detectors.



Even though the individual channels are calibrated, they are not exactly centred around the same mean and they also have different variances. Summing all the data into a single histogram is not necessarily the most elegant solution from a statistical point of view since the resulting peaks might no longer follow a single Gaussian distribution, but instead they could be slightly skewed. When enough statistics are available the fitting can be done independently to every channel, and the maximum-likelihood estimator can be obtained by calculating the weighted mean and its standard deviation. However, the energy error due to the calibration does not get smaller as the sample size increases, for example, with the JURIGAM 3, in the most optimal case with a very clean spectrum, stationary source, and high statistics, the energy calibration uncertainty alone can account at least 0.2–0.6 keV, which is usually more than the fitting errors.

$\gamma$  rays that Compton scatter out of one Clover Ge-detector crystal can hit the adjacent Ge crystal instead of the BGO shield. The resulting diagonal  $\gamma$ - $\gamma$  energy lines can be seen in Figure 42. In these cases, a Clover detector can be operated like an active shield and the escaped  $\gamma$ -ray energy can be recovered by adding it back to the original event. Add back improves the detection efficiency, especially for the higher energy  $\gamma$  rays. In the data stream, these related events typically come within 80 ns of each other. The add-back events have a slightly worse energy resolution, and there appears to also be an additional, pretty constant, 0.5 keV down-offset per an add-backed fold. Digitisation or truncation/rounding errors could be the cause, but then it is not clear why those errors would correspond to  $\sim 2$  raw ADC channels. It could also arise from the calibration errors as the raw Clover events are first calibrated before they are added back together. Having different coefficients for every add-back combination could be done, but just adding the 0.5 keV per fold seems to perform well enough. Many approaches can be taken when the Doppler correction is also needed to be done for an add-back event. In practice, the best results seem to be achieved when the Doppler correction is done only after the individual events have been summed together and by using the detection angle of the event that had the largest energy. Even summing the counts from the diagonal Clover crystals or from events with folds more than 2, seems to produce correct spectra.

There is another unexplained systematic discrepancy within the  $\gamma$ -ray data. The  $\gamma$ -ray energy of a transition measured in-beam seems to be consistently  $\sim 1$ – $2$  keV lower than when that same transition is observed in the focal plane. The discrepancy appears to not come from the Doppler correction, but might be related to the different count rates. To obtain the most accurate and unbiased decay or  $\gamma$ -ray energy and intensity values, it might be worth considering to give up some statistics and exclude channels that have poor resolution and possibly even exclude all add-back events. The total error of relative intensities comes from the efficiency calibration error, background, and peak area fittings from which the background is the hardest to estimate.

For the DSSD, another electronic error source exists. Even though the MWD algorithm is better than some other methods for dealing with fast subsequent events, even it shows some artefacts when microsecond range recoil-decays occur

in the same DSSD pixel. The MWD cannot properly recover the signal baseline for the second event due to the exponentially decaying gradient of the preceding pulse, causing a sigmoid shaped energy distortion as the function of the decay time. If the energy of such an event is to be extracted, the best scenario would be to have the full traces recorded and optimise the energy extraction algorithm in the offline analysis. However, semi-empirical correction may be applied to the distorted energies for easier gating.

Besides the calibration error and electronic noise, a different kind of uncertainty arises from the background. The advantage of the binned data is that it brings out the background of a spectrum in a form which can be more easily estimated. Due to a lack of better alternatives, a linear background is usually assumed over the relatively narrow width of a measured energy peak during the

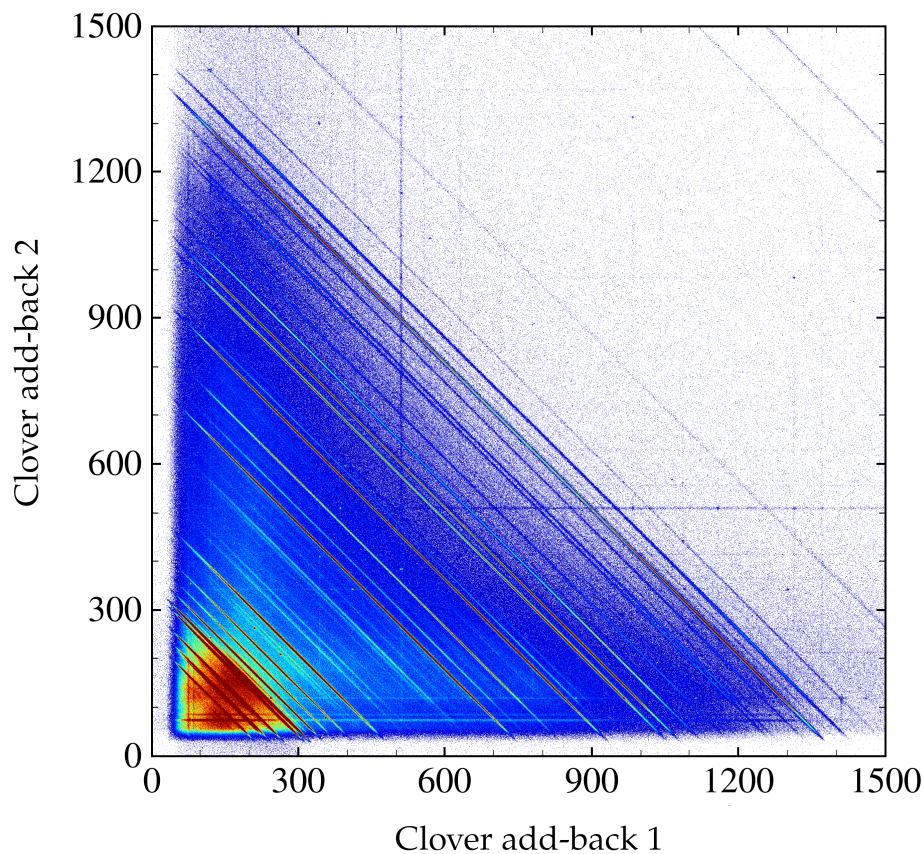


FIGURE 42 Compton scattered events appear as diagonal lines in  $\gamma$ - $\gamma$  coincidence matrices. In this figure, the energies of the events seen in neighbouring Clover crystals within 80 ns have been plotted. This corresponds to the Clover Compton add-back condition used in the experiment. Ideally, only diagonal lines would be seen, but some events that are not Compton scattered photons and should not be summed inevitably get tagged due to random correlations. These false correlations increase with the count rate. Too short of a coincidence time condition lets Compton events pass and too long of a time window increases the random correlations. True Compton events can arrive within a 400 ns time window, but 80 ns is optimal for tagging most of them while still not entering into the next cyclotron beam pulse period.

fitting. Accurately fitting a combined linear and Gaussian function over a limited data range can be difficult, and the uncertainties can be high. Sometimes, the linear component is just forced by hand, and its uncertainties are approximated. In addition to empirical methods, statistical background subtraction methods can also be used to improve the peak-to-background ratio. A typical JUROGAM 3  $\gamma$ -ray photopeak can have several different background components. A background arising from the Compton tails of higher energy transitions, direct overlap of close-by peaks (multiplet), neutron activation of the germanium itself, Coulomb excitations, contaminant nuclei in an RDT gate, and random background. Samples from the Coulomb excitation and neutron activation background are easier to obtain since they extend relatively unchanged outside the main DSSD–JUROGAM 3 time correlation distribution, as can be seen in Figure 38. The only caveat is that the neutron activation contribution is not exactly symmetric before and after the main distribution, and how it behaves under the peak is not precisely known, so background samples from both sides of the distribution should be used. An RDT contamination gate is a little harder to derive, but if the resolution of the DSSD and the peak separation is sufficient, as in the case of discrete energy decays, gating on both sides of a decay peak can give at least some estimate. Not much can be done to other background components in singles spectra during offline analysis, other than perhaps multi-component fits.  $\gamma$ - $\gamma$  coincidences are more impervious to the Coulomb and neutron background since they hardly correlate in the time domain. Compton and multiplet events, on the other hand, are in real prompt coincidence with the other  $\gamma$  rays, and thus, that background persists in the coincidence spectra. The background component of coincidence spectra can be estimated by creating separate coincidence spectra by gating on regions next to the peak, or on different regions of the peak itself. However, the background obtained in this manner may not always accurately reflect the true background under the peak. In the case of high-fold data, higher-order coincidence plots clean the spectra further [85], but working with multidimensional plots is also more involved. In any case, as with any statistical method, both the spectrum being subtracted and the one being subtracted from have to have enough statistical significance to produce meaningful results.

Another mostly independent observable is the time. More specifically, this usually considers the lifetime of a state. Nuclei are statistically independent, and the radioactive decay is a random process. Standard methods to determine the lifetime when only a part of the decay time distribution is available, or a background component is present, and when the sample size is sufficiently large, are exponential decay fitting and logarithmic time axis method [86], as was done in this work. Extracting the mean lifetime on an event-by-event basis is only acceptable when the sample is clean. A correction is needed if the whole decay time distribution is unavailable. For example, the setup used in this work is not sensitive to radioactive decays that happen during the signal integration time of the parent event, so a correction is needed, especially for lifetimes below 100  $\mu$ s, i.e. subtract the dead time from the mean value. The correlation window should also cleanly encompass several lifetimes so as not to introduce any bias, otherwise that

has to be corrected too. Even though the system has a 10 ns global clock, the total timestamp error of an event can be much larger due to the time response of the detector and the signal chain effects like time-walk. These errors are even larger between events observed in different detectors, such as between DSSD events and correlated  $\gamma$  rays, or between  $\gamma$ - $\gamma$  coincidences. Some of these errors are not normally distributed or energy independent, so appropriate precautions must be taken.

Error analysis is seldom straightforward and underlying statistical methods rely on certain assumptions regarding the data. In these complex systems, purely statistical uncertainties of the fitting parameters tend to underestimate the real errors. Systematic and random error contributions from the background and the sorting are often hard to estimate. More sophisticated approaches like resampling Monte-Carlo/bootstrapping methods or even proper simulations can provide more realistic error estimations [87, 88], however, an experimentalist should always be wary of the limitations of the statistical methods used.

## 5.7 Setup limitations and things to watch out for

Every measuring setup has its own intrinsic limitations that an experimentalist should be aware of. While some biases can originate from the experimental setup itself, some may also be introduced during the data analysis process, if sufficient care is not exercised. For example, all the analysis techniques used, such as the filtering thresholds and gates should be thoroughly checked and their effects understood. As mentioned, one of the goals of developing own analysis software was to gain more insight into the data, especially due to the use of modern, highly abstracted, digital DAQs. This section discusses some of the setup's limitations and what kind of effects different thresholds have on the data.

### 5.7.1 Nanosecond scale isomeric states

One of the limitations of the in-beam  $\gamma$ -ray spectroscopy experiments performed with the JUROGAM 3 combined with MARA or RITU, or separator setups in general, is that they are not sensitive to isomeric states with certain lifetimes. Particularly difficult are states with half-lives between 10–100 ns or a chain of multiple few nanosecond states. Since the nuclei of the interest are not stopped at the target position, it means that at typical recoil velocities, they would mostly decay inside the separator where there are no detectors. The upper lifetime detection limit at the focal plane array, on the other hand, is limited by the background rate. These isomeric states can hinder the prompt  $\gamma$ - $\gamma$  coincidence analysis because if their existence is not recognised, an incorrect level scheme may be deduced. Such states are found in the region under study in the present experiment. For example,  $^{210,211}\text{Rn}$  have various known nanosecond scale states [89, 90]. A couple of Francium examples from the present data are also shown in Figure 43.

In Figure 43(a), a recoil- $\alpha$ -decay tagged prompt  $\gamma$ -ray energy spectrum of  $^{210}\text{Fr}$  shows the strongest peak at 257 keV. However, this transition is not the transition from the first excited state, but instead, it sits above an isomeric state with a half-life of  $\sim 40$  ns [91]. Transitions below this state are not seen at the focal plane spectrometer either, since they decay during the flight through the separator. A similar situation can be seen in the recoil- $\alpha$ -decay tagged prompt  $\gamma$ -ray energy spectrum of  $^{208}\text{Fr}$ , in Figure 43(b), but its ground-state transition at 632 keV is barely observable, which is due to another branch feeding past the isomeric state. However, the exact level scheme of these nuclei is little unclear, even after considering the isomeric states, the present data may not entirely agree with the previously published level schemes in References [91–94].

In addition to the isomeric states, ground-state decays can also happen inside the separator, if the half-life of the nucleus is sufficiently short. So, if the decay does not kick the recoil out of the trajectory, prompt  $\gamma$  rays observed when tagged by the recoil-decays at the focal plane can actually belong to the parent nucleus of the one identified by the decay properties. Fast decay events can also directly pileup with the recoil implantation energy and go unnoticed. Fast subsequent decay-decay events can, of course, also pileup leading to anomalously large apparent decay energies or broadening of  $\alpha$ -decay peaks in the case of conversion electron summing.

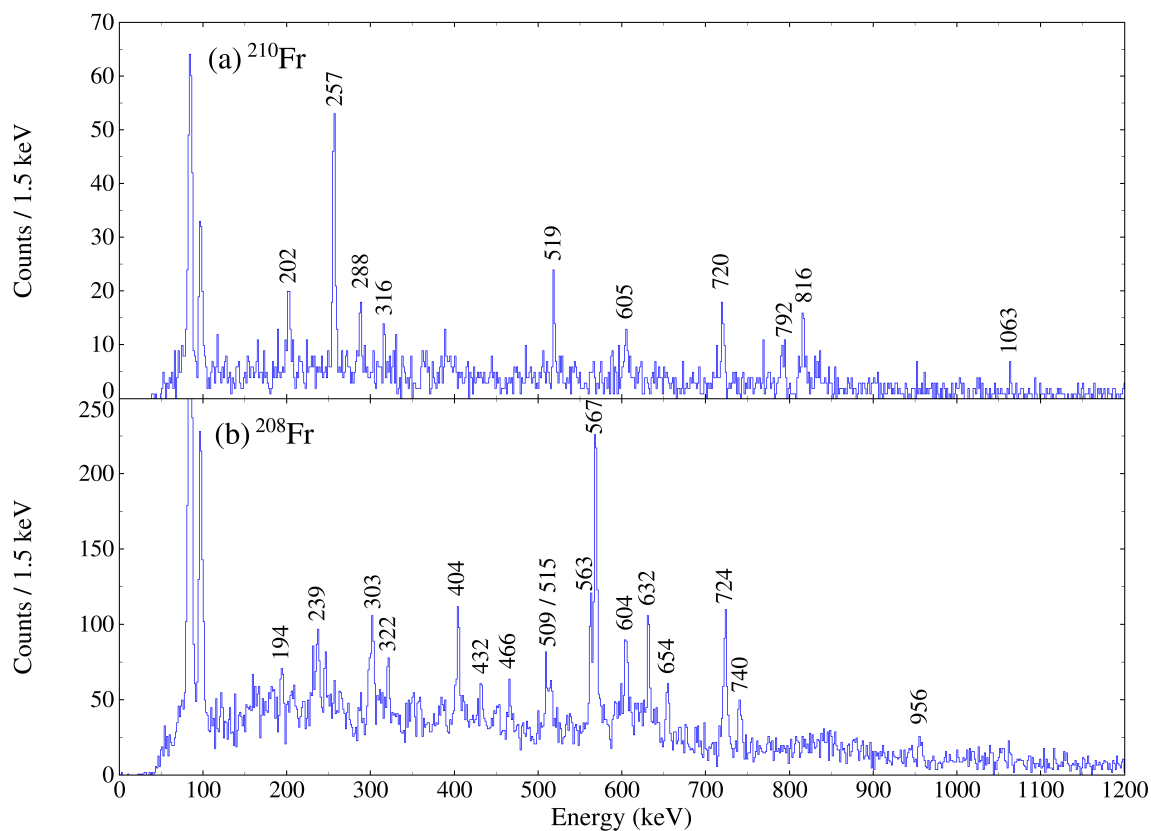


FIGURE 43 Recoil- $\alpha$ -decay tagged prompt  $\gamma$ -ray energy spectrum of (a)  $^{210}\text{Fr}$  and (b)  $^{208}\text{Fr}$ . Both of these nuclei have many nanosecond scale isomeric states that make determining their level structures challenging.



### 5.7.2 Contaminants and other reaction channels

In addition to fusion-evaporation residues, other reaction products can also find their way to the focal plane of MARA (or RITU) either by having the same  $A/q$  ratio or by scattering. The presence of various beam and target-like few nucleon transfer reaction products could be identified based on the  $\gamma$  rays observed at the focal plane. A decay tagged  $\gamma$ -ray energy spectrum from the focal plane, with some peaks labelled, is shown in Figure 44. More nuclei were also present, but they are not shown/labelled here. Another risk with these often long-lived transfer products is the contamination of the target chamber and the DSSD. In this experiment, so many of these transfer reaction products were produced that the  $\gamma$  rays they emitted, even relatively long after the beam was stopped at the target position, partly contaminated the detection efficiency calibration data. At least one photopeak was overlapped with a relatively important calibration point, which then had to be omitted, causing uncertainties in that energy region to be higher. While it is generally a good practice to do end-of-experiment calibrations as soon as possible, sometimes it might better to do a longer background run first whilst waiting for the residual activity to properly diminish.

An additional, prompt  $\gamma$ -ray correlating, recoil distribution was observed during the  $^{40}\text{Ar} + ^{175}\text{Lu}$  reaction. Figure 45 shows the expected recoil distribution and the anomalous double distribution with a slightly faster and more energetic component. Combined observation of prompt and delayed  $\gamma$  rays, X-rays as well as internal conversion electrons in the DSSD, revealed the presence of  $^{177}\text{Ir}$ . A small  $^{141}\text{Pr}$  impurity appears to have been present in one of the lutetium targets and fusion-evaporation products from the reaction  $^{40}\text{Ar} + ^{141}\text{Pr}$  had also come through the separator. Praseodymium and lutetium are both rare-earth metals, and they can naturally occur together. More about the findings regarding  $^{177}\text{Ir}$  are discussed in chapter 6, in section 6.3.

The beam also induced Coulomb excitations in the target nuclei as can be seen by looking at the regions outside the JUROGAM 3-DSSD event time gate for  $^{37}\text{Cl} + ^{180}\text{Hf}$ , shown in Figure 38. Coulomb excitation was even stronger with the reaction  $^{40}\text{Ar} + ^{175}\text{Lu}$ , and the  $\gamma$  rays belonging to lutetium were quite intense even in the recoil- $\alpha$ -decay tagged prompt  $\gamma$ -ray energy spectra as discussed in the article I.

### 5.7.3 Sorting biases

In addition to physical reasons, the recoil- $\alpha$ -decay tagged prompt  $\gamma$ -ray energy spectra can also be contaminated by incorrectly correlated DSSD events. The false correlations can be the result of wrongly selected DSSD strip/pixel, or, a bias was unintentionally introduced by imposing unfavourable energy thresholds, or due to too high count rates. It is not always guaranteed that a tagged decay belongs to the previous recoil nor that time correlated  $\gamma$  rays belong to that recoil. Many biases are hard to catch as the effect might not be immediately obvious and only present itself when the data is plotted in a very specific way. When the event

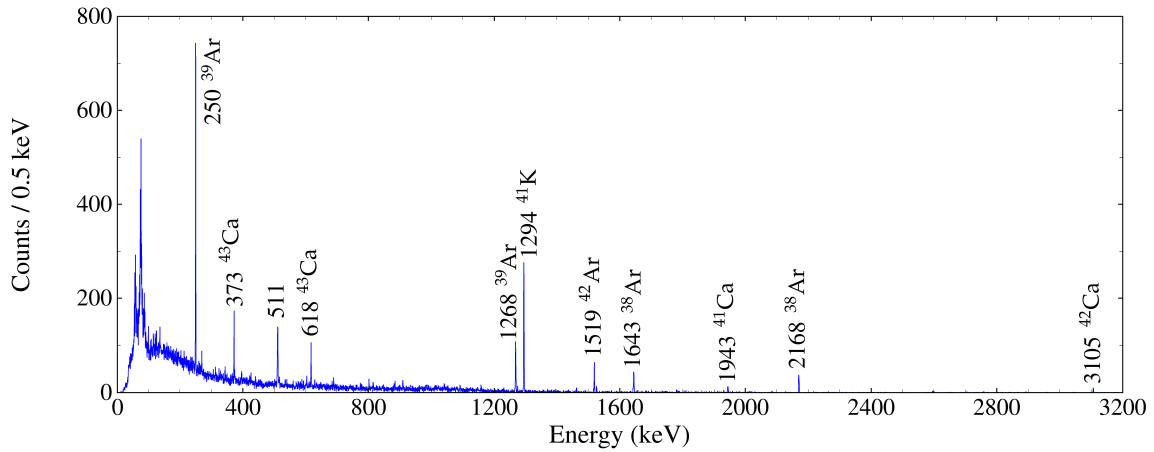


FIGURE 44 Focal plane ( $\beta$ ) decay tagged  $\gamma$ -ray energy spectrum from the reaction  $^{40}\text{Ar} + ^{175}\text{Lu}$  shows the presence of various beam-like transfer products.

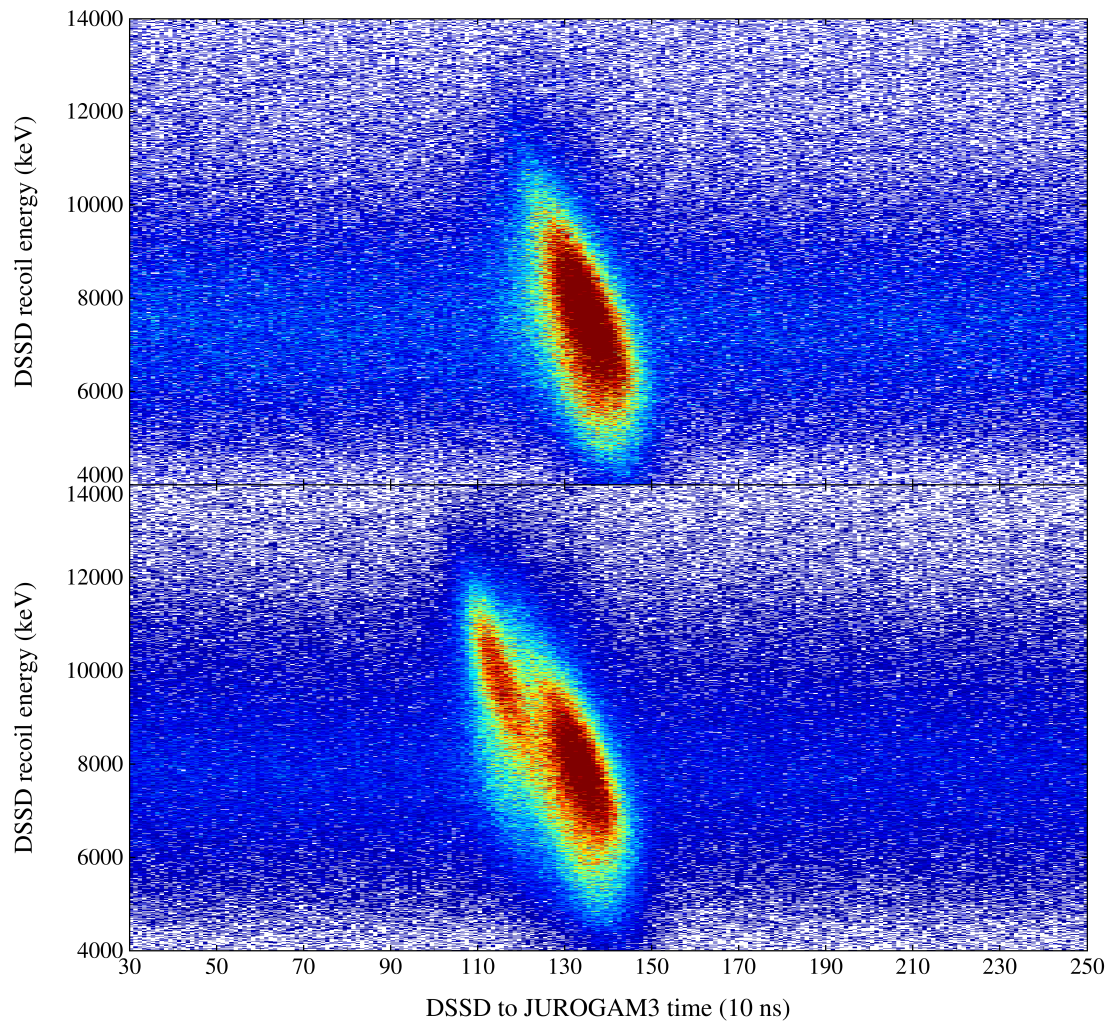


FIGURE 45 Top: JUROGAM3–DSSD time-of-flight versus DSSD recoil event energy from the reaction  $^{40}\text{Ar} + ^{175}\text{Lu}$ . A normal, singular recoil distribution is seen. Bottom: A similar plot with different  $^{175}\text{Lu}$  target shows an additional distribution with a slightly larger energy and faster flight time. The extra events are from a  $^{141}\text{Pr}$  impurity in an older  $320\text{-}\mu\text{g}/\text{cm}^2$  thick target.



rates are too high, recoil-decay correlations can appear correct, especially if the nuclei of the interest is the most abundant one at the focal plane, but in reality it is just a result of statistics and is more of recoil tagging than RDT at that point.  $\gamma$ -ray correlations can also look good for some group of recoil-decay tagged events and still fail for another group. For example, recoil- $\alpha$ -decay tagged prompt  $\gamma$ -ray energy spectrum of  $^{207}\text{Fr}$ , shown in Figure 46, is contaminated with transitions belonging to  $^{211}\text{Ac}$ .  $^{207}\text{Fr}$  was produced directly in the reaction, but the majority of its presence is accounted by the  $\alpha$ -decay of  $^{211}\text{Ac}$ . In this case,  $^{211}\text{Ac}$  recoils for which a correct  $\alpha$ -decay has been missed for one reason or another, or they have been correlated to a wrong pixel, get mostly paired with the daughter  $^{207}\text{Fr}$   $\alpha$ -decays. In this case the decay time distribution does not reveal the problem because the half-life of  $^{211}\text{Ac}$  is much shorter than the half-life of  $^{207}\text{Fr}$ .

As mentioned, another way these correlation biases can be introduced is the DSSD energy thresholds. There are few points along the data chain in which hard software thresholds can be set. The first one is the CFD threshold in the FPGA, the second one is in the analysis code before parsing the logical DSSD events, and the third place is after the event parsing. The effect of these three thresholds overlap, but there are still important differences between them.

The CFD threshold and filtering of the raw readings before parsing should be only used to discard actual (low amplitude) electronic noise. Since the CFD threshold is a simple level comparator, it is not very good at removing noise that has a short duration or oscillates, and has high one-off peak values. A channel can have a high noise count rate, but it might still have a mostly clean spectrum at higher energies. If a channel does not react to a slight rise of the CFD threshold, raising it more will likely just remove good signals at higher energies. If the noise rate of a channel gets so high that the bandwidth and stability of the FPGA is at risk it may be disabled altogether. However, disabling a channel is not without consequences, especially if it is a DSSD channel, as is explained shortly. Only a physical filter can help if the intrinsic count rate limit of a detector has been reached.

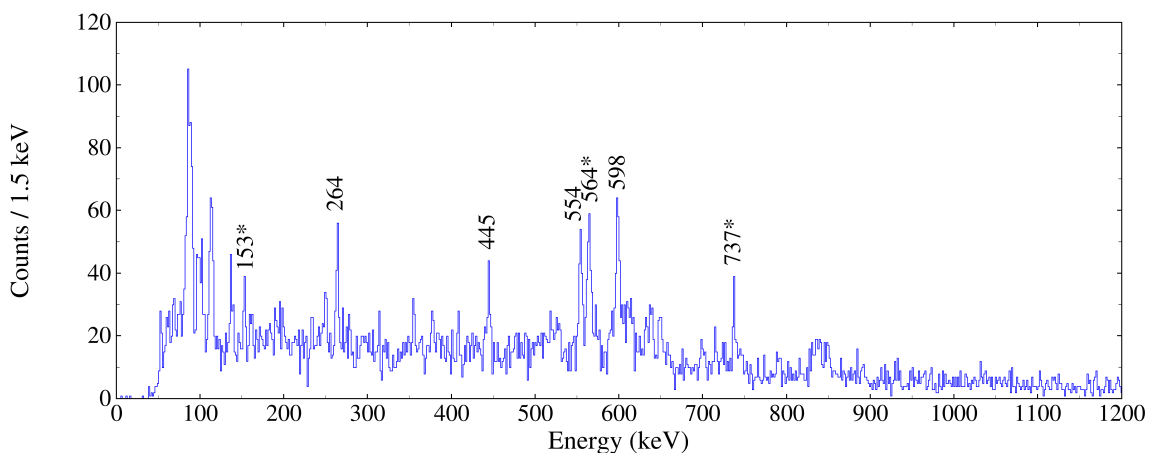


FIGURE 46 Recoil- $\alpha$ -decay tagged prompt  $\gamma$ -ray energy spectrum of  $^{207}\text{Fr}$ , in which the transitions marked with an asterisk (\*) actually belong to  $^{211}\text{Ac}$ . Other transitions are known to belong to  $^{207}\text{Fr}$  [95].

Filtering raw ADC readings, on the other hand, is slightly different as they have already been treated by the FPGA. The energy threshold at this stage can be more effective at removing the oscillating noise that the CFD threshold could not get rid of. This threshold cannot prevent high rate stability issues of the DAQ, but if done in a separate filtering software, it can considerably reduce the amount of data written to a disk. However, these filtering thresholds are also a little bit dangerous as the data is then irreversibly lost. Typically, the software filters only impose time gates for the JUROGAM3 data based on the events detected at the focal plane, which is more safe in terms of not creating biases that remove important events. If a significant reduction in the data volume is gained by removing low-energy noise, it may be done afterwards, for secondary copies of the data.

A more important consequence of the filtering of the DSSD readings before the event building process is how it may skew the parsing logic. As described, the parsing algorithm assigns the event's X–Y quasi-pixel based on the highest energy reading strips. A common practice to suppress a DSSD strip has been to set its gain coefficient to zero in the calibration file when the strip has bad resolution, for example. However, this only removes the parsed event, if the event buffer X and Y arrays included one X–Y pair, which is very often not the case. This can have undesired consequences. For example, imagine that in the data the algorithm is trying to parse are strips X-1 with an energy of 500 keV, X-44 with 100 keV, and Y-11 with 500 keV. If the calibration coefficient of X-1 is arbitrarily set to zero, the algorithm will link, likely completely unrelated, counts at channels X-44 and Y-11 together. A similar thing can also happen if an upper energy threshold is introduced. For example, if over-range events that do not have the correct full energy are removed by a strict upper energy threshold, there is a high chance that cross-talk, induced by the high energy event, or the neighbouring strip, gets randomly correlated in the same event buffer to the next highest energy and just ends up contaminating the lower energy region. High-energy events are usually accompanied by more stray counts in random strips than the other events. Saturated over-range events also pose another risk. If a stream from which the logical DSSD event is to be parsed contains more than one X or Y side over-range events the pixel assignment essentially happens randomly. So, while having a high DSSD gain increases the resolution, it can also increase incorrectly assigned recoils, if they saturate the dynamic energy range.

Another energy calibration-related risk is gain coefficients that are too high. If a too high calibration coefficient is used for a DSSD strip, it is possible that all logical event streams containing that particular strip, even as a noise count, will be falsely assigned to that strip/pixel and with non-real energy in the parsing process. Moreover, there is a difference between a DSSD strip not being biased and its output signal just being partially or fully lost. If the strip is not biased, some of the charge may be collected by the adjacent strips, whereas if its output signal is missing, actual information is lost. Missing strips can also be problematic in terms of the correlations too. As seen in the Figure 31, if a strip is missing, some of the events that should have been assigned to that strip get correlated to the adjacent strips instead. The correlations to these strips happen randomly, so

a recoil and its decay event in a broken strip region can end up in different adjacent strips. There is also the question of whether it is correct to assume that the strip/pixel that had the highest energy is the one where the event originated. For recoils this seems to hold, but light decay particles certainly can travel between pixels, especially if their origin is near the edge of a strip. Charge drift also makes the Y-coordinate selection more uncertain. Setting DSSD energy thresholds before the event parsing should be treated with utmost care, and they should be set as low as possible so that only uncorrelated electronic noise gets removed. The main reason why the DSSD noise should be removed in the first place is that it makes determining the start and end of a real DSSD event more difficult.

If setting a DSSD energy threshold or turning off strips or pixels has to be done, it is best to do it after the event parsing process. Ignoring strips and pixels at this point is pretty safe since it only reduces statistics while improving the quality of the spectra and correlations. Energy thresholds should be still carefully selected as they will nevertheless influence the event–event correlations. For example, if an energy range of decay events is set from 1–10 MeV, in attempt to remove  $\beta$ -decays, most escape  $\alpha$ -decays events also get removed. This is not always a big issue, but sometimes, for example, in the case of  $^{207}\text{Fr}$  in this data set, the spectrum in Figure 46 would be completely drowned by the  $^{211}\text{Ac}$  transitions as all the escape events get falsely correlated to the child nucleus. The same is true for the upper energy limit also, since high energy  $\alpha$ -decays or pileup events or fission fragments can be missed. The effects of some thresholds and gates can be very hard to predict, especially if a low cross section reaction channel is studied and statistics are low. The use of the limits might be more justified when it is done to remove the beam-related events that have not been vetoed out by the MWPC condition.

Sometimes, other restrictions may be imposed for the logical DSSD events. For example, requiring that the X and Y strip energies should not differ more than  $\pm 50$  keV or  $\pm 1\%$ . However, while such restrictions can provide an apparent improvement in the DSSD event distributions and energy peak FWHM, they can also influence the event–event correlations. Low energy  $\beta$  events can have larger X–Y energy differences due to their range. Sometimes, both strips just do not collect all the charge, broken strips have larger differences, and over-range events regularly have big differences, especially if the preamplifiers have been set to different gain ranges. Filtering DSSD events based on X–Y energy differences, therefore, arbitrarily cuts out real decay and recoil events, which again alters the event–event correlations. Furthermore, X–Y energy difference gates also create geometric patterns in the DSSD distributions, indicating a systemic bias in this method. Removing events on a pixel-by-pixel or a strip-by-strip basis almost always yields a better result and is generally a safer choice. For example, very good results can be obtained by excluding (1,1) and (1,72) quasi-pixels as is demonstrated in Figure 47. These pixels seem to collect most of the electronic noise and stray charges from the inactive regions and are responsible for most of the artefacts in many plots (punch-through, de-ToF, recoil-decay etc.). Sometimes, when looking for new weak decays, it might be a good idea to remove the

edge strips completely and possibly the middle X-strips that do not have as good punch-through veto due to the gap. In extreme cases, all misbehaving strips and strips adjacent to missing and broken strips may also be removed.

It should be noted that depending on where a strict energy condition is introduced, it is very easy to produce peaks in the spectra that look real. Since different channels have slightly different gains, setting a limit for the raw ADC reading does not necessarily result in a sharp threshold edge in the final spectrum, but instead the edge may look like an edge of smooth Gaussian distribution. Furthermore, if the dynamic range of a channel is exceeded, a Gaussian peak appears in

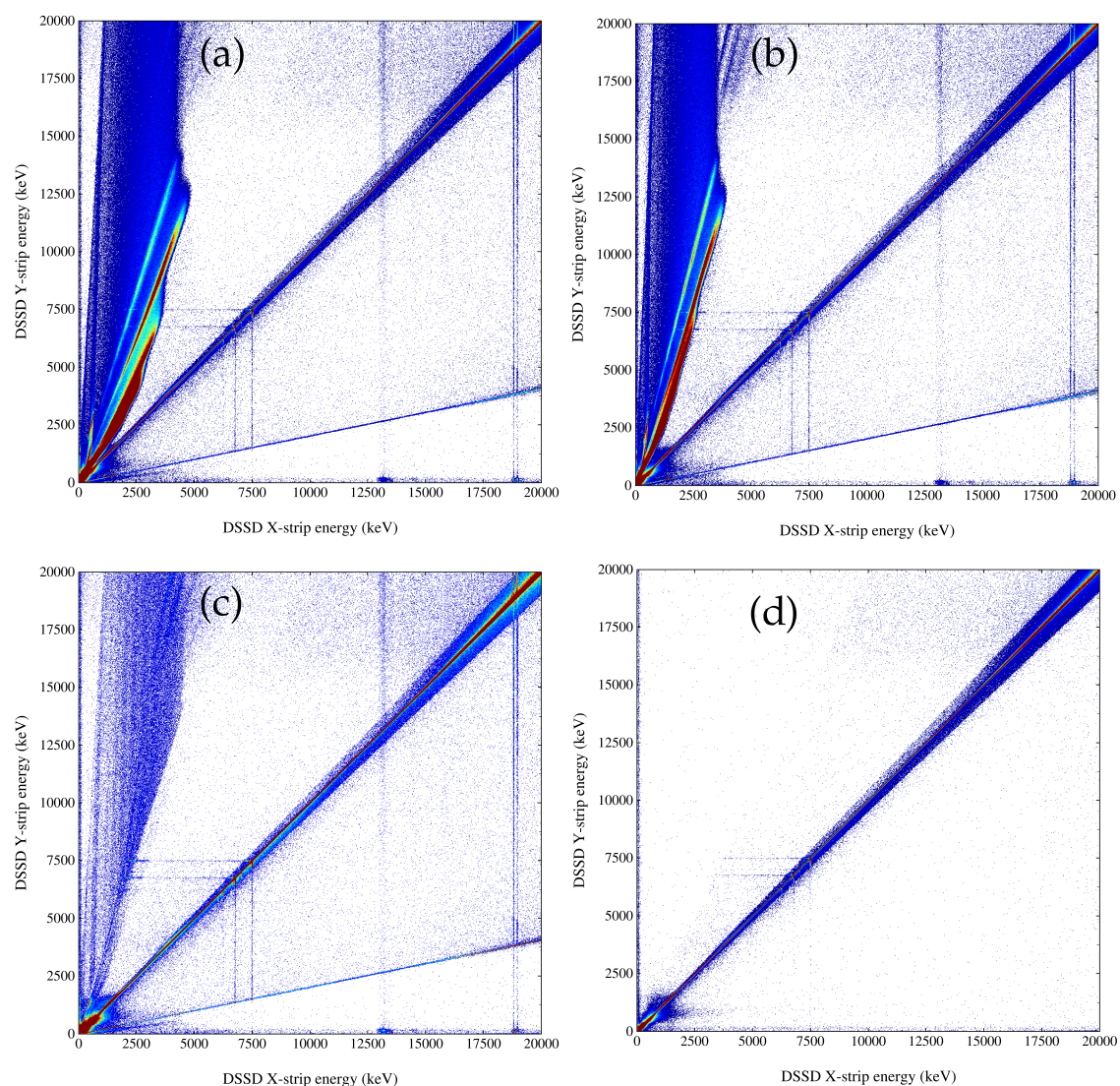


FIGURE 47 A comparison between the different approaches to clean up noisy DSSD events shown in X–Y energy plot. (a) All parsed events, no filter/threshold. (b) X-1 strip calibration coefficient set to zero. This has almost no effect on the noise. (c) Removing events from the pixels (1,1) and (1,72). The biggest noise contamination is gone. (d) Removing most strips that have bad or non-linear ADC/DoS channels or are next to a missing strip, including all the edge strips. Counts still left on the very edges are from events in which one of the strips is still saturated from the previous event.



the data, as is seen in Figure 36. Other gates, such as time and event fold gates can pose similar risks. For example, setting too long DSSD–MWPC time gate can systematically discard short-lived activities, while longer ones still get correlated correctly. When trying to judge the validity of a result of a gate or threshold based on some plotted data, it is also easy to fall victim to more subtle biases. For example, a DSSD recoil-decay distribution may look completely normal after setting an energy threshold for decay events, however, if recoil events are “correctly” selected, then due to how the correlations are selected, recoil-decay distribution can, by definition, only mirror the recoil distribution.

As described in section 5.3, the recoil-decay correlations are constructed so that every event classified as a recoil ends the previous recoil-decay-...-decay chain and starts a new one. As such, a high rate of recoils that are either stable or have very long half-lives as well as the background arising from their eventual decays can be problematic since they can end or get correlated to incorrect chains. It is also easy to see why removing events can have unintended effects on these correlations. The recoil-decay time distribution is subtly influenced by the process by which the chains are parsed, so sometimes it might also be useful to check recoil-recoil and decay-decay time plots to see if a random correlation background might influence the results. In an ideal case, a new recoil would hit a pixel only until after the previous one has decayed, events are detected with 100% efficiency, and only correctly assigned to their pixels, which, of course, is not possible. Another approach would be to force all recoils to correlate in some number of subsequent decays. A recent attempt has been made by Karvanen et al. [96] to try to establish a statistical theory for this method while taking into account the missed events. In short, the DSSD event–event correlations have three uncertainties: has an event been assigned with the correct quasi-pixel, has an event been missed, has an event been classified correctly. These boil down to the question: are subsequent events related? Utmost care should be always exercised when using any threshold, even if the results look good at the first glance, to not skew these correlations.

## 6 JR154: PROMPT AND DELAYED $\gamma$ -RAY SPECTROSCOPY OF NEUTRON DEFICIENT TRANS-LEAD NUCLEI

The aim of this study was to investigate the neutron-deficient nuclei  $^{213}\text{Ac}$  and  $^{211}\text{Ac}$ . The even-odd isotope  $^{211}\text{Ra}$  was not mentioned in the experiment proposal. However, it became evident during the experiment that it, too, was sufficiently produced in the reaction  $^{40}\text{Ar} + ^{175}\text{Lu}$  and new in-beam data could be obtained for it also. The physics related to  $^{211}\text{Ra}$  is close to the actinium nuclei, so it was natural to include it in the same article. Since these nuclei and the obtained results are thoroughly discussed in the article I, only a short summary is given here. However, in this chapter, some parts that were left out from the article regarding the odd-odd nucleus  $^{212}\text{Ac}$  are presented. The possibility to improve the data on the radium nuclei in this region using similar in-beam spectroscopy and recoil-decay-tagging methods is also mentioned.

### 6.1 Summary of $^{213}\text{Ac}$ , $^{211}\text{Ac}$ , and $^{211}\text{Ra}$

For both,  $^{213}\text{Ac}$  and  $^{211}\text{Ac}$ , level schemes were established up to spin  $^{23/2^-}$  and excitation energy of  $\sim 2\text{ MeV}$ . The level energies of the low-lying yrast  $^{9/2^-}$ ,  $^{13/2^-}$ ,  $^{17/2^-}$ , and  $^{21/2^-}$  states in  $^{213}\text{Ac}$  and  $^{211}\text{Ac}$  closely follow their respective even-even radium core  $0^+$ ,  $2^+$ ,  $4^+$ , and  $6^+$  state energies, as shown in Figure 48. This suggests that the odd proton in the  $h_{9/2}$  orbital in the actinium nucleus hardly participates in these excitations, but rather it acts as an inert “spectator” nucleon. Similar behaviour has been observed, for example, in the nearby francium and astatine isotopes [28–31]. No longer-living isomeric states nor deformation effects were yet observed in  $^{213}\text{Ac}$  or  $^{211}\text{Ac}$ , which was perhaps to be expected. However, as discussed in section 5.7.1, metastable states in the range of 10–100 ns might have been missed. It is also possible that some low-energy transitions were not seen due to their high internal conversion ratios and the strong X-ray background.

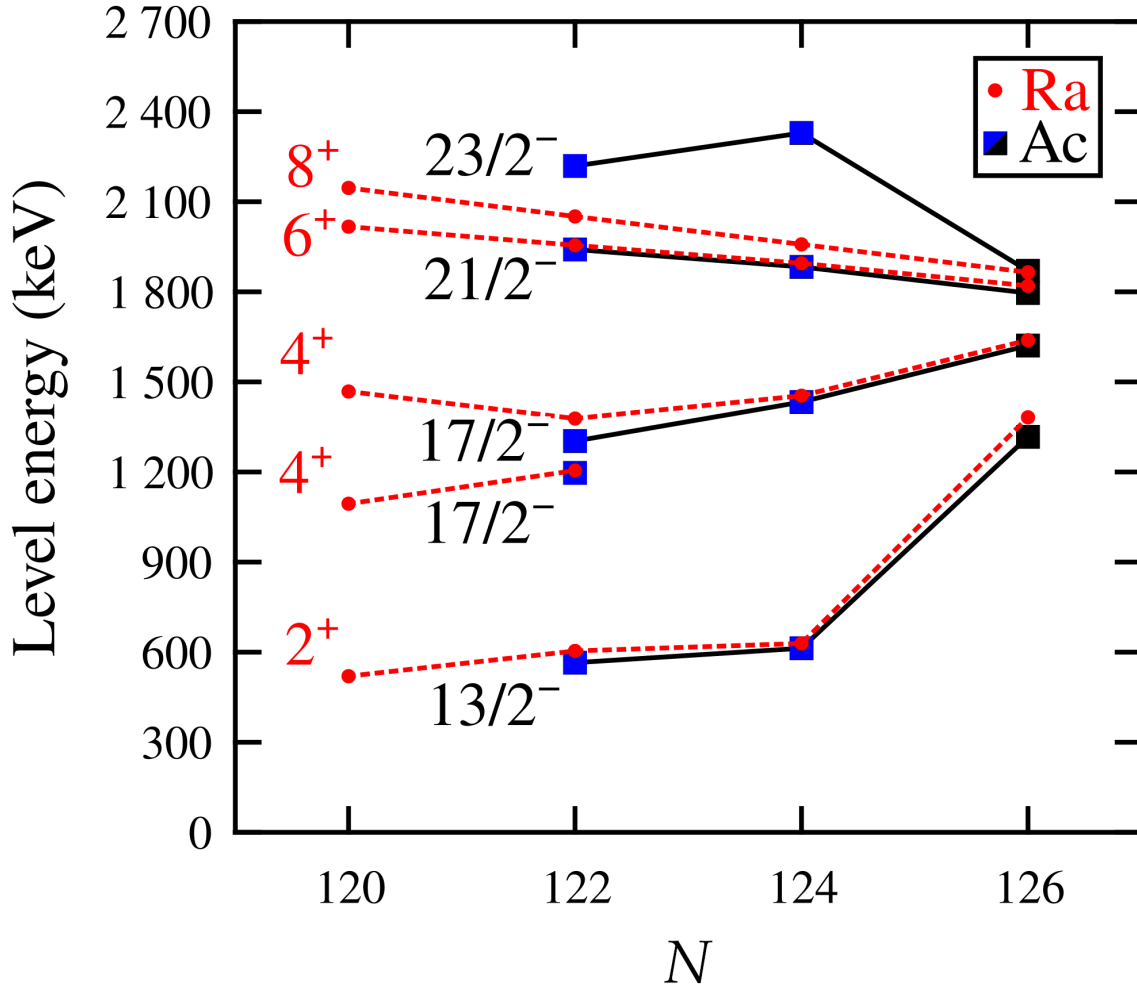


FIGURE 48 Level-energy systematics of selected negative-parity states in odd-mass actinium isotopes, compared to positive-parity states in even-even radium isotopes (circles). The deviation of the energy of the  $23/2^-$  state from that of the  $8^+$  state is similar to that observed in Fr (and At) nuclei, possibly indicating the start of breaking down of the core effect. Or possibly due to miss-assigned states in either nuclei due to low-energy transitions. The blue squares are from the present study, other points are taken from References [35, 97–100]. Adapted with permission from [I], copyright 2024, American Physical Society.

As mentioned,  $^{211}\text{Ra}$  was also produced in the  $^{40}\text{Ar} + ^{175}\text{Lu}$  reaction. Prior to this work, four transitions from the  $\alpha$ -decay studies [101, 102] and the 395–802-keV  $\gamma$ -ray cascade [103], depopulating the  $^{13/2^+}$  isomeric state, were known in this nucleus. Separate recoil- $\alpha$ -decay and recoil-electron tags allowed us to extend its level scheme and two de-excitation paths bypassing the  $^{13/2^+}$  isomeric state were also identified. The physics case with the  $^{211}\text{Ra}$  is similar to that of the  $^{213}\text{Ac}$  in that it has an odd neutron instead of a proton when compared to the  $^{212}\text{Ra}$  nucleus. One of the newly observed  $\gamma$ -ray cascades that bypass the  $^{13/2^+}$  isomeric state, closely resembles the known ground-state band in the  $^{212}\text{Ra}$ , further suggesting that it can be considered as the even-even core for the  $^{211}\text{Ra}$  as well. Systematic trends can be also observed as a function of the proton number along the  $N = 123$  isotone line, as shown in Figure 49.



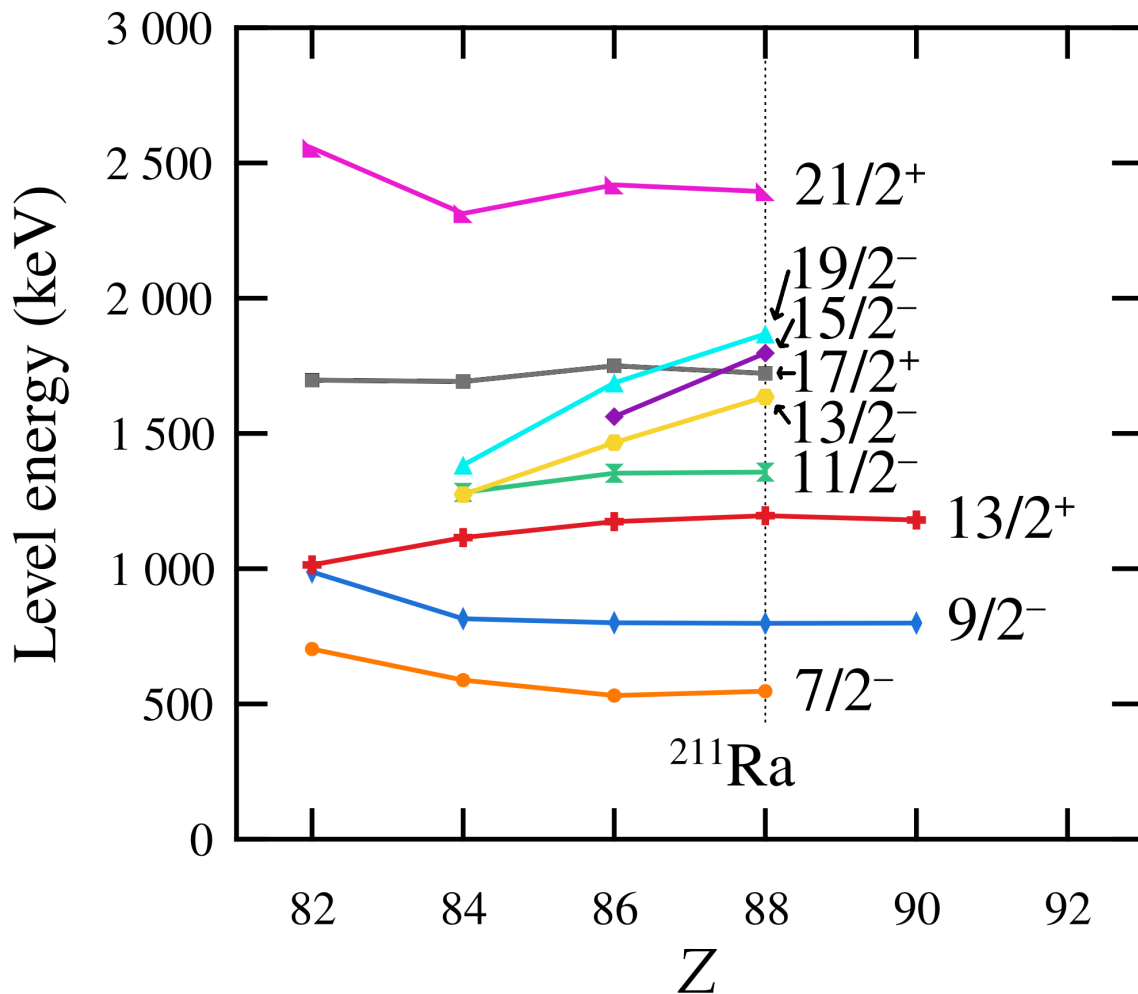


FIGURE 49 Level-energy systematics of selected states in  $N = 123$  isotones. The points on the dotted line ( $Z = 88$ ) are the proposed levels in  $^{211}\text{Ra}$  from the present study. The other points were taken from References [104–107]. Reprinted with permission from [1], copyright 2024, American Physical Society.

## 6.2 Odd-odd isotope $^{212}\text{Ac}$

Both reactions used in this experiment also produced the odd-odd isotope  $^{212}\text{Ac}$ . In the article, it is mentioned how it contaminated the  $\alpha$ -decay peak when trying to tag for  $^{213}\text{Ac}$  using the  $^{37}\text{Cl} + ^{180}\text{Hf}$  reaction. However, not much else was discussed, since the physics related to the odd-odd nuclei is rather different compared to the physics of the nuclei that were the main focus of this experiment. The structure of the odd-odd nuclei is also, in general, more fragmented than those of odd-even or even-even nuclei, which makes building the level scheme and the interpretation of the different states more challenging. Especially given the limited statistics in this study. However, the proposed level scheme for  $^{212}\text{Ac}$ , which has been constructed based on the relatively scarce prompt  $\gamma$ - $\gamma$  coincidences is now presented in Figure 50. The level scheme is a little too speculative to show in a peer-reviewed article, as the placement of the transitions is not completely unambiguous.

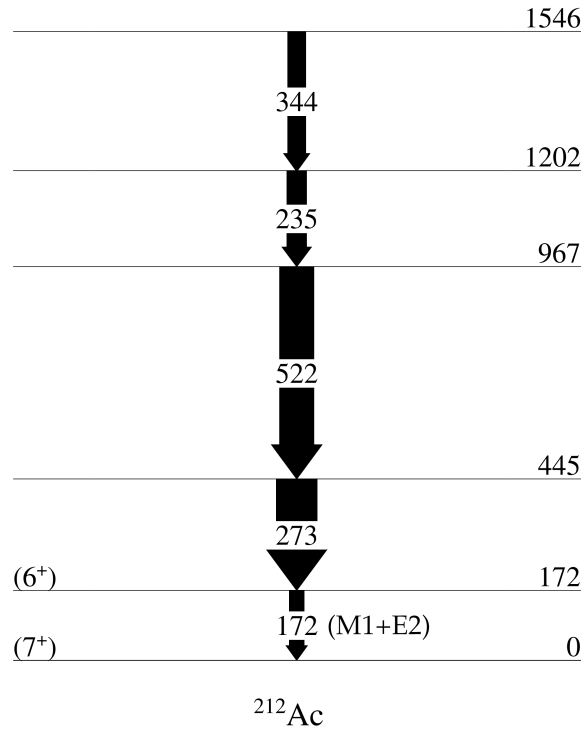


FIGURE 50 The proposed level scheme for  $^{212}\text{Ac}$ . Arrow widths indicate the efficiency corrected, relative  $\gamma$ -ray intensities. The 172 keV transition is placed as the first transition, since its angular distribution appears to hint towards  $\Delta J = 1$ , as shown in Figure 41, and by supposing an M1 + E2 character, the internal conversion correction would make it the most intense line. This is also backed up by calculations in Reference [108] that suggest the first excited  $J^\pi = 6^+$  level at  $\sim 200$  keV. A complete list of all the observed  $\gamma$ -ray transitions and their properties can be found in the article I.

### 6.3 Isomeric states in $^{177}\text{Ir}$

As discussed, one of the lutetium targets had a  $^{141}\text{Pr}$  impurity.  $^{177}\text{Ir}$ , produced via  $4n$  evaporation, appears to be the dominant reaction channel in the reaction  $^{40}\text{Ar} + ^{141}\text{Pr}$  at 182 MeV, as indicated by the recoil tagged prompt  $\gamma$ -ray energy spectrum in 51(a) (gating on the faster recoils shown in Figure 45). Since this nucleus certainly requires a remeasurement, this section is only a qualitative discussion and no precise values or uncertainties are reported, even though it would be possible for some quantities.

In  $^{177}\text{Ir}$ , there are two supposed isomeric states that have been deduced based on the non-observation of ground-state termination transition of  $d_{5/2}$  and  $h_{11/2}$  bands [109]. Minimum half-lives of 100 ns have been assigned based on the coincidence time gates, but the expected half-life for the  $d_{5/2}$  band-head state is  $\sim 1 \mu\text{s}$ . The  $h_{11/2}$  band is not fixed in the excitation energy. A lot of the evaluated data also seems to be from private communication.

In the present data, several isomeric states are present. IC electron distributions with half-lives of  $\sim 30$  ms and  $\sim 10 \mu\text{s}$  were observed in the DSSD. There also

appears to be  $\sim 100 \mu\text{s}$  and  $\sim 1 \mu\text{s}$  activities, but the first one is weak and the second one comes after another longer-living state. It is not certain if all of these states belong to  $^{177}\text{Ir}$ , but it seems likely since the recoil-tagged spectrum only shows  $^{177}\text{Ir}$  transitions. Also, the  $\sim 30 \text{ms}$  activity appears to be in a coincidence with several known low-lying states observed in an  $^{181}\text{Au}$   $\alpha$ -decay study [110]. It also correlates with some prompt  $\gamma$  rays. However, determining where it exactly lies, requires more data. The  $\sim 10 \mu\text{s}$  activity is a more straightforward case. It brings up distinctive M1 and E2 cascades at the target position, as shown in Figure 51(b), and multiple known  $^{177}\text{Ir}$  transitions are also observed delayed at the focal plane, see Figure 51(c). The origin of this isomer could be a three-quasiparticle configuration, similar to in the isotone  $^{175}\text{Re}$  [111, 112]. One of the delayed transitions could also be depopulating the isomeric state at the bottom of the  $h_{11/2}$  band.

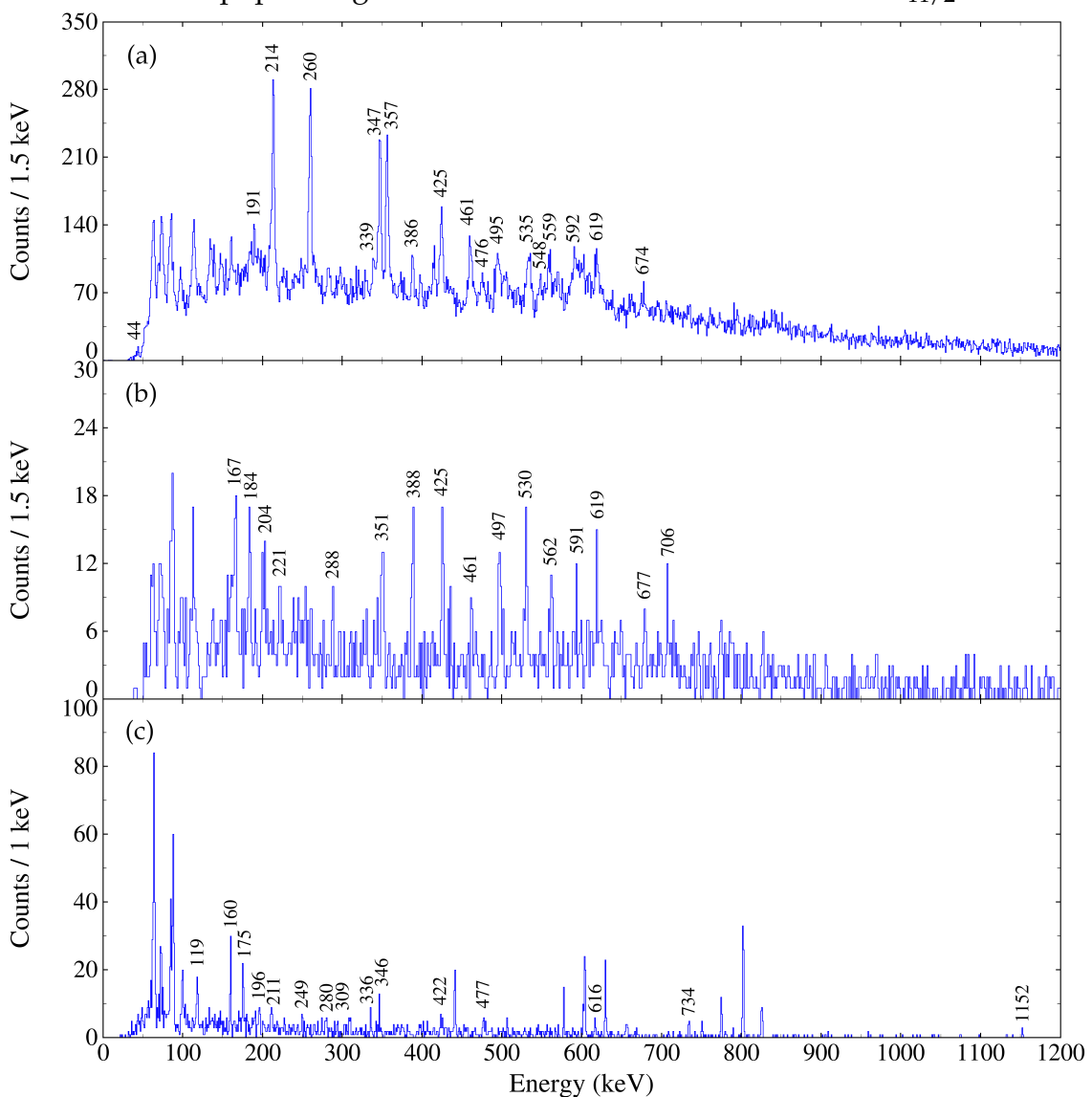


FIGURE 51 (a) Recoil tagged prompt  $\gamma$ -ray energy spectrum for  $^{177}\text{Ir}$ . Several known transitions from bands in Reference [109] are visible. (b) Recoil-e ( $\sim 10 \mu\text{s}$  isomer) tagged prompt  $\gamma$ -ray energy spectrum for  $^{177}\text{Ir}$ . Adjacent M1 and E2 cascades seems to be present. (c) FP  $\gamma$ -ray energy spectrum in coincidence with  $\sim 10 \mu\text{s}$  half-life electrons. Unmarked peaks are from radium isotopes.

## 6.4 Towards the drip line and remeasuring radium isotopes

The work towards exploring even more exotic nuclei closer and closer to the proton drip line will continue. The main challenge in these experiments will be the rapidly diminishing production cross sections. Current experiments are already pushing the boundaries of what the existing  $\gamma$ -ray spectrometer setups can do. New and more efficient devices will be needed in the future to perform experiments reaching even more exotic regions of the nuclear chart.

However, more work could still be done in the less exotic regions too. Whilst studying the known low-lying levels of the radium and francium isotopes, to compare them to the  $^{213}\text{Ac}$  and  $^{211}\text{Ac}$ , it became evident that the data on those nuclei could be improved. Possibly by using a similar setup and techniques as used in the present experiment. Extensive work has been done in the past to study the high-spin structure of these nuclei, but the longer-living isomeric states present in these nuclei have complicated the low-energy, low-spin studies. The in-beam RDT technique excels at resolving the level structure of nuclei if they can be tagged cleanly by isomeric transitions and/or ground-state decays. Longer-living isomeric states that impede untagged thick-target and pulsed-beam methods would be an advantage in this case. Ordering transitions in cascades below longer-living isomeric states is difficult, and they are often only based on the systematics of the neighbouring nuclei or theoretical calculations. However, in this region, the neighbouring nuclei may also suffer from the same problem, and the theoretical predictions largely rely on the experimental input themselves, which is not an ideal situation.

In Figure 52, recoil- $\alpha$ -decay tagged prompt  $\gamma$ -ray energy spectra of  $^{210}\text{Ra}$  and  $^{212}\text{Ra}$  are shown. The most recent level schemes on these nuclei are reported by Ressler et al. [98] and Palazzo et al. [35], respectively. For reference, the partial level schemes for these nuclei are also shown in Figure 53. Both of these nuclei have known low-lying  $8^+$  isomeric states whose half-lives are in the order of microseconds. All previously known  $\gamma$ -ray transitions depopulating those states were also observed at the focal plane Ge-array as expected. However,  $^{212}\text{Ra}$  has an even shorter-living  $11^-$  isomeric state above the  $8^+$  isomeric state [35, 113], whose reported de-excitation path could not be unambiguously verified with the present data.

What is particularly interesting is that these two recoil- $\alpha$ -decay tagged spectra still show the transitions depopulating the  $8^+$  isomeric states, which possibly indicates the presence of an alternative de-excitation path. As a matter of fact, Ressler et al. [98] already reported the same observation for  $^{210}\text{Ra}$ , while our  $\alpha$ -decay tagged spectrum in Figure 52(a) shows most of the transitions they observed, their relative intensities suggest a slightly different ordering. It is also not clear how the bypassing of the  $8^+$  state would proceed based on this level scheme or why exactly the 307-keV transition appears more intense than the 217-keV transition in the present data. In addition to the previously known transitions, three new transitions were observed at 489 keV, 565 keV, and 955 keV.

Within these, several energy sums can be constructed, therefore, more statistics and clear  $\gamma$ - $\gamma$  coincidences are needed to untangle the level scheme properly. The 565-keV transition appears to not be a contamination from the most abundant nu-

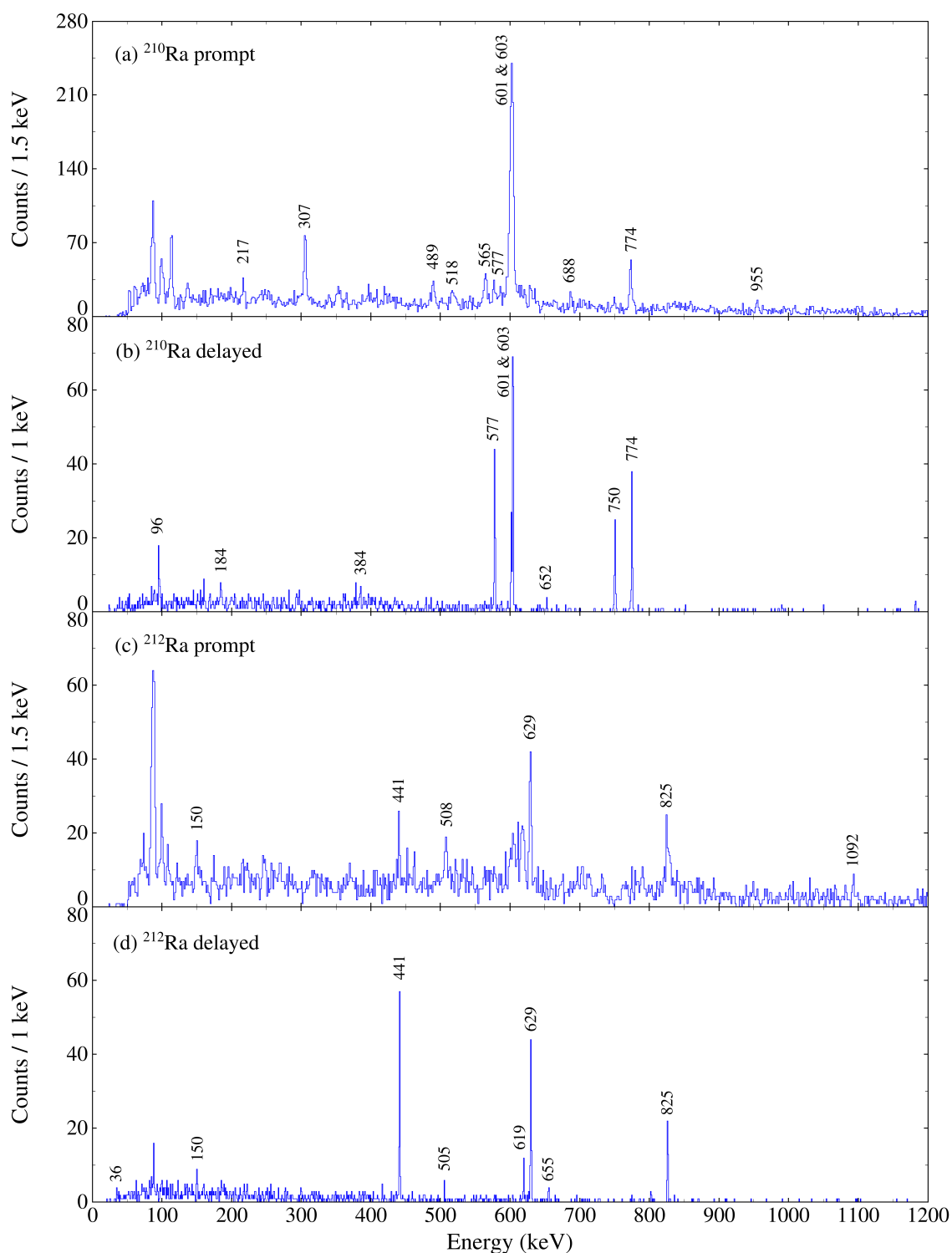


FIGURE 52 (a) Recoil- $\alpha$ -decay tagged prompt  $\gamma$ -ray energy spectrum of  $^{210}\text{Ra}$ . (b) Recoil- $\alpha$ -decay tagged fast (0–2  $\mu\text{s}$ ) delayed  $\gamma$ -ray energy spectrum of  $^{210}\text{Ra}$ . (c) Recoil- $\alpha$ -decay tagged prompt  $\gamma$ -ray energy spectrum of  $^{212}\text{Ra}$ . (d) Recoil- $\alpha$ -decay tagged fast (0–2  $\mu\text{s}$ ) delayed  $\gamma$ -ray energy spectrum of  $^{212}\text{Ra}$ .

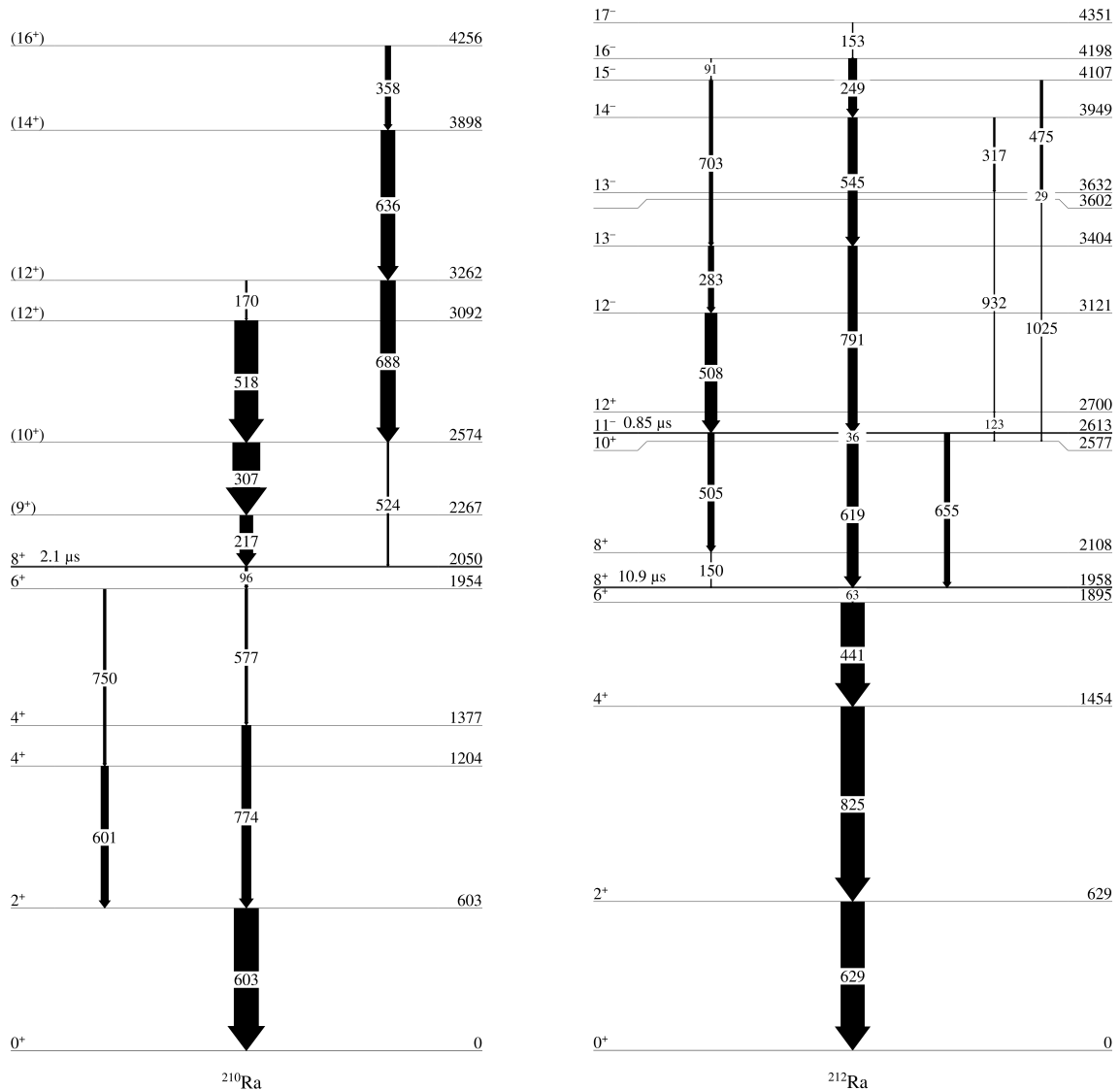


FIGURE 53 Partial level schemes of  $^{210}\text{Ra}$  and  $^{212}\text{Ra}$  reproduced based on the data reported in References [35, 98].

cleus,  $^{211}\text{Ac}$ , in the same dataset, since it has prompt coincidences with 307-keV and 601/603-keV transitions. Additionally, it also appears in a delayed coincidence with the 774-keV and 750-keV transitions observed at the focal plane, as does the 307-keV transition. Gating with different delayed  $\gamma$  rays also brings up different prompt transitions, albeit that could be just due to low statistics. All the known transitions below the isomer also appear at the focal plane, as shown in Figure 52(b). There might also be a couple of unknown delayed transitions, such as a fast 184-keV transition.

Similarly, the 629, 825, and 441-keV transitions that depopulate the  $T_{1/2} = 10.9 \mu\text{s}$ ,  $8^+$  isomeric state in  $^{212}\text{Ra}$  also appear in the recoil- $\alpha$ -decay tagged spectrum in Figure 52(c). There is also the shorter-living,  $T_{1/2} = 0.85 \mu\text{s}$ ,  $11^-$  isomeric state just above the  $8^+$  state, and the 36, 150, 505, 619, and 655-keV transitions depopulating it are also observed in the focal plane, as seen in Figure 52(d). A large fraction of their intensities are lost inside MARA, but they

still provide some interesting information. For example, the 655-keV transition appears to be in a coincidence with IC electrons that are not coming from the 63-keV transition, as shown in Figure 54(a). Moreover, its lifetime at the focal plane seems to be longer than the 619-keV transition, as shown by the intensity difference in spectra in Figures 54(b) and 54(c). Differing lifetimes might suggest a more complex de-excitation path. However, it is again hard to say for certain due to the limited statistics.

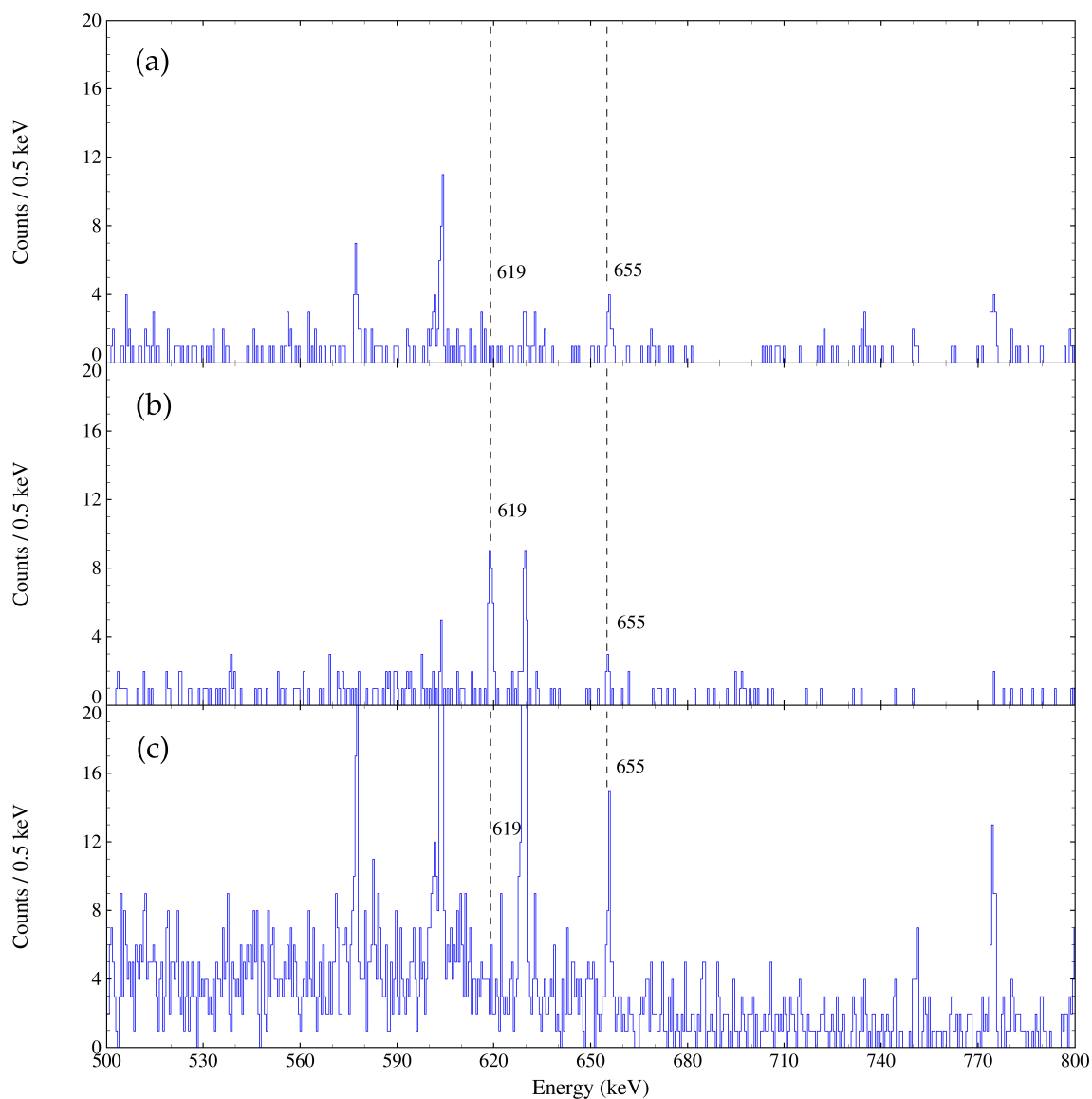


FIGURE 54 (a) Delayed  $\gamma$ -ray energy spectrum observed in the focal plane Ge-array within 0–50  $\mu$ s after the recoil implantation when tagged with recoil-electron (100–250 keV) chains in the DSSD. Only the 655-keV transition is visible. However, the 619-keV transition is clearly visible if the electron energy gate is set on 0–100 keV range instead. (b) Recoil tagged FP  $\gamma$ -ray energy spectrum within 0–2  $\mu$ s of the implantation. 619-keV transition is much stronger than the 655-keV transition (c) Same as (b), but with 2–50  $\mu$ s  $\gamma$ -ray correlation time limits. 655-keV transition is now much stronger, suggesting it has a longer lifetime than the 619-keV transition.



While it is technically possible that some of the intensity imbalance could be explained by the direct population below the isomeric states, it still seems unlikely that it alone would produce quite as striking an abundance as observed here, especially since transitions way above the isomeric states are also seen. Furthermore, for the other radium and francium nuclei present in the data, that have similar isomeric states, but without bypassing de-excitation paths, only transitions above the isomeric states were seen as expected. However, those are also produced in different evaporation channels that may be populated slightly higher up in excitation energy. It is not hard to imagine that these nuclei have many isomeric states and, for example,  $^{208}\text{Rn}$  and  $^{206}\text{Rn}$  have plenty of known transitions bypassing their  $8^+$  isomeric states [114]. Whatever the case may be, further investigations should be warranted, not only for  $^{210}\text{Ra}$  and  $^{212}\text{Ra}$ , but other isotopes in this region closer and at the  $N = 126$  shell as well.

## 7 SUMMARY

The RITU separator and the associated infrastructure were thoroughly refurbished. Sensors, the vacuum system, and magnet power supplies were connected to a central remote control and monitoring system. The old focal plane setup, GREAT, was dismantled and replaced with a modern, more efficient setup. The new focal plane is compatible with the MARA separator focal plane setup, which considerably reduces the operational complexity running these two devices side by side. The last couple of years have shown that switching between the MARA and RITU campaigns can be done in just couple of days if necessary. Having a backup option available is extremely beneficial should any component unexpectedly fail.

A new automatic liquid nitrogen filling system was developed for cooling the germanium detectors of the JUROGAM 3 and focal plane arrays. The new system is fully remote controllable from any device that has a regular web client. The performance and reliability of the new system have been found to be very good. The system has lowered the average LN<sub>2</sub> consumption, reduced detector warm-ups, and work load of the users considerably. It has also increased the overall working safety significantly.

A new multithreaded analysis program was written to analyse TDR data from MARA and RITU experiments. The program introduced many helpful tools that speed up the analysis process and give more versatility in sorting data. The new program was applied to the analysis of the data from an in-beam  $\gamma$ -ray spectroscopic study of the neutron-deficient trans-lead nuclei  $^{211,213}\text{Ac}$  and  $^{211}\text{Ra}$ . The experiment was performed using the JUROGAM 3 germanium-detector array and the MARA separator employing the fusion-evaporation reactions  $^{40}\text{Ar} + ^{175}\text{Lu}$  and  $^{37}\text{Cl} + ^{180}\text{Hf}$ . Excited states in  $^{211}\text{Ac}$  were observed for the first time. Level schemes were constructed, corrected, and extended for the aforementioned nuclei. The low-lying core-excited states in  $^{211}\text{Ac}$  and  $^{213}\text{Ac}$ , whose excitation energies follow the systematic trends of their respective core states in even-even isotones  $^{210}\text{Ra}$  and  $^{212}\text{Ra}$  were identified. The odd proton does not appear to be active in these states. The ground-state half-lives for these nuclei and for the  $^{13/2^+}$  isomeric state of  $^{211}\text{Ra}$  were remeasured.

## REFERENCES

- [1] C. Weizsäcker. *Z. Phys. A* 96 (1935). DOI: [10.1007 / BF01337700](https://doi.org/10.1007/BF01337700) (Cit. on p. 11).
- [2] H. A. Bethe and R. F. Bacher. *Rev. Mod. Phys.* 8 (1936). DOI: [10.1103 / RevModPhys.8.82](https://doi.org/10.1103/RevModPhys.8.82). (Cit. on p. 11).
- [3] M. G. Mayer. *Phys. Rev.* 74 (1948). DOI: [10.1103 / PhysRev.74.235](https://doi.org/10.1103/PhysRev.74.235). (Cit. on p. 12).
- [4] M. G. Mayer. *Phys. Rev.* 75 (1949). DOI: [10.1103 / PhysRev.75.1969](https://doi.org/10.1103/PhysRev.75.1969). (Cit. on p. 12).
- [5] O. Haxel, J. H. D. Jensen, and H. E. Suess. *Phys. Rev.* 75 (1949). DOI: [10.1103 / PhysRev.75.1766.2](https://doi.org/10.1103/PhysRev.75.1766.2). (Cit. on p. 12).
- [6] H. A. Wilson. *Phys. Rev.* 77 (1950). DOI: [10.1103 / PhysRev.77.516](https://doi.org/10.1103/PhysRev.77.516). (Cit. on p. 12).
- [7] P. F. A. Klinkenberg. *Rev. Mod. Phys.* 24 (1952). DOI: [10.1103 / RevModPhys.24.63](https://doi.org/10.1103/RevModPhys.24.63). (Cit. on p. 12).
- [8] M. G. Mayer. *Phys. Rev.* 78 (1950). DOI: [10.1103 / PhysRev.78.16](https://doi.org/10.1103/PhysRev.78.16). (Cit. on p. 12).
- [9] M. G. Mayer. *Phys. Rev.* 78 (1950). DOI: [10.1103 / PhysRev.78.22](https://doi.org/10.1103/PhysRev.78.22). (Cit. on p. 12).
- [10] T. Terasawa. *Prog. theor. exp.* 23.1 (1960). DOI: [10.1143 / PTP.23.87](https://doi.org/10.1143/PTP.23.87). (Cit. on p. 12).
- [11] J.-i. Fujita and H. Miyazawa. *Prog. Theor. Phys.* 17.3 (1957). DOI: [10.1143 / PTP.17.366](https://doi.org/10.1143/PTP.17.366). (Cit. on p. 12).
- [12] J.-i. Fujita and H. Miyazawa. *Prog. Theor. Phys.* 17.3 (1957). DOI: [10.1143 / PTP.17.360](https://doi.org/10.1143/PTP.17.360). (Cit. on p. 12).
- [13] T. Uesaka. *Eur. Phys. J. Plus* 131.11 (2016). DOI: [10.1140 / epjp / i2016-16403-1](https://doi.org/10.1140/epjp/i2016-16403-1). (Cit. on p. 12).
- [14] J. Dobaczewski, W. Nazarewicz, T. R. Werner, J. F. Berger, C. R. Chinn, and J. Dechargé. *Phys. Rev. C* 53 (1996). DOI: [10.1103 / PhysRevC.53.2809](https://doi.org/10.1103/PhysRevC.53.2809). (Cit. on p. 12).
- [15] T. Otsuka, T. Suzuki, R. Fujimoto, H. Grawe, and Y. Akaishi. *Phys. Rev. Lett.* 95 (2005). DOI: [10.1103 / PhysRevLett.95.232502](https://doi.org/10.1103/PhysRevLett.95.232502). (Cit. on p. 12).
- [16] R. F. Casten. *Nuclear Structure from a Simple Perspective*. Oxford University Press, 2001. ISBN: 9780198507246. DOI: [10.1093 / acprof : oso / 9780198507246.001.0001](https://doi.org/10.1093/acprof:oso/9780198507246.001.0001) (Cit. on p. 13).
- [17] S. G. Nilsson. *Binding states of individual nucleons in strongly deformed nuclei*. Tech. rep. 16. 1955. URL: <https://cds.cern.ch/record/212345> (Cit. on p. 13).

- [18] S. Hilaire and M. Girod. *Eur. Phys. J. A* 33.2 (2007). DOI: [10.1140 / epja / i2007-10450-2](https://doi.org/10.1140/epja/i2007-10450-2). (Cit. on pp. 14, 16).
- [19] *AMEDEE database*. URL: [https://www-phynu.cea.fr/science\\_en\\_ligne/carte\\_potentiels\\_microscopiques/carte\\_potentiel\\_nucleaire\\_eng.htm](https://www-phynu.cea.fr/science_en_ligne/carte_potentiels_microscopiques/carte_potentiel_nucleaire_eng.htm) (Cit. on p. 14).
- [20] M. Liu and C. Yuan. *Int. J. Mod. Phys. E* 32.12 (2023). DOI: [10.1142 / S0218301323300035](https://doi.org/10.1142/S0218301323300035). (Cit. on p. 15).
- [21] M. Bender, P.-H. Heenen, and P.-G. Reinhard. *Rev. Mod. Phys.* 75 (2003). DOI: [10.1103/RevModPhys.75.121](https://doi.org/10.1103/RevModPhys.75.121). (Cit. on p. 15).
- [22] G. Colò. *Adv. Phys.: X* 5.1 (2020). DOI: [10.1080 / 23746149.2020.1740061](https://doi.org/10.1080/23746149.2020.1740061). (Cit. on p. 15).
- [23] Y. Alhassid, G. F. Bertsch, L. Fang, and B. Sabbey. *Phys. Rev. C* 74 (2006). DOI: [10.1103/PhysRevC.74.034301](https://doi.org/10.1103/PhysRevC.74.034301). (Cit. on p. 15).
- [24] R. Julin, J. Kantele, M. Luontama, T. Poikolainen, and V. Rahkonen. *Phys. Lett. B* 65.4 (1976). DOI: [10.1016/0370-2693\(76\)90236-7](https://doi.org/10.1016/0370-2693(76)90236-7). (Cit. on p. 15).
- [25] M. Leino, J. Äystö, T. Enqvist, P. Heikkinen, A. Jokinen, M. Nurmia, A. Ostrowski, W. Trzaska, J. Uusitalo, K. Eskola, P. Armbruster, and V. Ninov. *Nucl. Instrum. Methods Phys. Res. Sect. B* 99.1 (1995). DOI: [10.1016 / 0168-583X\(94\)00573-7](https://doi.org/10.1016/0168-583X(94)00573-7). (Cit. on pp. 15, 18).
- [26] R. Julin, T. Grahn, J. Pakarinen, and P. Rahkila. *J. Phys. G: Nucl. Part. Phys.* 43.2 (2016). DOI: [10.1088/0954-3899/43/2/024004](https://doi.org/10.1088/0954-3899/43/2/024004). (Cit. on p. 15).
- [27] *IAEA chart of nuclides*. URL: <https://www-nds.iaea.org/relnsd/vcharthtml/VChartHTML.html> (Cit. on p. 16).
- [28] K. Auranen, J. Uusitalo, S. Juutinen, U. Jakobsson, T. Grahn, P. T. Greenlees, K. Hauschild, A. Herzán, R. Julin, J. Konki, M. Leino, J. Pakarinen, J. Partanen, P. Peura, P. Rahkila, P. Ruotsalainen, M. Sandzelius, J. Sarén, C. Scholey, J. Sorri, and S. Stolze. *Phys. Rev. C* 91 (2015). DOI: [10.1103 / PhysRevC.91.024324](https://doi.org/10.1103/PhysRevC.91.024324). (Cit. on pp. 15, 93).
- [29] K. Auranen, J. Uusitalo, S. Juutinen, H. Badran, F. Defranchi Bisso, D. Cox, T. Grahn, P. T. Greenlees, A. Herzán, U. Jakobsson, R. Julin, J. Konki, M. Leino, A. Lightfoot, M. J. Mallaburn, O. Neuvonen, J. Pakarinen, P. Papadakis, J. Partanen, P. Rahkila, M. Sandzelius, J. Sarén, C. Scholey, J. Sorri, S. Stolze, and Y. K. Wang. *Phys. Rev. C* 97 (2018). DOI: [10.1103/PhysRevC.97.024301](https://doi.org/10.1103/PhysRevC.97.024301). (Cit. on pp. 15, 93).
- [30] U. Jakobsson, J. Uusitalo, S. Juutinen, M. Leino, T. Enqvist, P. T. Greenlees, K. Hauschild, P. Jones, R. Julin, S. Ketelhut, P. Kuusiniemi, M. Nyman, P. Peura, P. Rahkila, P. Ruotsalainen, J. Sarén, C. Scholey, and J. Sorri. *Phys. Rev. C* 85 (2012). DOI: [10.1103/PhysRevC.85.014309](https://doi.org/10.1103/PhysRevC.85.014309). (Cit. on pp. 15, 93).

- [31] U. Jakobsson, S. Juutinen, J. Uusitalo, M. Leino, K. Auranen, T. Enqvist, P. T. Greenlees, K. Hauschild, P. Jones, R. Julin, S. Ketelhut, P. Kuusiniemi, M. Nyman, P. Peura, P. Rahkila, P. Ruotsalainen, J. Sarén, C. Scholey, and J. Sorri. *Phys. Rev. C* 87 (2013). DOI: [10.1103/PhysRevC.87.054320](https://doi.org/10.1103/PhysRevC.87.054320). (Cit. on pp. 15, 93).
- [32] P. Möller, A. Sierk, T. Ichikawa, and H. Sagawa. *At. Data and Nucl. Data Tables* 109-110 (2016). DOI: [10.1016/j.adt.2015.10.002](https://doi.org/10.1016/j.adt.2015.10.002). (Cit. on p. 16).
- [33] K. S. Krane and D. Halliday. *Introductory nuclear physics*. Wiley, 1987. ISBN: 978-0-471-80553-3 (Cit. on p. 16).
- [34] P. E. Hodgson. *Cont. Physic* 35.5 (1994). DOI: [10.1080/00107519408222099](https://doi.org/10.1080/00107519408222099). (Cit. on p. 16).
- [35] T. Palazzo, G. J. Lane, A. E. Stuchbery, A. J. Mitchell, A. Akber, M. S. M. Gerathy, S. S. Hota, T. Kibédi, B. Q. Lee, N. Palalani, and M. W. Reed. *Phys. Rev. C* 97 (2018). DOI: [10.1103/PhysRevC.97.014323](https://doi.org/10.1103/PhysRevC.97.014323). (Cit. on pp. 17, 94, 98, 100).
- [36] J. Sarén. “MARA vacuum-mode separator”. PhD thesis. University of Jyväskylä, 2011. ISBN: 978-951-39-4512-1. URL: <http://urn.fi/URN:ISBN:978-951-39-4512-1> (Cit. on pp. 18, 32).
- [37] J. Sarén, J. Uusitalo, M. Leino, P. Greenlees, U. Jakobsson, P. Jones, R. Julin, S. Juutinen, S. Ketelhut, M. Nyman, P. Peura, and P. Rahkila. *Nucl. Instrum. Methods Phys. Res. Sect. B* 266 (2008). DOI: [10.1016/j.nimb.2008.05.027](https://doi.org/10.1016/j.nimb.2008.05.027) (Cit. on pp. 18, 32).
- [38] J. Uusitalo, J. Sarén, J. Partanen, and J. Hilton. *Acta Phys. Pol. B* 50.3 (2019). DOI: [10.5506/aphyspolb.50.319](https://doi.org/10.5506/aphyspolb.50.319). (Cit. on p. 18).
- [39] J. Pakarinen, J. Ojala, P. Ruotsalainen, H. Tann, H. Badran, T. Calverley, J. Hilton, T. Grahn, P. T. Greenlees, M. Hytönen, A. Illana, A. Kauppinen, M. Luoma, P. Papadakis, J. Partanen, K. Porras, M. Puskala, P. Rahkila, K. Ranttila, J. Sarén, M. Sandzelius, S. Szvec, J. Tuunanen, J. Uusitalo, and G. Zimba. *Eur. Phys. J. A* 56.5 (2020). DOI: [10.1140/epja/s10050-020-00144-6](https://doi.org/10.1140/epja/s10050-020-00144-6). (Cit. on p. 18).
- [40] R. S. Simon, K. -. Schmidt, F. P. Heßberger, S. Hlavac, M. Honusek, G. Münzenberg, H. -. Clerc, U. Gollerthan, and W. Schwab. *Z. Phys. A* 325.2 (1986). DOI: [10.1007/bf01289651](https://doi.org/10.1007/bf01289651). (Cit. on p. 18).
- [41] C. A. Bertulani. *Nuclear Reactions*. 2010. URL: <https://arxiv.org/abs/0908.3275> (Cit. on p. 19).
- [42] R. Stock. *Encyclopedia of Nuclear Physics and its Applications*. Encyclopedia of Applied Physics. Wiley, 2013. ISBN: 978-3-527-64926-6 (Cit. on p. 19).
- [43] B. Martin. *Nuclear and Particle Physics: An Introduction*. Wiley, 2006. ISBN: 978-0-470-02532-1 (Cit. on p. 19).

- [44] O. Tarasov and D. Bazin. *Nucl. Instrum. Methods Phys. Res. Sect. B* 266.19 (2008). Proceedings of the XVth International Conference on Electromagnetic Isotope Separators and Techniques Related to their Applications. DOI: [10.1016/j.nimb.2008.05.110](https://doi.org/10.1016/j.nimb.2008.05.110). (Cit. on p. 21).
- [45] A. Gavron. *Phys. Rev. C* 21 (1980). DOI: [10.1103/PhysRevC.21.230](https://doi.org/10.1103/PhysRevC.21.230). (Cit. on p. 21).
- [46] J. Blatt and V. Weisskopf. *Theoretical Nuclear Physics*. Dover Books on Physics Series. Dover Publications, 1991. ISBN: 978-0-486-66827-7 (Cit. on p. 21).
- [47] J. Lilley. *Nuclear Physics: Principles and Applications*. Manchester Physics Series. Wiley, 2013. ISBN: 978-1-118-72332-6 (Cit. on pp. 21, 28).
- [48] L. Zhu, J. Su, C. Li, and F.-S. Zhang. *Phys. Lett. B* 829 (2022). DOI: [10.1016/j.physletb.2022.137113](https://doi.org/10.1016/j.physletb.2022.137113). (Cit. on p. 22).
- [49] D. M. Cullen, N. Amzal, A. J. Boston, P. A. Butler, A. Keenan, E. S. Paul, H. C. Scraggs, A. M. Bruce, C. M. Parry, J. F. C. Cocks, K. Helariutta, P. M. Jones, R. Julin, S. Juutinen, H. Kankaanpää, H. Kettunen, P. Kuusiniemi, M. Leino, M. Muikku, and A. Savelius. *Phys. Rev. C* 58 (1998). DOI: [10.1103/PhysRevC.58.846](https://doi.org/10.1103/PhysRevC.58.846). (Cit. on p. 24).
- [50] C. Scholey, D. M. Cullen, E. S. Paul, A. J. Boston, P. A. Butler, T. Enqvist, C. Fox, H. C. Scraggs, S. L. Shepherd, O. Stezowski, A. M. Bruce, P. M. Walker, M. Caamaño, J. Garcés Narro, M. A. Bentley, D. T. Joss, O. Dorvaux, P. T. Greenlees, K. Helariutta, P. M. Jones, R. Julin, S. Juutinen, H. Kankaanpää, H. Kettunen, P. Kuusiniemi, M. Leino, M. Muikku, P. Nieminen, P. Rahkila, and J. Uusitalo. *Phys. Rev. C* 63 (2001). DOI: [10.1103/PhysRevC.63.034321](https://doi.org/10.1103/PhysRevC.63.034321). (Cit. on p. 24).
- [51] E. Liukkonen. “New K130 cyclotron at Jyväskylä”. In *Proc. Cyclotrons’92*. Vancouver, Canada, 1992. URL: <https://epaper.kek.jp/c92/papers/i-03.pdf> (Cit. on p. 25).
- [52] P. Heikkinen and E. Liukkonen. “K130 Cyclotron - The First Years of Full Operation”. *14th International Conference on Cyclotrons and Their Applications*. 1996. URL: <https://inspirehep.net/files/a5e944c22eac8685635a8719d146083d> (Cit. on p. 25).
- [53] H. Koivisto, M. Hendolin, and J. Ärje. *Rev. Sci. Instrum.* 68.7 (1997). DOI: [10.1063/1.1148183](https://doi.org/10.1063/1.1148183). (Cit. on p. 25).
- [54] H. Koivisto, J. Ärje, and M. Nurmia. *Rev. Sci. Instrum.* 69.2 (1998). DOI: [10.1063/1.1148539](https://doi.org/10.1063/1.1148539). (Cit. on p. 25).
- [55] M. Moszyński, A. Syntfeld-Każuch, L. Swiderski, M. Grodzicka, J. Iwanowska, P. Sibczyński, and T. Szcześniak. *Nucl. Instrum. Methods Phys. Res. Sect. A* 805 (2016). DOI: [10.1016/j.nima.2015.07.059](https://doi.org/10.1016/j.nima.2015.07.059). (Cit. on p. 28).



- [56] J. Ojala, J. Pakarinen, P. Papadakis, J. Sorri, M. Sandzelius, D. M. Cox, K. Auranen, H. Badran, P. J. Davies, T. Grahn, P. T. Greenlees, J. Henderson, A. Herzán, R.-D. Herzberg, J. Hilton, U. Jakobsson, D. G. Jenkins, D. T. Joss, R. Julin, S. Juutinen, T. Kibédi, J. Konki, G. J. Lane, M. Leino, J. Limatainen, C. G. McPeake, O. Neuvonen, R. D. Page, E. Parr, J. Partanen, P. Peura, P. Rahkila, J. Revill, P. Ruotsalainen, J. Sarén, C. Scholey, S. Stolze, J. Uusitalo, A. Ward, and R. Wadsworth. *Commun. Phys.* 5.1 (2022). DOI: [10.1038/s42005-022-00990-4](https://doi.org/10.1038/s42005-022-00990-4). (Cit. on p. 29).
- [57] G. Duchêne, F. Beck, P. Twin, G. de France, D. Curien, L. Han, C. Beausang, M. Bentley, P. Nolan, and J. Simpson. *Nucl. Instrum. Methods Phys. Res. Sect. A* 432.1 (1999). DOI: [10.1016/S0168-9002\(99\)00277-6](https://doi.org/10.1016/S0168-9002(99)00277-6). (Cit. on p. 30).
- [58] *Mirion Clover-type Germanium detector datasheet*. URL: [https://mirionprodstorage.blob.core.windows.net/prod-20220822/cms4\\_mirion/files/pdf/spec-sheets/c39840\\_clover\\_detector\\_super\\_spec\\_3.pdf](https://mirionprodstorage.blob.core.windows.net/prod-20220822/cms4_mirion/files/pdf/spec-sheets/c39840_clover_detector_super_spec_3.pdf) (Cit. on p. 30).
- [59] U.K. — FRANCE EUROGRAM Collaboration. *Nucl. Phys. A* 520 (1990). DOI: [10.1016/0375-9474\(90\)91182-Q](https://doi.org/10.1016/0375-9474(90)91182-Q). (Cit. on p. 31).
- [60] D. Bazzacco, B. Cederwall, J. Cresswell, G. Duchêne, J. Eberth, W. Gast, J. Gerl, W. Korten, I. Lazarus, R. Lieder, J. Simpson, and D. Weisshaar. *AGATA, Technical Proposal for an Advanced Gamma Tracking Array for the European Gamma Spectroscopy Community*. Ed. by J. Gerl and W. Korten. AGATA collaboration, 1991. URL: <https://hal.science/hal-00729050> (Cit. on p. 31).
- [61] S. Akkoyun et al. *Nucl. Instrum. Methods Phys. Res. Sect. A* 668 (2012). DOI: [10.1016/j.nima.2011.11.081](https://doi.org/10.1016/j.nima.2011.11.081). (Cit. on p. 31).
- [62] S. Paschalis, I. Lee, A. Macchiavelli, C. Campbell, M. Cromaz, S. Gros, J. Pavan, J. Qian, R. Clark, H. Crawford, D. Doering, P. Fallon, C. Lionberger, T. Loew, M. Petri, T. Stezelberger, S. Zimmermann, D. Radford, K. Lagergren, D. Weisshaar, R. Winkler, T. Glasmacher, J. Anderson, and C. Beausang. *Nucl. Instrum. Methods Phys. Res. Sect. A* 709 (2013). DOI: [10.1016/j.nima.2013.01.009](https://doi.org/10.1016/j.nima.2013.01.009). (Cit. on p. 31).
- [63] J. Sarén, J. Uusitalo, and H. Joukainen. *Nucl. Instrum. Methods Phys. Res. Sect. B* 541 (2023). DOI: [10.1016/j.nimb.2023.04.040](https://doi.org/10.1016/j.nimb.2023.04.040). (Cit. on p. 32).
- [64] H. Joukainen, J. Sarén, and P. Ruotsalainen. *Nucl. Instrum. Methods Phys. Res. Sect. A* 1027 (2022). DOI: [10.1016/j.nima.2021.166253](https://doi.org/10.1016/j.nima.2021.166253). (Cit. on p. 36).
- [65] R. Page, A. Andreyev, D. Appelbe, P. Butler, S. Freeman, P. Greenlees, R.-D. Herzberg, D. Jenkins, G. Jones, P. Jones, D. Joss, R. Julin, H. Kettunen, M. Leino, P. Rahkila, P. Regan, J. Simpson, J. Uusitalo, S. Vincent, and R. Wadsworth. *Nucl. Instrum. Methods Phys. Res. Sect. B* 204 (2003). 14th International Conference on Electromagnetic Isotope Separators and Techniques Related to their Applications. DOI: [10.1016/S0168-583X\(02\)02143-2](https://doi.org/10.1016/S0168-583X(02)02143-2). (Cit. on pp. 36, 62).

- [66] *Micron BB20 datasheet*. URL: <http://www.micronsemiconductor.co.uk/wp-content/uploads/2020/09/M020-2-MSL-Catalogue-2.pdf> (Cit. on p. 37).
- [67] *Mirion germanium detector user manual*. URL: [https://www.aps.anl.gov/files/APS-Uploads/DET/Detector-Pool/Spectroscopic-Detectors/Canberra/Germanium\\_Detectors\\_Manual.pdf](https://www.aps.anl.gov/files/APS-Uploads/DET/Detector-Pool/Spectroscopic-Detectors/Canberra/Germanium_Detectors_Manual.pdf) (Cit. on p. 43).
- [68] D. Lersch, G. Pascovici, B. Birkenbach, B. Bruyneel, J. Eberth, H. Hess, P. Reiter, A. Wiens, and H. Georg Thomas. *Nucl. Instrum. Methods Phys. Res. Sect. A* 640.1 (2011). DOI: [10.1016/j.nima.2011.02.080](https://doi.org/10.1016/j.nima.2011.02.080). (Cit. on p. 53).
- [69] Smith, R., Menegazzo, R., Aufranc, C., Bez, N., Burrows, I., Cahoreau, M., Debras, G., Gibelin, L., Goasduff, A., Grant, A., Joannem, T., Karkour, N., Karolak, M., Kieffer, J., Lotodé, A., Million, B., Morrall, P. S., Ramina, L., Rampazzo, M., Roger, A., Simpson, J., Solenne, N., Stézowski, O., Tzvetkov, S., Zago, L., and Zielińska, M. *Eur. Phys. J. A* 59.7 (2023). DOI: [10.1140/epja/s10050-023-01046-z](https://doi.org/10.1140/epja/s10050-023-01046-z). (Cit. on p. 53).
- [70] *LN<sub>2</sub> system of the GEARS setup*. URL: <https://c7076-gears.chem.sfu.ca/ln2.html> (Cit. on p. 53).
- [71] M. Lauer. “*Digital Signal Processing for segmented HPGe Detectors: Preprocessing Algorithms and Pulse Shape Analysis*”. PhD thesis. Heidelberg University, 2004. URL: <http://cds.cern.ch/record/811708> (Cit. on p. 60).
- [72] *MIDAS documentation*. URL: <http://npg.dl.ac.uk/MIDAS/DataAcq/index.html> (Cit. on p. 62).
- [73] P. Rahkila. *Nucl. Instrum. Methods Phys. Res. Sect. A* 595.3 (2008). DOI: [10.1016/j.nima.2008.08.039](https://doi.org/10.1016/j.nima.2008.08.039). (Cit. on p. 64).
- [74] G. Betz, H.-J. Isele, E. Rössle, and G. Hortig. *Nucl. Instr. Meth.* 121.3 (1974). DOI: [10.1016/0029-554X\(74\)90217-1](https://doi.org/10.1016/0029-554X(74)90217-1). (Cit. on p. 76).
- [75] P. Doornenbal. *Prog. theor. exp.* 2012.1 (2012). DOI: [10.1093/ptep/pts076](https://doi.org/10.1093/ptep/pts076). (Cit. on p. 77).
- [76] M.-M. Bé and V. P. Chechev. *Nucl. Instrum. Methods Phys. Res. Sect. A* 728 (2013). DOI: [10.1016/j.nima.2013.05.134](https://doi.org/10.1016/j.nima.2013.05.134). (Cit. on p. 77).
- [77] S. Hurtado, M. García-León, and R. García-Tenorio. *Nucl. Instrum. Methods Phys. Res. Sect. A* 594.3 (2008). DOI: [10.1016/j.nima.2008.07.028](https://doi.org/10.1016/j.nima.2008.07.028). (Cit. on p. 77).
- [78] R. M. Diamond, E. Matthias, J. O. Newton, and F. S. Stephens. *Phys. Rev. Lett.* 16 (1966). DOI: [10.1103/PhysRevLett.16.1205](https://doi.org/10.1103/PhysRevLett.16.1205). (Cit. on p. 78).
- [79] T. Yamazaki. *Nucl. Data Sheets. Sec. A* 3.1 (1967). DOI: [10.1016/S0550-306X\(67\)80002-8](https://doi.org/10.1016/S0550-306X(67)80002-8). (Cit. on p. 78).
- [80] E. Der Mateosian and A. Sunyar. *At. Data Nucl. Data Tables* 13.4 (1974). DOI: [10.1016/0092-640X\(74\)90007-2](https://doi.org/10.1016/0092-640X(74)90007-2). (Cit. on p. 78).
- [81] P. Taras and B. Haas. *Nucl. Instrum. Methods* 123.1 (1975). DOI: [10.1016/0029-554X\(75\)90080-4](https://doi.org/10.1016/0029-554X(75)90080-4). (Cit. on p. 78).

- [82] K. Krane, R. Steffen, and R. Wheeler. *At. Data and Nucl. Data Tables* 11.5 (1973). DOI: [10.1016/S0092-640X\(73\)80016-6](https://doi.org/10.1016/S0092-640X(73)80016-6). (Cit. on p. 80).
- [83] K. Starosta, T. Morek, C. Droste, S. Rohoziński, J. Srebrny, A. Wierzychucka, M. Bergström, B. Herskind, E. Melby, T. Czosnyka, and P. Napiorkowski. *Nucl. Instrum. Methods Phys. Res. Sect. A* 423.1 (1999). DOI: [10.1016/S0168-9002\(98\)01220-0](https://doi.org/10.1016/S0168-9002(98)01220-0). (Cit. on p. 80).
- [84] K. H. Knuth. *Optimal Data-Based Binning for Histograms*. 2013. URL: <https://arxiv.org/abs/physics/0605197> (Cit. on p. 80).
- [85] D. Radford. *Nucl. Instrum. Methods Phys. Res. Sect. A* 361.1 (1995). DOI: [10.1016/0168-9002\(95\)00184-0](https://doi.org/10.1016/0168-9002(95)00184-0). (Cit. on p. 83).
- [86] K. H. Schmidt. *Eur. Phys. J. A* 8.1 (2000). DOI: [10.1007/s100500070129](https://doi.org/10.1007/s100500070129). (Cit. on p. 83).
- [87] R. Andrae, T. Schulze-Hartung, and P. Melchior. *Dos and don'ts of reduced chi-squared*. 2010. URL: <https://arxiv.org/abs/1012.3754> (Cit. on p. 84).
- [88] P. Young. *Everything you wanted to know about Data Analysis and Fitting but were afraid to ask*. 2014. URL: <https://arxiv.org/abs/1210.3781> (Cit. on p. 84).
- [89] A. Poletti, A. Byrne, G. Dracoulis, T. Kibèdi, and P. Davidson. *Nucl. Phys. A* 756.1 (2005). DOI: [10.1016/j.nuclphysa.2005.03.020](https://doi.org/10.1016/j.nuclphysa.2005.03.020). (Cit. on p. 84).
- [90] A. Poletti, G. Dracoulis, S. Poletti, A. Byrne, A. Stuchbery, and J. Gerl. *Nucl. Phys. A* 442.1 (1985). DOI: [10.1016/0375-9474\(85\)90139-3](https://doi.org/10.1016/0375-9474(85)90139-3). (Cit. on p. 84).
- [91] D. Kanjilal, S. Saha, S. Bhattacharya, A. Goswami, R. Kshetri, R. Raut, S. Muralithar, R. P. Singh, G. Mukherjee, and B. Mukherjee. *Phys. Rev. C* 84 (2011). DOI: [10.1103/PhysRevC.84.064321](https://doi.org/10.1103/PhysRevC.84.064321). (Cit. on p. 85).
- [92] V. Margerin, G. J. Lane, G. D. Dracoulis, N. Palalani, M. L. Smith, and A. E. Stuchbery. *Phys. Rev. C* 93 (2016). DOI: [10.1103/PhysRevC.93.064309](https://doi.org/10.1103/PhysRevC.93.064309). (Cit. on p. 85).
- [93] G. D. Dracoulis, P. M. Davidson, G. J. Lane, A. P. Byrne, T. Kibèdi, P. Nieminen, H. Watanabe, and A. N. Wilson. *Phys. Rev. C* 79 (2009). DOI: [10.1103/PhysRevC.79.054313](https://doi.org/10.1103/PhysRevC.79.054313). (Cit. on p. 85).
- [94] D. Kanjilal, S. Bhattacharya, A. Goswami, R. Kshetri, R. Raut, S. Saha, R. Bhowmik, J. Gehlot, S. Muralithar, R. Singh, G. Jnaneswari, G. Mukherjee, and B. Mukherjee. *Nucl. Physics A* 842.1 (2010). DOI: [10.1016/j.nuclphysa.2010.04.003](https://doi.org/10.1016/j.nuclphysa.2010.04.003). (Cit. on p. 85).
- [95] D. J. Hartley, E. P. Seyfried, W. Reviol, D. G. Sarantites, C. J. Chiara, O. L. Pechenaya, K. Hauschild, A. Lopez-Martens, M. P. Carpenter, R. V. F. Janssens, D. Seweryniak, and S. Zhu. *Phys. Rev. C* 78 (2008). DOI: [10.1103/PhysRevC.78.054319](https://doi.org/10.1103/PhysRevC.78.054319). (Cit. on p. 88).
- [96] J. Karvanen, M. Niilo-Rämä, J. Sarén, and S. Kärkkäinen. *J. R. Stat. Soc., C: Appl. Stat.* 71.1 (2022). DOI: [10.1111/rssc.12519](https://doi.org/10.1111/rssc.12519). (Cit. on p. 92).

- [97] J. Ressler, C. Beausang, H. Ai, H. Amro, M. Babilon, J. Caggiano, R. Casten, G. Gürdal, A. Heinz, R. Hughes, E. Mccutchan, D. Meyer, C. Plettner, J. Qian, M. Sciacchitano, N. Thomas, E. Williams, N. Zamfir, and A. Wright. *Phys. Rev. C* 7108 (2005). DOI: [10.1103/PhysRevC.71.014302](https://doi.org/10.1103/PhysRevC.71.014302). (Cit. on p. 94).
- [98] J. J. Ressler, C. W. Beausang, H. Ai, H. Amro, M. A. Caprio, R. F. Casten, A. A. Hecht, S. D. Langdown, E. A. McCutchan, D. A. Meyer, P. H. Regan, M. J. S. Sciacchitano, A. Yamamoto, and N. V. Zamfir. *Phys. Rev. C* 69 (2004). DOI: [10.1103/PhysRevC.69.034331](https://doi.org/10.1103/PhysRevC.69.034331). (Cit. on pp. 94, 98, 100).
- [99] D. J. Decman, H. Grawe, H. Kluge, and K. H. Maier. *Z. Phys. A* 310.1-2 (1983). DOI: [10.1007/bf01433610](https://doi.org/10.1007/bf01433610). (Cit. on p. 94).
- [100] A. Stuchbery, G. Dracoulis, T. Kibédi, A. Byrne, B. Fabricius, A. Poletti, G. Lane, and A. Baxter. *Nucl. Phys. A* 548.1 (1992). DOI: [10.1016/0375-9474\(92\)90081-T](https://doi.org/10.1016/0375-9474(92)90081-T). (Cit. on p. 94).
- [101] F. P. Heßberger, S. Hofmann, I. Kojouharov, and D. Ackermann. *Eur. Phys. J. A* 22.2 (2004). DOI: [10.1140/epja/i2003-10233-9](https://doi.org/10.1140/epja/i2003-10233-9). (Cit. on p. 94).
- [102] P. Kuusiniemi, F. P. Heßberger, D. Ackermann, S. Hofmann, B. Sulignano, I. Kojouharov, and R. Mann. *Eur. Phys. J. A* 25.3 (2005). DOI: [10.1140/epja/i2005-10117-0](https://doi.org/10.1140/epja/i2005-10117-0). (Cit. on p. 94).
- [103] K. Hauschild, A. Yerebin, O. Dorvaux, A. Lopez-Martens, A. Belozerov, C. Briançon, M. Chelnokov, V. Chepigin, S. Garcia-Santamaria, V. Gorshkov, F. Hanappe, A. Kabachenko, A. Korichi, O. Malyshev, Y. Oganessian, A. Popeko, N. Rowley, A. Shutov, L. Stuttgé, and A. Svirikhin. *Nucl. Instrum. Methods Phys. Res. Sect. A* 560.2 (2006). DOI: [10.1016/j.nima.2006.01.107](https://doi.org/10.1016/j.nima.2006.01.107). (Cit. on p. 94).
- [104] J. Khuyagbaatar, S. Hofmann, F. P. Heßberger, D. Ackermann, S. Antalic, H. G. Burkhard, S. Heinz, B. Kindler, A. F. Lisetskiy, B. Lommel, R. Mann, K. Nishio, H. J. Schött, and B. Sulignano. *Eur. Phys. J. A* 34.4 (2007). DOI: [10.1140/epja/i2007-10512-5](https://doi.org/10.1140/epja/i2007-10512-5). (Cit. on p. 95).
- [105] A. Poletti, G. Dracoulis, C. Fahlander, and A. Byrne. *Nucl. Phys. A* 440.1 (1985). DOI: [10.1016/0375-9474\(85\)90045-4](https://doi.org/10.1016/0375-9474(85)90045-4). (Cit. on p. 95).
- [106] V. Rahkonen, B. Fant, C. Herrlander, K. Honkanen, A. Källberg, and T. Weckström. *Nucl. Phys. A* 441.1 (1985). DOI: [10.1016/0375-9474\(85\)90165-4](https://doi.org/10.1016/0375-9474(85)90165-4). (Cit. on p. 95).
- [107] J. H. Hamilton, V. Ananthakrishnan, A. V. Ramayya, W. M. LaCasse, D. C. Camp, J. J. Pinajian, L. H. Kern, and J. C. Manthuruthil. *Phys. Rev. C* 6 (1972). DOI: [10.1103/PhysRevC.6.1265](https://doi.org/10.1103/PhysRevC.6.1265). (Cit. on p. 95).
- [108] R. Ferrer, A. Barzakh, B. Bastin, R. Beerwerth, M. Block, P. Creemers, H. Grawe, R. de Groote, P. Delahaye, X. Flécharde, S. Franchoo, S. Fritzsche, L. P. Gaffney, L. Ghys, W. Gins, C. Granados, R. Heinke, L. Hijazi, M. Huyse, T. Kron, Y. Kudryavtsev, M. Laatiaoui, N. Lecesne, M. Loiselet, F. Lutton, I. D. Moore, Y. Martínez, E. Mogilevskiy, P. Naubereit, J. Piot, S. Raeder, S. Rothe, H. Savajols, S. Sels, V. Sonnenschein, J.-C. Thomas, E.

- Traykov, C. V. Beveren, P. V. den Bergh, P. V. Duppen, K. Wendt, and A. Zadvornaya. *Nat. Commun.* 8.1 (2017). DOI: [10.1038/ncomms14520](https://doi.org/10.1038/ncomms14520). (Cit. on p. 96).
- [109] G. Dracoulis, B. Fabricius, T. Kibedi, A. Baxter, A. Byrne, K. Lieb, and A. Stuchbery. *Nucl. Phys. A* 534.1 (1991). DOI: [10.1016/0375-9474\(91\)90562-K](https://doi.org/10.1016/0375-9474(91)90562-K). (Cit. on pp. 96 sq.).
- [110] C. R. Bingham, M. B. Kassim, M. Zhang, Y. A. Akovali, K. S. Toth, W. D. Hamilton, H. K. Carter, J. Kormicki, J. von Schwarzenberg, and M. M. Jarrio. *Phys. Rev. C* 51 (1995). DOI: [10.1103/PhysRevC.51.125](https://doi.org/10.1103/PhysRevC.51.125). (Cit. on p. 97).
- [111] T. Kibédi, G. Dracoulis, B. Fabricius, A. Byrne, and A. Stuchbery. *Nucl. Phys. A* 539.1 (1992). DOI: [10.1016/0375-9474\(92\)90239-G](https://doi.org/10.1016/0375-9474(92)90239-G). (Cit. on p. 97).
- [112] R. A. Bark, S. W. Ødegård, R. Bengtsson, I. G. Bearden, G. B. Hagemann, B. Herskind, F. Ingebretsen, S. Leoni, H. Ryde, T. Shizuma, K. Strähle, P. O. Tjøm, and J. Wrzesinski. *Phys. Rev. C* 52 (1995). DOI: [10.1103/PhysRevC.52.R450](https://doi.org/10.1103/PhysRevC.52.R450). (Cit. on p. 97).
- [113] T. Kohno, M. Adachi, S. Fukuda, M. Taya, M. Fukuda, H. Taketani, Y. Gono, M. Sugawara, and Y. Ishikawa. *Phys. Rev. C* 33 (1986). DOI: [10.1103/PhysRevC.33.392](https://doi.org/10.1103/PhysRevC.33.392). (Cit. on p. 98).
- [114] B. G. Ritchie, F. T. Avignone, H. K. Carter, R. L. Mlekodaj, and E. H. Spejewski. *Phys. Rev. C* 23 (1981). DOI: [10.1103/PhysRevC.23.1717](https://doi.org/10.1103/PhysRevC.23.1717). (Cit. on p. 102).

# INCLUDED ARTICLE

## I

### In-beam $\gamma$ -ray spectroscopy of $^{211,213}\text{Ac}$ and $^{211}\text{Ra}$

by

J. Louko, K. Auranen, J. Uusitalo, A. D. Briscoe, T. Grahn, P. T. Greenlees, A. Illana, H. Joukainen, R. Julin, H. Jutila, M. Leino, M. Luoma, J. Ojala, J. Pakarinen, A. Raggio, P. Rahkila, J. Romero, P. Ruotsalainen, M. Sandzelius, J. Sarén, A. Tolosa-Delgado and G. Zimba









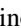









Physical Review C 110 (2024)

Reprinted with kind permission of American Physical Society.  
©2024 American Physical Society.





In-beam  $\gamma$ -ray spectroscopy of  $^{211,213}\text{Ac}$  and  $^{211}\text{Ra}$ 

J. Louko <sup>1,\*</sup>, K. Auranen <sup>1</sup>, J. Uusitalo <sup>1</sup>, A. D. Briscoe <sup>1,†</sup>, T. Grahn <sup>1</sup>, P. T. Greenlees <sup>1</sup>, A. Illana <sup>1,‡</sup>, H. Joukainen <sup>1</sup>,  
R. Julin <sup>1</sup>, H. Jutila <sup>1</sup>, M. Leino <sup>1</sup>, M. Luoma <sup>1</sup>, J. Ojala <sup>1</sup>, J. Pakarinen <sup>1</sup>, A. Raggio <sup>1</sup>, P. Rahkila <sup>1</sup>,  
J. Romero <sup>1,2</sup>, P. Ruotsalainen <sup>1</sup>, M. Sandzelius <sup>1</sup>, J. Sarén <sup>1</sup>, A. Tolosa-Delgado <sup>1,§</sup> and G. Zimba <sup>1,||</sup>

<sup>1</sup>Accelerator Laboratory, Department of Physics, University of Jyväskylä, FI-40014 Jyväskylä, Finland

<sup>2</sup>University of Liverpool, Department of Physics, Oliver Lodge Laboratory, Liverpool L69 7ZE, United Kingdom



(Received 10 May 2024; accepted 28 August 2024; published 11 September 2024)

The first in-beam  $\gamma$ -ray spectroscopic study of the neutron-deficient actinium isotopes  $^{211,213}\text{Ac}$  has been carried out at the Accelerator Laboratory of the University of Jyväskylä using a highly selective recoil-decay tagging method with the JUROGAM 3 germanium-detector array and MARA separator. The nuclei of interest were produced using the  $^{175}\text{Lu}(^{40}\text{Ar}, 4n)^{211}\text{Ac}$  and  $^{180}\text{Hf}(^{37}\text{Cl}, 4n)^{213}\text{Ac}$  fusion-evaporation reactions. Excited states in  $^{211}\text{Ac}$  were observed for the first time. In  $^{211}\text{Ac}$  and  $^{213}\text{Ac}$  low-lying core-excited states whose excitation energies follow the systematic trends of their respective core states in even-even isotones  $^{210}\text{Ra}$  and  $^{212}\text{Ra}$  were identified. Additionally, we were able to extend the level scheme of  $^{211}\text{Ra}$ , which was also produced in the  $^{40}\text{Ar} + ^{175}\text{Lu}$  reaction. We also remeasured the half-lives of the ground states of these nuclei and also that of the ( $^{13}/_2^+$ ) isomeric state of  $^{211}\text{Ra}$ .

DOI: [10.1103/PhysRevC.110.034311](https://doi.org/10.1103/PhysRevC.110.034311)

## I. INTRODUCTION

Extensive research of nuclear structure and shape evolution [1] in the  $N < 126$ , translead region has been ongoing for several decades at the Accelerator Laboratory of the University of Jyväskylä (JYFL-ACCLAB) and other laboratories. Early studies utilized, for example,  $\alpha$ -decay spectroscopy, later extended by in-beam techniques. In the  $\alpha$ -decay process, states with similar initial and final state structures are favored, which can indirectly provide information about the deformation of the initial state if the final state structure is known and vice versa [2]. Experiments employing in-gas laser ionization and spectroscopy techniques [3] have also confirmed results from the decay studies by measuring ground-state charge distributions and observed enlarged radii when the ground state becomes deformed.

In-beam  $\gamma$ -ray spectroscopy can be used to probe the developing shape change of nuclei before it is seen for the ground state. The information is gained by studying a range of nuclei and their level-energy systematics. In-beam  $\gamma$ -ray spectroscopy can also reveal shape coexistence of excited states by observing rotational bands based on different shapes [4].

Measurements of excited states provide a good benchmark for nuclear theories and give valuable input for further developments. In general, the shape evolution predicted by current mean-field models [5,6] in the region of interest of the present work is reproduced quite well. Once leaving the spherical  $N = 126$  shell closure towards the proton drip line a shape change towards weak oblate deformation is predicted, and closer to the  $N = 104$  neutron midshell a strong prolate deformation takes over. However, experimental confirmation becomes more challenging due to the decreasing production cross sections and short lifetimes when approaching the proton drip line.

Due to the experimental challenges, not much is known about the structure of odd-even actinium ( $Z = 89$ ) isotopes in this region. Besides  $\alpha$ -decay studies [7–11], only one in-gas laser spectroscopic study has been carried out [12]. No  $\gamma$ -ray transitions were known in  $^{211}\text{Ac}$  and just five transitions were tentatively placed to the level scheme of  $^{213}\text{Ac}$  in Ref. [9]. In the isotope  $^{211}\text{Ra}$ , six  $\gamma$ -ray transitions were known [13–15], all of which reside below the ( $^{13}/_2^+$ ) isomeric state. The main motivation of this work was to continue studying this not yet so well-known area of the nuclear chart, and especially investigate low-lying excited states of actinium and radium isotopes and their level-energy systematics.

## II. EXPERIMENTAL DETAILS

The nuclei of interest were produced using two different fusion-evaporation reactions,  $^{40}\text{Ar} + ^{175}\text{Lu}$  and  $^{37}\text{Cl} + ^{180}\text{Hf}$ . Experimental production cross section for  $^{211}\text{Ac}$  and  $^{213}\text{Ac}$  were in the order of  $50\ \mu\text{b}$  with beam energies of 182 and 170 MeV, respectively. While these were independent measurements, it later proved to be advantageous to do

\*Contact author: [jussi.i.louko@jyu.fi](mailto:jussi.i.louko@jyu.fi)

<sup>†</sup>Present address: University of Liverpool, Department of Physics, Oliver Lodge Laboratory, Liverpool L69 7ZE, United Kingdom.

<sup>‡</sup>Present address: Grupo de Física Nuclear and IPARCOS, Universidad Complutense de Madrid, CEI Moncloa, E-28040 Madrid, Spain.

<sup>§</sup>Present address: European Organization for Nuclear Research (CERN), Geneva, Switzerland.

<sup>||</sup>Present address: Facility for Rare Isotope Beams, Michigan State University, 640 South Shaw Lane, East Lansing, MI 48824, USA.

TABLE I. Beam and target summary.

Beam	$E_{\text{beam}}^{\text{lab}}$ (MeV)	$I_{\text{beam}}$ (pnA)	Target	$d_{\text{target}}$ ( $\mu\text{g}/\text{cm}^2$ )	Duration (h)
$^{40}\text{Ar}^{8+}$	182	14	$^{175}\text{Lu}^{\text{a}}$	930	55
$^{40}\text{Ar}^{8+}$	186	15	$^{175}\text{Lu}^{\text{a}}$	320	2
$^{40}\text{Ar}^{8+}$	182	20	$^{175}\text{Lu}^{\text{a}}$	320	44
$^{40}\text{Ar}^{8+}$	182	19	$^{175}\text{Lu}^{\text{a}}$	460	66
$^{37}\text{Cl}^{7+}$	170	10	$^{180}\text{Hf}^{\text{b}}$	180 <sup>c</sup>	126
$^{37}\text{Cl}^{7+}$	170	12	$^{\text{nat}}\text{Hf}^{\text{b}}$	500	16

<sup>a</sup>47  $\mu\text{g}/\text{cm}^2$  carbon charge reset foil downstream from the target.

<sup>b</sup>21  $\mu\text{g}/\text{cm}^2$  carbon charge reset foil downstream from the target.

<sup>c</sup>Estimation, based on an  $\alpha$ -particle energy-loss measurement.

cross-checking between these data sets to solve some ambiguities regarding the presence of neighboring isotopes. For more details regarding the beam and target combinations used, see Table I.

The beams were provided by the electron-cyclotron resonance ion source and the K130 cyclotron of JYFL-ACCLAB. The JUROGAM 3 germanium-detector array [16] was deployed for the detection of prompt  $\gamma$  rays at the target position. Stacked tin and copper absorbers of thicknesses 0.25 mm and 0.5 mm, respectively, were placed in front of the germanium detectors to decrease the x-ray yield. Reaction products of interest were separated from the unreacted primary beam and other unwanted particles using the MARA vacuum-mode mass separator [17,18], and they were subsequently identified at the focal plane using the highly selective recoil-decay tagging (RDT) method [19,20].

The MARA focal plane consisted of a multiwire proportional counter (MWPC) with 0.9- $\mu\text{m}$  thick mylar foil windows, a 300- $\mu\text{m}$  thick double-sided silicon-strip detector (DSSD), and 1-mm thick punch-through veto detectors. Three broad-energy germanium detectors, surrounding the focal-plane chamber, were used to detect  $\gamma$  rays after the de-excitation of directly populated long-lived isomeric states or after decays to excited states.

This instrumentation, combined with the triggerless total data readout data-acquisition system [21], makes it possible to

apply different gating conditions and use various correlation techniques during the offline analysis. For further details of typical setups and the other techniques used with MARA, see Ref. [22] and references therein.

### III. RESULTS

During the analysis, an event is constructed around the DSSD data. If the given  $X$  and  $Y$  strip signals have a similar amplitude and time, an event is assigned to that quasipixel. This event can then have multiple attributes. For example, it can be classified as a fusion-recoil event based on its implantation energy and time of flight between the DSSD and the MWPC. Alternatively, it can be classified as a decay event, if its energy is in a suitable range and signals were not detected in the MWPC nor in the punch-through detectors. Otherwise, it is considered as another type of beam related event such as a scattered target- or beam-like particle or a lighter punch-through particle of unspecified origin and it can be ignored for the purpose of tagging correlations.

If there are subsequent recoil and decay events in the same DSSD pixel, they can be plotted in a tagging plot, as shown in Fig. 1. Once an event is tagged in this manner, temporal correlations can be made to prompt  $\gamma$ -ray events seen by the germanium detectors at the target position. After the transitions belonging to the nucleus of interest were identified, a

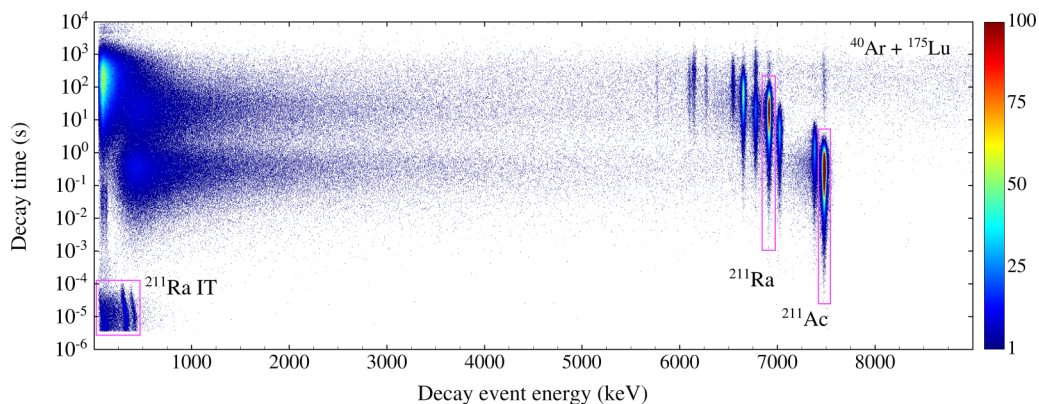


FIG. 1. Decay time as a function of the decay energy for the decay events following a recoil-implantation event in the same pixel of the DSSD. Three example gates are shown in pink, one for the internal conversion electrons from the  $^{211}\text{Ra}$  isomeric 395 keV  $M2$  transition (IT) and two for the  $\alpha$  decays as indicated.

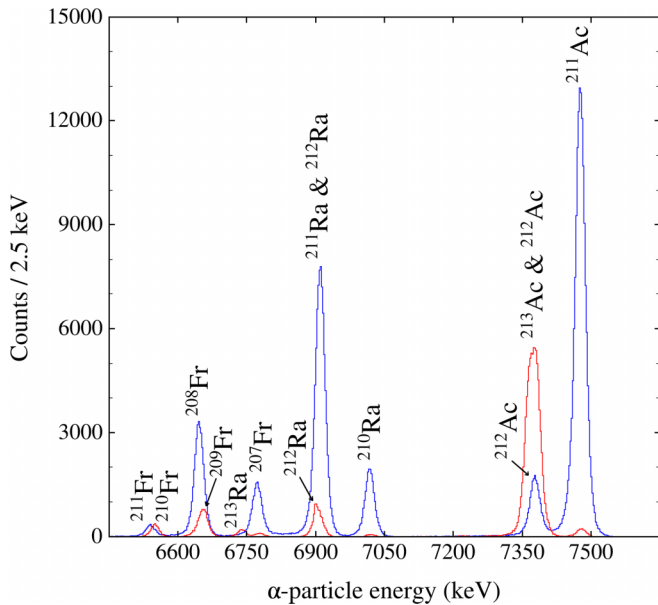


FIG. 2. Recoil-decay correlated  $\alpha$ -particle energy spectra from reactions  $^{40}\text{Ar} + ^{175}\text{Lu}$  (blue) and  $^{37}\text{Cl} + ^{180}\text{Hf}$  (red).

level scheme could be constructed based on transition intensities, energy sums, and  $\gamma$ - $\gamma$  coincidences.

### A. Isotope $^{213}\text{Ac}$

When studying the nucleus  $^{213}\text{Ac}$ , the main contaminant was its neighbor,  $^{212}\text{Ac}$ , produced in the  $5n$  channel. The  $\alpha$ -particle energy and half-life of these two nuclei are very similar, and even the decay properties of daughter nuclei are similar. However, the previously unknown transitions of  $^{212}\text{Ac}$  were reliably identified through a cross-bombardment in the reaction  $^{40}\text{Ar} + ^{175}\text{Lu}$ . Energy spectra of  $\alpha$  particles from these two reactions are shown in Fig. 2. The relative shifts in the yields of the products are apparent. The clean  $^{212}\text{Ac}$   $\alpha$ -peak allowed us to distinguish the transitions belonging to it and  $^{213}\text{Ac}$ , see blue histogram in Fig. 2. Origin of the transitions were also confirmed by separately setting gates on either side of the doublet  $\alpha$  peak in the reaction  $^{37}\text{Cl} + ^{180}\text{Hf}$ . The lower energy side of the  $\alpha$  peak enhanced the transitions of  $^{213}\text{Ac}$ , while the higher energy side enhanced the transitions belonging to  $^{212}\text{Ac}$ , which is consistent with the reported  $\alpha$ -particle energies of  $^{213}\text{Ac}$  and  $^{212}\text{Ac}$  in the literature, 7360(6) keV and 7379(8) keV, respectively [23,24].

Two  $\gamma$ - $\gamma$  coincidence spectra are shown in Fig. 3. The coincidence  $\gamma$ -ray energy spectrum with the gate set on the 613-keV ground-state transition in Fig. 3(a) shows all three other strong peaks present in the singles spectrum in Fig. 4(a) and additionally the peak at 1116 keV is also present. The 450-keV transition is also in coincidence with the 446-keV transition as seen in Fig. 3(b). In fact, the 613-keV, 821-keV, 450-keV, and 446-keV transitions are mutually coincident, suggesting their placement in one cascade.

The 613-keV, 821-keV, 450-keV transitions were also observed in the  $\alpha$ -decay study of  $^{217}\text{Pa}$  [9]. However, we were able to establish their correct sequence based on the in-beam  $\gamma$ -ray intensities. Spins and parities for 467-keV and 634-keV

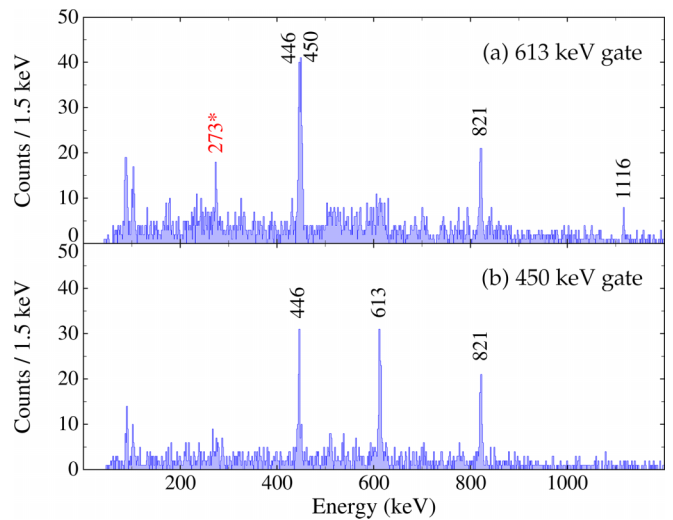


FIG. 3.  $^{213}\text{Ac}$   $\alpha$ -decay tagged prompt coincidence  $\gamma$ -ray energy spectra gated on the (a) 613-keV and (b) 450-keV  $\gamma$ -ray transitions. The 273-keV transition marked in red (\*) is from the contaminant  $^{212}\text{Ac}$ .

states seen in the aforementioned  $\alpha$ -decay study are suggested on the basis of the hindrance-factor systematics presented in Ref. [25]. The constructed level scheme is shown in Fig. 5. Not all transitions could be confidently placed on it. A list of all observed transitions and their relative intensities can be found in Table II. Spin and parity assignments and suggested configurations for selected states are discussed in Sec. IV.

The half-life of  $^{213}\text{Ac}$  was determined from the 446-450-821-613-keV  $\gamma$ -gated recoil- $\alpha$  correlations, using the logarithmic time-scale method, described in Ref. [26]. The obtained result was 771(14) ms, which is in an agreement the reported literature value of 738(16) ms [27].

### B. Isotope $^{212}\text{Ac}$

Several transitions belonging to the isotope  $^{212}\text{Ac}$  could be clearly seen with both reactions. The shell-model calculations in Ref. [3], suggest that the ground state should have a spin and parity of  $7^+$ , above which  $6^+$  and  $5^+$  states lie at around 200 keV of excitation energy. We observed several suitable transitions in this energy range, as is seen in the recoil- $\alpha$  gated  $\gamma$ -ray energy spectrum in Fig. 4(b). However, limited data did not allow for construction of the level scheme. A summary of the observed transitions and their prompt coincidences is presented in Table II. The half-life of  $^{212}\text{Ac}$  was determined from the recoil- $\alpha$  correlations of the non- $^{213}\text{Ac}$  contaminated  $^{40}\text{Ar} + ^{175}\text{Lu}$  dataset, using the logarithmic time-scale method [26]. The obtained result was 881(15) ms, which is in a good agreement with the half-life of 880(35) ms reported in Ref. [28].

### C. Isotope $^{211}\text{Ac}$

Identification of the transitions belonging to the  $^{211}\text{Ac}$  nucleus was more straightforward as no strong overlapping activities were present. A recoil- $\alpha$  gated  $\gamma$ -ray energy spectrum is shown in Fig. 4(c).

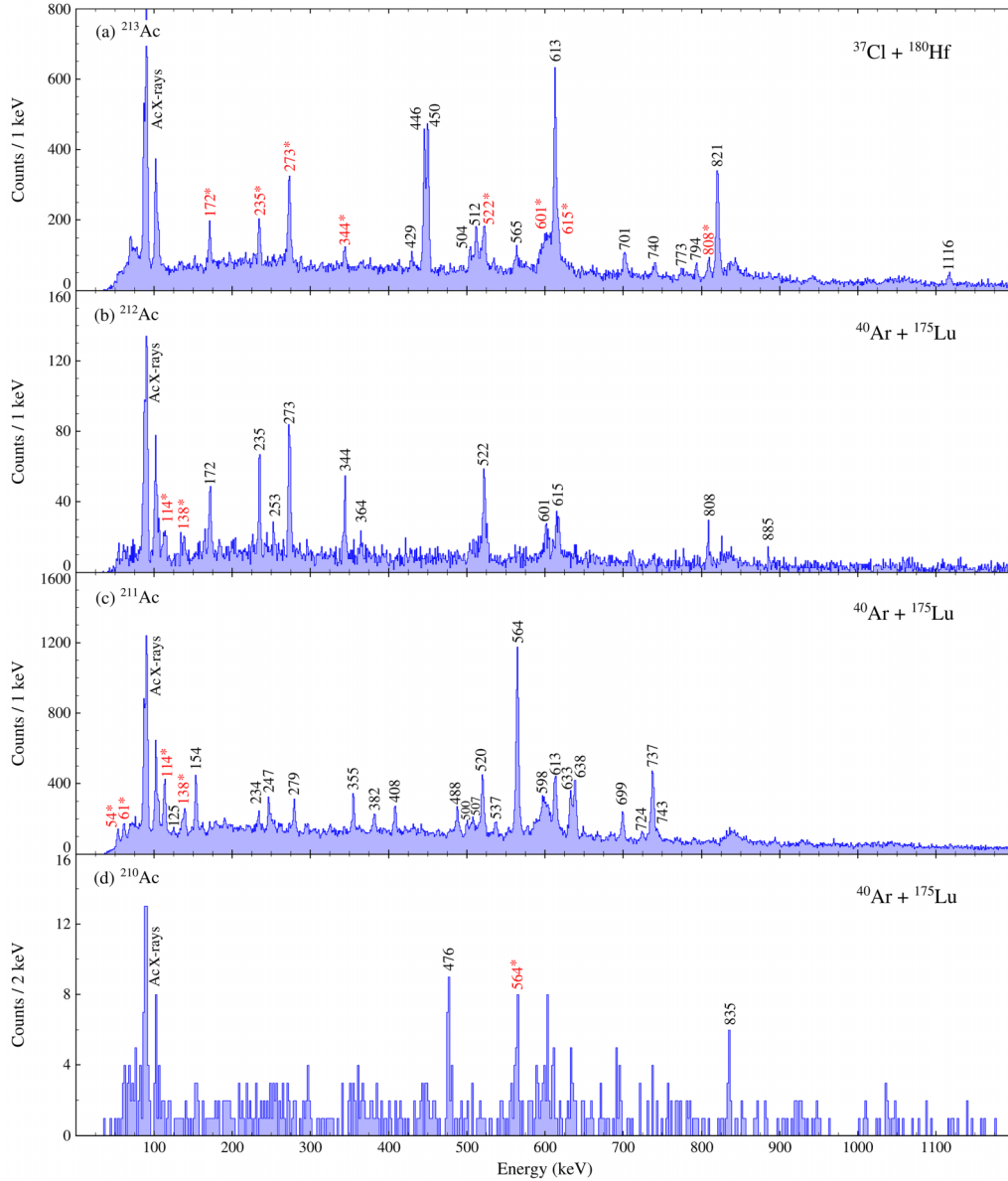


FIG. 4. (a) Recoil- $\alpha$  gated prompt  $\gamma$ -ray energy spectrum for  $^{213}\text{Ac}$ . Transitions marked in red (\*) belong to the contaminant of  $^{212}\text{Ac}$ , as can be clearly seen by comparing it to the spectrum, shown in (b). (b) Recoil- $\alpha$  gated prompt  $\gamma$ -ray energy spectrum for  $^{212}\text{Ac}$ . Transitions marked in red (\*), originate from the target ( $^{175}\text{Lu}$ ) due to beam induced Coulomb excitations. (c) Recoil- $\alpha$  gated prompt  $\gamma$ -ray energy spectrum for  $^{211}\text{Ac}$ . Transitions marked in red (\*) originate from Coulomb excitations of the  $^{175}\text{Lu}$  target. (d) Prompt  $\gamma$ -ray energy spectrum for  $^{210}\text{Ac}$ , which was obtained by applying a tight recoil- $\alpha$ - $\alpha$  gate, favoring the decay properties of  $^{210}\text{Ac}$ . A contaminant line from  $^{211}\text{Ac}$  is marked in red (\*).

Selected  $\gamma$ -ray coincidence spectra are shown in Fig. 6. The spectrum in Fig. 6(a) shows the transitions placed above the proposed 564-keV ground state transition. Notably, the 488-613-keV cascade is missing and the 537-keV transition is present. Based on the energy sums and systematics, the 488-613-keV cascade is then assigned to feed the ground state in parallel with the 564-keV transition in a similar manner as in the neighboring odd-even isotone  $^{209}\text{Fr}$  [29]. The 633-keV and 743-keV transitions seen in the spectra of Figs. 6(a) and 6(c) are placed to form an alternative decay path from the 1940 keV state to the 564 keV state. The 638-keV gated spectrum in Fig. 6(b) shows the main band

and the transition is also in a prompt coincidence with the 154-keV transition. However, in the 279-keV gated spectrum Fig. 6(c), the 154-keV transition is not present, suggesting its placement in parallel with the 279-keV transition. This placement is also supported by the observed 125-keV transition, in coincidence with the 154-keV transition, which completes the energy sum. Based on the energy sums and systematics as well as  $\gamma$ - $\gamma$  coincidences and intensities, we were able to place 11 out of 22 transitions into the level scheme, shown in Fig. 7, and give tentative spin and parity assignments as well as configurations for the states. List of all observed transitions and their properties are given in Table II.

TABLE II. Properties of the transitions assigned to  $^{210-213}\text{Ac}$  and  $^{211}\text{Ra}$ . Relative  $\gamma$ -ray transition intensities ( $I_{\gamma}^{\text{rel.}}$ ) are measured from the recoil- $\alpha$ -gated  $\gamma$ -ray singles spectra and corrected by the efficiency obtained using  $^{152}\text{Eu} + ^{133}\text{Ba}$  mixed source. Spin and parity of the initial ( $I_i^{\pi}$ ) and final states ( $I_f^{\pi}$ ) and multipolarities ( $\sigma L$ ) are to be considered as tentative. For  $^{212}\text{Ac}$ , prompt  $\gamma$ - $\gamma$  coincidences are given. Reported errors are nominal  $1\sigma$  interval and they include statistical uncertainties of the fittings as well as estimated experimental uncertainties associated with the Doppler correction and background.

Nucleus	$E_{\gamma}$ (keV)	$I_{\gamma}^{\text{rel.}}$ (%)	$I_i^{\pi}$	$I_f^{\pi}$	$\sigma L$
$^{213}\text{Ac}$	429.4(7)	8(1)			
	445.9(5)	60(5)	(23/2 <sup>-</sup> )	(21/2 <sup>-</sup> )	(M1 + E2)
	450.3(5)	74(5)	(21/2 <sup>-</sup> )	(17/2 <sup>-</sup> )	(E2)
	466.5(2) <sup>a</sup>		(7/2 <sup>-</sup> )	9/2 <sup>-</sup>	(M1 + E2)
	504.2(6)	17(2)			
	512.1(6) <sup>b</sup>	33(3)			
	565.3(8) <sup>b</sup>	16(3)			
	612.5(6)	100(8)	(13/2 <sup>-</sup> )	9/2 <sup>-</sup>	(E2)
	634.3(1) <sup>a</sup>		(11/2 <sup>-</sup> )	9/2 <sup>-</sup>	(M1 + E2)
	701.2(7) <sup>b</sup>	19(3)			
	740.4(9) <sup>b</sup>	12(3)			
	773.4(6) <sup>b</sup>	7(2)			
	793.7(6) <sup>b</sup>	14(2)			
	820.5(6)	80(8)	(17/2 <sup>-</sup> )	(13/2 <sup>-</sup> )	(E2)
	1115.7(6)	13(2)		(13/2 <sup>-</sup> )	
Prompt $\gamma$ - $\gamma$ coincidences					
$^{212}\text{Ac}$	171.8(5)	34(6)	235.0, 273.2, 344.0, 364.3, 521.9		
	235.0(4)	47(7)	171.8, 273.2, 344.0, 521.9		
	252.9(5)	10(2)	273.2		
	273.2(5)	100(15)	171.8, 235.0, 252.9, 344.0, 521.9, 884.7		
	344.0(4)	44(7)	171.8, 235.0, 273.2, 521.9		
	364.3(5)	8(2)	171.8, 521.9		
	521.9(4)	84(13)	171.8, 235.0, 273.2, 344.0, 364.3, 808.3		
	601.3(6)	41(6)			
	615.2(5)	51(8)			
	808.3(4)	39(6)	521.9		
	884.7(6)	21(5)	273.2		
$^{211}\text{Ac}$	125.0(6)	5(1)	(23/2 <sup>-</sup> )		
	153.8(6)	14(1)		(21/2 <sup>-</sup> )	
	234.1(7) <sup>b</sup>	5(1)			
	246.9(6) <sup>b</sup>	7(1)			
	279.3(6)	9(1)	(23/2 <sup>-</sup> )	(21/2 <sup>-</sup> )	(M1 + E2)
	355.0(6) <sup>b</sup>	13(1)			
	381.7(6) <sup>b</sup>	8(1)			
	408.2(6) <sup>b</sup>	12(1)			
	487.9(6)	14(1)	(15/2 <sup>-</sup> )	(11/2 <sup>-</sup> )	(E2)
	500.1(6) <sup>b</sup>	4(1)			
	507.1(6) <sup>b</sup>	21(2)			
	520.0(6) <sup>b</sup>	31(1)			
	536.7(6)	9(1)	(15/2 <sup>-</sup> )	(13/2 <sup>-</sup> )	(M1 + E2)
	564.4(6)	100(4)	(13/2 <sup>-</sup> )	9/2 <sup>-</sup>	(E2)
	598.2(6) <sup>b</sup>	11(4)			
	612.8(6)	32(2)	(11/2 <sup>-</sup> )	9/2 <sup>-</sup>	(M1 + E2)
	632.8(6)	33(2)	(17/2 <sup>-</sup> )	(13/2 <sup>-</sup> )	(E2)
	638.2(6)	32(2)	(21/2 <sup>-</sup> )	(17/2 <sup>-</sup> )	(E2)
	698.7(6) <sup>b</sup>	17(1)			
723.9(6) <sup>b</sup>	5(1)				
737.2(6)	58(4)	(17/2 <sup>-</sup> )	(13/2 <sup>-</sup> )	(E2)	
743.1(7)	5(1)	(21/2 <sup>-</sup> )	(17/2 <sup>-</sup> )	(E2)	
$^{210}\text{Ac}$	476.1(6)	100(6)			
	834.6(6)	80(7)			



TABLE II. (Continued.)

Nucleus	$E_\gamma$ (keV)	$I_\gamma^{rel.}$ (%)	$I_1^\pi$	$I_f^\pi$	$\sigma L$
$^{211}\text{Ra}$	146.4(6)	15(1)	(19/2 <sup>-</sup> )	(17/2 <sup>+</sup> )	(E1)
	161.4(6)	7(1)	(15/2 <sup>-</sup> )	(13/2 <sup>-</sup> )	(M1 + E2)
	196.2(7) <sup>b</sup>	9(3)			
	252.5(7) <sup>b</sup>	17(4)			
	263.6(6)	24(2)			
	395.4(2) <sup>c</sup>		(13/2 <sup>+</sup> )	(9/2 <sup>-</sup> )	(M2)
	439.3(6)	48(4)	(15/2 <sup>-</sup> )	(11/2 <sup>-</sup> )	(E2)
	462.5(7) <sup>b</sup>	11(2)			
	514.7(6)	56(4)		(15/2 <sup>-</sup> )	
	526.0(6)	54(6)	(17/2 <sup>+</sup> )	(13/2 <sup>+</sup> )	(E2)
	531.2(6)	69(6)	(7/2 <sup>-</sup> )	5/2 <sup>-</sup>	(M1 + E2)
	601.4(6)	100(8)	(15/2 <sup>-</sup> )	(13/2 <sup>+</sup> )	(E1)
	671.9(6)	16(2)	(21/2 <sup>+</sup> )	(17/2 <sup>+</sup> )	(E2)
	791.1(6)	39(3)		(15/2 <sup>-</sup> )	
	800.3(6) <sup>d</sup>	71(4)	(9/2 <sup>-</sup> )	5/2 <sup>-</sup>	(E2)
	825.8(6)	49(3)	(11/2 <sup>-</sup> )	(7/2 <sup>-</sup> )	(E2)
834.1(6)	22(3)	(13/2 <sup>-</sup> )	(9/2 <sup>-</sup> )	(E2)	
873.7(6) <sup>b</sup>	16(2)				

<sup>a</sup>Energy taken from Ref. [9].

<sup>b</sup>Could not be placed in the level scheme with confidence.

<sup>c</sup>Energy measured at the focal plane.

<sup>d</sup>Energy measured at the focal plane was 801.5(2) keV.

The half-life of  $^{211}\text{Ac}$  was determined again from the recoil- $\alpha$  correlations, using the logarithmic time-scale method [26]. The obtained half-life, 228(4) ms, is in an agreement with the literature value of 210(30) ms [30].

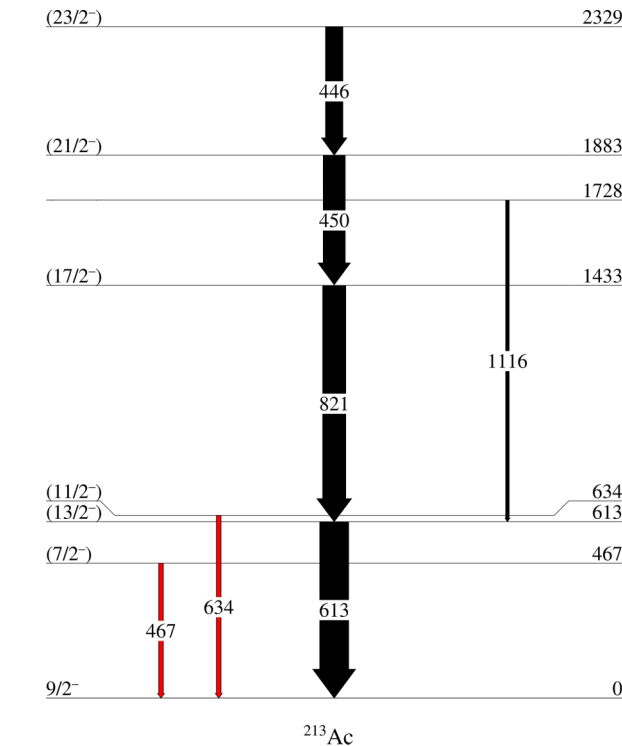


FIG. 5. The proposed level scheme for  $^{213}\text{Ac}$ . Transitions in red are from the  $\alpha$ -decay work of Ref. [9].

#### D. Isotope $^{210}\text{Ac}$

A small concentration of events was observed in the side of the main  $^{211}\text{Ac}$  group of the recoil-gated decay-decay

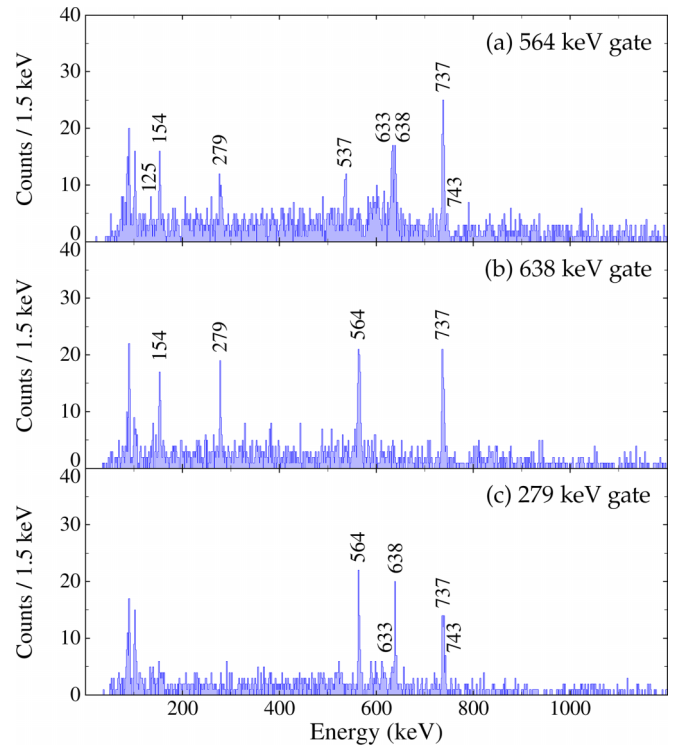


FIG. 6.  $^{211}\text{Ac}$   $\alpha$ -decay tagged prompt coincidence  $\gamma$ -ray energy spectra gated on the (a) 564-keV, (b) 638-keV, and (c) 279-keV  $\gamma$ -ray transitions.

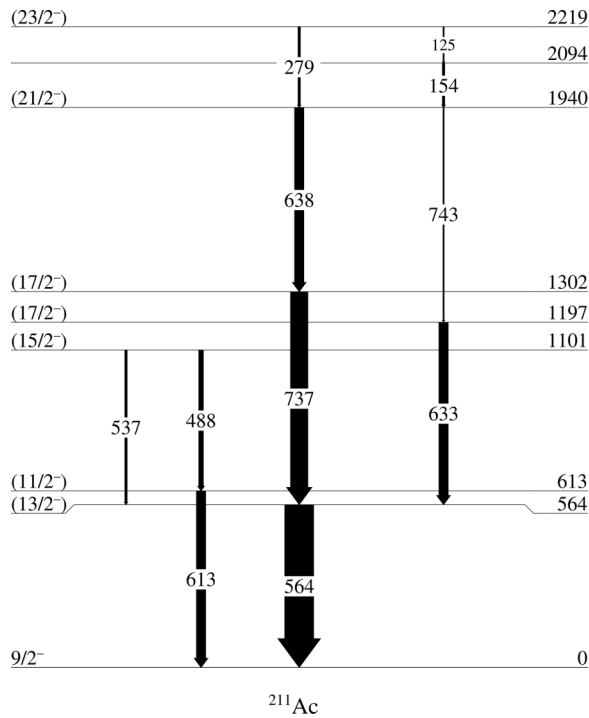


FIG. 7. The proposed level scheme for  $^{211}\text{Ac}$ , as deduced from the present data.

matrix. The  $\alpha$ -particle energies and decay times of this group match the neighboring isotope  $^{210}\text{Ac}$  and its daughter nuclei  $^{206}\text{Fr}$ . The application of a stringent recoil- $\alpha$ - $\alpha$  gate to this group brought up the prompt  $\gamma$ -ray energy spectrum shown in Fig. 4(d). Two candidate transitions at energies of 476 keV and 835 keV are clearly distinguished from the  $^{211}\text{Ac}$  residual background, and those were then assigned to  $^{210}\text{Ac}$ . Properties of these transitions are listed in Table II.

### E. Isotope $^{211}\text{Ra}$

A byproduct of the reaction  $^{40}\text{Ar} + ^{175}\text{Lu}$  was the isotope  $^{211}\text{Ra}$ , which was produced through the  $1p3n$  channel. The 395-keV and 800-keV transitions depopulating the  $(^{13/2}^+)$  isomeric state were known prior to this study [15], but we were now able to expand the level scheme considerably. The half-life of the  $(^{13/2}^+)$  isomeric state was long enough to be observed at the focal plane. Separate recoil-decay tagging could be made either with the  $\alpha$  decays, or with the internal-conversion electrons originating from the 395-keV  $M2$  transition that depopulates the isomeric state, see Fig. 8. A delayed  $\gamma$ -ray energy spectrum measured within 50  $\mu\text{s}$  after  $^{211}\text{Ra}$  recoil implantation at the focal-plane Ge array is shown in the inset of Fig. 8. The spectrum shows the 395-keV  $M2$  transition, 801.5(2)-keV transition [same as the 800.3(6)-keV transition at target position], and x rays from the internal conversion of the 395-keV  $M2$  transition. The efficiency corrected intensity ratio of these two transitions agrees well with that reported in Ref. [13].

The internal-conversion electron gated spectrum (red in Fig. 8) clearly shows the transitions at 146, 264, 515, 526, 601, 672, and 791 keV, therefore, they must lie above the isomeric state. Furthermore, the transitions at 439, 531, 800, 826, and 834 keV are completely missing from this spectrum.

These two prompt spectra in Fig. 8, along with the prompt  $\gamma$ - $\gamma$  coincidences of 826-keV and 834-keV [Figs. 9(a) and 9(b)], and transition energy sums, suggest that there are two decay paths bypassing the  $(^{13/2}^+)$  isomeric state. One via the 834-keV transition and the other via the 439-826-531-keV cascade. It is worth of mentioning that the  $\alpha$ -decay properties of  $^{211}\text{Ra}$  are very similar to those of  $^{212}\text{Ra}$ , and the energies of the presently observed 439 and 826-keV transitions are close to those of the  $6^+ \rightarrow 4^+$  and  $4^+ \rightarrow 2^+$  transitions in  $^{212}\text{Ra}$ , respectively. However, contamination from  $^{212}\text{Ra}$  is low as indicated by the nonobservation of the  $^{212}\text{Ra}$   $2^+ \rightarrow 0^+$

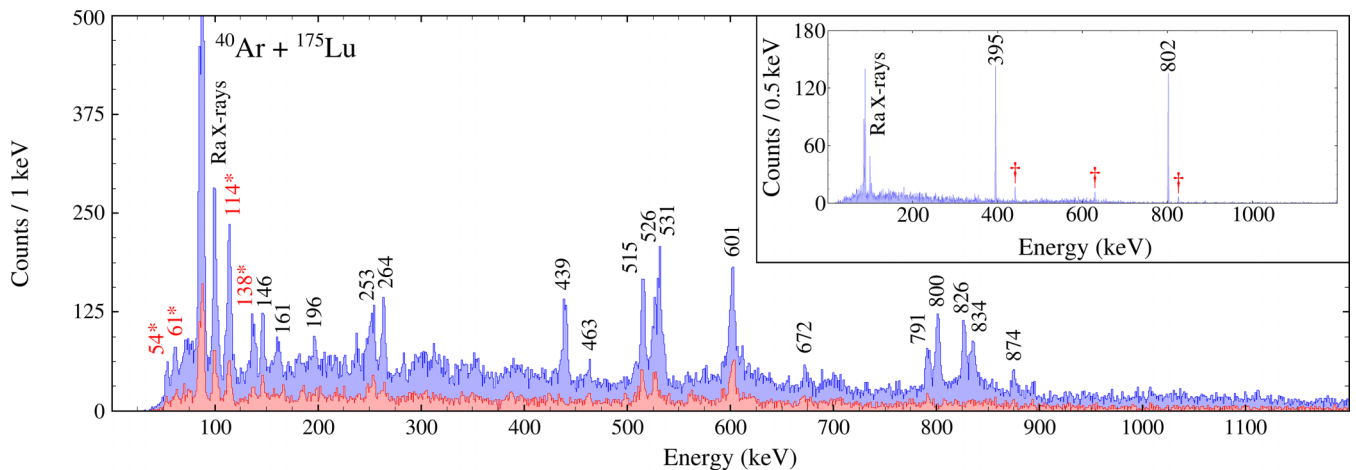


FIG. 8. Two different  $\gamma$ -ray energy spectra for  $^{211}\text{Ra}$  from the present study. The blue spectrum was obtained with the gate set on  $^{211}\text{Ra}$   $\alpha$  decays, as shown in Fig. 1. The red spectrum was obtained with the gate on the internal conversion electrons, as shown in the bottom left corner in Fig. 1, separating transitions feeding the isomeric  $(^{13/2}^+)$  state. The inset shows the  $\alpha$ -decay gated delayed transitions of  $^{211}\text{Ra}$  observed in the focal-plane Ge-array. Transitions marked in red (\*) originate from coulomb excitations of the  $^{175}\text{Lu}$  target in the main panel and red (†) in the inset mark transitions of  $^{212}\text{Ra}$ .

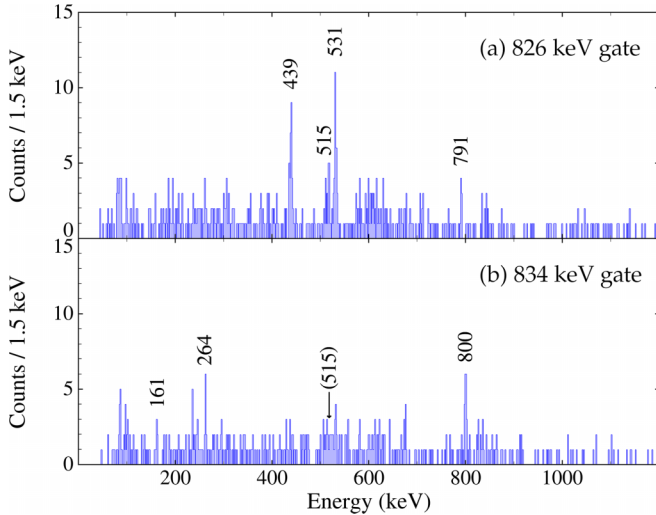


FIG. 9.  $^{211}\text{Ra}$   $\alpha$ -decay tagged prompt coincidence  $\gamma$ -ray energy spectra gated on the (a) 826-keV and (b) 834-keV  $\gamma$ -ray transitions.

transition at the energy of 629 keV in the  $\alpha$ -decay tagged prompt  $\gamma$ -ray energy spectrum shown in blue in Fig. 8. The proposed level scheme for  $^{211}\text{Ra}$  is presented in Fig. 10, and a summary of the observed transitions can be found in Table II.

The half-life of the ground state of  $^{211}\text{Ra}$  was determined from the recoil- $\alpha$  correlations, using the logarithmic

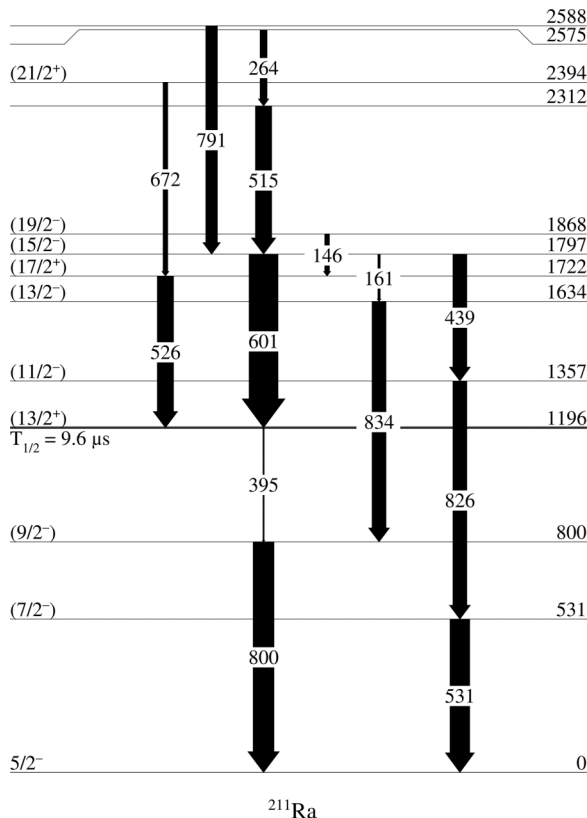


FIG. 10. Proposed level scheme for  $^{211}\text{Ra}$ . Intensity of the delayed 395-keV transition is not to scale.

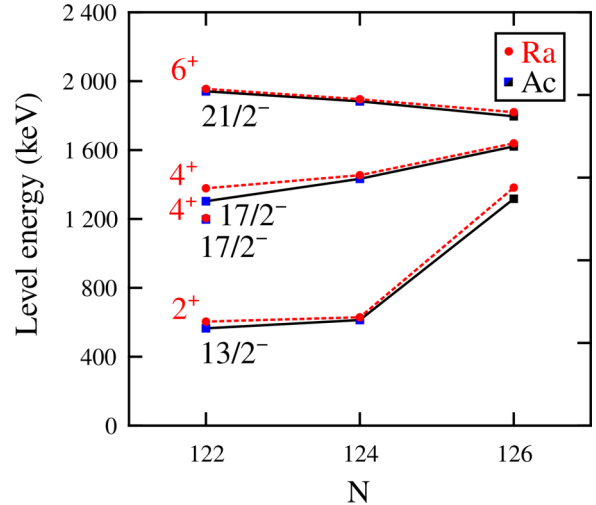


FIG. 11. Level-energy systematics of selected negative-parity states in odd-mass actinium isotopes, compared to positive-parity states in even-even radium isotopes (circles). The blue squares are from the present study, other points are taken from Refs. [36–39].

time-scale method [26]. The obtained result was 13.7(2) s, which is in a good agreement with the literature value of 13(2) s [30]. Additionally, the internal conversion electron correlations were used to obtain a half-life of 9.6(2)  $\mu\text{s}$  for the ( $^{13/2^+}$ ) isomeric state by applying the semilogarithmic scale linear least-square fit method. This is also in a good agreement with the two latest values of 9.7(6)  $\mu\text{s}$  reported in Ref. [15] and 9.4(5)  $\mu\text{s}$  reported in Ref. [31].

#### IV. DISCUSSION

In nearby odd- $A$  astatine and francium isotopes it has been observed that the low-lying negative parity yrast states follow the systematics of their respective even-even isotones, see, for example Refs. [32–35] and references therein. This phenomenon can be interpreted as the nucleus having an even-even core and a weakly coupled “spectator” nucleon. The resulting energies of the yrast states are almost the same as those in the core nucleus, but the angular momentum of the odd nucleon is added.

Similarly, the level energies of the ( $^{13/2^-}$ ), ( $^{17/2^-}$ ), and ( $^{21/2^-}$ ) yrast states in odd-even  $^{213}\text{Ac}$  and  $^{211}\text{Ac}$  follow the energies of the  $2^+$ ,  $4^+$ , and  $6^+$  states of their even-even radium core as illustrated in Fig. 11. The energies of these radium equivalent states in the actinium isotopes are a bit lower, but no sudden changes that could indicate a shape or configuration change were observed as expected. The majority of the states in the  $^{213}\text{Ac}$  and  $^{211}\text{Ac}$  are therefore interpreted arising from the weak coupling of the odd  $h_{9/2}$  quasiproton to the associated even-even core states. Spins and parities for the other states are suggested based on the systematics of the lighter odd-even isotones.

In Table III, suggested dominant configurations of the observed states are given. They are based on similarities with the francium isotones and assignments in Refs. [29,40]. While the ( $^{21/2^-}$ ) states in  $^{213}\text{Ac}$  and  $^{211}\text{Ac}$  still represent a coupling

TABLE III. Configurations proposed to  $^{213,211}\text{Ac}$  and  $^{211}\text{Ra}$ .

Nucleus	$E_{\text{level}}$ (keV)	$I^\pi$	Configuration
$^{213}\text{Ac}$	0	$9/2^-$	$\pi(h_{9/2}) \otimes  ^{212}\text{Ra}; 0^+\rangle$
	467	$(7/2^-)$	$\pi(f_{7/2}) \otimes  ^{212}\text{Ra}; 0^+\rangle$ or $\pi(h_{9/2}) \otimes  ^{212}\text{Ra}; 2^+\rangle$
	613	$(13/2^-)$	$\pi(h_{9/2}) \otimes  ^{212}\text{Ra}; 2^+\rangle$
	634	$(11/2^-)$	$\pi(h_{9/2}) \otimes  ^{212}\text{Ra}; 2^+\rangle$
	1433	$(17/2^-)$	$\pi(h_{9/2}) \otimes  ^{212}\text{Ra}; 4^+\rangle$
	1883	$(21/2^-)$	$\pi(h_{9/2}) \otimes  ^{212}\text{Ra}; 6^+\rangle$
	2329	$(23/2^-)$	$\pi(h_{9/2}^2 f_{7/2})$
$^{211}\text{Ac}$	0	$9/2^-$	$\pi(h_{9/2}) \otimes  ^{210}\text{Ra}; 0^+\rangle$
	564	$(13/2^-)$	$\pi(h_{9/2}) \otimes  ^{210}\text{Ra}; 2^+\rangle$
	613	$(11/2^-)$	$\pi(h_{9/2}) \otimes  ^{210}\text{Ra}; 2^+\rangle$
	1101	$(15/2^-)$	$\pi(h_{9/2}) \otimes  ^{210}\text{Ra}; 4_1^+\rangle$
	1197	$(17/2^-)$	$\pi(h_{9/2}) \otimes  ^{210}\text{Ra}; 4_1^+\rangle$
	1302	$(17/2^-)$	$\pi(h_{9/2}) \otimes  ^{210}\text{Ra}; 4_2^+\rangle$
	1940	$(21/2^-)$	$\pi(h_{9/2}) \otimes  ^{210}\text{Ra}; 6^+\rangle$
	2219	$(23/2^-)$	$\pi(h_{9/2}^2 f_{7/2})$
$^{211}\text{Ra}$	0	$5/2^-$	$\nu(f_{5/2}^{-1}) \otimes  ^{212}\text{Ra}; 0^+\rangle$
	531	$(7/2^-)$	$\nu(f_{5/2}^{-1}) \otimes  ^{212}\text{Ra}; 2^+\rangle$
	800	$(9/2^-)$	$\nu(f_{5/2}^{-1}) \otimes  ^{212}\text{Ra}; 2^+\rangle$
	1196	$(13/2^+)$	$\nu(i_{13/2}^{-1}) \otimes  ^{212}\text{Ra}; 0^+\rangle$
	1357	$(11/2^-)$	$\nu(f_{5/2}^{-1}) \otimes  ^{212}\text{Ra}; 4^+\rangle$
	1634	$(13/2^-)$	$\nu(f_{5/2}^{-1}) \otimes  ^{212}\text{Ra}; 4^+\rangle$
	1722	$(17/2^+)$	$\nu(i_{13/2}^{-1}) \otimes  ^{212}\text{Ra}; 2^+\rangle$
	1797	$(15/2^-)$	$\nu(f_{5/2}^{-1}) \otimes  ^{212}\text{Ra}; 6^+\rangle$
	1868	$(19/2^-)$	$\nu(f_{5/2}^{-1}) \otimes  ^{212}\text{Ra}; 8^+\rangle$
	2394	$(21/2^+)$	$\nu(i_{13/2}^{-1}) \otimes  ^{212}\text{Ra}; 4^+\rangle$

of the  $h_{9/2}$  quasiproton to the rather pure  $6^+$  member of the proton  $h_{9/2}^6$  seniority multiplet of the radium core, opening of the  $N = 126$  closed shell generates several  $4^+$  and especially  $2^+$  states with mixed configurations seen as a sudden drop of energies of the low-lying yrast states in these nuclei. In  $^{212}\text{Ra}$ , the  $2^+$  state can be associated with a dominant neutron  $(p_{1/2}^{-1} f_{5/2}^{-1})_{2^+}$  configuration and in  $^{210}\text{Ra}$  with a dominant neutron  $(p_{1/2}^{-2} f_{5/2}^{-2})_{2^+}$  configuration [36,37].

Similarly to  $^{209}\text{Fr}$ , we observe two  $(\frac{17}{2}^-)$  states in  $^{211}\text{Ac}$ , the upper one being favored in the de-excitation of the  $(\frac{21}{2}^-)$  state by  $E2$  transitions. Therefore, as in  $^{209}\text{Fr}$ , it is assigned with a coupling of the  $h_{9/2}$  quasiproton to the  $4_2^+$  core state of the dominant proton  $h_{9/2}^6$  configuration. The lower (yrast)  $(\frac{17}{2}^-)$  state represents a coupling of the same proton to a  $4_1^+$  state of a dominant neutron  $(p_{1/2}^{-2} f_{5/2}^{-2})_{4^+}$  configuration. Such  $4^+$  states with similar assignments have been observed in  $^{210}\text{Ra}$  [37].

The case of the even-odd  $^{211}\text{Ra}$  is similar to that of  $^{211}\text{Ac}$  and  $^{213}\text{Ac}$ , but instead of the extra proton, it has an active neutron-hole in the  $f_{5/2}$  shell. Its structure therefore resembles that of its heavier neighboring even-even isotope  $^{212}\text{Ra}$ . Consequently, the level energy systematics of  $N = 123$  isotones exhibit smooth behavior, as shown in Fig. 12. The list of

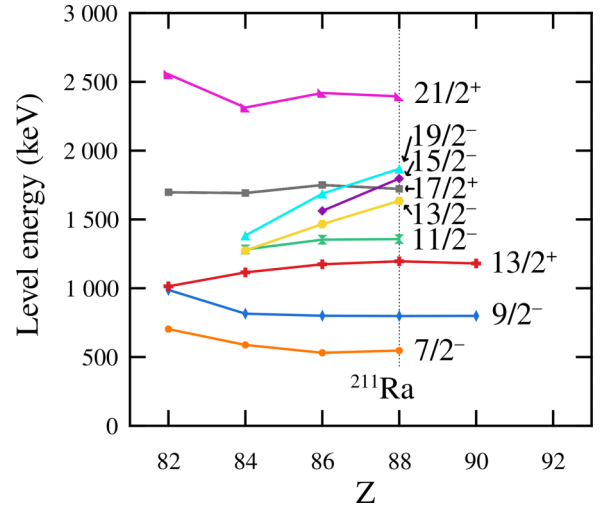


FIG. 12. Level-energy systematics of selected states in  $N = 123$  isotones. The points on the dotted line ( $Z = 88$ ) are the proposed levels in  $^{211}\text{Ra}$  from the present study. The other points are taken from Refs. [42–45].

suggested configurations for observed states of  $^{211}\text{Ra}$  can be found in Table III.

Both  $^{212}\text{Ra}$  and  $^{210}\text{Ra}$  have a low-lying isomeric  $8^+$  state with a half-life of several microseconds, but no signs of such metastable states were seen in  $^{213}\text{Ac}$  nor in  $^{211}\text{Ac}$ . However, nuclei in this area of the nuclear chart are known to have isomeric states with half-lives around 10–100 ns. For example, in nearby astatine and francium nuclei, isomeric states with a spin and parity of  $\frac{25}{2}^+$  or  $\frac{29}{2}^+$  are commonly present [29,32,33,40,41]. Our setup was not sensitive to decays of isomeric states within this time regime as they would predominantly decay in flight, outside both the target and focal-plane positions, and thus would remain unnoticed. The time of flight through the separator was close to 1.3  $\mu\text{s}$ . The presence of such nanosecond-scale isomers might explain the sudden termination of the observed cascades above the  $(\frac{23}{2}^-)$  state. Furthermore, the strong internal conversion branches and resulting strong x-ray background, could also prevent us from observing low-energy transitions, also abundant in nearby nuclei. The level structure of nearby nuclei fragments above the  $\frac{21}{2}^-$  state, which makes it difficult to construct level schemes, especially with limited statistics.

However, the recoil-decay tagging method is one of the few feasible ways to probe the excited states of actinium isotopes. A clean tag is needed for unambiguous identification of reaction products as the nuclei in this region share remarkably similar decay properties. The power of combining an in-flight separator with the RDT method lies on the unprecedented selectivity gained from the multiple tagging conditions at the focal plane. When employed with an efficient Ge-detector array at the target area, it enables a clean identification of cascades of prompt  $\gamma$ -ray transitions, including those bypassing isomers. Moreover, the observed intensities of prompt  $\gamma$  rays allow the order of transitions in a cascade to be determined, which is difficult in off-beam detection of  $\gamma$  rays emitted in

TABLE IV. Summary of the measured half-lives ( $T_{\frac{1}{2}}^{\text{meas.}}$ ) together with the values from literature ( $T_{\frac{1}{2}}^{\text{lit.}}$ ).

Nucleus	$T_{\frac{1}{2}}^{\text{meas.}}$	$T_{\frac{1}{2}}^{\text{lit.}}$
$^{211}\text{Ra}$	13.7(2) s	13(2) s [30]
$^{211\text{m}}\text{Ra}$	9.6(2) $\mu\text{s}$	9.7(6) $\mu\text{s}$ [15]
$^{211}\text{Ac}$	228(4) ms	210(30) ms [30]
$^{212}\text{Ac}$	881(15) ms	880(35) ms [28]
$^{213}\text{Ac}$	771(14) ms	738(16) ms [27]

the decay of isomers. For these reasons the low-lying level structure of many radium, francium, and astatine isotopes in this region are not without ambiguities and could certainly benefit from further studies using in-beam RDT methods to, for example, probe de-excitation paths bypassing the  $8^+$  and other isomeric states.

## V. SUMMARY

In the present work, we have established the first level scheme for the isotope  $^{211}\text{Ac}$ , corrected and extended the level scheme for the isotope  $^{213}\text{Ac}$ . We have shown that the energies of their ( $\frac{13}{2}^-$ ), ( $\frac{17}{2}^-$ ), ( $\frac{21}{2}^-$ ) states closely follow the energies of their respective even-even core states in a similar manner as has been seen in the other odd-even nuclei in this region.  $\gamma$ -ray

transitions assigned to the odd-odd  $^{210}\text{Ac}$  and  $^{212}\text{Ac}$  isotopes were identified but no level scheme was constructed. We also extended the level scheme of even-odd isotope  $^{211}\text{Ra}$  beyond the ( $\frac{13}{2}^+$ ) isomeric state, and identified two parallel decay paths bypassing the metastable state. This enabled us to assign configurations and extend systematics of high-spin states of  $N = 123$  isotones up to  $Z = 88$ . Additionally, we measured the half-lives for all isotopes and isomeric states present in the data, for which an improvement could be made. These values are summarized in Table IV.

The data obtained in the present work and the corresponding metadata are available online [46].

## ACKNOWLEDGMENTS

This work was supported by the Research Council of Finland under Contracts No. 323710, No. 347154, No. 353786 (personal research projects, KA), and No. 339245. The project has received funding from the EU Horizon 2020 research and innovation programme under Grant Agreement No. 861198–LISA–H2020–MSCA–ITN–2019. The authors thank the GAMMAPOOL European Spectroscopy Resource for the loan of the germanium detectors and GSI target laboratory for providing the carbon foils and targets for this experiment. The authors would also like to express their gratitude to the technical staff of the Accelerator Laboratory at the University of Jyväskylä for their support.

- [1] R. Julin, T. Grahn, J. Pakarinen, and P. Rahkila, *J. Phys. G: Nucl. Part. Phys.* **43**, 024004 (2016).
- [2] C. Qi, R. Liotta, and R. Wyss, *Prog. Part. Nucl. Phys.* **105**, 214 (2019).
- [3] R. Ferrer, A. Barzakh, B. Bastin, R. Beerwerth, M. Block, P. Creemers, H. Grawe, R. de Groote, P. Delahaye, X. Fléchar, S. Franchoo, S. Fritzsche, L. P. Gaffney, L. Ghys, W. Gins, C. Granados, R. Heinke, L. Hijazi, M. Huyse, T. Kron *et al.*, *Nat. Commun.* **8**, 14520 (2017).
- [4] J. Ojala, J. Pakarinen, P. Papadakis, J. Sorri, M. Sandzelius, D. M. Cox, K. Auranen, H. Badran, P. J. Davies, T. Grahn, P. T. Greenlees, J. Henderson, A. Herzán, R.-D. Herzberg, J. Hilton, U. Jakobsson, D. G. Jenkins, D. T. Joss, R. Julin, S. Juutinen *et al.*, *Commun. Phys.* **5**, 213 (2022).
- [5] S. Hilaire and M. Girod, *Eur. Phys. J. A* **33**, 237 (2007).
- [6] P. Möller, A. Sierk, T. Ichikawa, and H. Sagawa, *At. Data Nucl. Data Tables* **109–110**, 1 (2016).
- [7] M. Leino, J. Uusitalo, T. Enqvist, K. Eskola, A. Jokinen, K. Loberg, W. H. Trzaska, and J. Äystö, *Z. Phys. A* **348**, 151 (1994).
- [8] F. P. Heßberger, S. Hofmann, D. Ackermann, V. Ninov, M. Leino, S. Saro, A. Andreyev, A. Lavrentev, A. G. Popeko, and A. V. Yeremin, *Eur. Phys. J. A* **8**, 521 (2000).
- [9] F. Heßberger, S. Hofmann, I. Kojouharov, D. Ackermann, S. Antalic, P. Cagarda, B. Kindler, B. Lommel, R. Mann, A. Popeko, S. Saro, J. Uusitalo, and A. Yeremin, *Eur. Phys. J. A* **15**, 335 (2002).
- [10] Z. Y. Zhang, Z. G. Gan, L. Ma, L. Yu, H. B. Yang, T. H. Huang, G. S. Li, Y. L. Tian, Y. S. Wang, X. X. Xu, X. L. Wu, M. H. Huang, C. Luo, Z. Z. Ren, S. G. Zhou, X. H. Zhou, H. S. Xu, and G. Q. Xiao, *Phys. Rev. C* **89**, 014308 (2014).
- [11] J. Wang, Z. Gan, Z. Zhang, M. Huang, L. Ma, M. Zhang, H. Yang, C. Yang, Y. Qiang, X. Huang, Z. Zhao, S. Xu, Z. Li, L. Chen, L. Sun, H. Zhou, X. Zhang, X. Wu, Y. Tian, Y. Wang *et al.*, *Phys. Lett. B* **850**, 138503 (2024).
- [12] C. Granados, P. Creemers, R. Ferrer, L. P. Gaffney, W. Gins, R. de Groote, M. Huyse, Y. Kudryavtsev, Y. Martínez, S. Raeder, S. Sels, C. Van Beveren, P. Van den Bergh, P. Van Duppen, K. Wrzosek-Lipska, A. Zadornaya, A. E. Barzakh, B. Bastin, P. Delahaye, L. Hijazi *et al.*, *Phys. Rev. C* **96**, 054331 (2017).
- [13] F. P. Heßberger, S. Hofmann, I. Kojouharov, and D. Ackermann, *Eur. Phys. J. A* **22**, 253 (2004).
- [14] P. Kuusiniemi, F. P. Heßberger, D. Ackermann, S. Hofmann, B. Sulignano, I. Kojouharov, and R. Mann, *Eur. Phys. J. A* **25**, 397 (2005).
- [15] K. Hauschild, A. Yeremin, O. Dorvaux, A. Lopez-Martens, A. Belozero, C. Briancón, M. Chelnokov, V. Chepigin, S. Garcia-Santamaria, V. Gorshkov, F. Hanappe, A. Kabachenko, A. Korichi, O. Malyshev, Y. Oganessian, A. Popeko, N. Rowley, A. Shutov, L. Stuttgé, and A. Svirikhin, *Nucl. Instrum. Methods Phys. Res. A* **560**, 388 (2006).
- [16] J. Pakarinen, J. Ojala, P. Ruotsalainen, H. Tann, H. Badran, T. Calverley, J. Hilton, T. Grahn, P. T. Greenlees, M. Hytönen, A. Illana, A. Kauppinen, M. Luoma, P. Papadakis, J. Partanen, K. Porras, M. Puskala, P. Rahkila, K. Ranttila, J. Sarén *et al.*, *Eur. Phys. J. A* **56**, 149 (2020).
- [17] J. Sarén, J. Uusitalo, M. Leino, P. Greenlees, U. Jakobsson, P. Jones, R. Julin, S. Juutinen, S. Ketelhut, M. Nyman, P. Peura,



- and P. Rahkila, *Nucl. Instrum. Methods Phys. Res. B* **266**, 4196 (2008).
- [18] J. Uusitalo, J. Sarén, J. Partanen, and J. Hilton, *Acta Phys. Pol. B* **50**, 319 (2019).
- [19] E. S. Paul, P. J. Woods, T. Davinson, R. D. Page, P. J. Sellin, C. W. Beausang, R. M. Clark, R. A. Cunningham, S. A. Forbes, D. B. Fossan, A. Gizon, J. Gizon, K. Hauschild, I. M. Hibbert, A. N. James, D. R. LaFosse, I. Lazarus, H. Schnare, J. Simpson, R. Wadsworth *et al.*, *Phys. Rev. C* **51**, 78 (1995).
- [20] R. S. Simon, K. H. Schmidt, F. P. Heßberger, S. Hlavac, M. Honusek, G. Münzenberg, H. G. Clerc, U. Gollerthan, and W. Schwab, *Z. Phys. A* **325**, 197 (1986).
- [21] I. Lazarus, E. Appelbe, P. Butler, P. Coleman-Smith, J. Cresswell, S. Freeman, R. Herzberg, I. Hibbert, D. Joss, S. Letts, R. Page, V. Pucknell, P. Regan, J. Sampson, J. Simpson, J. Thornhill, and R. Wadsworth, *IEEE Trans. Nucl. Sci.* **48**, 567 (2001).
- [22] J. Sarén, J. Uusitalo, and H. Joukainen, *Nucl. Instrum. Methods Phys. Res. B* **541**, 33 (2023).
- [23] M. Martin, *Nucl. Data Sheets* **108**, 1583 (2007).
- [24] J. Chen and F. Kondev, *Nucl. Data Sheets* **126**, 373 (2015).
- [25] P. Kuusiniemi, F. P. Heßberger, D. Ackermann, S. Hofmann, and I. Kojouharov, *Eur. Phys. J. A* **22**, 429 (2004).
- [26] K. H. Schmidt, *Eur. Phys. J. A* **8**, 141 (2000).
- [27] M. Basunia, *Nucl. Data Sheets* **181**, 475 (2022).
- [28] H. Yang, L. Ma, Z. Zhang, L. Yu, G. Jia, M. Huang, Z. Gan, T. Huang, G. Li, X. Wu, Y. Fang, Z. Wang, B. Gao, and W. Hua, *J. Phys. G: Nucl. Part. Phys.* **41**, 105104 (2014).
- [29] G. D. Dracoulis, P. M. Davidson, G. J. Lane, A. P. Byrne, T. Kibédi, P. Nieminen, H. Watanabe, and A. N. Wilson, *Phys. Rev. C* **79**, 054313 (2009).
- [30] B. Singh, D. Abriola, C. Baglin, V. Demetriou, T. Johnson, E. McCutchan, G. Mukherjee, S. Singh, A. Sonzogni, and J. Tuli, *Nucl. Data Sheets* **114**, 661 (2013).
- [31] A. D. Bacelar, A. Bruce, Z. Podolyák, N. Al-Dahan, M. Górska, S. Lalkovski, S. Pietri, M. Ricciardi, A. Algora, N. Alkhomashi, J. Benlliure, P. Boutachkov, A. Bracco, E. Calore, E. Casarejos, I. Cullen, A. Deo, P. Detistov, Z. Dombradi, C. Domingo-Pardo *et al.*, *Phys. Lett. B* **723**, 302 (2013).
- [32] K. Auranen, J. Uusitalo, S. Juutinen, U. Jakobsson, T. Grahn, P. T. Greenlees, K. Hauschild, A. Herzán, R. Julin, J. Konki, M. Leino, J. Pakarinen, J. Partanen, P. Peura, P. Rahkila, P. Ruotsalainen, M. Sandzelius, J. Sarén, C. Scholey, J. Sorri, and S. Stolze, *Phys. Rev. C* **91**, 024324 (2015).
- [33] K. Auranen, J. Uusitalo, S. Juutinen, H. Badran, F. Defranchi Bisso, D. Cox, T. Grahn, P. T. Greenlees, A. Herzán, U. Jakobsson, R. Julin, J. Konki, M. Leino, A. Lightfoot, M. J. Mallaburn, O. Neuvonen, J. Pakarinen, P. Papadakis, J. Partanen, P. Rahkila *et al.*, *Phys. Rev. C* **97**, 024301 (2018).
- [34] U. Jakobsson, J. Uusitalo, S. Juutinen, M. Leino, T. Enqvist, P. T. Greenlees, K. Hauschild, P. Jones, R. Julin, S. Ketelhut, P. Kuusiniemi, M. Nyman, P. Peura, P. Rahkila, P. Ruotsalainen, J. Sarén, C. Scholey, and J. Sorri, *Phys. Rev. C* **85**, 014309 (2012).
- [35] U. Jakobsson, S. Juutinen, J. Uusitalo, M. Leino, K. Auranen, T. Enqvist, P. T. Greenlees, K. Hauschild, P. Jones, R. Julin, S. Ketelhut, P. Kuusiniemi, M. Nyman, P. Peura, P. Rahkila, P. Ruotsalainen, J. Sarén, C. Scholey, and J. Sorri, *Phys. Rev. C* **87**, 054320 (2013).
- [36] T. Palazzo, G. J. Lane, A. E. Stuchbery, A. J. Mitchell, A. Akber, M. S. M. Gerathy, S. S. Hota, T. Kibédi, B. Q. Lee, N. Palalani, and M. W. Reed, *Phys. Rev. C* **97**, 014323 (2018).
- [37] J. J. Ressler, C. W. Beausang, H. Ai, H. Amro, M. A. Caprio, R. F. Casten, A. A. Hecht, S. D. Langdown, E. A. McCutchan, D. A. Meyer, P. H. Regan, M. J. S. Sciacchitano, A. Yamamoto, and N. V. Zamfir, *Phys. Rev. C* **69**, 034331 (2004).
- [38] D. J. Decman, H. Grawe, H. Kluge, and K. H. Maier, *Z. Phys. A* **310**, 55 (1983).
- [39] A. Stuchbery, G. Dracoulis, T. Kibédi, A. Byrne, B. Fabricius, A. Poletti, G. Lane, and A. Baxter, *Nucl. Phys. A* **548**, 159 (1992).
- [40] A. Byrne, G. Dracoulis, C. Fahlander, H. Hübel, A. Poletti, A. Stuchbery, J. Gerl, R. Davie, and S. Poletti, *Nucl. Phys. A* **448**, 137 (1986).
- [41] K. Yadav, A. Y. Deo, Madhu, D. Sahoo, P. C. Srivastava, S. Suman, S. K. Tandel, A. Sharma, I. Ahmed, K. Katre, K. R. Devi, S. Dutt, S. Kumar, Yashraj, S. Muralithar, and R. P. Singh, *Phys. Rev. C* **107**, 054303 (2023).
- [42] J. Khuyagbaatar, S. Hofmann, F. P. Heßberger, D. Ackermann, S. Antalic, H. G. Burkhard, S. Heinz, B. Kindler, A. F. Lisetskiy, B. Lommel, R. Mann, K. Nishio, H. J. Schött, and B. Sulignano, *Eur. Phys. J. A* **34**, 355 (2007).
- [43] A. Poletti, G. Dracoulis, C. Fahlander, and A. Byrne, *Nucl. Phys. A* **440**, 118 (1985).
- [44] V. Rahkonen, B. Fant, C. Herrlander, K. Honkanen, A. Källberg, and T. Weckström, *Nucl. Phys. A* **441**, 11 (1985).
- [45] J. H. Hamilton, V. Ananthakrishnan, A. V. Ramayya, W. M. LaCasse, D. C. Camp, J. J. Pinajian, L. H. Kern, and J. C. Manthuruthil, *Phys. Rev. C* **6**, 1265 (1972).
- [46] <https://doi.org/10.23729/62121f8e-6d57-46b8-b74c-be32d7672957>